



SCICHEM Version 3.3

Technical Documentation

3002022845

SCICHEM Version 3.3

Technical Documentation

3002022845

Technical Update, December 2021

EPRI Project Manager

E. Knipping

EPRI

3420 Hillview Avenue, Palo Alto, California 94304-1338 • PO Box 10412, Palo Alto, California 94303-0813 • USA
800.313.3774 • 650.855.2121 • askepri@epri.com • www.epri.com

DISCLAIMER OF WARRANTIES AND LIMITATION OF LIABILITIES

ELECTRIC POWER RESEARCH INSTITUTE, INC. ("EPRI") RESERVES ALL RIGHTS IN THE PROGRAM AS DELIVERED. THE PROGRAM OR ANY PORTION THEREOF MAY NOT BE REPRODUCED IN ANY FORM WHATSOEVER EXCEPT AS PROVIDED BY LICENSE, WITHOUT THE CONSENT OF EPRI.

A LICENSE UNDER EPRI'S RIGHTS IN THE PROGRAM CAN BE OBTAINED DIRECTLY FROM EPRI.

THE EMBODIMENTS OF THIS PROGRAM AND SUPPORTING MATERIALS MAY BE INDEPENDENTLY AVAILABLE FROM ELECTRIC POWER SOFTWARE CENTER (EPSC) FOR AN APPROPRIATE DISTRIBUTION FEE.

Electric Power Software Center (EPSC)
9625 Research Drive
Charlotte, NC 28262

THIS NOTICE MAY NOT BE REMOVED FROM THE PROGRAM BY ANY USER THEREOF.

NEITHER EPRI, ANY MEMBER OF EPRI, THE ORGANIZATION(S) BELOW, NOR ANY PERSON ACTING ON BEHALF OF ANY OF THEM:

1. MAKES ANY WARRANTY OR REPRESENTATION WHATSOEVER, EXPRESS OR IMPLIED, INCLUDING ANY WARRANTY OF MERCHANTABILITY OR FITNESS OF ANY PURPOSE WITH RESPECT TO THE PROGRAM; OR
2. ASSUMES ANY LIABILITY WHATSOEVER WITH RESPECT TO ANY USE OF THE PROGRAM OR ANY PORTION THEREOF OR WITH RESPECT TO ANY DAMAGES WHICH MAY RESULT FROM SUCH USE.

RESTRICTED RIGHTS LEGEND: USE, DUPLICATION, OR DISCLOSURE BY THE GOVERNMENT IS SUBJECT TO RESTRICTION AS SET FORTH IN PARAGRAPH (G) (3) (I), WITH THE EXCEPTION OF PARAGRAPH (G) (3) (I) (B) (5), OF THE RIGHTS IN TECHNICAL DATA AND COMPUTER SOFTWARE CLAUSE IN FAR 52.227-14, ALTERNATE III.

REFERENCE HEREIN TO ANY SPECIFIC COMMERCIAL PRODUCT, PROCESS, OR SERVICE BY ITS TRADE NAME, TRADEMARK, MANUFACTURER, OR OTHERWISE, DOES NOT NECESSARILY CONSTITUTE OR IMPLY ITS ENDORSEMENT, RECOMMENDATION, OR FAVORING BY EPRI.

THE FOLLOWING ORGANIZATIONS, UNDER CONTRACT TO EPRI, PREPARED THIS REPORT:

Sage-Xator

Ramboll

NOTE

For further information about EPRI, call the EPRI Customer Assistance Center at 800.313.3774 or e-mail askepri@epri.com.

© 2021 Electric Power Research Institute (EPRI), Inc. All rights reserved. Electric Power Research Institute and EPRI are registered marks of the Electric Power Research Institute, Inc. in the U.S. and worldwide.

ACKNOWLEDGMENTS

The following organizations, under contract to the Electric Power Research Institute (EPRI), prepared this report:

Xator
3686 Quakerbridge Road
Suite 102
Hamilton, NJ 08619

Principal Investigators
D. S. Henn
R. I. Sykes

Ramboll
7250 Redwood Boulevard
Suite 105
Novato, CA 94945

Principal Investigator
P. Karamchandani

This report describes research sponsored by EPRI.

This publication is a corporate document that should be cited in the literature in the following manner:

SCICHEM Version 3.3: Technical Documentation. EPRI, Palo Alto, CA: 2021. 3002022845.

ABSTRACT

SCICHEM, which stands for SCIPUFF with Chemistry, is used to model the transport, dispersion, and chemical reaction of gaseous and aerosol releases in the atmosphere using gas-phase, aqueous-phase, and aerosol chemistry treatments comparable to those in photochemical grid models (PGMs). In SCIPUFF, atmospheric turbulence is modeled using second-order closure, and a collection of three-dimensional Gaussian puffs is used to represent a time-dependent concentration field. SCICHEM can be used to study the impact on air quality from single or multiple sources.

The technical basis of SCICHEM 3.3 is described in this document. A section describing several test calculations and comparison with observational data is also included.

Keywords

Air quality model

NO_x

Ozone

Particulate matter

SCIPUFF

SCICHEM

Single-source applications

Secondary pollutants

Deliverable Number: 3002022845

Product Type: Software

Product Title: SCICHEM Version 3.3: Technical Documentation

PRIMARY AUDIENCE: Users of the SCICHEM air quality model and reviewers of modeling results

KEY RESEARCH QUESTION

The technical basis of SCICHEM 3.3 is described in this document. A section describing several test calculations and comparison with observational data is also included.

RESEARCH OVERVIEW

SCICHEM—SCIPUFF with Chemistry—is used to model the transport, dispersion, and chemical reaction of gaseous and aerosol releases in the atmosphere using gas-phase, aqueous-phase, and aerosol chemistry treatments comparable to those in photochemical grid models (PGMs). In SCIPUFF, atmospheric turbulence is modeled using second-order closure, and a collection of three-dimensional Gaussian puffs is used to represent a time-dependent concentration field. SCICHEM can be used to study the impact on air quality from single or multiple sources.

KEY FINDINGS

- The technical basis of SCICHEM 3.3 is described, including a section describing several test calculations and comparison with observational data.
- SCICHEM uses a collection of Gaussian puffs to represent an arbitrary three-dimensional, time-dependent concentration field and incorporates an efficient scheme for splitting and merging puffs.
- Wind shear effects are accurately modeled, and puffs are split when they grow too large for a single point meteorology to be representative. These techniques allow the puff model to describe complex flow effects on dispersion, such as terrain-driven circulation.
- Individual puffs use a time step appropriate for resolving its local evolution rate so that the multiscale range can be accurately described in the time domain without using a small step for the entire calculation.
- The model uses several types of meteorological inputs, including surface and upper air observations or three-dimensional grid data.
- Planetary boundary layer turbulence is represented explicitly in terms of surface heat flux and shear stress using parameterized profile shapes.
- SCICHEM uses gaseous and particle materials and can handle multiple sources with different geometries.

WHY THIS MATTERS

SCICHEM is a Lagrangian photochemical puff model that is an alternative to steady-state Gaussian plume models for modeling of ambient SO₂ and NO₂ concentrations. SCICHEM also provides an alternative to more resource-intensive photochemical grid models for single-source air quality modeling applications involving formation of secondary pollutants such as ozone and fine particulate matter.

HOW TO APPLY RESULTS

How to setup and run the model is described in the SCICHEM Version 3.3 User's Guide.

LEARNING AND ENGAGEMENT OPPORTUNITIES

- Training on SCICHEM will be offered after model releases and may also be offered at air quality modeling conferences.

EPRI CONTACTS: Eladio Knipping, Program Manager, eknipping@epri.com

PROGRAM: Atmospheric Models and Ambient Measurements, P234

Together...Shaping the Future of Energy™

EPRI

3420 Hillview Avenue, Palo Alto, California 94304-1338 • PO Box 10412, Palo Alto, California 94303-0813 USA

[800.313.3774](tel:800.313.3774) • [650.855.2121](tel:650.855.2121) • askepri@epri.com • www.epri.com

© 2021 Electric Power Research Institute (EPRI), Inc. All rights reserved. Electric Power Research Institute and EPRI are registered marks of the Electric Power Research Institute, Inc. in the U.S. and worldwide.

CONTENTS

| | |
|--|------------|
| ABSTRACT | V |
| EXECUTIVE SUMMARY | VII |
| 1 INTRODUCTION | 1-1 |
| 2 TRANSPORT AND DIFFUSION | 2-1 |
| 2.1 Puff Moment Equations | 2-1 |
| 2.1.1 Gaussian Moment Definition | 2-1 |
| 2.1.2 Moment Transport Equations | 2-2 |
| 2.1.3 Turbulence Closure Diffusion Model | 2-3 |
| 2.2 Concentration Fluctuation Variance | 2-11 |
| 2.2.1 Concentration Variance Equation | 2-11 |
| 2.2.2 Scalar Fluctuation Dissipation Timescale | 2-13 |
| 2.2.3 Vertical Wind Shear Effects | 2-17 |
| 2.2.4 Puff Interaction Treatment | 2-19 |
| 2.2.5 Conditional Average Dispersion | 2-23 |
| 2.3 Surface Deposition | 2-25 |
| 2.4 Surface Integrals | 2-26 |
| 2.4.1 Surface Dose or Dosage Integration | 2-26 |
| 2.4.2 Surface Deposition Integration | 2-28 |
| 3 REACTIVE CHEMISTRY | 3-1 |
| 3.1 Gas-Phase Chemistry | 3-1 |
| 3.2 Aerosol and Aqueous-Phase Chemistry | 3-3 |
| 4 NUMERICAL TECHNIQUES | 4-1 |
| 4.1 Finite Difference Schemes | 4-1 |
| 4.2 Puff Splitting | 4-4 |
| 4.2.1 Splitting Scheme | 4-4 |
| 4.2.2 Splitting Criteria | 4-7 |
| 4.3 Puff Merging Scheme | 4-10 |
| 4.4 Puff Inversion Capping | 4-13 |
| 4.5 Adaptive Timesteps | 4-15 |
| 4.6 Static Puffs | 4-17 |
| 4.7 Adaptive Surface Grids | 4-19 |
| 4.8 Chemistry Solvers | 4-20 |
| 5 GAS MATERIALS AND DYNAMIC EFFECTS | 5-1 |
| 5.1 Gas Material Properties | 5-1 |
| 5.2 Buoyancy and Momentum Rise | 5-1 |
| 5.2.1 Mean Flow Dynamics | 5-1 |
| 5.2.2 Buoyant Gas Representation | 5-4 |
| 5.2.3 Turbulent Entrainment | 5-5 |

| | |
|---|-------------|
| 5.2.4 Inversion Penetration | 5-6 |
| 5.3 Dense Gas Effects | 5-7 |
| 5.3.1 Mean Flow Dynamics | 5-7 |
| 5.3.2 Dynamics with Uncertainty | 5-11 |
| 5.3.3 Turbulent Entrainment | 5-12 |
| 5.3.4 Surface Drag | 5-13 |
| 5.3.5 Terrain Effects | 5-14 |
| 6 PARTICLE MATERIALS | 6-1 |
| 6.1 Particle Material Properties | 6-1 |
| 6.2 Particle Gravitational Settling | 6-1 |
| 6.2.1 Particle Fall Velocity | 6-1 |
| 6.2.2 SCICHEM Implementation | 6-2 |
| 6.3 Particle Dry Deposition | 6-3 |
| 6.3.1 Surface Deposition Process | 6-3 |
| 6.3.2 Particle Deposition Efficiencies | 6-5 |
| 6.4 Precipitation Washout | 6-7 |
| 6.5 Effects on Diffusion | 6-7 |
| 7 MULTICOMPONENT MATERIALS | 7-1 |
| 7.1 Multicomponent Material Properties | 7-1 |
| 7.2 Multicomponent Dry Deposition | 7-1 |
| 7.2.1 Dry Deposition and Gravitational Settling of Aerosols | 7-1 |
| 7.2.2 Dry Deposition of Gases | 7-1 |
| 7.3 Multicomponent Precipitation Washout | 7-1 |
| 7.3.1 Wet Deposition of Multicomponent Aerosols | 7-1 |
| 7.3.2 Wet Deposition of Multicomponent Gases | 7-1 |
| 8 SOURCE SPECIFICATION | 8-1 |
| 8.1 Continuous Sources | 8-1 |
| 8.2 Instantaneous Sources | 8-2 |
| 8.3 Linear Decay | 8-2 |
| 9 METEOROLOGY SPECIFICATION | 9-1 |
| 9.1 Background | 9-1 |
| 9.2 Observational Input | 9-1 |
| 9.3 Gridded Input | 9-4 |
| 9.3.1 File Format Types | 9-4 |
| 9.3.2 Terrain | 9-5 |
| 9.4 Mean Field Interpolation | 9-6 |
| 9.5 Mass Consistency | 9-7 |
| 9.6 Nested Meteorological Fields | 9-8 |
| 9.7 Smoothed Meteorological Fields | 9-9 |
| 10 PLANETARY BOUNDARY LAYER | 10-1 |

| | |
|---|-------------|
| 10.1 Governing Parameters | 10-1 |
| 10.1.1 Monin-Obukhov Length, L | 10-1 |
| 10.1.2 Friction Velocity, u_* | 10-2 |
| 10.1.3 Temperature Scale, θ_* | 10-3 |
| 10.1.4 Convective Velocity Scale, w_* | 10-4 |
| 10.2 Specifying PBL Parameters | 10-4 |
| 10.2.1 Roughness Height | 10-5 |
| 10.2.2 Reference Height and Velocity | 10-5 |
| 10.2.3 Surface Heat Flux | 10-5 |
| 10.2.4 Boundary Layer Height | 10-10 |
| 10.3 PBL Mean Profiles | 10-13 |
| 10.4 Vegetative/Urban Canopy Profiles | 10-15 |
| 10.5 Surface Layer Interpolation | 10-17 |
| 10.5.1 Homogeneous Land Cover | 10-17 |
| 10.5.2 Inhomogeneous Land Cover | 10-19 |
| 11 TURBULENCE SPECIFICATION | 11-1 |
| 11.1 Planetary Boundary Layer | 11-1 |
| 11.2 Vegetative/Urban Canopy Layer | 11-3 |
| 11.3 Mesoscale/Synoptic Scale | 11-4 |
| 11.4 Meteorological Uncertainties | 11-5 |
| 12 MODEL OUTPUT | 12-1 |
| 12.1 Local Concentration Values | 12-1 |
| 12.1.1 Tracer Concentration | 12-1 |
| 12.1.2 Multicomponent Species Concentration | 12-2 |
| 12.2 Probabilistic Calculation | 12-5 |
| 12.2.1 Probability Density Function | 12-5 |
| 13 MODEL EVALUATION STUDIES | 13-1 |
| 13.1 Short-Range Diffusion | 13-1 |
| 13.1.1 Pasquill-Gifford-Turner Stability Categories | 13-1 |
| 13.1.2 Model Data Archive | 13-2 |
| 13.1.3 Instantaneous Dispersion | 13-5 |
| 13.1.4 CONFLUX | 13-8 |
| 13.2 Long-Range Diffusion | 13-11 |
| 13.3 Dynamic Rise Effects | 13-15 |
| 13.3.1 Momentum Jet | 13-15 |
| 13.3.2 Buoyant Plume | 13-17 |
| 13.3.3 Buoyant Puff | 13-20 |
| 13.4 Dense Gas Effects | 13-22 |
| 13.5 Chemical Transformations | 13-23 |
| 14 REFERENCES | 14-1 |

LIST OF FIGURES

| | |
|--|-------|
| Figure 2-1 Vertical velocity probability density functions for neutral (solid line) and free convection (dashed line) conditions, based on the model of Luhar et al. (1996) | 2-11 |
| Figure 2-2 Nondimensional fluctuation dissipation timescale as a function of dimensionless time for a shear-distorted Gaussian puff. The solid line is the analytic solution (Equation 2-67). Dashed line is the model prediction from Equations 2-68 and 2-70. | 2-18 |
| Figure 4-1 Maximum dimensionless error, ε_S , from splitting a single Gaussian puff as a function of separation distance, δ_S . The error is relative to the maximum concentration value in the original Gaussian, and the separation distance of the puffs after splitting is relative to the original Gaussian spread. Results are shown for both one-dimensional and two-dimensional splits. | 4-6 |
| Figure 4-2 Schematic illustration of puff reflection for a split below the ground surface | 4-7 |
| Figure 4-3 Schematic illustration of the adaptive multigrid for locating puffs. Grid cell numbers are represented as C- n , and two levels of refinement are shown. See text for a description of the cell storage rules. | 4-12 |
| Figure 4-4 Schematic illustration of the use of static puffs to represent a continuous source. The shaded puff is stored as the release description at the end of the static phase. | 4-17 |
| Figure 5-1 Schematic illustration of slumping dense cloud | 5-9 |
| Figure 5-2 Simplified velocity field representation for a dense cloud | 5-9 |
| Figure 10-1 Schematic illustration of the idealized velocity profile in the planetary boundary layer | 10-14 |
| Figure 10-2 Canopy velocity profile shapes from Equations 10-50 and 10-51 compared with the experimental data of Cionco (1972). | 10-16 |
| Figure 10-3 Example of surface layer interpolation. Open circles indicate observation or outer domain velocities used for interpolation. The solid line is the interpolated velocity profile. The long dash lines are surface layer profiles scaled to pass through the interpolating points below the surface layer height $z_s^{(o)}$. Sections of the interpolated profile are labeled with the corresponding cases (i)–(iv) from the text. | 10-18 |
| Figure 10-4 Example of surface layer interpolation for inhomogeneous land cover. This example shows how an idealized surface layer profile with no canopy is interpolated to a location where $h_c^{(n)} = 10\text{ m}$ and $\alpha_c^{(n)} = 3$ | 10-21 |
| Figure 11-1 Normalized error variance growth for forecast and persistence assumptions | 11-6 |
| Figure 12-1 Schematic illustration of a positive species perturbation concentration | 12-3 |
| Figure 12-2 Schematic illustration of a negative species perturbation concentration | 12-3 |
| Figure 12-3 Local total concentration with and without enhanced spread | 12-5 |
| Figure 13-1 Comparison between SCIPUFF predictions (solid lines) and the PGT dispersion curves for Categories A through F | 13-2 |
| Figure 13-2 Comparison between the observed maximum concentrations and SCIPUFF predictions for the passive releases in the Model Data Archive. Various experiments are indicated by the letter codes. | 13-4 |
| Figure 13-3 Comparison between SCIPUFF predictions and the observational data of Weil et al. (1993) | 13-6 |
| Figure 13-4 Comparison between SCIPUFF predictions and the observational data of Mikkelsen et al. (1987) | 13-7 |

| | |
|--|-------|
| Figure 13-5 Comparison between SCIPUFF predictions and the observational data of Högström (1964) | 13-8 |
| Figure 13-6 Comparison between SCIPUFF predictions of mean concentration and the observational data from CONFLUX 1994 | 13-9 |
| Figure 13-7 Comparison between SCIPUFF predictions of standard deviation to mean concentration ratio and the observational data of CONFLUX 1994 | 13-10 |
| Figure 13-8 Comparison of mean concentration between SCIPUFF predictions and ETEX data (Mosca et al., 1997). Contours are 0.01, 0.02, 0.05, 0.1, 0.2, 0.5, 1, 2, 5, 10, 20, and 50 ngm ⁻³ | 13-12 |
| Figure 13-9 Comparison between 3-hr average concentrations from SCIPUFF predictions (dashed) and ETEX data (solid line) at 9 selected locations (Mosca et al., 1997). Concentration is in ngm ⁻³ | 13-13 |
| Figure 13-10 Momentum (non-buoyant) jet centerline height, z'/r_0 , as a function of downstream distance for a range of R . Symbols are the data of Gordier (1959), from Hirst (1971); solid lines are the SCIPUFF predictions..... | 13-16 |
| Figure 13-11 Comparison between SCIPUFF predictions of momentum jet centerline heights for a range of R (solid lines) and the “one-third” law (Equation 13-3), with two values of β (short dashes, $\beta = 0.6$; long dashes, $\beta = 0.5$) | 13-17 |
| Figure 13-12 Comparison between SCIPUFF predictions for buoyancy-dominated jet centerline heights (solid lines) and theory given by Equation 13-5 (dashed lines). Case A: $R = 10$, $F_b^2/U_a^4 F_m = 0.01$; Case B: $R = 10$, $F_b^2/U_a^4 F_m = 1$; Case C: $R = 1$, $F_b^2/U_a^4 F_m = 1$ | 13-19 |
| Figure 13-13 Comparison of SCIPUFF buoyancy-dominated jet centerline heights in a uniformly stratified background (solid lines) with Equation 13-6 (dashed lines). For all cases, $R = 10$. Case A: $F_b^2/U_a^4 F_m = 0.01$, $F_b N/U_a^4 = 0.00572$; Case B: $F_b^2/U_a^4 F_m = 1$, $F_b N/U_a^4 = 0.00572$; Case C: $F_b^2/U_a^4 F_m = 1$, $F_b N/U_a^4 = 0.181$ | 13-20 |
| Figure 13-14 Centroid height of a light bubble released into a neutral quiescent background. Symbols are the data of Mantrom and Haigh (1973); solid lines are the SCIPUFF predictions. The Reynolds number for the experiments is based on the initial bubble diameter and the terminal velocity of a corresponding non-entraining sphere. Case A is for a single puff release with a Gaussian spread of $D_0/2$; Case B is for a release composed of 136 puffs representing a uniform distribution of mass within a spherical bubble of diameter D_0 . (a) early time behavior; (b) expanded scale showing late-time behavior. | 13-21 |
| Figure 13-15 Comparison between the observed maximum concentrations and SCIPUFF predictions for the dense gas releases in the Model Data Archive. Various experiments are indicated by the letter codes..... | 13-23 |
| Figure 13-16 Results for Plume 5 at 20 km on August 25, 1998 | 13-24 |
| Figure 13-17 Results for Plume 7 at 55 km on August 25, 1998 | 13-24 |
| Figure 13-18 Results for Plume 2 at 18 km on August 26, 1998 | 13-25 |
| Figure 13-19 Results for Plume 4 at 27 km on August 26, 1998 | 13-25 |
| Figure 13-20 Results for Plume 2 at 11 km on July 6, 1999 | 13-26 |
| Figure 13-21 Results for Plume 9 at 65 km on July 6, 1999 | 13-26 |
| Figure 13-22 Results for Plume 2 at 16 km on July 15, 1999 | 13-27 |
| Figure 13-23 Results for Plume 11 at 106 km on July 15, 1999 | 13-27 |

LIST OF TABLES

| | |
|--|-------|
| Table 10-1 Suggested values for surface roughness (Saucier, 1987) | 10-5 |
| Table 10-2 Relationship between stability index, PGT stability class, Monin-Obukhov length, L , and an assumed boundary layer depth, z_i , if not specified as input..... | 10-6 |
| Table 10-3 Suggested values for surface albedo as a function of land use and season (Paine, 1987)..... | 10-9 |
| Table 10-4 Suggested values for Bowen ratio as a function of land use and season (Paine, 1987)..... | 10-9 |
| Table 13-1 Statistical measures for the SCIPUFF prediction of ETEX data | 13-14 |
| Table 13-2 Average Hourly Emissions Data | 13-28 |

1

INTRODUCTION

SCIPUFF is a Lagrangian transport and diffusion model for atmospheric dispersion applications. The acronym SCIPUFF stands for Second-order Closure Integrated PUFF and describes two basic aspects of the model. First, the numerical technique employed to solve the dispersion model equations is the Gaussian puff method (Bass, 1980) in which a collection of three-dimensional puffs is used to represent an arbitrary time-dependent concentration field. Second, the turbulent diffusion parameterization used in SCIPUFF is based on the second-order turbulence closure theories of Donaldson (1973) and Lewellen (1977), providing a direct connection between measurable velocity statistics and the predicted dispersion rates. SCIPUFF has now been expanded to include gas and aqueous-phase chemistry and aerosol thermodynamics. The reactive SCIPUFF model is referred to as *SCICHEM*.

The Lagrangian puff methodology affords several advantages for atmospheric dispersion applications from localized sources. The Lagrangian scheme avoids the artificial diffusion problems inherent in any Eulerian advection scheme and allows an accurate treatment of the wide range of length scales as a plume or cloud grows from a small source size and spreads onto larger atmospheric scales. This range may extend from a few meters up to continental or global scales of thousands of kilometers. In addition, the puff method provides robust prediction under coarse resolution conditions, giving a flexible model for rapid assessment when detailed results are not required. The model is highly efficient for multiscale dispersion problems because puffs can be merged as they grow, and resolution is therefore adapted to each stage of the diffusion process.

The efficiency of SCICHEM has been improved by the implementation of adaptive time stepping and output grids. Each puff uses a time step appropriate for resolving its local evolution rate so that the multiscale range can be accurately described in the time domain without using a small step for the entire calculation. The output spatial fields are also computed on an adaptive grid, avoiding the need for the user to specify grid information and providing a complete description of the concentration field within computational constraints.

The generality of the turbulence closure relations provides a dispersion representation for arbitrary conditions. Empirical models based on specific dispersion data are limited in their range of application, but the fundamental relationship between the turbulent diffusion and the velocity fluctuation statistics is applicable for a much wider range. Our understanding of the daytime planetary boundary layer velocity fluctuations provides reliable input for the second-order closure description of dispersion for these conditions. For larger scales and upper atmosphere stable conditions, the turbulence description is based on climatological information, but the closure framework is in place to accept improvement as our understanding of these regimes improves. The closure model has been applied on local scales up to 50-km range (Sykes et al., 1988) and on continental scales up to 3000-km range (Sykes et al., 1993c).

The second-order closure model also provides the probabilistic feature of SCICHEM through the prediction of the concentration fluctuation variance. In addition to giving a mean value for the concentration field, SCICHEM provides a quantitative value for the random variation in the concentration value because of the stochastic nature of the turbulent diffusion process. This uncertainty estimate is used to provide a probabilistic description of the dispersion result, and gives a quantitative characterization of the reliability of the prediction. For many dispersion calculations, the prediction is inherently uncertain because of a lack of detailed knowledge of the wind field, and a probabilistic description is the only meaningful approach.

SCICHEM is capable of modeling two material types—gases and particles—and multiple sources, both continuous plumes and instantaneous puffs. The following sections describe the technical basis of the SCICHEM dispersion prediction as well as the treatment of additional physical phenomena, such as particle deposition rates and reactive chemistry.

2

TRANSPORT AND DIFFUSION

2.1 Puff Moment Equations

2.1.1 Gaussian Moment Definition

SCIPUFF uses a Gaussian puff representation for the concentration field of a dispersing contaminant. In this section, we will restrict discussion to gaseous materials; solid particles are discussed in Section 5. A three-dimensional Gaussian is completely described by its spatial integral moments up to second order and can be written in the form

$$c(\mathbf{x}) = \frac{Q}{(2\pi)^{3/2} (Det(\sigma))^{1/2}} \exp \left[-\frac{1}{2} \sigma_{ij}^{-1} (x_i - \bar{x}_i)(x_j - \bar{x}_j) \right] \quad \text{Eq. 2-1}$$

For general atmospheric dispersion problems, we must also consider the effects of the ground surface and the capping inversion at the top of the planetary boundary layer, which are usually represented as reflective surfaces. The reflection description for the generalized Gaussian is described in Section 12.1. For our present discussion, we restrict attention to the moment equations, which are independent of the shape assumption.

Using an angle bracket to denote an integral over all space, the spatial moments in Equation 2-1 are defined as

Zeroth moment - mass

$$Q = \langle c \rangle \quad \text{Eq. 2-2}$$

First moment - centroid

$$Q \bar{x}_i = \langle c x_i \rangle \quad \text{Eq. 2-3}$$

Second moment - spread

$$Q \sigma_{ij} = \langle c (x_i - \bar{x}_i)(x_j - \bar{x}_j) \rangle \quad \text{Eq. 2-4}$$

Note that this generalized tensor definition of the moments is completely independent of any specific coordinate system and can therefore describe an arbitrarily oriented Gaussian shape. The full moment description requires 10 numbers to represent the mass, the 3 centroid coordinates, and 6 spread moments because σ_{ij} is a symmetric second-rank tensor. The moments describe the unreflected Gaussian shape, but local concentration values must account for surface reflection as described in Section 12.1. The evaluation of the ambient meteorological variables should also strictly use the true centroid location of the reflected puff, but this involves complex calculations. We therefore simply use the larger of \bar{z} and $\sqrt{\sigma_{33}}$ as the height (above the ground surface) at which the meteorological field variables, such as velocity and turbulence, is evaluated.

The specific Gaussian variation (Equation 2-1) applies to an individual puff, but in general the local concentration field will be composed of a sum of contributions from several such puffs. The details of the concentration calculation are described in Section 12.1. Here, we describe the transport and diffusion model equations for the individual puff moments.

2.1.2 Moment Transport Equations

The advection-diffusion equation for a scalar quantity in an incompressible flow field can be written as

$$\frac{\partial c}{\partial t} + \frac{\partial}{\partial x_i}(u_i c) = k \nabla^2 c + S \quad \text{Eq. 2-5}$$

where $u_i(\mathbf{x}, t)$ is the turbulent velocity field, k is the molecular diffusivity, and S represents the source terms. Surface deposition, described in Section 2.3, is an example of a source term, but other terms associated with different materials are described in Sections 6.

The atmospheric velocity field is generally turbulent, so we use the Reynolds averaging technique to define a mean and a turbulent fluctuation value. Denoting the mean by an overbar and the fluctuation by a prime, we have $u = \bar{u} + u'$, and a similar decomposition can be applied to the concentration, c . The Reynolds averaged conservation equation for the mean scalar concentration is therefore

$$\frac{\partial \bar{c}}{\partial t} + \frac{\partial}{\partial x_i}(\bar{u}_i \bar{c}) = -\frac{\partial}{\partial x_i}(\overline{u'_i c'}) + k \nabla^2 \bar{c} + \bar{S} \quad \text{Eq. 2-6}$$

where $-\overline{u'_i c'}$ is the turbulent concentration flux.

At this point, the averaging in the overbar involves an unspecified ensemble of velocity fields. In some cases, the ensemble may be considered to include the conventional planetary boundary layer turbulence only, and the mean wind, $\bar{\mathbf{u}}$, is defined in the usual sense. The dispersion framework developed here is more general, however, and can include larger scale variability—or may be more restrictive and ignore meandering motions. The specification of the turbulent fluctuation values is discussed more fully in Section 11.

Neglecting source terms, S , for the present, Equation 2-6 is readily integrated over the spatial dimensions to give conservation of mass

$$\frac{dQ}{dt} = 0 \quad \text{Eq. 2-7}$$

where Q now represents the integrated mean concentration, \bar{c} . Note that Equation 2-7 applies to an inert conserved tracer, with no loss or transformation processes; these effects will be described later.

Equations for the higher spatial moments of \bar{c} are obtained similarly but require some assumption about the spatial variation of the velocity field. The simplest assumption is a constant

velocity based on the value at the puff centroid, but this neglects any effect of shear. We therefore use a linear representation for the local velocity field

$$\bar{u}_i(\mathbf{x}) = \bar{u}_i(\bar{\mathbf{x}}) + (x_j - \bar{x}_j) \frac{\partial \bar{u}_i}{\partial x_j} \quad \text{Eq. 2-8}$$

where the velocity gradient is also evaluated at the centroid location.

Multiplying Equation 2-6 by x_i and integrating by parts gives

$$\frac{d\bar{x}_i}{dt} = \frac{\langle \bar{u}_i \bar{c} \rangle}{Q} + \frac{\langle u'_i c' \rangle}{Q} \quad \text{Eq. 2-9}$$

where the first term on the right-hand side represents transport by the mean wind and the second term is the turbulent drift. The latter arises from correlation between the velocity fluctuations and the concentration fluctuations. Substituting for $\bar{\mathbf{u}}$ from Equation 2-8 and assuming any symmetric spatial distribution for c , the velocity gradient term vanishes to give

$$\frac{d\bar{x}_i}{dt} = \bar{u}_i(\bar{\mathbf{x}}) + \frac{\langle u'_i c' \rangle}{Q} \quad \text{Eq. 2-10}$$

The second-moment equation is obtained by multiplying Equation 2-6 by $x'_i x'_j$, where $x'_i = x_i - \bar{x}_i$, and integrating by parts to give

$$\frac{d\sigma_{ij}}{dt} = \sigma_{ik} \frac{\partial \bar{u}_j}{\partial x_k} + \sigma_{jk} \frac{\partial \bar{u}_i}{\partial x_k} + \frac{\langle x'_i u'_j c' \rangle}{Q} + \frac{\langle x'_j u'_i c' \rangle}{Q} \quad \text{Eq. 2-11}$$

where the first two terms represent the shear distortion of the puff and the second two terms represents the turbulent diffusion, as described by Sykes and Henn (1995). The pairs of terms are required for the ij -symmetry of the second-moment tensor.

This completes the specification of the moment equations in the absence of external source terms, S , but we have introduced turbulent flux moments in Equations 2-10 and 2-11. This is the essence of the turbulence closure problem, in which the Reynolds average operator always introduces higher order fluctuation correlations. The turbulent fluctuations must be modeled empirically at some level, and we next discuss the turbulence closure technique used in SCIPUFF.

2.1.3 Turbulence Closure Diffusion Model

2.1.3.1 Second-Order Closure Framework

The diffusion model in SCIPUFF is based on second-order turbulence closure, which provides a transport equation for the second-order fluctuation terms. First-order closure prescribes the turbulent fluxes in terms of the local mean gradients using an empirical turbulent diffusivity, but a more general relation can be obtained from a higher order closure. It is not our intention to review turbulence closure theory here—only to provide the basic model description; the

interested reader can find detailed discussions in the literature, for example, Mellor and Herring (1973), Launder et al. (1975), and Lewellen (1977).

The equations for the puff moments involve the turbulent flux of concentration, and a rigorous conservation equation can be derived for this quantity from the scalar and momentum equations. Neglecting the molecular diffusion terms, the flux transport equation can be written in the form

$$\frac{\partial}{\partial t} \overline{u'_i c'} + \overline{u_j} \frac{\partial}{\partial x_j} \overline{u'_i c'} = -\overline{u'_i u'_j} \frac{\partial \bar{c}}{\partial x_j} - \overline{u'_j c'} \frac{\partial \bar{u}_i}{\partial x_j} - \frac{\partial}{\partial x_j} \overline{u'_i u'_j c'} - \overline{c' \frac{\partial p'}{\partial x_i}} + \frac{g_i}{T_0} \overline{c' \theta'} \quad \text{Eq. 2-12}$$

This equation involves higher order terms, such as the triple correlation and the pressure correlation, which must be modeled empirically. We use the model of Lewellen (1977) to form a closed equation for the turbulent flux, giving

$$\begin{aligned} \frac{\partial}{\partial t} \overline{u'_i c'} + \overline{u_j} \frac{\partial}{\partial x_j} \overline{u'_i c'} = & -\overline{u'_i u'_j} \frac{\partial \bar{c}}{\partial x_j} - \overline{u'_j c'} \frac{\partial \bar{u}_i}{\partial x_j} + \frac{\partial}{\partial x_j} \left(v_c q \Lambda \frac{\partial}{\partial x_j} \overline{u'_i c'} \right) \\ & - A \frac{q}{\Lambda} \overline{u'_i c'} + \frac{g_i}{T_0} \overline{c' \theta'} \end{aligned} \quad \text{Eq. 2-13}$$

where $A = 0.75$ and $v_c = 0.3$ are empirical model constants. The turbulent velocity scale, q , is defined as $q^2 = \overline{u'_i u'_i}$, and Λ is the turbulent length scale; these quantities will be discussed more fully next. The buoyancy term uses the Boussinesq approximation, and $g_i = (0, 0, g)$ is the gravitational acceleration, T_0 is the reference temperature, and θ' is the potential temperature fluctuation.

The general equation (2-13) for the turbulent fluxes can be integrated spatially to provide transport equations for the flux moments in Equations 2-10 and 2-11. However, the multiple tensor indices give a large number of correlations to consider in the general case. We therefore introduce some restrictions for the atmospheric dispersion cases that allow us to neglect many of the correlations. First, we consider only the vertical component of the turbulent drift, $\langle \overline{u'_i c'} \rangle$, because advection by the mean wind will generally dominate in the horizontal directions. Second, the only off-diagonal component of the flux moment tensor, $\langle x'_i \overline{u'_j c'} \rangle$, to be considered will be the symmetric horizontal term

$$X_{12} = \langle x'_1 \overline{u'_2 c'} \rangle + \langle x'_2 \overline{u'_1 c'} \rangle \quad \text{Eq. 2-14}$$

In general, the off-diagonal terms represent puff distortions resulting from velocity covariances. Such covariances are usually generated by wind shear, which will dominate the distortion process through the mean shear terms in Equation 2-11. The horizontal distortion is retained for the special case of large-scale horizontal fluctuations, as described in Section 11.3. With these restrictions, we now describe the horizontal and vertical diffusion representations.

2.1.3.2 Horizontal Diffusion

Equations for the two diagonal horizontal moments are derived directly from Equation 2-13 as

$$\frac{d}{dt}\langle x' \overline{u'c'} \rangle = Q \overline{u'^2} - A \frac{q}{\Lambda} \langle x' \overline{u'c'} \rangle \quad \text{Eq. 2-15}$$

and

$$\frac{d}{dt}\langle y' \overline{v'c'} \rangle = Q \overline{v'^2} - A \frac{q}{\Lambda} \langle y' \overline{v'c'} \rangle \quad \text{Eq. 2-16}$$

where we have used the component values for the velocity and position vectors, that is, $x'_i = (x', y', z')$ and $u'_i = (u', v', w')$.

Under steady homogeneous conditions, Equation 2-16 gives a very simple prediction for the effective horizontal diffusivity and lateral spread. The diffusivity in the y -direction can be defined as

$$K_y = \frac{\langle y' \overline{v'c'} \rangle}{Q} \quad \text{Eq. 2-17}$$

Then, if $K_y = 0$ at $t = 0$, the solution for K_y is

$$K_y = \overline{v'^2} \tau (1 - \exp(-t/\tau)) \quad \text{Eq. 2-18}$$

where the horizontal timescale $\tau = \Lambda/(Aq)$. The solution for the lateral spread, $\sigma_y^2 = \sigma_{22}$, is then

$$\sigma_y^2 = \sigma_0^2 + 2\overline{v'^2} \tau (t - \tau + \tau \exp(-t/\tau)) \quad \text{Eq. 2-19}$$

where σ_0 is the initial spread.

The solution (Equation 2-19) is consistent with Taylor's (1921) exact analytic result for turbulent diffusion in homogeneous stationary conditions, with an exponential form for the Lagrangian velocity autocorrelation function and an integral timescale of τ .

The preceding discussion uses a single length scale, Λ , to describe the horizontal turbulence spectrum, but this is insufficient for a proper description of the atmospheric spectrum. The wide range of length scales demands a more complicated treatment, because each length scale is associated with a distinct timescale. We consider three distinct horizontal turbulence components, representing shear-driven turbulence, buoyancy-driven turbulence, and a large-scale component representing mesoscale or synoptic scale velocity fluctuations. The three components will be denoted by subscripts S , B , and L , respectively. The specification of the three components is discussed in Section 11. The three components are assumed to be statistically independent so that the correlations can simply be summed, giving

$$\langle y' \overline{v'c'} \rangle = \langle y' \overline{v'c'} \rangle_S + \langle y' \overline{v'c'} \rangle_B + \langle y' \overline{v'c'} \rangle_L \quad \text{Eq. 2-20}$$

and a similar relation for the x -component.

Evolution equations for the horizontal velocity correlation integrals are exactly like Equation 2-16, except that the turbulent velocity and length scales represent the specific component, that is,

$$\frac{d}{dt} \langle y' \overline{v'c'} \rangle_s = Q \overline{v_s'^2} - A \frac{q_s}{\Lambda_s} \langle y' \overline{v'c'} \rangle_s \quad \text{Eq. 2-21}$$

Similar equations are used for the B and L components.

We generally assume that the boundary layer components are isotropic (in the horizontal plane), so that we require only a single correlation variable for the S and B terms. Buoyancy generation is clearly isotropic in the horizontal, but the shear component implies a preferred direction. It is also well known that the shear-driven streamwise turbulence intensity is larger than the lateral component. In the presence of a mean wind shear, the explicit velocity gradient terms in Equation 2-11 enhance the spread in the streamwise direction, but this has been found to underestimate streamwise diffusion in the surface layer. An empirical enhancement factor is therefore included to increase the turbulent diffusivity in the mean wind direction within the surface layer. Comparison with field data for instantaneous puff releases indicated that a factor of approximately 10 is required to match observations. This factor is much larger than the ratio of the velocity variances and is presumably associated with an increased Lagrangian correlation timescale for streamwise velocity fluctuations. In practice, therefore, we define an enhancement factor

$$f(z) = \begin{cases} 9(1 - z/z_s)^2 & z < z_s \\ 0 & z \geq z_s \end{cases} \quad \text{Eq. 2-22}$$

where the surface layer depth, z_s , is defined in Section 10. In Equation 2-22, the surface layer depth is not allowed to exceed $-5L$ in convective conditions; L is the Monin-Obukhov length, also defined in Section 10.

The total correlation integrals are then written as

$$\langle x' \overline{u'c'} \rangle = f_{xx} \langle y' \overline{v'c'} \rangle_s + \langle y' \overline{v'c'} \rangle_B + \langle x' \overline{u'c'} \rangle_L \quad \text{Eq. 2-23}$$

$$\langle y' \overline{v'c'} \rangle = f_{yy} \langle y' \overline{v'c'} \rangle_s + \langle y' \overline{v'c'} \rangle_B + \langle y' \overline{v'c'} \rangle_L \quad \text{Eq. 2-24}$$

where the shear-enhancement factors are $f_{xx} = 1 + f \cos^2 \theta$, $f_{yy} = 1 + f \sin^2 \theta$, and θ is the mean flow direction, $\tan^{-1} \overline{v}/\overline{u}$. An off-diagonal term $f \sin \theta \cos \theta \langle y' \overline{v'c'} \rangle_s$ is also generated by the arbitrary tensor rotation and is added to the anisotropic large-scale component, X_{12} .

Because the large-scale component is not assumed to be isotropic, it requires both x - and y -components as well as the off-diagonal X_{12} defined by Equation 2-14, which satisfies

$$\frac{d}{dt} X_{12} = 2Q \overline{u'v'_L} - A \frac{q_L}{\Lambda_L} X_{12} \quad \text{Eq. 2-25}$$

Details of the specification of the velocity fluctuations and length scales are provided in Section 11.

2.1.3.3 Vertical Diffusion

The vertical diffusion parameterization is more complicated than the horizontal for two reasons. First, the inhomogeneity is more pronounced in the vertical direction so that vertical gradients cannot be ignored; second, the buoyancy forces introduce an additional phenomenon in the vertical direction. Dealing first with the first moment of the vertical flux, $\langle z' \overline{w'c'} \rangle$, integration of the full second-order closure expression in Equation 2-13) gives

$$\frac{d}{dt} \langle z' \overline{w'c'} \rangle = Q \overline{w'^2} - A \frac{q_V}{\Lambda_V} \langle z' \overline{w'c'} \rangle + \frac{g}{T_0} \langle z' \overline{c'\theta'} \rangle \quad \text{Eq. 2-26}$$

where the subscript V denotes the vertical component for the turbulence velocity and scale.

A similar equation can be derived for the temperature correlation, using the model equations of Lewellen (1977), as

$$\frac{d}{dt} \langle z' \overline{c'\theta'} \rangle = Q \overline{w'\theta'} - 2bs \frac{q_V}{\Lambda_V} \langle z' \overline{c'\theta'} \rangle - \frac{d\bar{\theta}}{dz} \langle z' \overline{w'c'} \rangle \quad \text{Eq. 2-27}$$

where $b = 0.125$ and $s = 1.8$ are turbulence model constants.

Equations 2-26 and 2-27 represent the full second-order closure model for the vertical flux but give oscillatory solutions for stable temperature gradients and can lead to negative values of the diffusivity. A more robust scheme is obtained by relaxing the vertical flux moment toward its equilibrium value on the appropriate timescale, similar to the horizontal equation (2-16). The equilibrium (steady-state) solution for the vertical diffusivity, defined as

$$K_z = \frac{\langle z' \overline{w'c'} \rangle}{Q} \quad \text{Eq. 2-28}$$

is obtained from Equation 2-26 as

$$K_z^{eq} = \frac{\Lambda_V}{Aq_V} \left(\overline{w'^2} + \frac{g}{T_0} G_z^{eq} \right) \quad \text{Eq. 2-29}$$

where

$$G_z = \frac{\langle z' \overline{c'\theta'} \rangle}{Q} \quad \text{Eq. 2-30}$$

Using a similar assumption for the temperature correlation, we obtain

$$G_z^{eq} = \frac{\Lambda_V}{2bsq_V} \left(\overline{w'\theta'} - \frac{d\bar{\theta}}{dz} K_z^{eq} \right) \quad \text{Eq. 2-31}$$

so that the equilibrium diffusivity is given by

$$K_z^{eq} = \frac{\Lambda_V}{Aq_V} \frac{\left(\overline{w'^2} + \frac{g}{T_0} \frac{\Lambda_V}{q_V} \frac{\overline{w'\theta'}}{2bs} \right)}{\left(1 + \frac{1}{2Abs} \frac{g}{T_0} \frac{\Lambda_V^2}{q_V^2} \frac{\partial \bar{\theta}}{\partial z} \right)} \quad \text{Eq. 2-32}$$

A simple equation for the vertical flux moment that satisfies the equilibrium equation and evolves on the proper timescale is therefore

$$\frac{d}{dt} \langle z' \overline{w'c'} \rangle = A \frac{q_V}{\Lambda_V} \left(Q K_z^{eq} - \langle z' \overline{w'c'} \rangle \right) \quad \text{Eq. 2-33}$$

and this is the model equation employed in SCIPUFF. The use of the late-time equilibrium value (Equation 2-32) in Equation 2-33 over-estimates the early time growth of the diffusivity under convective conditions, however, because the buoyancy term in Equation 2-26 develops on the same turbulence timescale as the diffusivity itself. We therefore approximate the equilibrium diffusivity in Equation 2-33 using Equation 2-29 but with a scaled value for G_z^{eq} . The buoyancy term is scaled by the ratio of K_z to K_z^{eq} so that the growth of the buoyancy correlation is represented as being proportional to the growth of the diffusivity.

The zeroth moment of the vertical flux—the turbulent vertical drift—is important in regions with vertical gradients of the turbulent correlations. The role of the drift term in the model is to account for nonuniformity in the vertical diffusivity, and the equilibrium drift velocity must be equal to the gradient of the equilibrium diffusivity. We therefore define a simplified equation for the flux moment as

$$\frac{d}{dt} \langle \overline{w'c'} \rangle = A \frac{q_V}{\Lambda_V} \left(Q \frac{\partial K_z^{eq}}{\partial z} - \langle \overline{w'c'} \rangle \right) \quad \text{Eq. 2-34}$$

It is emphasized that Equation 2-34 is required for consistency with the simplified diffusivity moment equation (2-33) and is not directly derived from the second-order closure model. The main purpose of Equation 2-34 is to maintain a uniform concentration distribution across a well-mixed layer when puffs are splitting, as described in Section 4.1. Vertical variations in the turbulence fields lead to differential diffusion rates, which can distort an initially uniform concentration profile unless the drift term is included. A similar effect is found in stochastic particle dispersion models as discussed by Thomson (1987).

2.1.3.4 Skew Turbulence

Under convective conditions, where the turbulence is driven by heating of the ground surface, it is well known that the buoyancy-driven eddies are asymmetric with respect to the vertical motion. Upward motions tend to be concentrated in narrow regions of relatively high velocity, while the downward motions are slower and occupy a larger area fraction. This asymmetry was first observed in the vertical dispersion of passive plumes in the laboratory experiments of Willis and Deardorff (1976, 1978). Lamb (1982) examined the probability density function (PDF) of

the vertical velocity fluctuations in Deardorff's (1974) numerical simulations of the convective boundary layer and clearly showed the positive skewness over most of the boundary layer depth.

The Gaussian puff modeling described in the previous sections uses only the second moment of the velocity fluctuations and consequently produces a vertically symmetric dispersion result, in the absence of wall or inversion reflections, and cannot represent the skewness effects as observed in the laboratory experiments. However, several researchers (for example, Misra, 1982; Baerentsen and Berkowicz, 1984) have noted that the skew PDF can be reasonably well represented by the sum of two Gaussian distributions, in the form

$$P(w) = \frac{\lambda_1}{\sqrt{2\pi} \sigma_{w1}} \exp\left(-\frac{(w - \bar{w}_1)^2}{2 \sigma_{w1}^2}\right) + \frac{\lambda_2}{\sqrt{2\pi} \sigma_{w2}} \exp\left(-\frac{(w - \bar{w}_2)^2}{2 \sigma_{w2}^2}\right) \quad \text{Eq. 2-35}$$

where the two components represent the updraft and downdraft populations. Note that the Gaussian components do not have zero mean velocity and represent mean motion within the population; the parameters of the distribution are chosen to match the overall moments of the vertical velocity field, which has zero mean. This formulation has the convenient property that the individual Gaussians are compatible with the SCIPUFF Gaussian closure model, so the skewness effects can be modeled using a two-population collection of Gaussian puffs. We associate one set of puffs with the updraft population and use the moments of the first term in Equation 2-35 in the vertical diffusion equations, while the second set uses moments from the second term and represents the downdraft population.

The general constraints on the parameters in Equation 2-35 are that the probability density must integrate to unity, so

$$\lambda_1 + \lambda_2 = 1 \quad \text{Eq. 2-36}$$

The mean vertical velocity is zero; therefore,

$$\lambda_1 \bar{w}_1 + \lambda_2 \bar{w}_2 = 0 \quad \text{Eq. 2-37}$$

The vertical velocity variance is $\overline{w'^2}$; therefore,

$$\lambda_1 (\sigma_{w1}^2 + \bar{w}_1^2) + \lambda_2 (\sigma_{w2}^2 + \bar{w}_2^2) = \overline{w'^2} \quad \text{Eq. 2-38}$$

Finally, the additional parameters also allow the skewness to be defined, so we also require

$$\lambda_1 (\bar{w}_1 \sigma_{w1}^2 + \bar{w}_1^3) + \lambda_2 (\bar{w}_2 \sigma_{w2}^2 + \bar{w}_2^3) = \overline{w'^3} \quad \text{Eq. 2-39}$$

where the skewness is defined as $S = \frac{\overline{w'^3}}{\overline{w'^2}^{3/2}}$.

The number of free variables in the general expression Equation 2-35 is actually 6, so it is strictly possible to fit up to 5 moments of the vertical velocity PDF. However, most formulations impose further simplifications, and we therefore limit the constraints to the first 3 moments. There have

been several suggested parameterizations for the skewed PDF shape, but we choose the approach of Luhar et al. (1996) because this has the desirable property that the PDF collapses smoothly toward the simple Gaussian form as the skewness tends to zero, which is the assumed value for neutral conditions.

Luhar et al. (1996) suggest making the mean velocities associated with the two Gaussians proportional to their standard deviations, with a proportionality constant that depends on skewness. Therefore,

$$w_1 = -m \sigma_{w1}, \quad \bar{w}_2 = m \sigma_{w2} \quad \text{Eq. 2-40}$$

where $m = \frac{2}{3} S^{1/3}$. The value of 2/3 is chosen to optimize the agreement with observations of the kurtosis (based on the fourth-order moment) of the vertical velocity fluctuations. The constraints (Equations 2-36 through 2-39) now determine the other parameters, so that we obtain

$$\sigma_{w1} = \sigma_w \left(\frac{\lambda_2}{\lambda_1 (1 + m^2)} \right)^{1/2}, \quad \sigma_{w2} = \sigma_w \left(\frac{\lambda_1}{\lambda_2 (1 + m^2)} \right)^{1/2} \quad \text{Eq. 2-41}$$

and

$$\lambda_2 = \frac{1}{2} \left[1 - \left(\frac{r}{4 + r} \right)^{1/2} \right], \quad \lambda_1 = 1 - \lambda_2 \quad \text{Eq. 2-42}$$

$$\text{where } r = \frac{(1 + m^2)^3 S^2}{m^2 (3 + m^2)^2}$$

It remains to specify the skewness, S , which we choose to represent simply as a constant value for the boundary layer above a height L , where L is the Monin-Obukhov length (see Section 10). We define the skewness in terms of the surface conditions as

$$S = \frac{0.6 w_*^2}{w_*^2 + 4u_*^2} \quad \text{Eq. 2-43}$$

so that S is zero in neutral conditions and 0.6 for free convection. Below a height L , the turbulence is increasingly dominated by the shear-stress productions term as we approach the surface. We define a “local” skewness value based on the shear- and buoyancy-driven vertical velocity variance contributions (see Section 11) in place of u_* and w_* , respectively, in Equation 2-43. The final value of skewness below height L is then linearly interpolated between the “local” value at the surface and Equation 2-43 at height L .

The result of the model (Equations 2-40 through 2-42) is a skewed Gaussian with $\lambda_1 = 0.62$ when the skewness is 0.6. This implies that 62% of the area is in the downdraft population, with a mean vertical velocity of $-0.39\sigma_w$ and standard deviation $0.69\sigma_w$, while the remaining 38% is

in the updraft population with a mean velocity of $0.62\sigma_w$ and standard deviation $1.11\sigma_w$. Here, σ_w is the standard deviation of the vertical velocity fluctuations, that is, $\sigma_w^2 = \overline{w'^2}$.

The comparison of the PDF shapes for neutral conditions, $S = 0$, and free convection conditions, $S = 0.6$, is shown in Figure 2-1.

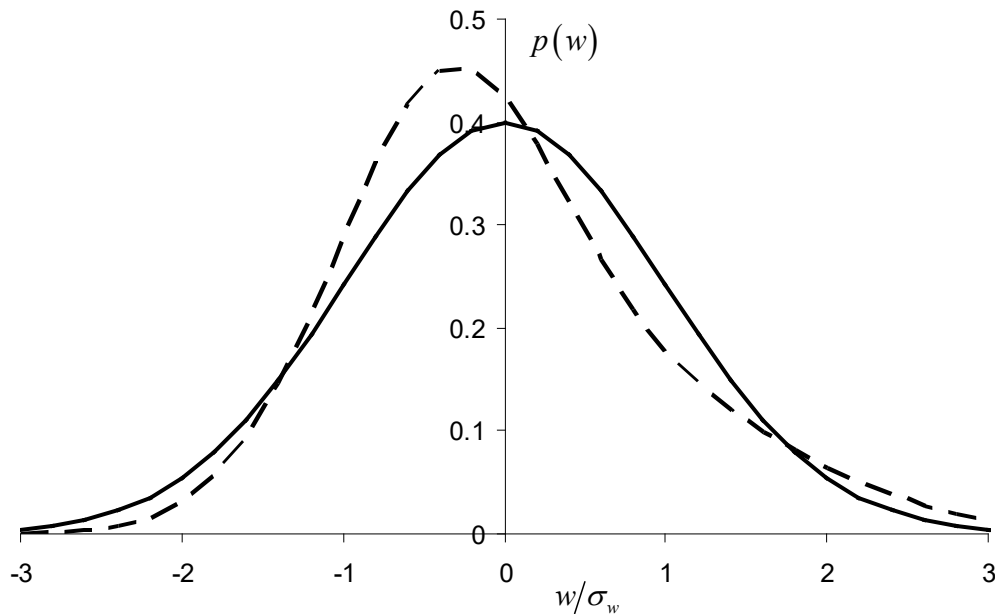


Figure 2-1
Vertical velocity probability density functions for neutral (solid line) and free convection (dashed line) conditions, based on the model of Luhar et al. (1996)

If the skewness defined in Equation 2-43 is non-zero, the two-population skew distribution is used to drive the two types of puff, which are released with the fraction of release mass equal to (λ_1, λ_2) as defined in Equation 2-42. Each puff derives its mean vertical velocity and velocity variance from the appropriate population and only changes its association with the skew population when it reaches a boundary or grows large enough to be effectively treated as well-mixed. A downdraft population puff switches to the updraft population when it reaches the ground, while an updraft puff switches when it reaches the capping inversion. Puffs are deemed well-mixed when their internal vertical scale, defined next in Section 2.2, becomes larger than 40% of the mixed-layer depth.

2.2 Concentration Fluctuation Variance

2.2.1 Concentration Variance Equation

The probabilistic aspect of the SCIPUFF dispersion prediction is based on the second-order closure model for the concentration fluctuation variance. The dispersion of any species in a turbulent velocity field is a random process because the turbulent fluctuations are effectively chaotic and cannot be measured or predicted in detail. The scalar concentration is therefore a

stochastic quantity, with a probability distribution that depends on the distribution of velocity fluctuations. Traditional deterministic estimates of atmospheric dispersion provide only a single concentration value as a function of space and time, and this corresponds to the mean value, \bar{c} , for some definition of the statistical ensemble. The mean value is the first moment of the probability distribution and contains no information about the statistical variability in the prediction. Higher moments are required to give a quantitative description of the variability. The probabilistic aspect of the SCIPUFF dispersion prediction is based on a transport equation for the statistical variance in the concentration value, which is the second moment of the probability distribution. The transport equation is based on the same second-order turbulence closure theory described in Section 2.1 for the mean dispersion rates. The mean and the variance are then used to provide a probabilistic prediction using a parameterized PDF, described in Section 12.2. The concentration fluctuation variance equation can be obtained from the scalar mass conservation equation (2-5) in the form

$$\frac{\partial \overline{c'^2}}{\partial t} + \frac{\partial}{\partial x_i} \left(\bar{u}_i \overline{c'^2} \right) = -2\overline{u'_i c'} \frac{\partial \bar{c}}{\partial x_i} - \frac{\partial}{\partial x_i} \left(\overline{u'_i c'^2} \right) - 2k \left(\frac{\partial \overline{c'}}{\partial x_i} \right)^2 + k \nabla^2 \overline{c'^2} \quad \text{Eq. 2-44}$$

where the first three terms on the right-hand side are identified as turbulent production, turbulent diffusion, and turbulent dissipation, respectively. The last term is direct molecular diffusion of the scalar variance and is negligible for the small values of molecular diffusivity relative to atmospheric dispersion scales. However, it is important to note that the **only** dissipation mechanism is molecular, as is evident from consideration of the total scalar variance equation

$$\frac{\partial \overline{c^2}}{\partial t} + \frac{\partial}{\partial x_i} \left(\bar{u}_i \overline{c^2} \right) = -\frac{\partial}{\partial x_i} \left(\overline{u'_i c^2} \right) - 2k \left(\frac{\partial \overline{c}}{\partial x_i} \right)^2 + k \nabla^2 \overline{c^2} \quad \text{Eq. 2-45}$$

where it can be seen that all the terms except dissipation are in flux form.

For very high values of the Schmidt number—that is, very small values of k —the molecular terms in both equations are effectively equal to the turbulent scalar dissipation

$$\varepsilon_c = 2k \left(\frac{\partial \overline{c'}}{\partial x_i} \right)^2 \quad \text{Eq. 2-46}$$

which is modeled using a dissipation timescale as

$$\varepsilon_c = \frac{\overline{c'^2}}{\tau_c} \quad \text{Eq. 2-47}$$

From the above, it is clear that the statistical variance in concentration due to random fluctuations in the velocity field is controlled by the turbulent flux and turbulent dissipation rate. SCIPUFF employs closure models for these terms to provide a prediction of the scalar fluctuation variance. The critical aspect of the prediction lies in the determination of the dissipation timescale, τ_c , associated with the turbulent eddies responsible for the dispersion,

and the recognition that large-scale eddies can simply meander the complete concentration field without producing a reduction in the variance.

2.2.2 Scalar Fluctuation Dissipation Timescale

The key aspect of the scalar variance prediction is the dissipation timescale. Proper characterization of the dissipation timescale allows an accurate prediction of the concentration fluctuation variance, as has been demonstrated in comparison with laboratory data (Sykes, Lewellen, and Parker, 1986) and with large-scale atmospheric dispersion observations (Sykes et al., 1993c). The second-order closure model for the dissipation rate was originally developed by Sykes et al. (1984) using the laboratory data of Fackrell and Robins (1982). A fundamental discovery in that study was that the scalar dissipation scales were an internal property of the scalar field itself, rather than being determined exclusively by the velocity fluctuations. Essentially, velocity eddies with scales larger than the scalar plume or cloud meander the entire scalar distribution but do not cause any nonlinear cascade of scalar fluctuation variance onto smaller scales. The turbulent cascade process is driven only by eddies with scales similar to the instantaneous plume size. This is not the case for persistent mean wind shear, which can distort a cloud by means of the continued stretching; this phenomenon is discussed in Section 2.2.3.

The general form for the scalar dissipation timescale is

$$\frac{1}{\tau_c} = \frac{q_c}{\Lambda_c} \quad \text{Eq. 2-48}$$

where q_c and Λ_c represent the velocity and length scales for the scalar fluctuations. The velocity scale is obtained from a simplified description of the turbulent kinetic energy spectrum, and the length scale is predicted from a transport equation. Before discussing the details of these parameterizations, however, we introduce a generalization of the dissipation model to account for the anisotropy between horizontal and vertical directions and the differences between plume and puff meandering.

The scalar variance dissipation model introduced by Sykes et al. (1984, 1986) uses a single estimate of the velocity and length scales to define the dissipation timescale in Equation 2-48. This is appropriate for the case of plume dispersion in two dimensions with near-isotropic turbulence. Under the more general conditions of larger scale horizontal dispersion and arbitrary sources, we require a characterization of the different dissipation rates associated with each direction. The vertical direction must be distinguished, and we also need two horizontal scales. The horizontal information is needed to distinguish between plume-type sources, where the diffusion occurs in two spatial dimensions, and puff-type sources, which diffuse in all three dimensions. As part of the concentration fluctuation prediction, we therefore require three length scales in addition to the fluctuation variance. The internal scales are denoted as Λ_c , Λ_{cH} , and Λ_{cV} for the horizontal lateral and streamwise as well as vertical directions, respectively.

The initial conditions for the internal length scales will be described as part of the source definition in Section 8. In this section, we describe the dissipation length and timescale parameterization. The two scales, Λ_c and Λ_{cV} , are used to characterize the horizontal and

vertical concentration fluctuation length scales. The second horizontal scale is used to determine the dissipation timescale only. We use these two concentration length scales to estimate the dissipation velocity scales, using a simplified Kolmogorov spectrum assumption to determine the appropriate energy for each of the ambient turbulence populations. Therefore, the horizontal velocity scale for the concentration fluctuations is modeled as

$$q_c^2 = q_{cL}^2 + q_{cB}^2 + q_{cS}^2 \quad \text{Eq. 2-49}$$

where

$$q_{cL}^2 = (\overline{u_L'^2} + \overline{v_L'^2}) \min \left(\left(\frac{\Lambda_L}{\Lambda_c} \right)^2, f_L \left(\frac{\Lambda_c}{\Lambda_L} \right)^{2/3} \right) \quad \text{Eq. 2-50}$$

$$q_{cB}^2 = (\overline{u_B'^2} + \overline{v_B'^2}) \min \left(\left(\frac{\Lambda_B}{\Lambda_c} \right)^2, \left(\frac{\Lambda_c}{\Lambda_B} \right)^{2/3} \right) \quad \text{Eq. 2-51}$$

$$q_{cS}^2 = (\overline{u_S'^2} + \overline{v_S'^2} + \overline{w_S'^2}) \min \left(\left(\frac{\Lambda_S}{\Lambda_c} \right)^2, \left(\frac{\Lambda_c}{\Lambda_S} \right)^{2/3} \right) \quad \text{Eq. 2-52}$$

Note that the large-scale contribution in Equation 2-50 contains an additional factor, f_L , which is applied to prevent double-counting of the boundary layer turbulence in the dissipation rate. The factor is unity if $\Lambda_c > 2\Lambda_B$; otherwise, we define the effective large-scale energy at the boundary layer scale as

$$q_{BL}^2 = (\overline{u_L'^2} + \overline{v_L'^2}) \left(\frac{\Lambda_B}{\Lambda_L} \right)^{2/3} \quad \text{Eq. 2-53}$$

For $\Lambda_c < \Lambda_B$, the factor is defined as

$$f_L = \frac{\max \left(0, q_{BL}^2 - \overline{u_B'^2} - \overline{v_B'^2} \right)}{q_{BL}^2} \quad \text{Eq. 2-54}$$

so that for scales smaller than the boundary layer scale, Λ_B , we effectively subtract the boundary layer scale energy from the large-scale component. A simple interpolation is used to provide a continuous factor between the two constant values, so that for $\Lambda_B < \Lambda_c < 2\Lambda_B$, we have

$$f_L = \alpha_{BL} + (1 - \alpha_{BL}) \frac{\max \left(0, q_{BL}^2 - \overline{u_B'^2} - \overline{v_B'^2} \right)}{q_{BL}^2} \quad \text{Eq. 2-55}$$

where the interpolation function is defined as

$$\alpha_{BL} = \left(\frac{\Lambda_c - \Lambda_B}{\Lambda_B} \right)^2 \left(3 - 2 \left(\frac{\Lambda_c - \Lambda_B}{\Lambda_B} \right) \right) \quad \text{Eq. 2-56}$$

so that the slope is continuous at the transition points.

The vertical dissipation fluctuation velocity scale is defined as the smaller of the two estimates

$$q_{cV}^{(1)} = q_V \min \left(\frac{\Lambda_V}{\Lambda_{cV}}, \left(\frac{\Lambda_{cV}}{\Lambda_V} \right)^{1/3} \right) \quad \text{Eq. 2-57}$$

$$q_{cV}^{(2)} = \frac{K_z^{eq}}{bs\Lambda_{cV}} \quad \text{Eq. 2-58}$$

where the second estimate accounts for the reduced dissipation under stable conditions. The turbulence model constants, b and s , were introduced in the previous section and take the values 0.125 and 1.8, respectively (Lewellen, 1977). The equilibrium vertical diffusivity, K_z^{eq} , is defined in Equation 2-29.

Using the two velocity scales defined previously, the scalar dissipation timescale is then modeled as

$$\frac{1}{\tau_c} = f_{diss} bs \left(\frac{q_c}{\Lambda_c} + \frac{q_c}{\Lambda_{cH}} + \frac{q_{cV}}{\Lambda_{cV}} \right) \quad \text{Eq. 2-59}$$

where f_{diss} is a dissipation enhancement factor, which has been found to be necessary in situations where there is no meander component of the turbulence.

The basic dissipation model, as noted above, was based on the elevated releases of Fackrell and Robins (1982), which contain significant meander. In situations where there is little or no meander, such as the surface releases of Fackrell and Robins, the basic model was found to over-predict the concentration fluctuation variance—and the effective dissipation rate must be doubled to achieve a good match. We therefore apply an enhancement factor based on the meander intensity, which is defined as the difference between the total turbulence and the dissipation scale turbulence as defined in Equations 2-50 through 2-52. This difference is computed only for components i the turbulence scale is larger than the internal scale, Λ_c , because this is the definition of meander. The meander component is therefore defined as

$$\begin{aligned}
q_{meander}^2 = & \left(\overline{u_L'^2} + \overline{v_L'^2} \right) \left\{ \begin{aligned} & \left(1 - f_L \left(\frac{\Lambda_c}{\Lambda_L} \right)^{2/3} \right) & \Lambda_c < \Lambda_L \\ & 0 & \Lambda_c \geq \Lambda_L \end{aligned} \right. \\
& + \left(\overline{u_B'^2} + \overline{v_V'^2} \right) \left\{ \begin{aligned} & \left(1 - \left(\frac{\Lambda_c}{\Lambda_L} \right)^{2/3} \right) & \Lambda_c < \Lambda_B \\ & 0 & \Lambda_c \geq \Lambda_B \end{aligned} \right. \\
& + \left(\overline{u_S'^2} + \overline{v_S'^2} + \overline{w_S'^2} \right) \left\{ \begin{aligned} & \left(1 - \left(\frac{\Lambda_c}{\Lambda_S} \right)^{2/3} \right) & \Lambda_c < \Lambda_S \\ & 0 & \Lambda_c \geq \Lambda_S \end{aligned} \right.
\end{aligned} \tag{Eq. 2-60}$$

and the total turbulence is simply

$$q_{total}^2 = \left(\overline{u_L'^2} + \overline{v_L'^2} \right) + \left(\overline{u_B'^2} + \overline{v_V'^2} \right) + \left(\overline{u_S'^2} + \overline{v_S'^2} + \overline{w_S'^2} \right) \tag{Eq. 2-61}$$

The enhancement factor is then defined as

$$f_{diss} = \begin{cases} 2\sqrt{1 - 3q_{meander}^2/q_{total}^2} & , q_{meander}^2 < 0.25q_{total}^2 \\ 1 & , q_{meander}^2 \geq 0.25q_{total}^2 \end{cases} \tag{Eq. 2-62}$$

so that the dissipation is doubled for no meander and unchanged for meander intensity greater than 25% of the total turbulence.

The internal fluctuation scales grow with the turbulent diffusion, and the internal velocity scale gives a measure of the growth rate. The model for the horizontal lateral internal length scales is

$$\frac{d\Lambda_c}{dt} = \left(\alpha_{cL}^2 q_{cL}^2 + \alpha_{cB}^2 q_{cB}^2 + \alpha_{cS}^2 q_{cS}^2 \right)^{1/2} \tag{Eq. 2-63}$$

where $\alpha_{cS} = \alpha_{cB} = 0.25$ and $\alpha_{cL} = 0.3$. The larger coefficient for the large-scale turbulence is required to match idealized ensemble calculations and is due to the two-dimensional nature of the turbulence. We note that the reduction of the coefficient at late time, as discussed in Sykes et al. (1984), has also been eliminated as a result of comparison with the ensemble calculations. The horizontal streamwise scale equation includes shear-dependent terms and is discussed in the next section.

The vertical scale growth is represented by

$$\frac{d\Lambda_{cV}}{dt} = \begin{cases} 0.25q_{cV}^{(1)} & , q_{cV}^{(2)} \geq q_{cV}^{(1)} \\ bsq_{cV}^{(2)} & , q_{cV}^{(2)} < q_{cV}^{(1)} \end{cases} \tag{Eq. 2-64}$$

2.2.3 Vertical Wind Shear Effects

The effect of a sustained vertical wind shear is to elongate a cloud along the direction of the shear, producing a thin “sheet” of material if the vertical diffusivity is relatively small. This process is often observed in dispersion in the free atmosphere above the turbulent boundary layer and near the surface under stable (usually nocturnal) conditions. If the vertical diffusivity is small, the internal scale of the cloud can be reduced as the cloud is thinned by the shear—and the effect of the vertical diffusivity is enhanced. A representation of this effect is included in the SCIPUFF model equations, based on an analytic result for the shear-modified diffusion problem.

We consider an initial spherical Gaussian of material, with spread σ_0 , in a wind shear, S , and a constant vertical diffusivity, K_z . We non-dimensionalize time using the shear rate so that $\tau = S t$ is the time variable, and use σ_0 as the unit length so that $\sigma_{ij} = \sigma_0^2 \hat{\sigma}_{ij}$. The dimensionless solution for the concentration field can then be expressed in terms of a single parameter

$$B = \frac{K_z}{S \sigma_0^2} \quad \text{Eq. 2-65}$$

For a constant shear and vertical diffusivity and zero horizontal diffusion, the nondimensional solution to the Gaussian moment equations (2-11) is

$$\begin{aligned} \hat{\sigma}_{11} &= 1 + \tau^2 + \frac{2}{3} B \tau^3 \\ \hat{\sigma}_{13} &= \tau + B \tau^2 \\ \hat{\sigma}_{33} &= 1 + 2B\tau \end{aligned} \quad \text{Eq. 2-66}$$

A simplified approximation for the dissipation timescale is obtained from the logarithmic rate of change of $\langle \overline{c^2} \rangle$. This is strictly valid only for high fluctuation intensity, because we assume that the total mean-square concentration is approximately equal to the variance; that is, the square of the mean is negligible. This is the regime for which the dissipation is most critical, however. Using the solution (Equation 2-66), the dissipation timescale is found to be

$$\begin{aligned} \frac{1}{S \tau_c} &= \frac{1}{S \langle \overline{c^2} \rangle} \frac{d}{dt} \langle \overline{c^2} \rangle \\ &= \frac{1 + \tau^2 + \frac{2}{3} B \tau^3}{B^{-1} + 2\tau + \frac{2}{3} \tau^3 + \frac{1}{3} B \tau^4} \end{aligned} \quad \text{Eq. 2-67}$$

The behavior of the dissipation timescale (Equation 2-67) is illustrated by the solid lines in Figure 2-2 for a range of values of B . For small values of B —that is, for small diffusivity—the timescale is almost constant until $\tau \approx 1$. Because time was nondimensionalized using the shear rate, this implies that the distortion must proceed for about one shear timescale before there is a significant change in the dissipation rate. As the cloud becomes sheared, the timescale is

reduced—corresponding to the reduced local thickness—and reaches a minimum value. The minimum depends on the diffusivity, and smaller values of diffusivity give a lower minimum (relative to the initial value) at later time. Eventually, however, the diffusivity dominates as the cloud becomes thinner, and thereafter the dissipation timescale increases linearly with time.

The dashed lines in Figure 2-2 show the predictions of a simplified model for Λ_{cV} . Using Equation 2-58 for the velocity scale, we modify the vertical scale equation (2-64) to include a term describing the shear-driven reduction, giving

$$\frac{d\Lambda_{cV}}{dt} = \frac{K_z}{\Lambda_{cV}} - f_{zi} S \frac{\sqrt{3}}{2} \frac{\Lambda_{cV}^2}{\Lambda_{cH}} \quad \text{Eq. 2-68}$$

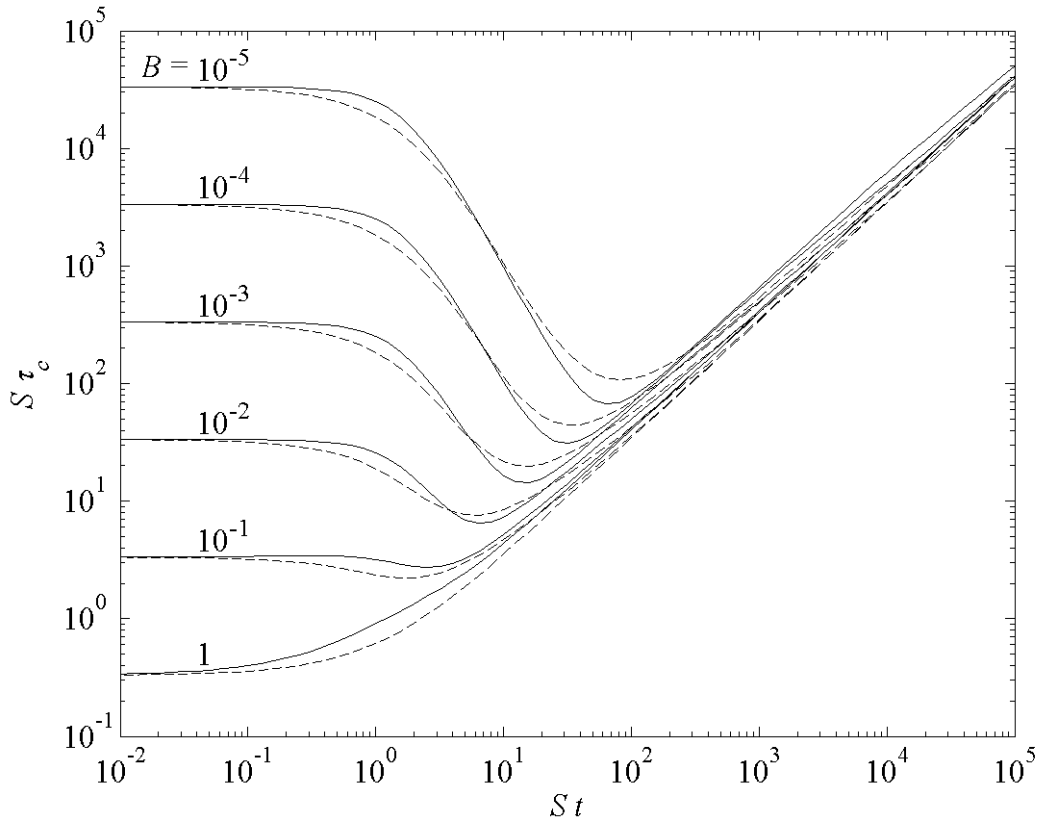


Figure 2-2
Nondimensional fluctuation dissipation timescale as a function of dimensionless time for a shear-distorted Gaussian puff. The solid line is the analytic solution (Equation 2-67). Dashed line is the model prediction from Equations 2-68 and 2-70.

The factor f_{zi} has been included to reduce the shear effect slightly under strongly stable conditions, where the shear reduction has been found to dissipate the variance too rapidly. The reduction factor is applied only in stable conditions when the Monin-Obukhov length, L , is less than the mixing-layer depth, Z_i , and in this case we define

$$f_{zi} = 1 - 0.35 \min \left(1 - \frac{L}{z_i}, 0.9 \right) \quad \text{Eq. 2-69}$$

so that under very strongly stable conditions we obtain the maximum reduction factor, with a value of $f_{zi} = 0.685$.

The shear term in Equation 2-68 depends on the horizontal scale, Λ_{cH} , which is generally increased by the wind shear and is modeled as

$$\frac{d\Lambda_{cH}}{dt} = \frac{\Lambda_c}{\Lambda_{cH}} \frac{d\Lambda_c}{dt} + S \frac{\sqrt{3}}{2} \Lambda_{cV} \max \left[0, 1 - \left(\frac{\Lambda_{cV}}{\Lambda_{cH}} \right)^p \left(\frac{S\Lambda_{cV}^2}{K_z} \right)^{1/3} \right] \quad \text{Eq. 2-70}$$

The last term in Equation 2-70 is included to reduce the shear effect when the two scales are comparable, and the diffusivity is significant compared with the shear distortion. The scale ratio is raised to the power, p , which is defined as

$$p = 2 - \min \left(1, 0.01 \frac{S\Lambda_{cV}^2}{K_z} \right) \quad \text{Eq. 2-71}$$

This adjustment gives a slightly better agreement with the analytic result for the higher diffusivity range, because it allows the horizontal scale to grow more rapidly in the early times.

In the SCIPUFF model, the terms involving the wind shear, S , from Equation 2-68 and 2-70 are added to the scale equations (2-63 and 2-64) with an appropriate definition of the shear rate.

Note that only one of the horizontal scales, Λ_{cH} , is increased by the presence of shear. For general meteorology, the shear rate is defined as

$$S^2 = \left(\frac{\partial \bar{u}}{\partial z} \right)^2 + \left(\frac{\partial \bar{v}}{\partial z} \right)^2 + \frac{1}{4} \left[\frac{1}{\overline{u'^2}} \left(\frac{\partial}{\partial z} \overline{u_L'^2} \right)^2 + \frac{1}{\overline{v_L'^2}} \left(\frac{\partial}{\partial z} \overline{v_L'^2} \right)^2 \right] \quad \text{Eq. 2-72}$$

This includes an estimate of the large-scale fluctuating shear in addition to the mean wind contribution. The fluctuation contribution assumes a linear velocity distribution with height as typical of the instantaneous distribution. This is a plausible assumption for large-scale variations, where the thermal wind relation dominates the tropospheric wind profile.

2.2.4 Puff Interaction Treatment

In addition to the three internal fluctuation length scales discussed in Section 2.2.2, the puffs must also include an equation for the concentration fluctuation variance. This is a nonlinear quantity and therefore requires a treatment of puff interactions. We have found that it is easier to deal with the total square concentration, $\overline{c^2}$, because the conservation equation is simpler than the fluctuation variance, $\overline{c'^2}$, cf. Equations 2-44 and 2-45. Because the total square concentration equation involves only a dissipation term, the puff transport equation is simply

$$\frac{d}{dt} \langle \overline{c^2} \rangle = - \frac{\langle \overline{c'^2} \rangle}{\tau_c} \quad \text{Eq. 2-73}$$

where the dissipation timescale, τ_c , has been defined in the previous section.

Note that the puff integral on the right-hand side of Equation 2-73 is the fluctuation variance, which must be estimated from the relation

$$\langle \overline{c^2} \rangle = \langle \overline{c'^2} \rangle + \langle \overline{c}^2 \rangle \quad \text{Eq. 2-74}$$

If we represent the mean concentration as a sum of Gaussian puffs, the expression for the local concentration is

$$\overline{c}(\mathbf{x}) = \sum_{\alpha} Q^{(\alpha)} G^{(\alpha)}(\mathbf{x}) \quad \text{Eq. 2-75}$$

where the sum is taken over all the contributing puffs, denoted by a superscript α , and $G^{(\alpha)}$ represents the spatial Gaussian distribution of puff- α . The square of the mean concentration is therefore

$$\overline{c}^2(\mathbf{x}) = \sum_{\alpha, \beta} Q^{(\alpha)} Q^{(\beta)} G^{(\alpha)}(\mathbf{x}) G^{(\beta)}(\mathbf{x}) \quad \text{Eq. 2-76}$$

and requires a sum over all puff pairs. The distribution of \overline{c}^2 among the individual puffs for substitution in Equation 2-74 is not unique, but an obvious partition is given by

$$\langle \overline{c}^2 \rangle^{(\alpha)} = Q^{(\alpha)} \sum_{\beta} Q^{(\beta)} I_{\alpha\beta} \quad \text{Eq. 2-77}$$

where the interaction integral is defined as

$$I_{\alpha\beta} = \langle G^{(\alpha)}(\mathbf{x}) G^{(\beta)}(\mathbf{x}) \rangle \quad \text{Eq. 2-78}$$

that is, the overlap integral between the two Gaussian puffs.

Ignoring surface reflections for the present, the Gaussian shape is conveniently specified using the inverse of the spread tensor as

$$G^{(\alpha)}(\mathbf{x}) = \frac{\exp(-A^{(\alpha)}(\mathbf{x}))}{(2\pi)^{3/2} D_{\alpha}^{1/2}} \quad \text{Eq. 2-79}$$

where $D_{\alpha} = \|\sigma^{(\alpha)}\|$ and $\|\cdot\|$ denotes the determinant. The exponential argument is

$$A^{(\alpha)}(\mathbf{x}) = \alpha_{ij} (x_i - \bar{x}_i^{(\alpha)}) (x_j - \bar{x}_j^{(\alpha)}) \quad \text{Eq. 2-80}$$

and

$$\alpha_{ij} = \frac{(\sigma_{ij}^{(\alpha)})^{-1}}{2} \quad \text{Eq. 2-81}$$

The product of the two Gaussians is then

$$G^{(\alpha)}(\mathbf{x}) G^{(\beta)}(\mathbf{x}) = \frac{\exp(-A^{(\alpha)}(\mathbf{x}) - A^{(\beta)}(\mathbf{x}))}{(2\pi)^3 (D_\alpha D_\beta)^{1/2}} \quad \text{Eq. 2-82}$$

and the exponential argument can be written in the form

$$\begin{aligned} A^{(\alpha\beta)}(\mathbf{x}) &= A^{(\alpha)}(\mathbf{x}) + A^{(\beta)}(\mathbf{x}) \\ &= \gamma_{ij} (x_i - \hat{x}_i - \bar{x}_i^{(\beta)}) (x_j - \hat{x}_j - \bar{x}_j^{(\beta)}) + c_{\alpha\beta} \end{aligned} \quad \text{Eq. 2-83}$$

where

$$c_{\alpha\beta} = \gamma_0 - \gamma_{ij} \hat{x}_i \hat{x}_j \quad \text{Eq. 2-84}$$

$$\gamma_{ij} = \alpha_{ij} + \beta_{ij} \quad \text{Eq. 2-85}$$

$$\gamma_0 = \alpha_{ij} \Delta_i \Delta_j \quad \text{Eq. 2-86}$$

$$\hat{x}_i = -\gamma_{ij}^{-1} \alpha_{jk} \Delta_k \quad \text{Eq. 2-87}$$

$$\Delta_i = \bar{x}_i^{(\beta)} - \bar{x}_i^{(\alpha)} \quad \text{Eq. 2-88}$$

Here, β_{ij} is the inverse of the moments of puff- β , defined similarly to Equation 2-81.

The overlap integral can then be computed directly as

$$I_{\alpha\beta} = \frac{\exp(-c_{\alpha\beta})}{(4\pi)^{3/2} (\|\gamma\| D_\alpha D_\beta)^{1/2}} \quad \text{Eq. 2-89}$$

Puff reflections at the surface and at a capping inversion are also accounted for in the puff interactions. We modify the interaction term to account for reflections as

$$I_{\alpha\beta} = Q^{(\alpha)} Q^{(\beta)} \int (G^{(\alpha)} + G_R^{(\alpha)}) (G^{(\beta)} + G_R^{(\beta)}) dV \quad \text{Eq. 2-90}$$

where the subscript R represents the reflected Gaussian and the volume integral is taken over the region $z > 0$. This gives four terms in the interaction integral, that is,

$$I_{\alpha\beta} = Q^{(\alpha)} Q^{(\beta)} \int (G^{(\alpha)} G^{(\beta)} + G_R^{(\alpha)} G_R^{(\beta)} + G^{(\alpha)} G_R^{(\beta)} + G_R^{(\alpha)} G^{(\beta)}) dV \quad \text{Eq. 2-91}$$

As shown in Section 12.1, the reflected Gaussian distribution for an individual puff is described by a simple multiplicative exponential factor. The distribution for a puff reflected at the ground surface is therefore obtained by multiplying the original Gaussian by $(1 + \exp(-R_\alpha z))$, where R_α is defined in Equation 12-9. Applying this reflection factor to the two interacting puffs and performing the overlap integral in the region $z > 0$ introduces a factor, f_R , in the integral $I_{\alpha\beta}$, where

$$f_R = \frac{1}{2} \left[\operatorname{erfc} \left(-(\hat{z} + \bar{z}_\beta) \sqrt{\Gamma_{33}} \right) + e^{-g_\alpha} \operatorname{erfc} \left(-z_\alpha \sqrt{\Gamma_{33}} \right) + e^{-g_\beta} \operatorname{erfc} \left(-z_\beta \sqrt{\Gamma_{33}} \right) + e^{-g_{\alpha\beta}} \operatorname{erfc} \left(-z_{\alpha\beta} \sqrt{\Gamma_{33}} \right) \right] \quad \text{Eq. 2-92}$$

Here,

$$\begin{aligned} z_\alpha &= (\hat{z} + \bar{z}_\beta) - \frac{R_\alpha}{2\Gamma_{33}} \\ z_\beta &= (\hat{z} + \bar{z}_\beta) - \frac{R_\beta}{2\Gamma_{33}} \\ z_{\alpha\beta} &= (\hat{z} + \bar{z}_\beta) - \frac{R_\alpha + R_\beta}{2\Gamma_{33}} \\ g_\alpha &= R_\alpha \left((\hat{z} + \bar{z}_\beta) - \frac{R_\alpha}{4\Gamma_{33}} \right) \\ g_\beta &= R_\beta \left((\hat{z} + \bar{z}_\beta) - \frac{R_\beta}{4\Gamma_{33}} \right) \\ g_{\alpha\beta} &= (R_\alpha + R_\beta) \left((\hat{z} + \bar{z}_\beta) - \frac{R_\alpha + R_\beta}{4\Gamma_{33}} \right) \end{aligned} \quad \text{Eq. 2-93}$$

and

$$\Gamma_{33} = \frac{1}{(\gamma^{-1})_{33}} \quad \text{Eq. 2-94}$$

The first two terms in the integrand in Equation 2-91 can be combined to give a simple integral over all space of $G^{(\alpha)} G^{(\beta)}$ if the reflected Gaussian satisfies the property

$$G_R^{(\alpha)}(x, y, z) = G^{(\alpha)}(x, y, -z) \quad \text{Eq. 2-95}$$

This is not true in general for skewed puffs, because we represent the reflected puff using a centroid that is displaced horizontally along the line from the original puff centroid to the surface maximum concentration location. However, if both puffs have the same skewness, so that the lines from the centroid to the surface maximum are parallel, the horizontal displacements will be the same for both reflected puffs. Because the integral is taken over all space, the horizontal displacement is immaterial—and the sum of the two terms is again equivalent to a complete

space integral of the unreflected Gaussian. We use this approximation for all interactions to save computational time, because we expect puffs that interact significantly to have similar skewness. The skewness is generated by the wind shear, and puffs in the same region will be subjected to the same shears, so that it is unlikely for puffs to overlap significantly with different skewness. The simplified surface reflection factor is therefore given by

$$f_R = 1 + \frac{1}{2} \left[e^{-g_\alpha} \operatorname{erfc}(-z_\alpha \sqrt{\Gamma_{33}}) + e^{-g_\beta} \operatorname{erfc}(-z_\beta \sqrt{\Gamma_{33}}) \right] \quad \text{Eq. 2-96}$$

The capping inversion reflection is treated in a similar way, with a simple reflection at the puff capping height, $z_c^{(\alpha)}$. The reflection factor is composed of two factors—one for each puff—but the enhanced factor (the error function term) is added only if the effective displacement is positive, that is, the overlap centroid lies below the reflection level.

In principle, the interaction calculation described previously should be made for all possible pairs of puffs. This is clearly impractical for a large number of puffs and is usually unnecessary because many pairs will be separated in space and the overlap integral will be negligible. SCIPUFF uses a three-dimensional grid with a multi-level adaptive technique in the horizontal plane to determine near-neighbor puffs. The technique is described in Section 4.3 in connection with the merging process. The multi-level technique allocates each puff to a horizontal grid cell based on the puff size. Interactions are calculated only for puffs in neighboring cells on this grid, because contributions to the overlap integral from puffs more remote than the neighbor cells are small.

The overlap integral is calculated only for puffs on the same horizontal grid, so that the interaction between puffs with different horizontal sizes is neglected. This is equivalent to an assumption of no correlation between such puffs, because the total variance is calculated as a sum of the contributions from each puff. If the variance is computed without interaction, a simple sum of variances implies uncorrelated fluctuations. This is a reasonable assumption for puffs of different sizes, because they must have different transport histories and are generally uncorrelated.

We also note that SCIPUFF can calculate multiple species and/or particle size groups in a single computation and that each puff is assigned a specific type descriptor to designate its material properties. Interactions are computed only for puffs of the same type, and correlations between different types are not calculated. Any subsequent combination sum of material types or particle size groups must estimate a cross-correlation if the variance is required. For the special case of multiple particle size bins, two variance calculations are stored so that statistics for the total material concentrations are available. SCIPUFF accounts for interactions among all puffs in the same size group and among all puffs of the same material and any size group. This provides a variance calculation for the concentration of the individual size group as well as a variance for the total concentration obtained as the sum over all size bins.

2.2.5 Conditional Average Dispersion

The second-order closure framework of SCIPUFF provides a prediction of the statistical variance in the concentration value, as described previously. This variance gives a measure of the uncertainty in the concentration prediction and depends on the velocity fluctuation statistics used

to determine the dispersion rates. Under some circumstances, a meaningful quasi-deterministic prediction can be obtained by restricting the definition of the turbulent velocity fluctuations. By ignoring the large-scale meandering motions in the turbulence, a conditional average result can be generated in which the uncertainty in the plume/cloud location is ignored. It must be recognized that the conditional average simply neglects the meandering component of the turbulence and provides a prediction of the small-scale diffusion effects.

The conditional average is obtained by specifying an averaging time, T_{av} . This timescale is converted into a length scale, Λ_{av} , using the local wind speed and is used to restrict the velocity variance to the diffusive range of scales. The averaging time should be thought of as a sampling time but can also be considered the release duration if this is shorter than the sample time. Therefore, an instantaneous measurement or an instantaneous release both imply a zero averaging time.

A reduction factor is applied to the velocity variances if the length scale of the velocity fluctuations is larger than the conditional average scale, which is defined as the larger of Λ_{av} and the instantaneous cloud scale. Turbulent motions on scales smaller than the instantaneous cloud are always diffusive in character, so this part of the spectrum must be included in the conditional average. When the instantaneous cloud is smaller than the conditional average scale, the averaging time determines the range of scales. A simple power law reduction, consistent with the Kolmogorov inertial range behavior of the energy spectrum, is assumed. Therefore, the boundary layer turbulence used in the dispersion model equations in Section 2.1.3 is defined as

$$\overline{u'^2_{BT}} = \overline{u'^2_B} \left(\frac{\Lambda_{HT}}{\Lambda_{HB}} \right)^{2/3} \quad \text{Eq. 2-97}$$

$$\overline{v'^2_{BT}} = \overline{v'^2_B} \left(\frac{\Lambda_{HT}}{\Lambda_{HB}} \right)^{2/3} \quad \text{Eq. 2-98}$$

$$\overline{w'^2_{BT}} = \overline{w'^2_B} \left(\frac{\Lambda_{VT}}{\Lambda_{VB}} \right)^{2/3} \quad \text{Eq. 2-99}$$

$$\overline{w'\theta'_{BT}} = \overline{w'\theta'_B} \left(\frac{\Lambda_{VT}}{\Lambda_{VB}} \right)^{4/3} \quad \text{Eq. 2-100}$$

where the conditional filter scales are

$$\Lambda_{HT} = \min \left[\Lambda_{HB}, \max(\Lambda_c, \Lambda_{av}) \right] \quad \text{Eq. 2-101}$$

$$\Lambda_{VT} = \min \left[\Lambda_{VB}, \max(\Lambda_{cV}, \Lambda_{av}) \right] \quad \text{Eq. 2-102}$$

The new velocity correlations and length scales, defined in Equations 2-97 through 2-102, are then used in the dispersion model equations. A similar procedure is applied to the large-scale velocity correlations and length scale.

The conditional average length scale, Λ_{av} , is defined in terms of the averaging timescale as

$$\Lambda_{av} = 0.03 V T_{av} \quad \text{Eq. 2-103}$$

where V is the local velocity scale, which includes both the mean velocity and the turbulence. Therefore,

$$V^2 = \overline{u_i u_i} + \overline{u_i'^2} \quad \text{Eq. 2-104}$$

and the conditional boundary layer component uses the boundary layer turbulence. The length scale for the large-scale component uses the large-scale velocity variance in Equation 2-104.

The conditional averaging representation is described in detail and compared with field data by Sykes and Gabruk (1997); the field data comparisons are included in Section 13, Model Evaluation Studies.

2.3 Surface Deposition

Surface deposition of the gaseous material introduces a source term into the concentration equation (2-5) and therefore modifies the puff moment equations. A simple constant deposition velocity, v_D , is used, so the puff mass conservation equation (2-7) becomes

$$\frac{dQ}{dt} = -F_s \quad \text{Eq. 2-105}$$

where the mass flux at the surface is defined as

$$F_s = v_D \int_{z=0} c dA \quad \text{Eq. 2-106}$$

Other deposition effects for particles are discussed in Section 6. Integrating the mean surface concentration for the generalized Gaussian puff gives

$$\int_{z=0} \bar{c} dA = \frac{Q}{\sqrt{2\pi D D_H}} \exp\left(-\alpha_{33} \bar{z}^2 + \alpha_{11} x_s^2 + \alpha_{22} y_s^2 + 2\alpha_{12} x_s y_s\right) \quad \text{Eq. 2-107}$$

where α_{ij} is defined in Equation 2-81 as half the inverse of the puff moment tensor σ_{ij} , D is the determinant of σ_{ij} , and

$$\begin{aligned} D_H &= \alpha_{11} \alpha_{22} - \alpha_{12}^2 \\ x_s &= (\alpha_{13} \alpha_{22} - \alpha_{23} \alpha_{12}) \frac{\bar{z}}{D_H} \\ y_s &= (\alpha_{23} \alpha_{11} - \alpha_{13} \alpha_{12}) \frac{\bar{z}}{D_H} \end{aligned} \quad \text{Eq. 2-108}$$

The expression in Equation 2-107 includes a factor of 2 to account for the surface reflection, as discussed in Section 12.1.

The flux term in Equation 2-105 can be used to define a deposition timescale

$$\tau_s = \frac{Q}{F_s}, \quad \text{Eq. 2-109}$$

which is then used to decay all the other concentration-weighted puff moments, such as $\langle x_i \overline{u'_j c'} \rangle$.

2.4 Surface Integrals

2.4.1 Surface Dose or Dosage Integration

The integrated surface dose is one of the optional output choices and is defined as

$$\chi_T(x, y, t) = \int_0^t c(x, y, 0, t') dt' \quad \text{Eq. 2-110}$$

This quantity is accumulated on an adaptive grid as described in Section 4.7.

The probabilistic aspect of the SCIPUFF prediction is also incorporated into the surface integral fields through a calculation of the variance of the integral, $\overline{\chi_T'^2}$. From Equation 2-110, we obtain the equation for the mean-square fluctuation integral as

$$\overline{\chi_T'^2}(t) = \int_0^t dt'' \int_0^t dt' \overline{c'(t'') c'(t')} \quad \text{Eq. 2-111}$$

which involves a two-time correlation for the concentration field. We have omitted the spatial coordinates in Equation 2-111 because the time variation is the only concern in this discussion.

We assume that the time correlation is exponential, that is,

$$\overline{c'(t'') c'(t')} = \overline{c'^2(t')} \exp\left(-\frac{|t'' - t'|}{T_c}\right) \quad \text{Eq. 2-112}$$

where T_c is the integral timescale for the concentration fluctuations. Substituting in Equation 2-111 and assuming that the time integration covers the range of the autocorrelation function, we obtain

$$\overline{\chi_T'^2}(t) = 2 \int_0^t dt' \overline{c'^2(t')} T_c(t') \quad \text{Eq. 2-113}$$

The estimation of the integral timescale for the surface concentration fluctuations, T_c , is currently based on the simplified meandering plume analyses of Gifford (1959) and Sykes (1984). These analyses show that the effect of intermittency is to reduce the integral timescale dramatically from the Eulerian wind fluctuation timescale and to introduce a logarithmic correction factor. The intermittency is measured by the concentration fluctuation intensity, and Sykes (1984) suggests the approximation

$$T_{cP} = \frac{T_E}{2} \frac{\bar{c}^2}{\bar{c}'^2} \ln \left(1 + 2 \frac{\bar{c}'^2}{\bar{c}^2} \right) \quad \text{Eq. 2-114}$$

for the meandering plume case, where T_E is the Eulerian velocity timescale. For the meandering plume model, the fluctuation intensity can be related to the concentration fluctuation scale, Λ_c , and the scale of the ambient turbulent velocity fluctuations, Λ_A . A generalized approximation for the intensity is then given by

$$I_c = \left(\frac{\Lambda_A^2}{\Lambda_c \Lambda_{cA}} \right)^{1/3} \quad \text{Eq. 2-115}$$

where the modified streamwise scale, Λ_{cA} , is defined as $\min(\Lambda_{cH}, \Lambda_A)$, so that it is equal to the concentration fluctuation scale for a puff release or the ambient scale for a plume.

Using this estimate of the intensity, we define an effective length scale as

$$\lambda_{cA} = \min \left(\frac{\Lambda_A}{I_c} \frac{\ln(1 + I_c)}{\ln(2)}, \Lambda_{cA} \left(2.5 - 1.5 \left(\frac{\Lambda_{cA}}{\Lambda_A} \right)^2 \right) \right) \quad \text{Eq. 2-116}$$

for $\Lambda_c \leq \Lambda_A$. The additional limit is applied for short-duration integrals associated with instantaneous releases in the near field and is independent of the effective fluctuation intensity; Equation 2-116 gives a scale $\lambda_A = 2.5 \Lambda_{cA}$ in this case. For $\Lambda_c > \Lambda_A$, we use $\lambda_{cA} = \Lambda_c$, and the proportionality constant in Equation 2-116 is chosen to match the two estimates at $\Lambda_c = \Lambda_A$.

The use of the generalized notation for the ambient scale results from the fact that there are three components of the ambient turbulence, and the various weighting factors in Equation 2-116 preclude the use of a composite scale based on the ambient velocity variances. The effective horizontal turbulence scale used to define the correlation timescale, Λ_y , is estimated using an energy-weighted average of the three horizontal scales obtained from Equation 2-116 for the three ambient components. Therefore,

$$\Lambda_y = \frac{\left(\overline{u_L'^2} + \overline{v_L'^2} \right) \lambda_{cL} + \left(\overline{u_B'^2} + \overline{v_B'^2} \right) \lambda_{cB} + \left(\overline{u_S'^2} + \overline{v_S'^2} + \overline{w_S'^2} \right) \lambda_{cS}}{q_T^2} \quad \text{Eq. 2-117}$$

where q_T^2 is the total turbulent energy.

We estimate the Eulerian scale of the turbulence as

$$T_E = 0.7 \frac{\Lambda_y}{\sqrt{\bar{u}^2 + \bar{v}^2 + q_H^2}} \quad \text{Eq. 2-118}$$

The estimate in Equation 2-116 is appropriate for continuous plumes, but instantaneous sources may have shorter timescales because of the short duration of passage. We therefore define a “time-of-passage” timescale as

$$T_{cH} = 0.7 \frac{\Lambda_{cH}}{\sqrt{u^2 + v^2 + q_H^2}} \quad \text{Eq. 2-119}$$

using the second horizontal concentration fluctuation scale. This timescale will be large for a continuous source, because Λ_{cH} represents the streamwise length scale. The correlation timescale is defined as the smaller of the two estimates, that is,

$$T_c = \min(T_{cP}, T_{cH}) \quad \text{Eq. 2-120}$$

The variance contribution is accumulated on the same surface grid as the mean, using the Gaussian shape of the mean concentration, so that

$$\overline{\chi_T'^2}(t + \Delta t) = \overline{\chi_T'^2}(t) + 2\overline{c} \Delta t T_c \frac{\langle \overline{c'^2} \rangle}{Q} \quad \text{Eq. 2-121}$$

In addition, the effective length scale of the fluctuations is calculated using the variance as a weighting factor applied to Λ_c .

2.4.2 Surface Deposition Integration

The mass deposited on the surface is computed in a similar way to the surface dose. In this case, the deposition is defined as

$$\chi_D(x, y, t) = \int_0^t v_D c(x, y, 0, t') dt' \quad \text{Eq. 2-122}$$

where v_D is the total deposition velocity, including gravitational settling for particles or droplets and turbulent dry deposition. The mean and variance of the deposition are calculated the same as the dose but with the extra factor of the deposition velocity. Conservation of total mass is ensured by estimating the deposited mass as the actual loss of mass from the puff in the time step Δt .

3

REACTIVE CHEMISTRY

3.1 Gas-Phase Chemistry

The full gas-phase chemistry mechanism distributed with SCICHEM 3.3 is similar to those used in well-established photochemical grid models, such as CAMx and CMAQ. The mechanism is a variant of version 6 of the Carbon Bond mechanism (CB6), referred to as CB6r2. Additional details on the CB6 mechanism are provided in Yarwood et al. (2010). In this section, we focus on how puff gas-phase chemistry is treated in SCICHEM.

Chemical reaction processes are described in SCICHEM using the concept of multicomponent material. The tracer or non-reactive contaminant is associated with a set of species concentrations, $\{s_i: i=1, n\}$. It is assumed that the associated species are transported and diffused in the same way as the conserved tracer material. The quadratic overlap term is already calculated by SCIPUFF for use in the concentration fluctuation variance equation. The mean squared scalar concentration, \bar{c}^2 , for puff α is written as

$$\int_v \bar{c}^{2(\alpha)} dv = Q^{(\alpha)} \sum_{\beta} I_{\alpha\beta} Q^{(\beta)} \quad \text{Eq. 3-1}$$

where the sum is taken over all the puffs and $I_{\alpha\beta}$, the interaction coefficient or the overlap integral between two Gaussian puffs, is given by $I_{\alpha\beta} = \int_v G^{(\alpha)}(\mathbf{x}) G^{(\beta)}(\mathbf{x}) dv$. The overlap definition is extended to the reactive species, and the effective species-A concentration perturbation for puff α is defined as

$$\hat{s}_A^{(\alpha)} = \sum_{\beta} I_{\alpha\beta} \int_v s_A^{(\beta)} dv \quad \text{Eq. 3-2}$$

In SCICHEM, the reactions are written in a generalized form as



where A, B and P_i represent individual species concentration, k is the reaction rate, and ζ and γ_i are the stoichiometric coefficients. If ζ is non-zero, the reaction is assumed first order in A and first order in B , and the overall reaction is considered second order. Note that the coefficient ζ is a multiplicative factor and does not imply higher order reactions. If ζ is zero, the reaction is first-order decay of A . The total reaction rate for the general reaction in Equation 3-6 using the concentration perturbation for puff α is given by

$$R = k(\hat{s}_A^{(\alpha)} + A_0)(\hat{s}_B^{(\alpha)} + B_0) \quad \text{Eq. 3-4}$$

where A_0 and B_0 are the ambient concentrations of species A and B , respectively. Because we step only the perturbation concentrations, the background reaction rate $-k(A_0B_0)$ is excluded in the equation so that

$$\hat{R} = k(\hat{S}_A^{(\alpha)}\hat{S}_B^{(\alpha)} + \hat{S}_A^{(\alpha)}B_0 + A_0\hat{S}_B^{(\alpha)}) \quad \text{Eq. 3-5}$$

This gives the desirable result that a release of zero emissions of reactive species does not cause any reactions to occur in the puffs. If there are M reactions, the species perturbation concentrations are advanced using a system of n differential equations summarized as

$$\frac{d\hat{S}_i^{(\alpha)}}{dt} = \sum_{j=1}^M a_{ij}\hat{R}_j \quad \text{Eq. 3-6}$$

where a_{ij} are the stoichiometric coefficients. For the bimolecular reaction in Equation 3-6, the coefficients become

$$\begin{aligned} a_{Aj} &= -1 \\ a_{Bj} &= -\zeta^{(j)} \\ a_{P_i j} &= \gamma_i^{(j)} \end{aligned} \quad \text{Eq. 3-7}$$

Here, index A denotes the species- A and so on. For linear reactions, a_{Bj} does not exist. Similarly, the product species P_i may also be absent.

In addition to the species concentrations, the set of species masses $\{m_i: i=1, n\}$ is advanced as described next.

The set of species masses $\{m_i: i=1, n\}$ associated with each puff- α is adjusted using the advanced perturbation concentrations and the overlap volume.

$$\frac{D}{Dt}m_i^{(\alpha)} = \hat{V} \frac{D}{Dt}\hat{S}_i^{(\alpha)} \quad \text{Eq. 3-8}$$

where the overlap volume \hat{V} is defined as

$$\hat{V} = \left(\sum_{\beta} I_{\alpha\beta} \right)^{-1} \quad \text{Eq. 3-9}$$

To account for the fact that the perturbation concentration in some puffs may be dominated by surrounding puffs, the reaction rate coefficients are multiplied by a reaction volume factor, f . Equation 3-8 for first-order reaction can then be written as

$$\frac{D}{Dt}m_A^{(\alpha)} = -f k \hat{V} \hat{S}_A^{(\alpha)} \quad \text{Eq. 3-10}$$

and for second-order reaction it becomes

$$\frac{D}{Dt} m_A^{(\alpha)} = \frac{D}{Dt} m_B^{(\alpha)} = -f k \hat{V} (\hat{S}_A^{(\alpha)} \hat{S}_B^{(\alpha)} + \hat{S}_A^{(\alpha)} B_0 + A_0 \hat{S}_B^{(\alpha)}) \quad \text{Eq. 3-11}$$

The equations can be rewritten as

$$\frac{D}{Dt} m_A^{(\alpha)} = -f k \hat{V} m_A^{(\alpha)} \frac{\hat{S}_A^{(\alpha)}}{m_A^{(\alpha)}} \quad \text{Eq. 3-12}$$

and

$$\frac{D}{Dt} m_A^{(\alpha)} = \frac{D}{Dt} m_B^{(\alpha)} = -f k \hat{V} \left(\frac{\hat{S}_A^{(\alpha)}}{2} m_B^{(\alpha)} \frac{\hat{S}_B^{(\alpha)}}{m_B^{(\alpha)}} + \frac{\hat{S}_B^{(\alpha)}}{2} m_A^{(\alpha)} \frac{\hat{S}_A^{(\alpha)}}{m_A^{(\alpha)}} + m_A^{(\alpha)} \frac{\hat{S}_A^{(\alpha)}}{m_A^{(\alpha)}} B_0 + A_0 m_B^{(\alpha)} \frac{\hat{S}_B^{(\alpha)}}{m_B^{(\alpha)}} \right) \quad \text{Eq. 3-13}$$

The reaction volume factor for a first-order reaction must be

$$f = f_A = \hat{V}^{-1} \frac{m_A^{(\alpha)}}{\hat{S}_A^{(\alpha)}} \quad \text{Eq. 3-14}$$

and, using this definition, the second-order reaction would be

$$\frac{D}{Dt} m_A^{(\alpha)} = \frac{D}{Dt} m_B^{(\alpha)} = -f k \left(\frac{\hat{S}_A^{(\alpha)}}{2} m_B^{(\alpha)} f_B^{-1} + \frac{\hat{S}_B^{(\alpha)}}{2} m_A^{(\alpha)} f_A^{-1} + m_A^{(\alpha)} f_A^{-1} B_0 + A_0 m_B^{(\alpha)} f_B^{-1} \right) \quad \text{Eq. 3-15}$$

Typically, the ratio of the species masses to overlap concentrations is the same for all species for a given puff, and the value of f should be

$$f = f_A = f_B \quad \text{Eq. 3-16}$$

However, in some circumstances, it is not the case—and we use the corresponding reaction rate factor for each species. The transport and diffusion terms are omitted from the evolution of the species concentration equations because these processes are represented by the evolution of the puff moments, which are calculated separately for the tracer material. Dry deposition of the reactive species is treated at the end of the chemistry step.

3.2 Aerosol and Aqueous-Phase Chemistry

Aerosol and aqueous-phase chemistry can be optionally treated in SCICHEM 3.3 using a runtime flag selection. The aerosol and aqueous-phase chemistry modules in SCICHEM 3.3 are based on the modules used in the U.S. EPA Community Multiscale Air Quality (CMAQ) model (Byun and Schere, 2006), Version 4.7.1. The SCICHEM 3.3 aerosol module is based on the AERO5 aerosol module in CMAQ. The module uses a modal approach with three modes to treat size distribution and includes the ISORROPIA II inorganic thermodynamic equilibrium module (Fountoukis and Nenes, 2007) and a secondary organic aerosol module (Carlton et al., 2010). The cloud chemistry module includes sulfur and organic oxidation aqueous phase chemistry (Carlton et al., 2008). Additional details on these modules are provided in Foley et al. (2010).

4

NUMERICAL TECHNIQUES

4.1 Finite Difference Schemes

The ordinary differential equations for the puff moments and properties are generally solved using a simple, explicit forward time-difference. However, all linear damping terms are represented implicitly, so that an equation of the form

$$\frac{d\phi}{dt} = F - \mu\phi \quad \text{Eq. 4-1}$$

is represented numerically as

$$\frac{\phi(t + \Delta t) - \phi(t)}{\Delta t} = F(t) - \mu(t)\phi(t + \Delta t) \quad \text{Eq. 4-2}$$

that is,
$$\phi(t + \Delta t) = \frac{\phi(t) + \Delta t F(t)}{1 + \Delta t \mu(t)} \quad \text{Eq. 4-3}$$

The puff mass and velocity-concentration moment equations can be expressed in the general form (Equation 4-1). The mean-square concentration integrals are treated differently using an exponential approximation, which gives an exact solution for a constant damping rate, μ , and forcing function, F . Therefore, for mean-square concentration

$$\phi(t + \Delta t) = \phi(t)e^{-\mu(t)\Delta t} + (1 - e^{-\mu(t)\Delta t}) \frac{F(t)}{\mu(t)} \quad \text{Eq. 4-4}$$

The puff centroid is advanced using the second-order Adams-Bashforth scheme

$$\bar{x}_i(t + \Delta t) = \bar{x}_i(t) + \frac{\Delta t}{2} [3\bar{u}_i(t) - \bar{u}_i(t - \Delta t)] \quad \text{Eq. 4-5}$$

This technique gives accurate trajectory calculations for idealized velocity fields such as the solid-body rotation flow and avoids the numerical diffusion produced by the trajectory divergence errors of a first-order scheme.

The puff second-moment tensor requires special treatment because it is important to maintain a realizable tensor with a positive determinant. The effective volume of the generalized Gaussian described by the six independent moments, σ_{ij} , is proportional to the square root of the determinant $D = \text{Det}(\sigma)$; this quantity is used to determine local concentrations and interaction terms. The evolution equation for the individual moments is given in Equation 2-11, but the turbulent diffusivities are modeled only for the diagonal components. Therefore, we have

$$\frac{d\sigma_{\alpha\alpha}}{dt} = 2\sigma_{\alpha k} \frac{\partial \bar{u}_\alpha}{\partial x_k} + 2 \frac{\langle x'_\alpha \bar{u}'_\alpha c' \rangle}{Q} \quad \text{Eq. 4-6}$$

for the diagonal components and

$$\frac{d\sigma_{\alpha\beta}}{dt} = \sigma_{\alpha k} \frac{\partial \bar{u}_\beta}{\partial x_k} + \sigma_{\beta k} \frac{\partial \bar{u}_\alpha}{\partial x_k} \quad \text{Eq. 4-7}$$

for the off-diagonal components ($\alpha \neq \beta$). The Greek subscript implies no summation in Equations 4-6 and 4-7. The volume of a fluid parcel is conserved in an incompressible flow, and in the absence of (turbulent) diffusion, conservation of the determinant is implied by Equation 2-11 if the velocity field is solenoidal. It is important that the velocity gradient terms conserve the determinant numerically; this is therefore a necessary property of the numerical scheme.

The evolution of σ_{ij} over one time step is computed using a sequence of steps, with the intermediate results for step m denoted by a subscript; for example, the m -th step for σ_{xx} is $\hat{\sigma}_{xxm}$. The initial step, with $m = 0$, accounts for the turbulent diffusion of the diagonal components, that is,

$$\hat{\sigma}_{xx0} = \sigma_{xx}(t) + 2\Delta t \frac{\langle x'u'c' \rangle}{Q} \quad \text{Eq. 4-8}$$

Here, Δt is the numerical time step and $\sigma_{xx}(t)$ indicates the value at the start of the time step. Equation 4-8 is used for both horizontal components, but the vertical diffusion is split into two partial steps—before and after the shear terms are included—which is discussed next. Off-diagonal components are not affected by this step, that is, $\hat{\sigma}_{xy0} = \sigma_{xy}(t)$.

The next step applies the diagonal velocity gradients using the relation

$$\hat{\sigma}_{\alpha\alpha1} = \hat{\sigma}_{\alpha\alpha0} \exp \left[2\Delta t \frac{\partial \bar{u}_\alpha}{\partial x_\alpha} \right] \quad \text{Eq. 4-9}$$

for all three diagonal components. The vanishing velocity divergence ensures the conservation of D after this step. Note that the zero divergence condition is enforced by setting $\partial \bar{w} / \partial z = -\nabla_H \cdot \mathbf{u}$. Again, the off-diagonal components are unchanged, so $\hat{\sigma}_{xy1} = \hat{\sigma}_{xy0}$.

The six off-diagonal velocity gradients are then applied sequentially in three pairs, $\partial u_\alpha / \partial x_\beta$ and $\partial u_\beta / \partial x_\alpha$. The first step uses (α, β) as (x, y) and the level-1

$$\hat{\sigma}_{xx2} = \frac{\hat{\sigma}_{xx1} + \Delta t \frac{\partial \bar{u}}{\partial y} \left(2\hat{\sigma}_{xy1} + \Delta t \frac{\partial \bar{u}}{\partial y} \hat{\sigma}_{yy1} \right)}{1 - \Delta t^2 \frac{\partial \bar{u}}{\partial y} \frac{\partial \bar{v}}{\partial x}} \quad \text{Eq. 4-10}$$

$$\hat{\sigma}_{yy2} = \frac{\hat{\sigma}_{yy1} + \Delta t \frac{\partial \bar{v}}{\partial x} \left(2\hat{\sigma}_{xy1} + \Delta t \frac{\partial \bar{v}}{\partial x} \hat{\sigma}_{xx1} \right)}{1 - \Delta t^2 \frac{\partial \bar{u}}{\partial y} \frac{\partial \bar{v}}{\partial x}} \quad \text{Eq. 4-11}$$

$$\hat{\sigma}_{xy2} = \frac{\hat{\sigma}_{xy1} + \Delta t \frac{\partial \bar{u}}{\partial y} \hat{\sigma}_{yy1} + \Delta t \frac{\partial \bar{v}}{\partial x} \hat{\sigma}_{xx1} + \Delta t^2 \frac{\partial \bar{u}}{\partial y} \frac{\partial \bar{v}}{\partial x} \hat{\sigma}_{xy1}}{1 - \Delta t^2 \frac{\partial \bar{u}}{\partial y} \frac{\partial \bar{v}}{\partial x}} \quad \text{Eq. 4-12}$$

$$\hat{\sigma}_{xz2} = \frac{\hat{\sigma}_{xz1} + \Delta t \frac{\partial \bar{u}}{\partial y} \hat{\sigma}_{yz1}}{\sqrt{1 - \Delta t^2 \frac{\partial \bar{u}}{\partial y} \frac{\partial \bar{v}}{\partial x}}} \quad \text{Eq. 4-13}$$

$$\hat{\sigma}_{yz2} = \frac{\hat{\sigma}_{yz1} + \Delta t \frac{\partial \bar{v}}{\partial x} \hat{\sigma}_{xz1}}{\sqrt{1 - \Delta t^2 \frac{\partial \bar{u}}{\partial y} \frac{\partial \bar{v}}{\partial x}}} \quad \text{Eq. 4-14}$$

The remaining diagonal moment, σ_{zz} , is unaffected by these two components of the velocity gradient. The other two off-diagonal velocity gradient pairs are included in a similar manner by cycling the indices and velocity components, $x \rightarrow y \rightarrow z$ and $u \rightarrow v \rightarrow w$, and the advanced time level with all the shear terms is obtained as $\hat{\sigma}_{\alpha\beta 4}$. This scheme is more complicated than the single gradient component used in earlier versions of SCIPUFF, but it reduces the errors arising from sequential application of the shear components while preserving the value of the determinant exactly. The relations (Equations 4-10 through 4-14) are only first-order accurate in time for a general shear tensor, but the conservation of the determinant is a more important property than accuracy for long-term stability of the scheme.

The interaction between strong vertical diffusion and vertical wind shear can produce inaccurate distortion of the puffs if the vertical spread is fully advanced with the diffusion prior to the shear effects. The coupled shear-diffusion in Equation 2-11 is complex, but if we consider only one vertical shear component, it can be shown that the shear terms are second-order accurate. In addition, the second-order accuracy of the coupled shear-diffusion can be obtained by applying one-third of the diffusion in the vertical spread as the initial estimator, that is,

$$\hat{\sigma}_{zz0} = \sigma_{zz}(t) + \frac{2}{3} \Delta t \frac{\langle z' \overline{w' c'} \rangle}{Q} \quad \text{Eq. 4-15}$$

The remaining diffusion is included after the shear distortion, so the final estimate for the vertical diagonal component is

$$\hat{\sigma}_{zz5} = \hat{\sigma}_{zz4} + \frac{4}{3} \Delta t \frac{\langle z' \overline{w' c'} \rangle}{Q} \quad \text{Eq. 4-16}$$

4.2 Puff Splitting

4.2.1 Splitting Scheme

The puff moment evolution equations given in Section 2.1 generally increase the size of the puff through turbulent diffusion and elongation along the direction of the wind shear. As the puff grows, the local representation of the turbulence and velocity fields using the puff centroid location becomes increasingly inaccurate. When the meteorological fields are inhomogeneous, the accuracy of the calculation can be maintained only by splitting puffs into smaller components that can sample the variations in the meteorology explicitly. A grid-based method for splitting puffs was presented by Sykes and Henn (1992), where the moment method of Egan and Mahoney (1972) was extended to include some shear effects. In this scheme, grid cells can be thought of as each containing a Lagrangian puff. As the puffs move and spread into neighboring grid cells in a time step, the masses are redistributed to maintain a single puff within each cell. We wish to avoid any numerical grid in the current method, however—so the redistribution cannot be based on the rectangular grid cells.

The objective of puff splitting is to represent the original Gaussian puff with several smaller, overlapping puffs that conserve all the puff moments and change local concentration values only by a small amount. For a split in the x -direction, the original puff is replaced by two smaller puffs as follows. The new centroid locations are displaced by a fraction, r , of the puff spread in the x -direction and by a distance proportional to the off-diagonal moment in the other two coordinate directions. Therefore,

$$\bar{x}_1^{(\alpha)} = \bar{x}_1 \pm r \sqrt{\sigma_{11}} \quad \text{Eq. 4-17}$$

$$\bar{x}_2^{(\alpha)} = \bar{x}_2 \pm r \frac{\sigma_{12}}{\sqrt{\sigma_{11}}} \quad \text{Eq. 4-18}$$

$$\bar{x}_3^{(\alpha)} = \bar{x}_3 \pm r \frac{\sigma_{13}}{\sqrt{\sigma_{11}}} \quad \text{Eq. 4-19}$$

where $\alpha = \{1, 2\}$ corresponds to the plus and minus sign, respectively. The diagonal moments for the new puffs are obtained using the following relations:

$$\sigma_{11}^{(\alpha)} = \sigma_{11} (1 - r^2) \quad \text{Eq. 4-20}$$

$$\sigma_{22}^{(\alpha)} = \sigma_{22} \left(1 - \frac{r^2 \sigma_{12}^2}{\sigma_{11} \sigma_{22}} \right) \quad \text{Eq. 4-21}$$

$$\sigma_{33}^{(\alpha)} = \sigma_{33} \left(1 - \frac{r^2 \sigma_{13}^2}{\sigma_{11} \sigma_{33}} \right) \quad \text{Eq. 4-22}$$

and the new off-diagonal moments are

$$\sigma_{12}^{(\alpha)} = \sigma_{12} (1 - r^2) \quad \text{Eq. 4-23}$$

$$\sigma_{13}^{(\alpha)} = \sigma_{13} (1 - r^2) \quad \text{Eq. 4-24}$$

$$\sigma_{23}^{(\alpha)} = \sigma_{23} - \frac{r^2 \sigma_{12} \sigma_{13}}{\sigma_{11}} \quad \text{Eq. 4-25}$$

Conservation of all puff moments is ensured by this procedure, and the moments of the new puffs are all reduced as well as realizable. The realizability constraints involve the Schwartz inequality between the diagonal and off-diagonal moments, for example, $\sigma_{12}^2 \leq \sigma_{11} \sigma_{22}$ and the strictly positive value for the determinant. These properties can be verified directly from the above relations.

The generalized puff description contains other information in addition to the moments discussed previously. The additional variables fall into two categories—either a conserved puff integral property (similar to the puff mass) or a puff value property (such as turbulence length scale). Integral properties are simply divided equally between the two new puffs, and the value properties are assigned equally to both.

The reduction in puff size is controlled by the parameter r , but a larger reduction in puff size reduces the amount of overlap between the new puffs and gives a poorer representation of the original Gaussian shape. For a puff with diagonal moment tensor, the splitting scheme described by Equations 4-17 through 4-25 creates a pair of Gaussian puffs with a dimensionless separation

$$\delta_s = \frac{\Delta}{\sigma} = \frac{2r}{\sqrt{1-r^2}} \quad \text{Eq. 4-26}$$

where Δ is the distance between the new centroid positions and $\sigma = \sqrt{\sigma_{11}^{(1)}}$ is the new spread in the x -direction.

In general, the difference in concentration distribution resulting from the splitting operation is difficult to specify for an arbitrary Gaussian, but the simple spherical puff with diagonal moments σ^2 provides an idealized case. Figure 4-1 shows the maximum difference between the original Gaussian and the sum of the two smaller Gaussians after splitting in one dimension—that is, x -direction only—and for a two-dimensional split in both x - and y -directions, which creates four puffs. The difference is given relative to the maximum concentration value in the original Gaussian and is plotted as a function of the dimensionless separation, δ_s . The one-

dimensional case clearly provides better overlap between the new puffs and smaller differences for the same separation.

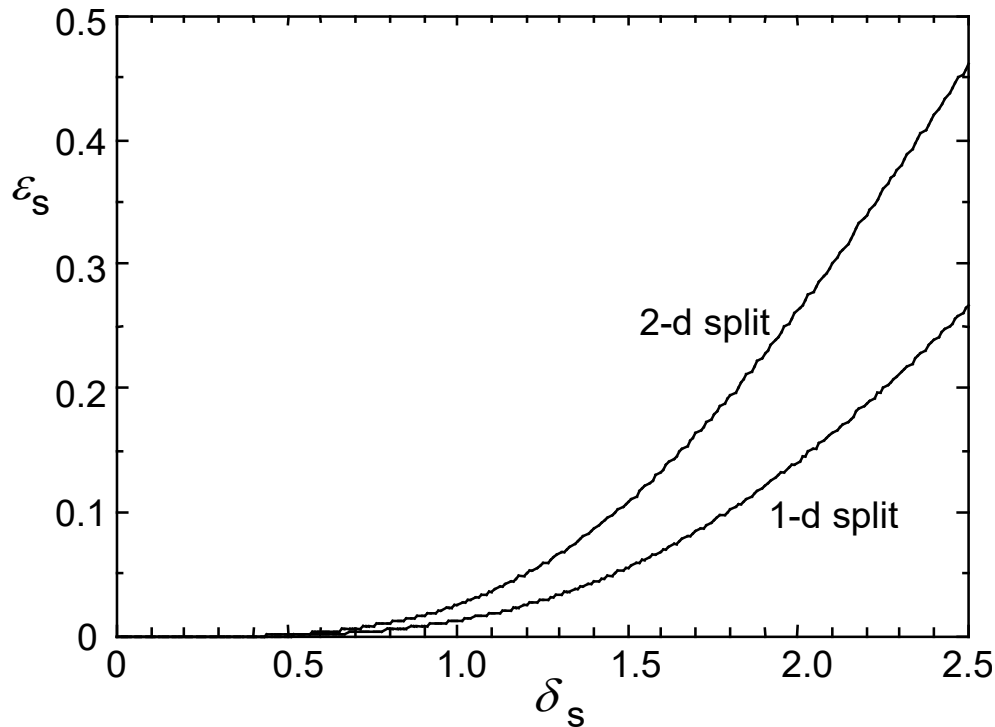


Figure 4-1
Maximum dimensionless error, ϵ_s , from splitting a single Gaussian puff as a function of separation distance, δ_s . The error is relative to the maximum concentration value in the original Gaussian, and the separation distance of the puffs after splitting is relative to the original Gaussian spread. Results are shown for both one-dimensional and two-dimensional splits.

A maximum local concentration change of 20% requires a dimensionless separation of less than 2.25 for a one-dimensional split, but it must be less than 1.8 for two dimensions. In practice, there will usually be additional overlap from other puffs; we have found that $r = 0.75$, that is, $\delta_s = 2.25$, gives the optimum size reduction with acceptable overlap. In diffusive applications, the puff size increases after splitting and reduces the effective separation and overlap errors.

The vertical displacement involved in splitting a puff can create puffs below the ground surface, so a reflection condition must be imposed in these cases. The reflection adjustment is applied if the newly created puff is below the ground. In this case, the puff centroid is relocated by reflecting the vertical coordinate and positioning the centroid along the original displacement line, as illustrated in Figure 4-2.

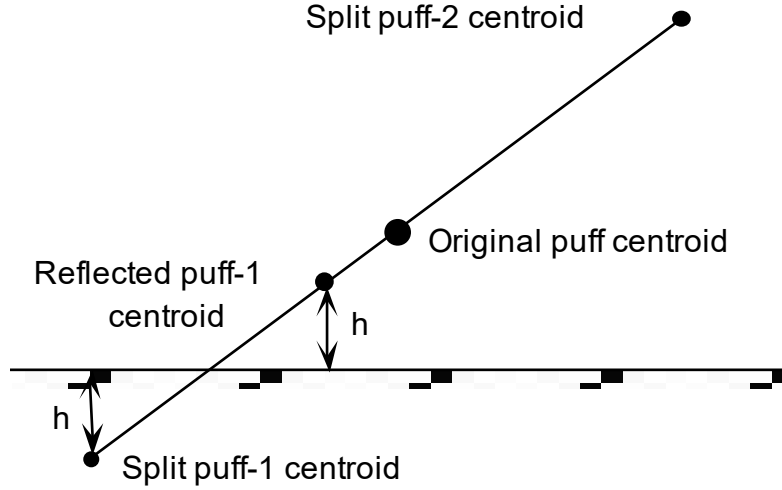


Figure 4-2
Schematic illustration of puff reflection for a split below the ground surface

A similar condition is imposed at the boundary layer capping inversion, $z = z_i$, to prevent diffusion of material through the interface from below. The inversion reflection is applied when a puff within the planetary boundary layer (PBL) splits and creates a new puff with $\bar{z} > z_i$. In this case, the puff will be reflected along the line joining its centroid to the original puff centroid.

In a stable boundary layer, there is no reflective capping inversion and puffs can exit the boundary layer through vertical splitting. Above the boundary layer, diffusion rates are small—so the time for an external puff to grow large enough to split back down into the boundary layer is relatively long. The imbalance between the effective mass flux out of the boundary layer through the splitting mechanism and the return flux from above can cause a buildup of mass just outside the boundary layer. To prevent this non-physical accumulation, a partial reflection is included in the splitting algorithm at the top of the stable layer. Therefore, if splitting a puff inside a stable layer produces a puff outside the layer, the equilibrium vertical diffusivity at the new puff location is compared with its current diffusivity value. Therefore,

$$f_{inv} = \frac{K_z^{eq}}{K_z} \quad \text{Eq. 4-27}$$

where the numerator is defined in Equation 2-32 and is calculated at the new puff location outside the boundary layer, and the denominator is defined in Equation 2-28. If the ratio f_{inv} is less than 1, the mass of the external puff is scaled by f_{inv} , and the remaining mass is restored to the lower puff inside the boundary layer.

4.2.2 Splitting Criteria

4.2.2.1 Vertical Criterion

The vertical puff moment, σ_{33} , gives the effective length of the puff in the vertical direction, and the basic criterion for vertical splitting is given by a fixed size, ΔV . We choose to split a puff

in the z -direction, for example, when $\sigma_{33} > \Delta V^2$. Here, ΔV should be chosen so that the linearization of the velocity and turbulence fields is valid for a Gaussian with smaller spread. In principle, ΔV should be based on the vertical structure of the wind field but is currently specified by a user input. The user specifies the vertical grid size, Δz_{merge} , used for checking for puff merging (see Section 4.3) with a default value of 250 m. The split criterion, ΔV , is then half Δz_{merge} ; this ensures that puff overlap is limited to neighboring grid levels.

Near the surface, where the wind field is known to vary rapidly in the vertical, a more restrictive criterion may be applied. There are two such cases. The first is for puffs within a canopy; see Section 10.2 for the wind profile description. If the canopy height is given by h_c , the puff centroid is lower than $2h_c$, and the puff vertical scale, Λ_{cV} , is also less than h_c , the split criterion is set to the smaller of ΔV and $h_c/4$.

The second case is for puffs inside the boundary layer, where the split criterion is set to the smaller of ΔV and $z_i/8$, where z_i is the boundary layer depth. A puff is judged to be inside the boundary layer if its centroid is within the layer and its vertical scale, Λ_{cV} , is also less than z_i . Note that with the default vertical resolution of 250 m, this criterion will be imposed for puffs inside a boundary layer that is less than 1000 m deep.

4.2.2.2 Horizontal Criterion

Horizontal splitting is generally controlled by the meteorological grid size, because that provides the scale for horizontal variations. The use of high-resolution meteorology or terrain can therefore lead to large numbers of puffs, because splitting generates puffs more rapidly when the size criterion ΔH is smaller. This is because it takes a shorter time for the puff to grow large enough to split, and the split also occurs in two horizontal dimensions. The default criterion is twice the meteorological grid size (the smaller of the x - and y -directional sizes), based on the assumption that the wind field is well-resolved, but user control is provided to adjust the criterion to be larger or smaller by factors of 2. Although the number of puffs can be reduced by increasing the value of ΔH , the accuracy of the calculation is impaired because the estimation of the velocity and velocity gradients can become unreliable. This is because the evaluation of the meteorological fields at the puff centroid may apply small-scale gradients to a larger puff that spans many grid lengths.

To obtain a more representative field estimate for a puff, SCIPUFF uses a hierarchy of horizontally smoothed, or filtered, fields to evaluate the meteorology. The construction of the smoothed fields is described in Section 9.7, with each level of smoothing effectively increasing the grid size by a factor of 2—but for this section we assume that all required fields exist. When a puff requests the local meteorology, the appropriate field is chosen based on the horizontal size of the puff, defined as

$$\sigma_H = \sqrt{\frac{\sigma_{11} + \sigma_{22}}{2}} \quad \text{Eq. 4-28}$$

The field is selected so that the grid size, defined as the square root of the horizontal area of the grid cell, is closest to the puff size. If multiple nested domains are present (see Section 9.6), only

domains containing the puff centroid are considered. Note that the fixed size criterion, ΔH , is based on the original unsmoothed field covering the selected domain—that is, this basic criterion does not depend on the size of the puff, but rather on the actual resolution of the local meteorology. However, we apply further checks to determine whether the size criterion, ΔH , is necessary.

Because the puff distortion representation is exact for a linear velocity variation, it is necessary to split a puff only when the velocity gradient varies significantly across the puff. The split criterion is therefore based on a measure of the second derivative of the velocity, where all derivatives are estimated using centered finite differences on the selected field. Further, a high rate of diffusion can dominate any shear distortion and make puff splitting unnecessary. Accordingly, the puff is split if

$$\sigma_H \geq L_2 \quad \text{Eq. 4-29}$$

where

$$L_2^2 = c_{L2} \frac{\partial \bar{u}_i}{\partial x_j} \left(\frac{\partial \bar{u}_i}{\partial x_j} + \frac{\partial \bar{u}_j}{\partial x_i} \right) \bigg/ \frac{\partial^2 \bar{u}_i}{\partial x_j \partial x_k} \frac{\partial^2 \bar{u}_i}{\partial x_j \partial x_k} \quad \text{Eq. 4-30}$$

and the repeated indices are summed over 1 and 2 only. Splitting may still be avoided if the diffusivity is large, so the puff must also satisfy

$$\sigma_H \geq L_K \quad \text{Eq. 4-31}$$

where

$$L_K^3 = c_K \frac{\left(\langle x' \bar{u}' c' \rangle + \langle y' \bar{v}' c' \rangle \right)}{\langle \bar{c} \rangle} \bigg/ \sqrt{\frac{\partial^2 \bar{u}_i}{\partial x_j \partial x_k} \frac{\partial^2 \bar{u}_i}{\partial x_j \partial x_k}} \quad \text{Eq. 4-32}$$

and the total effective diffusivities are defined in Equations 2-23 and 2-24. The constants in Equations 4-30 and 4-32 are chosen empirically to minimize the number of puff splits without degrading the accuracy of the calculation. The values are chosen as $c_{L2} = 0.04$ and $c_K = 0.5$, and the actual split criterion is the largest of L_2 , L_K , and ΔH . Note that if a puff succeeds in growing without splitting, it will use a velocity-based criterion from a smoothed field, which inherently gives a larger split criterion because of the filtering of the gradients. This process is justified by the observation that smaller scale inhomogeneities are insignificant for a large puff, because the concentration field is essentially constant on the smaller scale and so advection and diffusion are negligible.

An additional splitting criterion is checked in the presence of terrain if the puff centroid is within $3\sqrt{\sigma_{33}}$ of the ground surface. This is to ensure that variations in terrain slope are resolved, which—in the case of a dense gas release, for example—may be important even in the absence of strong velocity variations. Instead of estimating second derivatives numerically, the terrain is evaluated at points offset from the puff centroid along the directions defined for horizontal

splitting: at the four points $(\bar{x}_1 + 2\sqrt{\sigma_{11}}, \bar{x}_2 + \sigma_{12}/\sqrt{\sigma_{11}})$, $(\bar{x}_1 - 2\sqrt{\sigma_{11}}, \bar{x}_2 - \sigma_{12}/\sqrt{\sigma_{11}})$, $(\bar{x}_1 + \sigma_{12}/\sqrt{\sigma_{22}}, \bar{x}_2 + 2\sqrt{\sigma_{22}})$, and $(\bar{x}_1 - \sigma_{12}/\sqrt{\sigma_{22}}, \bar{x}_2 - 2\sqrt{\sigma_{22}})$. The split criterion is set to ΔH if the terrain elevation at any of these locations differs from that at the centroid by an amount larger than Λ_{cV} .

A further splitting criterion involves the splitting of puffs over a sloping surface, where it has been determined that the simplified location adjustment for off-diagonal moments in Equations 4-17 through 4-19 can result in a non-physical rotation of the puff under certain conditions. The adjustment does ensure realizable puffs, but it does not perfectly conserve the orientation of the puff. If the splitting algorithm used the principal axes for the split directions, the orientation would be preserved, but calculation of the principal axes is computationally expensive. The small errors from the Cartesian split can accumulate if the puff persists on a fixed slope over a long period. Under nocturnal conditions where the puff diffuses much more rapidly along the slope compared with the vertical direction, it is possible for a puff to rotate into a horizontal orientation after many splitting operations over a period of hours, and this produces an erroneous surface concentration pattern. This phenomenon is avoided by rotating the puff into a coordinate frame aligned with the slope prior to the splitting algorithm, then rotating the puffs back into the Cartesian frame after the split operation. The rotation is applied if the terrain slope is significant and the puff is close to the surface. Because the rotation is an additional computational burden, a further check to determine if the puff is anisotropic is applied. This rotation is used only if the normal puff spread is less than half the vertical moment, σ_{33} , indicating a tilted anisotropic puff. The normal spread moment is defined as

$$\sigma_{nn} \geq n_i n_j \sigma_{ij} \quad \text{Eq. 4-33}$$

where n_i is the unit normal to the ground surface.

4.3 Puff Merging Scheme

Unfortunately, the splitting process can rapidly lead to excessive numbers of puffs unless some form of merging is employed to reduce the numbers. In general, splitting the puff distribution will create many overlapping puffs that can be merged together as a single Gaussian. The merging rules are actually much simpler than the splitting rules, because the only requirement is moment conservation. Therefore, if superscripts 1 and 2 represent two puffs deemed sufficiently close to one another to merge, they can be combined as follows:

$$Q = Q^{(1)} + Q^{(2)} \quad \text{Eq. 4-34}$$

$$Q \bar{x}_i = Q^{(1)} \bar{x}_i^{(1)} + Q^{(2)} \bar{x}_i^{(2)} \quad \text{Eq. 4-35}$$

$$Q \sigma_{ij} = Q^{(1)} (\sigma_{ij}^{(1)} + \Delta \bar{x}_i^{(1)} \Delta \bar{x}_j^{(1)}) + Q^{(2)} (\sigma_{ij}^{(2)} + \Delta \bar{x}_i^{(2)} \Delta \bar{x}_j^{(2)}) \quad \text{Eq. 4-36}$$

where $\Delta \bar{x}_i^{(\alpha)} = \bar{x}_i^{(\alpha)} - \bar{x}_i$.

Other puff variables are combined according to their type. Integral properties are combined, such as the puff mass in Equation 4-34, as a sum of the two values. Value properties are mass weighted and combined like the puff centroid in Equation 4-35.

The difficulty associated with merging lies in deciding which puff pairs are eligible. In general, if we have N puffs, there are N^2 possible pair combinations—and it rapidly becomes impractical to consider all such pairs when N is large. Some techniques have been suggested for ordering randomly located, multidimensional data with the objective of determining nearest neighbors (for example, Boris, 1986), but we have chosen to use an adaptive multigrid location scheme.

The basic concept of the grid location scheme is to assign each puff to a grid box; a search for near-neighbors can then be carried out by searching over the neighboring grid cells. Two technical difficulties arise in the application of this concept. First, the grid cell size should be determined by the size of the puff itself so that a puff overlaps only a finite number of neighboring grid cells. Second, we must account for an arbitrary number of puffs within each grid cell. Therefore, we cannot simply allocate storage for a fixed grid with a fixed number of puffs in each cell.

The first problem is solved using an adaptive grid in the horizontal plane. In atmospheric cases, the vertical resolution is restricted by the stable stratification, so a fixed grid size of Δz_{merge} is used. However, the horizontal scale varies widely—so an initial coarse grid is defined with size Δ_0 equal to half the size of the calculation domain. Each cell of this coarse grid can be individually refined to create four additional cells with size $\Delta_1 = \Delta_0/2$. The new cells are simply added to the end of the list of cells, and a pointer from the Δ_0 -cell contains the location of the first of the four refined cells. This procedure can be continued as far as computer storage allows.

This successive refinement procedure has the advantage that all coarser levels of the grid are available in addition to the most refined level. Each cell of the grid stores two integer variables: the pointer for the subsequent refinement (if it exists) and the number identifier of the puff located in that cell. The choice of refinement level for locating a puff on the adaptive grid is determined by the largest of the horizontal moments, that is, the grid size $\Delta_n = \Delta_0/2^n$ such that

$$\Delta_n < 4\sigma_{\max} \leq \Delta_{n-1} \quad \text{Eq. 4-37}$$

where $\sigma_{\max}^2 = \max(\sigma_{11}, \sigma_{22})$. The factor of 4 ensures that $\Delta_n \geq 2\sigma_{\max}$, so non-neighbor cells are separated by at least $2\sigma_{\max}$ and their neglect in the overlap calculation of Section 2.2.4 is justified.

A schematic illustration of the puff allocation is shown in Figure 4-3, in which a single puff with index number α is located in cell number 12 (denoted by C12). The puff is allocated to the second level of grid refinement; the grid system generated by this puff is also shown. The grid cells are indicated by the C-number, and the two numbers stored for each cell are given in parentheses in the figure. The first number is the first grid cell of a refined block of four cells and is zero for no refinement. The second number is the index of the puff contained in this cell, and a zero indicates no puff in the cell. When both numbers are zero for a cell, we have omitted the number pair in some cases. Therefore, all cells except C12 contain no puffs and show the second

number as zero. Cell 4 shows the refinement to the first level and points to cell 5, which is further refined and points to cell 9. Clearly, many puffs will produce a much more complicated grid and index structure, but this simple adaptive refinement provides an efficient location scheme for locating arbitrary collections of puffs.

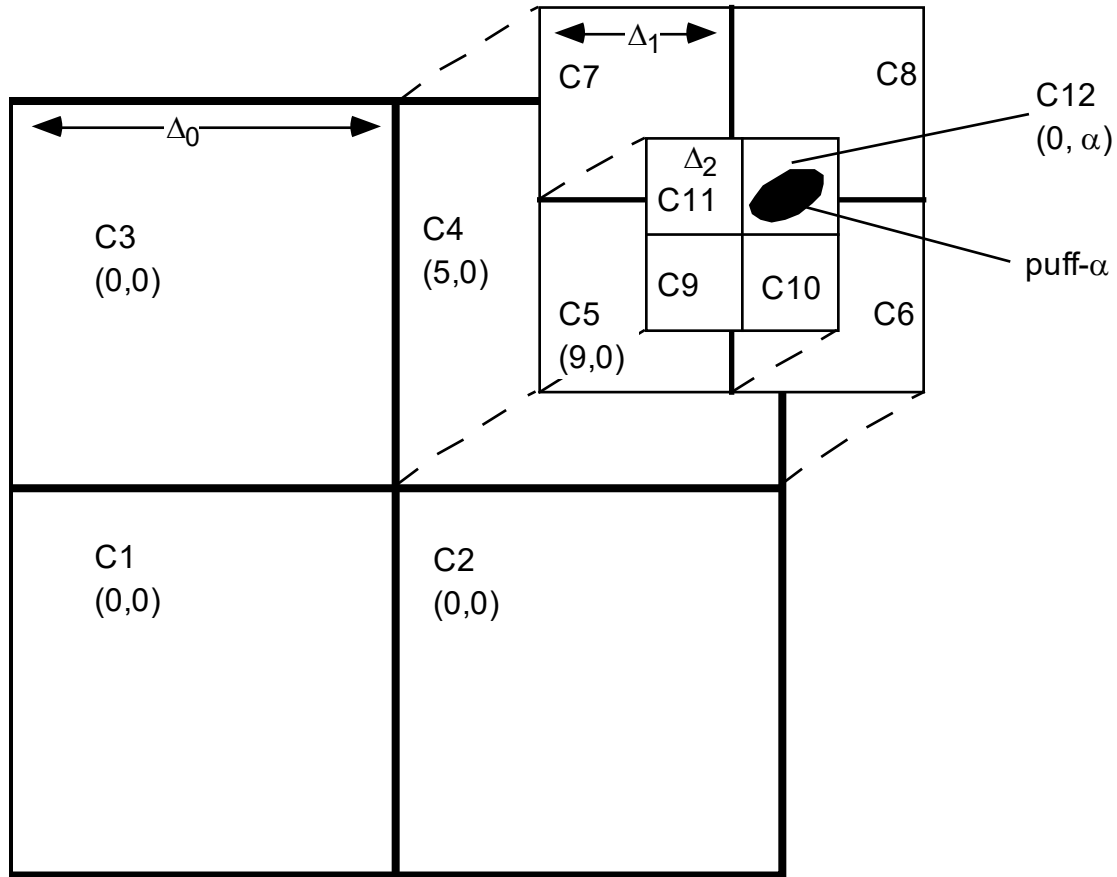


Figure 4-3
Schematic illustration of the adaptive multigrid for locating puffs. Grid cell numbers are represented as C-*n*, and two levels of refinement are shown. See text for a description of the cell storage rules.

In locating the puffs on the grid, the index number of the first puff placed in a cell is stored in the grid cell storage location, but if other puffs share the same cell, their indices must be saved elsewhere. Unlimited numbers of puffs can be accommodated by using a linked list; each puff carries a pointer to designate the next puff in the cell. Therefore, if puff number *j* is found to share a grid cell with a previous occupant—for example, puff number *i*—the list pointer in puff *i* is set to point to puff *j*. In practice, the entire list for the cell must be scanned and the new puff added to the end of the list. However, because the cells are adapted to the puff size, it is highly unlikely that a single cell will contain more than a few puffs.

The use of the adaptive grid technique in conjunction with the linked list provides an efficient method for sorting a large number of puffs with arbitrary locations and moments, giving a compact list of puff pairs to test for possible merging. We note that a search over the list in each grid cell finds most of the candidate pairs, although puffs allocated to different cells but lying

very close to one another across the boundary will be missed. In practical terms, it is more efficient to miss some merges rather than scan multiple cells.

The actual merging of a candidate pair is based on the overlap integral of the two Gaussian functions, which can be written in the form

$$I = \frac{1}{(2\pi)^{3/2} D_{12}} \exp(-A_{12}) \quad \text{Eq. 4-38}$$

where D_{12} is a combination of the two determinants and the exponential argument depends on both puff moments and their separation. This integral is computed as part of the concentration fluctuation variance calculation (see Section 2.2). For two identical, spherical Gaussians with separation distance, Δ and diagonal moments, σ^2 , the argument can be written very simply as $A_{12} = \Delta^2 / 4\sigma^2$. A pair is merged if $A_{12} < \delta_m^2 / 4$, so that δ_m is a measure of the centroid separation relative to the size of the two puffs. We note that the separation is not a direct indication that the two puffs are nearly coincident, because they could be of different size or shape. However, the multigrid sorting scheme ensures that the pair has similar overall size, and it is unlikely that two such puffs will arrive at the same spatial position with very different shear histories. A more reliable merge criterion can be developed to account for the shape differences as well as the centroid separation, but we have not yet found this to be necessary.

As discussed in connection with the splitting process, the merging criterion determines the extent of puff overlap because a small value for δ_m will maintain more overlap before merging a pair of puffs. It is important to ensure consistency between the split and merge criteria, however, in the sense that a newly created split pair should not satisfy the merge criterion. In practice, we maintain a distinct gap between the two criteria, and a reasonable value for δ_m is found to be 1.73 in conjunction with the split criterion, $r = 0.75$, that is, $\delta_s = 2.25$.

In addition to the overlap criterion, merging is restricted to puffs of the same material type and particle size bin as well as position relative to the boundary layer cap, z_i . Puffs within the mixed layer, $z < z_i$, are not merged with puffs outside the mixed layer because this could result in artificially diffusing material across the capping inversion. The puffs are also required to have similar concentration fluctuation scales, Λ_c , so that puffs of significantly different size cannot be merged even if they are spatially coincident.

4.4 Puff Inversion Capping

Under daytime mixing conditions, the atmospheric boundary layer is typically capped by a temperature inversion, which provides a limit on the vertical extent of the turbulent layer. The depth of the mixed layer is denoted by z_i , and the specification of this inversion height is described in Section 10.2. Although there is entrainment across this layer, the flux through the inversion is relatively small—and the vertical diffusivities are also usually much smaller in the free atmosphere above the boundary layer. The simplest assumption is therefore to approximate the inversion as an impenetrable surface and apply a perfect reflection condition for the puff concentration distribution.

The level at which the reflection is applied cannot simply be defined as the local inversion height, z_i , because the inversion can move up or down as the turbulent layer grows during the daytime or collapses in the evening. If the capping level were reduced, the local concentrations would increase as the mass became compressed into a thinner layer, and this would violate the mass conservation law. We therefore associate a capping height, z_c , with each puff and adjust the capping level in response to the local boundary layer changes experienced by the puff. A capping height of zero is used to indicate no reflection.

We first define a capped boundary layer as one in which the surface heat flux is non-negative and the overlying atmosphere is stable, that is, a positive potential temperature gradient. The specification of the surface heat flux is described in Section 10.2. Upon release of a puff, z_c is initialized as

$$z_c = \begin{cases} z_i & \text{if the boundary layer is capped} \\ 0 & \text{otherwise} \end{cases}$$

so that zero indicates no cap. At each time step, the puff cap is modified according to the following rules:

Case A: Boundary layer capped and $\bar{z} \leq z_i$

This implies that the puff centroid lies inside a capped boundary layer. If the puff is effectively contained within the layer, then z_c is set to the larger of z_i and the existing cap. Containment is defined by the condition that either the puff is almost entirely within the boundary layer or the puff is already capped and the cap is within or close to the current boundary layer. The former condition is defined as $\bar{z} + 1.5\sigma_z \leq z_i$, and the latter as $z_c \leq z_i + \Delta z_i$ where $\sigma_z = \sqrt{\sigma_{33}}$ and the tolerance Δz_i is defined below.

If the puff is not contained, it extends beyond the current boundary layer. This situation can arise when a convective boundary layer grows and partially entrains an existing puff or a puff advects through an inhomogeneous boundary layer. In this case, the vertical diffusivity calculated at the puff centroid within the boundary layer is inappropriate for the part of the puff outside the boundary layer. Therefore, a correct description requires that the puff be split into two parts—one contained within the capped boundary layer and the other outside. The puff within the boundary layer receives the appropriate mass calculated from an integral of the Gaussian distribution up to the boundary depth, z_i , but its centroid location and moments are maintained. The external puff receives the remaining mass with a centroid location and vertical moments calculated from the Gaussian shape function.

The tolerance Δz_i is included to avoid excessive creation of puffs with small mass outside the boundary layer when the boundary layer depth changes slightly. The tolerance is set to the larger of $0.3z_i$ and Δz_{merge} and therefore allows puffs to become completely contained if they are already capped within 30% of the boundary layer depth. The tolerance is further relaxed for shallow boundary layers, when the vertical splitting resolution is larger than $0.3z_i$. Note that this

tolerance does not apply to uncapped puffs that are partially entrained; creation of small mass puffs is avoided in this case when the fractional mass above the boundary layer is less than 5%.

Case B: All other situations

This includes puffs above the boundary layer or uncapped boundary layers, such as those found under stable conditions. If the puff is already uncapped, it remains in that state; otherwise, a check is made to test whether the cap should be moved or completely removed. If the puff is sufficiently below its cap, that is, $\bar{z} + 4\sigma_z \leq z_c$, the cap is removed; otherwise, the new cap is defined as

$$z_c = z_c^{(old)} + \left(\bar{w} + 0.01 \sqrt{w'^2} \right) \Delta t \quad \text{Eq. 4-39}$$

The cap is allowed to move due to advection by the mean vertical velocity component and grows as a result of turbulent diffusion by the vertical velocity fluctuations. The 1% factor on the vertical velocity standard deviation is included to allow the cap to dissipate slowly under stable nocturnal conditions. The cap is not allowed to fall below the current boundary layer depth or the vertical puff spread, σ_z .

4.5 Adaptive Timesteps

The description of dispersion over a wide range of spatial scales, from a small source up to hundreds of kilometers, for example, also involves a wide range of timescales. Because small spatial scales are usually associated with short timescales, close to a localized source an accurate description of the dispersion process requires a small time step. As the plume or cloud spreads onto larger scales, however, the timescales will also increase. The discrete Lagrangian framework of the Gaussian puff model allows an efficient treatment of the time dependence because puffs can be advanced individually using an appropriate step for each one. The only interaction between puffs is through the overlap integrals in the interaction terms; these are the only terms that require special consideration when using multiple time steps.

A large time step, Δt_L , is defined for the calculation. This time step must resolve the meteorological changes and any other time dependence in externally specified parameters, such as source variations. The large time step is successively halved to obtain appropriate puff time steps, and the multiple time steps are forced to bring all the puffs into synchronization at intervals of Δt_L . External parameters are updated only on the large time step. Within a large time step, however, an individual puff uses its own locally determined step to integrate for the period Δt_L .

At the beginning of a large time step, the list of puffs is scanned to determine the smallest step required for this period. This gives the number of small internal steps for the period, which must be of the form 2^M because the local steps are obtained by successive halving. Although a puff can change its time step during the Δt_L interval, the smallest time step is not allowed to fall below the initial level of $2^{-M} \Delta t_L$, so that the number of steps is fixed for the period. In practice, this is not restrictive because the timescales are usually increasing as the puff grows.

The time step for each puff is chosen as the minimum from a list of requirements. Therefore,

$$\Delta t \leq \min(\Delta t_c, \Delta t_u, \Delta t_w, \Delta t_K, \Delta t_{shear}) \quad \text{Eq. 4-40}$$

where the subscripts c , u , w , K , and $shear$ denote the time-step limits for dissipation of concentration fluctuation variance, horizontal advection, vertical advection, vertical diffusion, and velocity shear, respectively. These time-step limits are defined next.

The dissipation time step is determined from the fluctuation variation dissipation timescale, as

$$\Delta t_c = \frac{\tau_c}{2} \quad \text{Eq. 4-41}$$

where τ_c is defined in Equation 2-48.

The horizontal advection restriction is determined by the horizontal flow speed,

$$\Delta t_u = \frac{\Delta_H}{\sqrt{\bar{u}^2 + \bar{v}^2}} \quad \text{Eq. 4-42}$$

where Δ_H is the local horizontal meteorological grid spacing. In addition, if the puff is contributing to a surface integral computation, its horizontal motion is restricted so that it does not travel more than one standard deviation in one time step. Therefore, Δ_H is not allowed to exceed

$$\Delta_p = \max\left(\sqrt{\frac{\sigma_{11}\bar{u}^2 + 2\sigma_{12}\bar{u}\bar{v} + \sigma_{22}\bar{v}^2}{\bar{u}^2 + \bar{v}^2}}, \Delta_{\min}\right) \quad \text{Eq. 4-43}$$

where Δ_{\min} is the user-specified minimum surface resolution.

The vertical advection time step is determined as

$$\Delta t_w = \frac{\Delta_V}{w_T} \quad \text{Eq. 4-44}$$

where Δ_V is the vertical puff resolution (specified by the user) and w_T is the total vertical velocity defined as the rate of change of \bar{z} in Equation 2-10, that is, the sum of the meteorological component, the gravitational settling, and the turbulent drift.

A diffusive time-step limit given by

$$\Delta t_K = \frac{\Delta_K^2}{2K_p} \quad \text{Eq. 4-45}$$

is applied to puffs inside a vegetative/urban canopy (see Section 10.4) or inside a stable boundary layer. For the canopy, Δ_K is defined as 1/4 of the canopy height. For a stable boundary layer, Δ_K is defined as 1/8 of the boundary layer depth. In all cases, Δ_K is not allowed to exceed Δ_V . The puff vertical diffusivity, K_p , is defined as $\langle z' w' c' \rangle / Q$.

Finally, the shear time-step limit is determined so that the Δt^2 term in Equation 4-10 does not change the diagonal puff moments by more than 25%. This limit is applied to each off-diagonal shear component individually. The diagonal shear components collectively restrict the time step so that no diagonal moment changes by more than a factor of $e^{1/2}$.

4.6 Static Puffs

Continuous releases may involve the generation of many puffs with a small time step, because the step size is determined by the source dimensions, which are often relatively small. Puffs will merge as they grow downstream, but the computational time can become restrictive if the source continues for a long duration. In these cases, it is reasonable to approximate the early development of the release as a steady-state plume, because the timescales of the plume are much faster than the changes in the meteorology. This could be achieved using an initial steady-state calculation to march the plume out to some downstream distance, at which point the puffs could be released into the general flow field with a larger time step. The difficulty with this approach is that some method of incorporating the plume phase into the output displays and surface integrals would need to be developed so that the initial part of the plume would not be neglected. In addition, a plume description would need to be stored in association with each continuous release.

A more integrated approach uses the concept of “static” puffs; these are puffs that represent the steady-state phase of the plume and are not advanced every time step. The advantage of this approach is that the quasi-steady plume is represented by the same type of puff as the general unsteady dispersing field to facilitate inclusion in the output calculations. The concept is illustrated schematically in Figure 4-4.

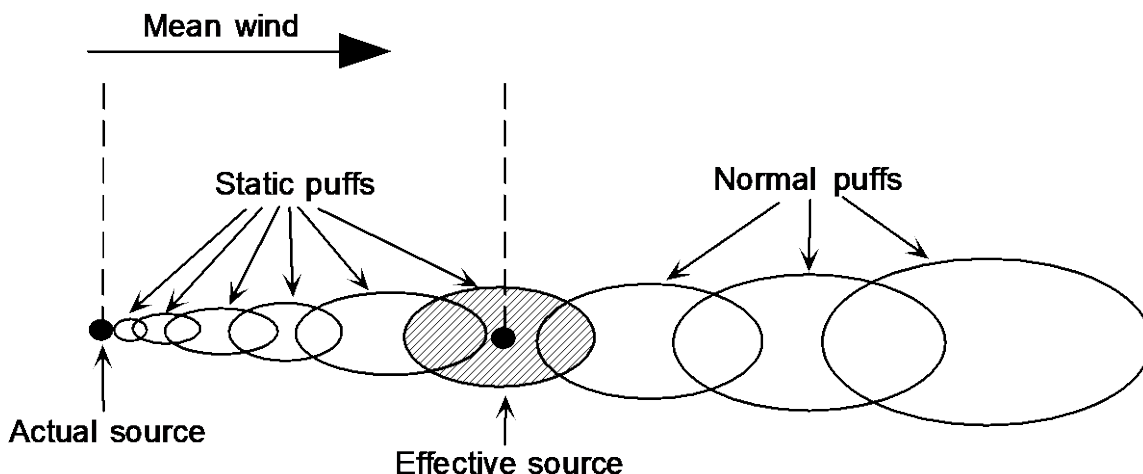


Figure 4-4
Schematic illustration of the use of static puffs to represent a continuous source. The shaded puff is stored as the release description at the end of the static phase.

The static puffs are generated by a steady plume calculation, described next, and are removed and regenerated when the meteorology is updated every large time step, Δt_L . The static puffs are also deleted from the calculation when the release terminates. The steady plume calculation is terminated after integrating the plume for $0.5\Delta t_L$ because we are assuming that the wind field is fixed for the large time step. The static integration is also terminated at 10% of the source

duration time, if this is smaller than $0.5\Delta t_L$, because we cannot consider the plume to be steady on timescales comparable with the release duration.

The static integration is not allowed to proceed if the puff splitting criterion is satisfied or if plumes from different sources interact because neither of these phenomena is described by the steady-state calculation. However, this restriction is relaxed for multiple plumes from the same source, for example, a distribution of particle or liquid droplet size groups. In this case, a collection of static puffs is advanced, calculating dynamic interactions and evaporative effects. Multiple materials, including dynamic gas releases, can be treated using static puffs if all the releases share the same location and geometry.

A static integration is initiated by creating the first puff exactly as a normal continuous release; the specification of continuous releases is described in Section 8.1. This puff is first copied as a static puff; then a normal time step is taken to produce the next static puff. At each integration step, a new time step is calculated so that the integration is as efficient as possible. When the time step changes, the puff moments must be adjusted to reflect the change because the puff now represents a different duration of the release. If the time step changes from Δt_1 to Δt_2 , we use the change ratio

$$r = \frac{\Delta t_2}{\Delta t_1} \quad \text{Eq. 4-46}$$

to adjust all the mass-weighted integral puff moments as

$$\langle c\phi \rangle_2 = r \langle c\phi \rangle_1 \quad \text{Eq. 4-47}$$

The puff moments are also adjusted to reflect the relationship between the time step and the streamwise length of the plume segment. Therefore,

$$\sigma_{ij}^{(2)} = \sigma_{ij}^{(1)} + \frac{\bar{u}_i^{(2)}\bar{u}_j^{(2)}\Delta t_2^2}{4} - \frac{\bar{u}_i^{(1)}\bar{u}_j^{(1)}\Delta t_1^2}{4} \quad \text{Eq. 4-48}$$

where the superscript (1) on the velocity denotes the value from the previous step. This adjustment ensures that the puff overlap is maintained as the time step increases.

The nonlinear interactions in the static puff integration are estimated by correcting the single puff interaction to account for the difference between a fully three-dimensional Gaussian puff and the two-dimensional Gaussian cylinder. The cylinder approximation is more representative of a steady-state plume, and the ratio of the overlap integrals for these two shape functions is

$$\frac{\langle \bar{c}^2 \rangle_{cyl}}{\langle \bar{c}^2 \rangle_{Gauss}} = \frac{2\sqrt{\pi}\sigma_s}{L_s} \quad \text{Eq. 4-49}$$

where s denotes the streamwise direction, L_s is the cylinder length, and

$$\sigma_s^2 = \frac{\overline{u_i u_j} \sigma_{ij}}{\overline{u_k u_k}} \quad \text{Eq. 4-50}$$

gives the Gaussian moment in the direction of the mean velocity. For low wind speed situations, where the turbulent diffusion dominates the mean advection, the Gaussian approximation is more appropriate than the cylinder, so we define an adjustment factor as

$$f_s = \frac{2\sqrt{\pi}\sigma_s}{L_s} - \left(\frac{2\sqrt{\pi}\sigma_s}{L_s} - 1 \right) \min \left(\frac{q^2}{\overline{u_k u_k}}, 1 \right) \quad \text{Eq. 4-51}$$

The factor in Equation 4-51 becomes unity when the turbulence dominates and provides a smooth transition to the cylindrical plume segment factor (Equation 4-49). The puff overlap integrals are therefore computed from the self-interaction term multiplied by the adjustment factor, f_s .

4.7 Adaptive Surface Grids

The wide range of scales needed to describe the dispersion from a small source is encountered in the surface dosage and deposition integrals described in Section 2.4. Close to the source, for example, the deposition field may be narrow, but effects may be required over a large domain. Using a uniformly spaced receptor grid to accumulate the integrals makes it difficult to resolve the values close to the source. Under specialized circumstances, it is possible to use locally refined grids such as an expanding radial distribution, but this is impractical for multiple sources and complex flows.

An adaptive grid technique is employed in SCICHEM to provide enhanced resolution wherever it is required. A coarse grid is defined to cover the calculation domain with a mesh of roughly square cells. Grid refinements are then defined with a factor of 2 decrease in cell size for each horizontal dimension. Grid cells finer than the top-level coarse grid are created as required during the calculation.

At each puff time step, the surface integrals are updated if the puff contribution is significant. Puffs with centroid locations more than $3\sigma_z$ above the local terrain are neglected in the surface calculation, and the local terrain is defined as the highest elevation within the horizontal area of the puff. The latter is estimated as

$$h_{\max} = h(\bar{x}, \bar{y}) + 3 \left(\sigma_x \left| \frac{\partial h}{\partial x} \right| + \sigma_y \left| \frac{\partial h}{\partial y} \right| \right) \quad \text{Eq. 4-52}$$

where the slopes are also estimated at the centroid location. In addition, a minimum concentration of interest can be specified, and surface contributions will be ignored if the maximum concentration in the puff falls below the minimum value.

For puffs that contribute to the surface integrals, a resolution scale is determined from the smaller of the two puff principal axes in the plane parallel to the local surface. Therefore,

$$\delta_{res}^2 = \frac{0.5}{\alpha_{xx} + \alpha_{yy} + \sqrt{(\alpha_{xx} - \alpha_{yy})^2 + 4\alpha_{xy}^2}} \quad \text{Eq. 4-53}$$

where the tensor α is defined in Equation 2-81 as half the inverse of the spread tensor, σ . Note that over sloping terrain, the tensor is rotated into the local coordinate frame. For a circular puff, the resolution scale is $\sigma_x / \sqrt{2}$.

Having determined the resolution scale, the grid level is selected as the largest cell that is smaller than δ_{res} . A scan over cells at the appropriate grid level is then made to calculate the Gaussian puff contribution at each cell out to roughly 6σ from the maximum surface concentration location. If a cell already exists, the contribution is simply added; otherwise, a new cell is created.

4.8 Chemistry Solvers

The system of stiff ordinary differential equations representing the chemical reactions is solved using the Livermore Solver for Ordinary Differential Equations (LSODE) package (Hindmarsh, 1983), which is available as public domain software. Although LSODE provides an accurate numerical solution to the stiff equation system, based on the user-defined tolerances, it is relatively expensive in computational terms. Therefore, the model allows the user to define “fast” and “slow” species for the reaction scheme. If a species is involved only in relatively slow transformations (compared with the dispersion timescale), a simple explicit scheme can be used. Slow species use the explicit scheme, while fast species use LSODE.

5

GAS MATERIALS AND DYNAMIC EFFECTS

5.1 Gas Material Properties

Gas materials are relatively simple and, in the absence of buoyancy and momentum dynamics, are transported as passive scalars using the representation described in Section 2.1.2. Gas materials can specify a constant deposition velocity, described in Section 2.3, and may also include a decay factor in the material definition (see the SCICHEM 3.3 User's Guide) or defined through a first-order reaction (see Section 3.1). However, the most significant effects of gas material dispersion are due to dynamically induced motions, resulting from initial release momentum, or buoyancy effects arising from density perturbations from the ambient air. The density differences may be the result of release temperature differences or a buoyant gas with a different density from that of air. Inclusion of dynamic effects is an option, controlled by an input specification, and may be ignored for a faster calculation.

The treatment of dynamic effects is described in the following sections. We also note that the vapor phase of a liquid material is treated the same as a gas material and can include the same dynamic effects.

5.2 Buoyancy and Momentum Rise

5.2.1 Mean Flow Dynamics

Many releases into the atmosphere involve a vertical rise phase because they are associated with heat or vertical momentum. This includes vertical jets and buoyant plumes from continuous sources and buoyant clouds from explosive releases. The buoyant rise is important because it can strongly influence the effective release height and the initial source size for the subsequent dispersion in the atmosphere. Although the rise dynamics can be incorporated into the source specification for a passive dispersion calculation, there are several reasons for providing an internal representation in the puff dispersion code.

First, the duration of the rise phase may preclude treatment as a source term—this phase is ignored by the dispersion calculation. Initialization at the end of the dynamic rise may be some considerable distance downstream of the source, and effects calculations in the intervening region would need to account for the rise phase. Second, the transition to a passive dispersion code requires an arbitrary choice for the position at which the dynamics can be neglected; an internal representation allows a continuous decay of the dynamic effects. Furthermore, the dispersion calculation provides a more consistent treatment of the meteorology, which can be inhomogeneous in both space and time. Finally, simplified algorithms for plume and puff rise may not be appropriate for finite duration or time-dependent sources.

To represent the buoyant rise dynamics, additional variables must be stored for each puff. The dynamic model is described by Sykes et al. (1999) and is based on the conservation equations for both buoyancy, $\langle \bar{\theta}_p \rangle$, and vertical momentum, $\langle \bar{w}_p \rangle$, where θ is the potential temperature, w is the vertical velocity, and the subscript p denotes the dynamic puff perturbation from the local ambient atmospheric value. The angle brackets denote the volume integral over an individual

puff. Only gaseous materials (including the vapor phase of a liquid material) can carry mean dynamics because we envision the materials being transported by a fluid medium. As we shall show next, the dynamic gas puffs will transport particles or any other material if the puffs overlap spatially.

The evolution of the mean dynamic variables is based on the Boussinesq momentum equation and the conservation of potential temperature, giving

$$\frac{d}{dt}\langle \bar{w}_p \rangle = \frac{g}{T_0}\langle \bar{\theta}_p \rangle \quad \text{Eq. 5-1}$$

$$\frac{d}{dt}\langle \bar{\theta}_p \rangle = -\frac{\partial \theta_B}{\partial z}\langle \bar{w}_p \rangle \quad \text{Eq. 5-2}$$

where θ_B is the ambient potential temperature. These equations neglect the pressure gradient in the momentum equation and simply represent the buoyant acceleration term in Equation 5-1 and the change in buoyancy due to vertical motion through a potential temperature gradient in Equation 5-2.

The mean dynamic variables in Equations 5-1 and 5-2 determine the equilibrium rise of a buoyant puff in a stable atmosphere, where the ambient temperature gradient is positive. The solution to Equations 5-1 and 5-2 will oscillate indefinitely about the equilibrium level. The vertical velocity itself will be damped because of turbulent entrainment, which increases the effective puff volume—but the integrated momentum and buoyancy will be undamped. Although the buoyancy is strictly conserved, the integrated vertical momentum will actually be reduced due to the generation of gravity waves, and the oscillation will be damped. We represent this effect with a simple linear damping on the vertical velocity integral, so that Equation 5-1 becomes

$$\frac{d}{dt}\langle \bar{w}_p \rangle = \frac{g}{T_0}\langle \bar{\theta}_p \rangle - c_w N \langle \bar{w}_p \rangle \quad \text{Eq. 5-3}$$

where N is the Brunt-Vaisala frequency and $c_w = 0.1$. N is defined non-zero only for stable temperature gradients, and the damping coefficient is arbitrarily chosen as 0.1 to provide a reasonably rapid adjustment to the equilibrium height.

Tracking the independent evolution of the dynamics of each puff is not sufficient to model the buoyant rise effects, however, because these effects are interactive. A plume of buoyant gas rises differently from an isolated buoyant puff because the flow field induced by the buoyancy has an influence on other parts of the plume. These effects are represented using correlation integrals for the momentum and buoyancy, which account for turbulent fluctuations in addition to the nonlinear interactions. The correlation equations are written as

$$\frac{d}{dt}\langle \overline{w_p c} \rangle = \frac{g}{T_0}\langle \overline{\theta_p c} \rangle - c_w N \langle \overline{w_p c} \rangle - \frac{\langle \overline{w'_p c'} \rangle}{\tau_c} \quad \text{Eq. 5-4}$$

$$\frac{d}{dt} \langle \overline{\theta_p c} \rangle = -\frac{\partial \theta_B}{\partial z} \langle \overline{w_p c} \rangle - \frac{\langle \overline{\theta_p' c'} \rangle}{\tau_c} \quad \text{Eq. 5-5}$$

where τ_c is the fluctuation dissipation timescale, defined in Equation 2-50, which must be modified to account for the dynamically induced turbulence. The turbulence model is described in the next section.

Note that the turbulent dissipation terms, the last terms in Equations 5-4 and 5-5, involve the fluctuation correlations, which are defined as

$$\langle \overline{w_p' c'} \rangle = \langle \overline{w_p c} \rangle - \langle \overline{w_p} \overline{c} \rangle \quad \text{Eq. 5-6}$$

$$\langle \overline{\theta_p' c'} \rangle = \langle \overline{\theta_p c} \rangle - \langle \overline{\theta_p} \overline{c} \rangle \quad \text{Eq. 5-7}$$

The mean overlap integrals, $\langle \overline{w_p c} \rangle$ and $\langle \overline{\theta_p c} \rangle$, are calculated in SCIPUFF in a similar manner to the mean concentration overlap terms, $\langle \overline{c^2} \rangle$, as described in Section 2.2.4. This effectively assumes the same Gaussian distribution for both vertical velocity and potential temperature. The reflection assumption on the vertical velocity field at the surface is a zero value condition, however, rather than a zero slope.

As noted, only gaseous materials can carry mean vertical momentum and perturbation temperature integrals. However, all puffs carry the dynamic correlation integrals in Equations 5-4 and 5-5 because their species concentrations can be correlated with dynamic variables due to overlapping with gaseous puffs. This phenomenon is accounted for through the puff interaction calculations, where the overlap integral with dynamic gaseous puffs is computed for every type of puff. Therefore, passive gas materials or particle materials co-located with a buoyant gas source will experience the same vertical velocity field as the buoyant gas itself.

The dynamic correlations provide an additional vertical velocity component, which is added to the ambient velocity field used to transport the puff centroid. Therefore, the equation for the vertical component of the centroid location becomes

$$\frac{d\bar{z}}{dt} = \bar{w}(\bar{x}) + \frac{\langle \overline{w_p' c'} \rangle}{Q} + \hat{w}_p \quad \text{Eq. 5-8}$$

where $Q = \langle \bar{c} \rangle$ is the integrated species mass, \bar{w} is the ambient vertical velocity, and the dynamic rise velocity is given by

$$\hat{w}_p = \frac{\langle \overline{w_p c} \rangle}{Q} \quad \text{Eq. 5-9}$$

We note that the model represents only the vertical component of the internal puff momentum so that the rise can be calculated. The horizontal velocity is not perturbed from the ambient wind field.

5.2.2 Buoyant Gas Representation

Buoyancy effects can arise directly from a density difference between the ambient air and the gas material. This is particularly important for dense gas effects, discussed in the next section, but is introduced here for the simpler case of buoyant rise. If the gas is lighter than air, it will tend to rise without any temperature perturbation. In this case, the buoyancy variable is actually

$$b_p = g \left(\frac{\theta}{T_0} - m \frac{\Delta \rho}{\rho_0} \right) \quad \text{Eq. 5-10}$$

where m is the mass mixing ratio, ρ_0 is the ambient air density, and $\Delta \rho$ is the density difference $\rho_{gas} - \rho_0$. Because the local species concentration value, c_{gas} , is equal to $m \rho_{gas}$, we can define a buoyancy factor

$$B_{gas} = \frac{\Delta \rho}{\rho_{gas} \rho_0} \quad \text{Eq. 5-11}$$

and write the buoyancy term as

$$b_p = g \left(\frac{\theta}{T_0} - B_{gas} c_{gas} \right) \quad \text{Eq. 5-12}$$

To treat non-Boussinesq density perturbations associated with very dense gases, we modify the gravity term to give

$$b_p = g \left(\frac{\theta}{T_0} - \frac{B_{gas} c_{gas}}{1 + B_{gas} c_{gas}} \right) \quad \text{Eq. 5-13}$$

so that the effective acceleration resulting from the gas density difference cannot exceed g . The correction factor in the denominator is applied only for positive density perturbations because lighter-than-air materials must still accelerate the surrounding air mass.

For cases with buoyant gas materials, that is, $B_{gas} \neq 0$ for at least one gas material, every puff must calculate an overlap integral with all the buoyant gases. Therefore,

$$\langle \overline{b_p c} \rangle = \left\langle \overline{c \sum_{gas} B_{gas} c_{gas}} \right\rangle \quad \text{Eq. 5-14}$$

where the sum is taken over all overlapping gas puffs. The dynamic puff integral equations are then modified to give

$$\frac{d}{dt} \langle \overline{w_p} \rangle = \frac{g}{T_0} \langle \overline{\theta_p} \rangle - \frac{g B_{gas} \langle \overline{c} \rangle}{1 + \hat{B}} - c_w N \langle \overline{w_p} \rangle \quad \text{Eq. 5-15}$$

for the buoyant gas puffs and

$$\frac{d}{dt} \langle \overline{w_p c} \rangle = \frac{g}{T_0} \langle \overline{\theta_p c} \rangle - \frac{g \langle \overline{b_p c} \rangle}{1 + \hat{B}} - c_w N \langle \overline{w_p c} \rangle - \frac{\langle \overline{w'_p c'} \rangle}{\tau_c} \quad \text{Eq. 5-16}$$

$$\frac{d}{dt} \langle \overline{b_p c} \rangle = - \frac{\langle \overline{b'_p c'} \rangle}{\tau_c} \quad \text{Eq. 5-17}$$

for all puffs. The non-Boussinesq density correction is defined as

$$\hat{B} = \max \left(0, \frac{\langle \overline{b_p c} \rangle}{\langle \overline{c} \rangle} \right) \quad \text{Eq. 5-18}$$

Note that the buoyancy correlation term is simply damped toward the mean overlap value, which is computed in the same way as the temperature overlap.

5.2.3 Turbulent Entrainment

The velocity field induced by the dynamic rise of a cloud is turbulent, and the ambient diffusion is enhanced by the internal turbulence of the cloud. The additional entrainment and dissipation are modeled using an estimate of the internal turbulent velocity and length scales. The entrainment model is based on earlier work on power plant plume rise (Sykes et al., 1988) and relates the turbulent velocity to the vertical rise rate. We define

$$q_p^2 = F_p (Ri_p) \hat{w}_p^2 \left(c_{q1} + c_{q2} \frac{V^2}{V^2 + \hat{w}_p^2} \right) \quad \text{Eq. 5-19}$$

where V is the ambient wind speed and

$$F_p = 1 + 4 Ri_p \quad \text{Eq. 5-20}$$

is a buoyancy factor, representing the increased turbulent energy production resulting from gravitational instabilities. The puff Richardson number is defined as

$$Ri_p = \frac{g \Lambda_p \left| \hat{\theta}_p / T_0 - \hat{b}_p \right|}{\hat{w}_p^2} \quad \text{Eq. 5-21}$$

where Λ_p is the length scale of the internal turbulence. The dynamic temperature and buoyancy variables are defined similarly to the dynamic vertical velocity as

$$\hat{\theta}_p = \frac{\langle \overline{\theta_p c} \rangle}{Q} \quad \text{Eq. 5-22}$$

$$\hat{b}_p = \frac{\langle \overline{b_p c} \rangle}{Q} \quad \text{Eq. 5-23}$$

The dynamic length scale, Λ_p , is defined equal to the length scale, Λ_c from Section 2.2.2, because this represents an instantaneous scale for the dispersing cloud. The empirical coefficients in Equation 5-19 are chosen as $c_{q1} = 0.4$ and $c_{q2} = 3.0$ from fitting jet rise data, as discussed in Section 13.3. In addition, an upper limit of 2 is imposed on F_p to prevent excessive entrainment velocities.

The dynamic velocity and length scales are used to define a dynamic diffusivity that is added to the spatial moment equations (5-24) to give

$$\frac{d\sigma_{ij}}{dt} = \sigma_{ik} \frac{\partial \bar{u}_j}{\partial x_k} + \sigma_{jk} \frac{\partial \bar{u}_i}{\partial x_k} + \frac{\langle x'_i \bar{u}'_j c' \rangle}{Q} + \frac{\langle x'_j \bar{u}'_i c' \rangle}{Q} + 2K_p \quad \text{Eq. 5-24}$$

where

$$K_p = 0.15 q_p \Lambda_p \quad \text{Eq. 5-25}$$

The internal dynamics also provide additional turbulent dissipation, and we modify the dissipation rate as

$$\frac{1}{\tau_c} = bs \left(\frac{q_c}{\Lambda_c} + \frac{q_c}{\Lambda_{cH}} + \frac{q_{cV}}{\Lambda_{cV}} \right) + 2bs \left(\frac{q_p}{\Lambda_p} + \frac{q_p}{\Lambda_c} + \frac{q_p}{\Lambda_{cH}} \right) \quad \text{Eq. 5-26}$$

The internal turbulence also modifies the rate equations for the internal length scales so that we obtain

$$\frac{d\Lambda_c}{dt} = \frac{d\Lambda_{cH}}{dt} = \alpha_{cH} q_c + 0.15 q_p \quad \text{Eq. 5-27}$$

where the first term arises from the ambient turbulence (Equation 2-51). The same additional velocity is added to the vertical internal scale Equation 2-68.

5.2.4 Inversion Penetration

When a dynamically rising puff encounters a capping inversion at the top of a mixed layer, the puff can either penetrate through the inversion into the stable atmosphere above or it may be trapped within the mixed layer. A simple energy test is used to determine one or the other alternative; SCIPUFF does not address partial penetration, where part of the puff is trapped and the rest passes through into the overlying stable region.

We assume that the ambient potential temperature profile is represented by a discontinuous jump of magnitude $\Delta\theta_{inv}$ at the inversion, with a linear gradient Γ above. A buoyant puff within the mixed layer has an effective temperature excess that includes both the dynamic temperature perturbation, $\hat{\theta}_p$, and the buoyant gas contribution, $\hat{b}_p T_0$. If a puff moves from the mixed layer up at a height z_p above the inversion, it experiences a temperature change from $\hat{\theta}_p - \hat{b}_p T_0$ initially to $\Delta\theta_{inv} + \Gamma z_p$ finally (all relative to the mixed layer temperature). The potential energy associated with raising this temperature difference through the height, z_p , is given by

$$PE = g' z_p \left(\Delta \theta_{inv} + \Gamma z_p - \hat{\theta}_p + \hat{b}_p T_0 \right) \quad \text{Eq. 5-28}$$

where $g' = g/T_0$.

The available kinetic energy is simply $w_p^2/2$, and equating kinetic and potential energies gives a maximum penetration distance

$$z_p = \frac{1}{2g'\Gamma} \left(-g'\Delta_p + \sqrt{g'^2\Delta_p^2 - 2g'\Gamma w_p^2} \right) \quad \text{Eq. 5-29}$$

where $\Delta_p = \Delta \theta_{inv} - \hat{\theta}_p + \hat{b}_p T_0$

We define the inversion temperature jump as

$$\Delta \theta_{inv} = 0.143\Gamma z_i \quad \text{Eq. 5-30}$$

based on the assumption that the entrainment region is roughly 1/7 of the boundary layer depth, z_i .

The criterion for puff penetration is that

$$z_p > \max(0.1z_i, \lambda_c); \quad \text{Eq. 5-31}$$

that is, the puff energy must be sufficient to carry it past the capping inversion by either 10% of the boundary layer depth or its own internal length scale, whichever is larger.

5.3 Dense Gas Effects

5.3.1 Mean Flow Dynamics

The puff treatment of buoyancy-driven dynamics described in the previous section must be modified for the description of dense gas dispersion. The most important feature of dense gas dynamics is the interaction with the solid ground surface, which causes lateral spreading as a dense cloud collapses and suppresses the vertical diffusion due to the stable buoyancy distribution. We first address the dynamic spreading effect in which the gravitational forcing term drives motion parallel to the ground instead of a vertical acceleration. The gravitational force is still directed vertically, but the lateral motion is induced by the pressure gradient—which was ignored in the buoyant rise situation. We therefore require a treatment of the equations of motion that include the surface-induced pressure gradient.

A convenient starting point for modeling the dynamics is the vorticity equation, obtained by taking the curl of the momentum equation, as described by Sykes et al. (1999), giving

$$\frac{\partial \omega_i}{\partial t} + u_j \frac{\partial \omega_i}{\partial x_j} = \omega_j \frac{\partial u_i}{\partial x_j} + \varepsilon_{ijk} \frac{g_j}{T_0} \frac{\partial \theta}{\partial x_k} + \nu \frac{\partial^2 \omega_i}{\partial x_j \partial x_j} \quad \text{Eq. 5-32}$$

where $\boldsymbol{\omega} = \nabla \times \mathbf{u}$ is the vorticity and ν is the kinematic viscosity. The buoyancy forcing is written using the Boussinesq approximation in Equation 5-32, and we note that the pressure gradient term vanishes. Forming the vertical component of the vorticity moment

$$P = \mathbf{e}_3 \cdot (\chi \boldsymbol{\omega}) \quad \text{Eq. 5-33}$$

where \mathbf{e}_3 is the unit vector in the vertical direction and, integrating over all space, we obtain

$$\frac{d\langle P \rangle}{dt} = \frac{g}{T_0} \langle \bar{\theta} \rangle + S_P \quad \text{Eq. 5-34}$$

where the angle brackets denote a spatial integral and S_P represents a surface integral term. Ignoring the surface term for the moment, it is evident that P is very closely related to the vertical momentum integral of the previous section. In fact, far from a solid boundary, $\langle P \rangle$ satisfies exactly the same evolution equation as $\langle \bar{w} \rangle$ and can therefore be identified with the integrated vertical momentum.

To use Equation 5-34 as a basis for the dense gas puff dynamics, we must represent the surface integral term and also relate the puff motions to the vorticity moment integral. Because the velocity field strictly vanishes at a solid boundary, the surface integral S_P involves only the viscous diffusion terms; we therefore represent it as a drag term, whose detailed specification is described next. The relationship between the vorticity moment integral and the puff dynamics is based on a simple shape assumption for the induced velocity field because the relationship between velocity and vorticity is linear. This allows us to superpose the velocity fields from neighboring puffs by simple addition and represent the interactions among a collection of dense puffs. The vorticity moment evolution equation (5-34) also depends linearly on the buoyancy integral so that the total vorticity moment can be represented by summing the moments of individual puffs. The puff evolution is still nonlinear because the dynamic fields are composed of the summation over all puffs, but the puff moments evolve independently—and the basis of the dynamics is contained in the shape assumption for the velocity field.

In general, the velocity field induced by a dense gas cloud involves an outward radial flux in the cloud itself, spreading the material horizontally over the ground surface. This horizontal divergence is accompanied by a vertical velocity gradient as material moves downward toward the ground. A schematic cross-section is illustrated in Figure 5-1. This flow field is associated with azimuthal vorticity, and we can obtain a general relation between the velocity magnitude and the vorticity moment.

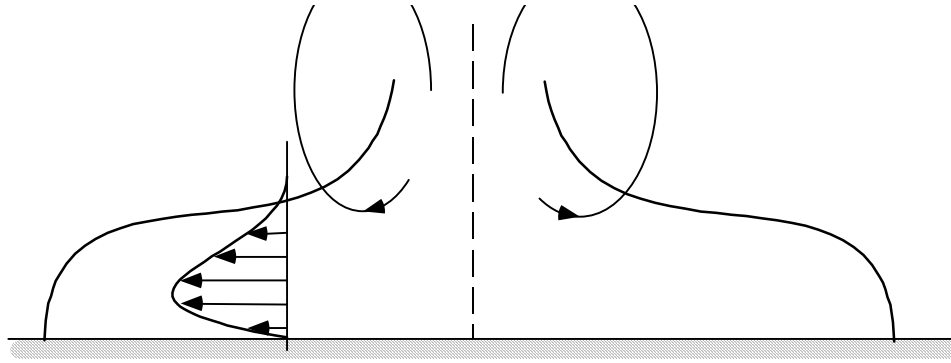


Figure 5-1
Schematic illustration of slumping dense cloud

We further simplify the representation by assuming that the vorticity is concentrated in a horizontal sheet where the velocity is discontinuous, as illustrated in Figure 5-2. The horizontal velocity components, u and v , are independent of z below the sheet and are zero above. The horizontal velocity field below the discontinuity is then used to move the scalar field. The vertical velocity is proportional to z and is determined by the horizontal divergence. This ignores the return circulation outside the dense gas cloud but captures the essential features of the motion of the dispersing contaminant.

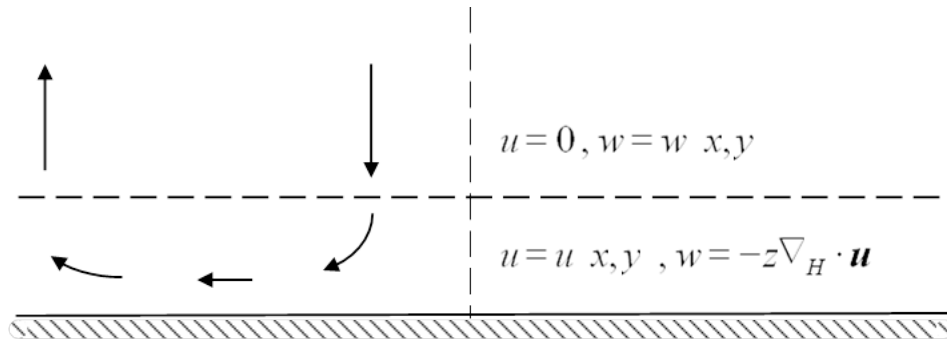


Figure 5-2
Simplified velocity field representation for a dense cloud

A simple assumption for the radial velocity field uses the Gaussian form to give

$$u_r = U_0 \frac{r}{L_H} \exp\left(-\frac{r^2}{L_H^2}\right) \quad \text{Eq. 5-35}$$

This satisfies the linear gradient requirement at the center of the puff and vanishes at large distances. We cannot assume circular symmetry, however, because SCIPUFF uses a generalized Gaussian description and the velocity shape assumption must be applied to elliptical puffs. When a puff is non-circular, the outflow along the longer axis of the ellipse is smaller than that along the shorter axis because the pressure gradient driving the flow is smaller. If we weight the outflow using the inverse of the axis length, the radial distribution given in Equation 5-35 can be generalized to an elliptical shape as

$$u_X = U_0 \frac{X}{L_X} \frac{L_Y}{L_H} \exp\left(-\frac{X^2}{L_X^2} - \frac{Y^2}{L_Y^2}\right) \quad \text{Eq. 5-36}$$

$$u_Y = U_0 \frac{Y}{L_Y} \frac{L_X}{L_H} \exp\left(-\frac{X^2}{L_X^2} - \frac{Y^2}{L_Y^2}\right) \quad \text{Eq. 5-37}$$

where X and Y are the principal axis coordinates in the horizontal plane with the puff centroid as origin and $2L_H^2 = L_X^2 + L_Y^2$. The length scales L_X and L_Y are related to the semi-major axes of the puff as

$$L_{X,Y} = C_{dl} \left(\frac{\sigma_{xx} + \sigma_{yy}}{2} \pm \frac{1}{2} \sqrt{(\sigma_{xx} - \sigma_{yy})^2 + 4\sigma_{xy}^2} \right) \quad \text{Eq. 5-38}$$

and the empirical coefficient C_{dl} is chosen to be 1.5. Note that the velocity components in Equations 5-36 and 5-37 must be rotated from the frame of the principal axes into the (x, y) calculation coordinates. Horizontal velocity gradients are computed by differentiating and rotating the four components appropriately. In the principal axis coordinates, the velocity gradients are

$$\frac{\partial u_X}{\partial X} = \left(1 - 2\frac{X^2}{L_X^2}\right) \frac{U_0}{L_X} \frac{L_Y}{L_H} \exp\left(-\frac{X^2}{L_X^2} - \frac{Y^2}{L_Y^2}\right) \quad \text{Eq. 5-39}$$

$$\frac{\partial u_Y}{\partial Y} = \left(1 - 2\frac{Y^2}{L_Y^2}\right) \frac{U_0}{L_Y} \frac{L_X}{L_H} \exp\left(-\frac{X^2}{L_X^2} - \frac{Y^2}{L_Y^2}\right) \quad \text{Eq. 5-40}$$

$$\frac{\partial u_X}{\partial Y} = -2\frac{X}{L_X} \frac{Y}{L_Y} \frac{U_0}{L_H} \exp\left(-\frac{X^2}{L_X^2} - \frac{Y^2}{L_Y^2}\right) \quad \text{Eq. 5-41}$$

$$\frac{\partial u_Y}{\partial X} = -2\frac{X}{L_X} \frac{Y}{L_Y} \frac{U_0}{L_H} \exp\left(-\frac{X^2}{L_X^2} - \frac{Y^2}{L_Y^2}\right) \quad \text{Eq. 5-42}$$

The scaling velocity, U_0 , is related to the vorticity moment, which we identify with $\langle \bar{w} \rangle$. Integrating the moment of the vorticity based on vertical gradients of the velocity field (Equations 5-36 and 5-37), we obtain

$$U_0 = -\frac{\langle \bar{w} \rangle}{\pi} \frac{L_H}{L_X^2 L_Y^2} \quad \text{Eq. 5-43}$$

Specification of the velocity field of an individual puff leads to the evolution equations for the puff moments, using both the velocity and the velocity gradients. These quantities are calculated at the puff centroid location by summing the contributions from all the overlapping puffs. Note that a single puff has no mean velocity at its centroid, because the components (Equations 5-36

and 5-37) vanish at the centroid, where $X = Y = 0$. Therefore, the total dynamic velocity perturbation from dense gas interactions is

$$u_d^{(\alpha)} = \sum_{\beta} u_x^{(\beta)}(\bar{\mathbf{x}}_{\alpha}) \quad \text{Eq. 5-44}$$

where the sum is taken over all dense gas puffs, and the summand represents the velocity field (Equations 5-36 and 5-37), after rotation into the project coordinate frame, evaluated at the centroid of puff- α . The other velocity component and all the horizontal gradients are computed in a similar manner.

The dynamically induced velocity and velocity gradients are simply added to the ambient flow field to produce the total transport and distortion of the puffs. The vertical velocity gradient is defined from the sum of the two horizontal divergence components, maintaining a total divergence of zero. The vertical component of velocity is defined from the velocity gradient, assuming zero as the surface boundary condition. Therefore,

$$\frac{\partial w_d}{\partial z} = - \left(\frac{\partial u_d}{\partial x} + \frac{\partial v_d}{\partial y} \right) \quad \text{Eq. 5-45}$$

where the subscript d denotes the overlap sum from all contributing puffs with dense dynamics. The vertical velocity is defined as

$$w_d = \bar{z} \frac{\partial w_d}{\partial z} \exp \left(- \frac{\bar{z}}{\Lambda_{cV}} \right) \quad \text{Eq. 5-46}$$

where \bar{z} is the puff centroid height and Λ_{cV} is a representative vertical scale height for the puff. The exponential decay factor is introduced to reduce the velocity for puffs further from the surface.

The dense gas effects are calculated only for puffs that interact with the ground surface. Negatively buoyant puffs remote from the surface will simply fall downward under the buoyancy forcing described in Section 5.2.1. Puffs are judged to interact with the ground when they have negative vertical momentum, $\langle \overline{w_p c} \rangle$, and their centroid is less than $2\Lambda_{cV}$ above the ground. The first requirement ensures that they are descending, and the second checks that they are in contact with the ground. When these conditions are satisfied, the ambient temperature gradient term in the buoyancy equations (5-2 and 5-5) is neglected because the vertical velocity integral is interpreted as a vorticity moment and there is no vertical transport at the solid surface.

5.3.2 Dynamics with Uncertainty

In situations in which the ensemble mean dispersion includes significant meandering, the horizontal scale assumption in Equation 5-38 is not representative of the near-instantaneous scales that drive the dynamics. The gradients will actually be underestimated because they use the ensemble puff spread in the denominator; however, the velocity gradients are applied to the ensemble puff moments and the effective rate of spread is overestimated. We therefore modify the estimate of the horizontal velocity gradients to include a multiplicative factor of

$$\left(\frac{\langle \bar{c}^2 \rangle}{\max(\langle \bar{c}^2 \rangle, \langle c'^2 \rangle)} \right)^{\Lambda_{cH} / (\Lambda_c + \Lambda_{cH})}$$

on the expressions 5-39 through 5-42. The reduction factor is empirical and is intended only to eliminate over-prediction of the horizontal spread when horizontal meandering is significant. The exponent discriminates between the one-dimensional meander of plumes, where Λ_{cH} is typically much larger than Λ_c , and two-dimensional meander for puffs, where the two scales are equal. The reduction factor is not applied to the vertical velocity gradient (Equation 5-45), however, because dense clouds do not meander in the vertical and the vertical velocity gradient controls the slumping of the cloud.

5.3.3 Turbulent Entrainment

The presence of the ground introduces stability effects on the turbulence in addition to the pressure gradient effects of the mean velocity field. In a free atmosphere, any density perturbation forms a vertical gradient that is stable on one side and unstable on the other. A free dense cloud is unstable on the lower side, while a positively buoyant perturbation is unstable on the upper side. However, when the density perturbation is constrained by the ground surface, a stable gradient is established throughout the cloud. The density gradient suppresses vertical turbulent diffusion because vertical motions transfer kinetic energy to potential energy as the density perturbations are mixed. This mechanism applies to the ambient turbulent motions as well as the dynamically induced motions in the slumping dense cloud.

When a puff is in dense ground effect, as determined by the ground interaction criterion in the previous section, a dense cloud turbulence entrainment model is applied. The framework is similar to the buoyant rise parameterization in Section 5.2.3, but we use different velocity, length scales, and stability dependence.

The internal velocity scale for a dense gas puff is based on the lateral velocities because the vertical motion is constrained. Similarly, we base the length scale on the vertical scale of the cloud because the turbulent eddies are also constrained by the solid boundary. The internal turbulent velocity scale is given by

$$q_d^2 = c_{q1} F_d^2 (Ri_d) V_d^2 \quad \text{Eq. 5-47}$$

where

$$V_d^2 = u_d^2 + v_d^2 + (\sigma_{xx} + \sigma_{yy}) \left(\frac{\partial w_d}{\partial z} \right)^2 \quad \text{Eq. 5-48}$$

$$F_d = \frac{1}{1 + C_{d2} Ri_d} \quad \text{Eq. 5-49}$$

and

$$Ri_d = \frac{g \Lambda_d \left| \hat{\theta}_p / T_0 - \hat{b}_p \right|}{V_d^2 + V^2} \quad \text{Eq. 5-50}$$

The dynamic velocity scale V_d represents the lateral “slumping” motion in the dense cloud. The gradient term is required to provide the velocity scale for the self-induced motions in a puff, because the mean self-induced velocity is zero at the puff centroid. The internal dynamic scale, Λ_d , is defined as the vertical puff scale, Λ_{cV} , because the vertical depth of the dense cloud characterizes the shear-generation scale. We note that the Richardson number is based on the total velocity because the balance between buoyancy and shear in the cloud determines the effective stability and ambient motions are included in the balance. The coefficient in Equation 5-49, C_{d2} , is chosen to be 10 on the basis of comparisons with laboratory data; note that the value of this coefficient is modified from previous versions of SCIPUFF due to the incorporation of the uncertainty effects as described in Section 5.3.2.

In addition to the stability effect on the internally generated turbulence, the formation of a stable layer at the ground affects the ambient turbulence as well as the ambient velocity profile. Because boundary layer turbulence is principally driven by interaction with the ground surface, the reduction of vertical transport through the dense cloud layer can significantly modify the local profiles. We represent this effect by applying the damping factor F_d to the equilibrium eddy diffusivity, K_z^{eq} , defined in Equation 2-32.

The mean ambient velocity is also reduced because of the suppression of vertical mixing, using a factor

$$0.7 + 0.3F_d$$

as suggested by Puttock (1988), based on field experiments. This simple factor gives a maximum speed reduction of 30% when the Richardson number is very high.

The turbulent diffusivity, dissipation timescale, and internal horizontal scale equation are modified as in Equations 5-25 through 5-27 but using q_d and Λ_d in place of q_p and Λ_p . In addition, the vertical compression effect is included in the equation for the internal vertical scale, Λ_{cV} .

5.3.4 Surface Drag

As the dense cloud moves over the ground surface, the frictional drag of the rough surface tends to reduce the lateral slumping rate. This effect is represented by the surface integral terms in Equation 5-34. We represent the drag effect through a damping coefficient on the vertical momentum (or vorticity moment) integrals, $\langle \overline{w_p} \rangle$ (or $\langle P \rangle$) and $\langle \overline{w_p c} \rangle$. In addition, the interaction with the ground introduces a heat flux directly into the cloud, and we assume that this exchange rate occurs at the same rate as the momentum exchange. The damping is therefore applied also to the temperature perturbation integrals.

The surface timescale is based on the roughness length and a wall-layer assumption. If we define an inverse timescale as

$$\tau_w^{-1} = \frac{1}{u_b} \frac{\partial u_b}{\partial t} \quad \text{Eq. 5-51}$$

and assume that

$$\frac{\partial u_b}{\partial t} = \frac{\partial \tau}{\partial z} \quad \text{Eq. 5-52}$$

where τ is the turbulent momentum flux, then using the height scale of the cloud and the wall-layer relation between the surface stress and local wind speed, we obtain

$$\tau_w^{-1} = \left(\kappa / \log \left(1 + \frac{\Lambda_d}{z_0} \right) \right)^2 \frac{\sqrt{V^2 + V_d^2}}{\Lambda_d} \quad \text{Eq. 5-53}$$

5.3.5 Terrain Effects

In the presence of sloping terrain, a dense cloud will tend to move down the slope under the influence of the gravitational forcing. A simplified description of this effect can be included in the model using an equilibrium relation between the buoyancy force and the surface drag to provide a horizontal velocity perturbation. Because the vertical momentum is simply an integral of the balance between the buoyancy force and the surface drag, as in Equation 5-34, we further assume that the terrain-induced horizontal motion is determined from the relations

$$u_d = w_p \frac{h_x}{\sqrt{1+h_x^2}} \quad \text{Eq. 5-54}$$

$$v_d = w_p \frac{h_y}{\sqrt{1+h_y^2}} \quad \text{Eq. 5-55}$$

Where \hat{w}_p is defined by Equation 5-9.

The terrain-induced velocity is added to the dynamic velocity, (u_d, v_d) , computed from the puff interactions as in Equation 5-44. The additional terrain component is used to move the centroid and also appears in the turbulent entrainment and surface drag terms.

6

PARTICLE MATERIALS

6.1 Particle Material Properties

SCICHEM allows several classes of material to be specified; this section describes the modeling of solid particle materials. Particles require a size description and include gravitational settling effects, in contrast to gaseous materials, which are absorbed at the surface with a fixed velocity. Each material is described by an 8-character identifier, which is used for output selection in cases with multiple materials. The user-specified choices of integrated surface output are also characteristics of each material and are specified as part of the material properties.

Particulate materials require a material density, ρ_p , and a set of size bin ranges $\{r_i : i = 1, N_p + 1\}$, which defines N_p bins or subgroups. The underlying concept is a representation of a continuous particle size distribution (PSD) by a discrete set of size bins. A unique puff “type” is associated with each bin so that each size group is tracked separately through the dispersion calculation. Puffs are allowed to merge only with other puffs of the same type—that is, same size bin—so that differential settling effects are represented correctly. The density and size range are used to determine the deposition effects as described in Sections 5.3 and 5.4.

6.2 Particle Gravitational Settling

6.2.1 Particle Fall Velocity

Particle fall velocities are computed using an equilibrium assumption and an empirical drag law relationship. The steady-state fall speed is obtained from the balance between gravitational acceleration and the aerodynamic drag force, giving

$$\frac{4}{3} \pi g \rho_p r_p^3 = F_p \quad \text{Eq. 6-1}$$

where r_p is the equivalent spherical particle radius, ρ_p is the particle material density, and F_p is the drag force.

The drag force is written in terms of a drag coefficient, c_D , as

$$F_p = \frac{1}{2} \rho_a c_D \pi r_p^2 v_g^2 \quad \text{Eq. 6-2}$$

where ρ_a is the air density and v_g is the particle fall speed. The drag coefficient is parameterized as a function of particle Reynolds number (Friedlander, 1977) as

$$c_D = \begin{cases} \frac{24}{\text{Re}} (1 + 0.158 \text{Re}^{2/3}) & \text{Re} < 1000 \\ 0.403 & \text{Re} \geq 1000 \end{cases} \quad \text{Eq. 6-3}$$

where

$$\text{Re} = \frac{2\rho_a v_g r_p}{\mu_a} \quad \text{Eq. 6-4}$$

and the viscosity of air, μ_a , is assumed to be constant at $1.6 \times 10^{-5} \text{ kgm}^{-1} \text{ s}^{-1}$. The air density is computed using the local temperature and pressure to account for variations with altitude.

These equations can be solved using iteration for $\text{Re} < 1000$, to determine the fall speed, v_g , as a function of air density, particle density, and particle size—that is,

$$v_g = V_g(\rho_a, \rho_p, r_p) \quad \text{Eq. 6-5}$$

Any realistic calculation of particle dispersion must recognize a PSD so that a puff representation must describe a finite range of particle sizes. If a particle bin is defined for the range $r_1 \leq r_p < r_2$, we define the mean particle diameter, \bar{r} , as the arithmetic mean of r_1 and r_2 and estimate the fall speed variation across the bin using a three-point distribution with an inverse particle size weighting. Therefore, the mean fall speed is given as

$$\left(\frac{1}{r_1} + \frac{1}{\bar{r}} + \frac{1}{r_2} \right) v_g = \frac{V_g(r_1)}{r_1} + \frac{V_g(\bar{r})}{\bar{r}} + \frac{V_g(r_2)}{r_2} \quad \text{Eq. 6-6}$$

and a fall speed variance can also be defined using the same weighting

$$\left(\frac{1}{r_1} + \frac{1}{\bar{r}} + \frac{1}{r_2} \right) (\sigma_g^2 + v_g^2) = \frac{V_g^2(r_1)}{r_1} + \frac{V_g^2(\bar{r})}{\bar{r}} + \frac{V_g^2(r_2)}{r_2} \quad \text{Eq. 6-7}$$

The implementation of the gravitational settling process in the puff model using the mean and the variance of the fall speed is described next.

6.2.2 SCICHEM Implementation

Gravitational settling introduces a source term into the concentration equation (2-5) and therefore modifies the puff moment equations. The source term can be written as

$$S = \frac{\partial}{\partial z} (v_g c) \quad \text{Eq. 6-8}$$

to represent a downward vertical mass flux. Because S does not vanish at the surface, the addition of gravitational settling implies a loss of material as it is deposited on the ground. The mass loss can be written as an integral over the surface area, A , giving

$$F_s = v_g \int_{z=0} c dA \quad \text{Eq. 6-9}$$

and the puff mass conservation equation must be modified to account for the deposition; this is described in Section 2.3.

The puff centroid equation reflects the settling velocity directly through the addition of the vertical velocity component, giving

$$t_s, t_p \geq t_n \quad \text{Eq. 6-10}$$

and the effects of the finite range of particle sizes on the vertical spread must also be considered. The difference in settling velocity of the different particle sizes within a size bin causes a vertical separation to develop, leading to an increase in the puff moment, σ_{33} . The variation in settling velocity acts in the same way as the ambient vertical velocity fluctuations but with a sustained effect because a particle size is fixed. The fall speed variation gives a linear growth of the vertical spread and is modeled simply as

$$\frac{d\sigma_{33}}{dt} = \text{Terms from (2.11)} + 2\sigma_g \sqrt{\sigma_{33}} \quad \text{Eq. 6-11}$$

This is not an accurate representation of particle size variability but provides a simple estimate of the increase in vertical spread and improves the ability to describe a continuous size distribution. The particle size bins should contain a relatively small variation in fall speed for an accurate calculation.

The equation for the squared concentration integral (Equation 2-73) also includes extra damping terms to represent the loss of concentration at the surface as well as the diffusive effects of particle size variations. The equation becomes

$$\frac{d}{dt} \langle c^2 \rangle = -\frac{\langle c'^2 \rangle}{\tau_c} - \langle c^2 \rangle \left(\frac{1}{\tau_s} + \frac{\sigma_g}{\Lambda_{cV}} \right) \quad \text{Eq. 6-12}$$

6.3 Particle Dry Deposition

6.3.1 Surface Deposition Process

Dry deposition refers to non-gravitational surface processes that remove material from the atmosphere, including collection and absorption phenomena. The surface deposition rate depends on both the contaminant material properties and on the character of the surface and the local meteorology. Gaseous deposition mechanisms are different from particle mechanisms, and different models are employed for the two types of material. The particle model is complicated by the dependence on particle size and on the surface roughness or vegetative canopy description. The SCICHEM representation is based on the description in Sykes et al. (1993a).

Dry deposition is typically described in terms of the deposition velocity v_d , which is defined by

$$v_d = F_c / c \quad \text{Eq. 6-13}$$

where c is the particle concentration and F_c is the total vertical particle flux near the surface, that is, the sum of the turbulent flux and molecular diffusion flux. This expression is derived from the scalar conservation equation by assuming stationarity and horizontal homogeneity (Businger, 1986). Note that c , F_c , and therefore v_d should strictly be defined at a specific reference height, typically 1–100 m above the surface or vegetative canopy height.

The representation in SCICHEM is simply achieved by adding the dry deposition velocity, v_d , to the gravitational fall speed, v_g , in the surface removal calculation (Equation 2-106). The remainder of this section describes the parameterization scheme for v_d .

The gaseous dry deposition rate depends on chemical properties of the gas, such as solubility or reactivity, and is currently specified as a constant value for each gaseous material. Therefore, v_d is a fixed input value for gases.

The dry deposition model for particles is based on the approach of Slinn (1982), who postulates that deposition velocity is equal to a collection efficiency multiplying the momentum deposition velocity

$$v_d = E u_*^2 / u_r \quad \text{Eq. 6-14}$$

where u_* is the surface friction velocity and u_r is the wind speed at the reference height, z_r . Slinn defines the total collection efficiency, E , in terms of the individual collection mechanism efficiencies as

$$E = 1 - (1 - E_B)(1 - E_{IN})(1 - E_{IM}) \quad \text{Eq. 6-15}$$

where E_B is the efficiency of the viscous sublayer flow within a millimeter of the surface elements, E_{IN} represents particle interception, and E_{IM} represents particle impaction. This approach is also taken by Davidson et al. (1982).

A simple logarithmic profile relation is used to determine the reference velocity in terms of the friction velocity, which is obtained from the local meteorological wind field as described in Section 11.1.2. However, under free convection conditions, the mean wind speed is very small and u_* vanishes. The turbulent deposition process does not vanish in this situation because individual convective eddies will transport momentum (and particles) to the surface. For the deposition parameterization, we need to define the average local friction speed, \bar{v}_* , based on the fluctuating surface momentum flux but independent of the horizontal direction of the flux. Sykes et al. (1993b) have used large eddy simulation to determine a simple expression for this mean friction velocity under free convection conditions and find that a good description is given by

$$\frac{\bar{v}_*}{w_*} = 0.46 \left(\frac{z_0}{z_i} \right)^{0.16} \quad \text{Eq. 6-16}$$

where w_* is the convective velocity scale, z_i is the mixed-layer depth, and z_0 is the surface roughness length. These quantities are defined in Section 11.1.

We combine this free convection limit with the shear-driven friction velocity in Equation 6-14 to give a final expression for the deposition velocity as

$$v_d = E \left(u_*^2 + \bar{v}_*^2 \right)^{1/2} \frac{\kappa}{\ln \left(1 + \frac{z_r - z_d}{z_0} \right)} \quad \text{Eq. 6-17}$$

where $\kappa = 0.4$ is von Kármán's constant and z_d is the displacement height. The next section describes the specification of the particle deposition efficiency, E . For the rest of the discussion, we shall use the effective value of the friction velocity $(u_*^2 + \bar{v}_*^2)^{1/2}$ in place of u_* .

6.3.2 Particle Deposition Efficiencies

6.3.2.1 Vegetative Canopy Model

In the region very close to a relatively smooth surface such as water, a flat plate, or canopy elements such as leaves or grass, Brownian motion can be important in transporting particles to the surface (assuming that surface roughness elements do not protrude through the viscous sublayer). This is particularly true for very small particles (diameter $< 0.1 \mu\text{m}$) which, because of their small inertia, can follow small-scale velocity fluctuations. Brownian motion results in the diffusion of particles, that is, transport from high to low concentration regions. As discussed in Lewellen (1985), experimental evidence indicates that the deposition resulting from Brownian motion can be expressed in terms of the Schmidt number, $Sc = \nu / D$, where ν is the kinematic viscosity of air and D is the particle diffusion coefficient. Values of D as a function of particle radius can be found in Friedlander (1977). The molecular collection efficiency is modeled as

$$E_B = f_D Sc^{-0.7} \quad \text{Eq. 6-18}$$

where f_D is the ratio of the viscous drag to the total canopy drag including pressure forces. This factor is needed because the particle deposition scales only with the momentum transport due to viscous forces, and we use a constant value $f_D = 1/3$ to represent the canopy effects. We follow Lewellen and Sheng (1980) in using a value of 0.7 for the power law dependence in Equation 6-18; this is close to Slinn's value of $2/3$.

Interception is essentially filtration in that particles are deposited when they are within a particle radius of the collecting elements (the characteristic size of the element is much greater than the particle radius). Particle inertia is ignored so that the particles are moving with the fluid around the collecting element. Many interception models are based on the filtering efficiency of cylindrical fibers in potential flow,

$$E_{IN} = \frac{2r_p}{a_f} \quad \text{Eq. 6-19}$$

where r_p is the particle radius and a_f is the filter fiber radius (Fuchs, 1964). However, for the more complex situation in a canopy, Slinn considers both "small" collectors such as vegetative hairs and "large" collectors such as grass blades and pine needles and proposes

$$E_{IN} = \left[f \left(\frac{r_p}{r_p + A_s} \right) + (1 - f) \left(\frac{r_p}{r_p + A_L} \right) \right] \quad \text{Eq. 6-20}$$

where A_s is the characteristic radius of "small" collectors, f is the fraction of total interception by these collectors, and A_L is the characteristic radius of large collectors. Slinn (1982) shows that this formulation is in good agreement with Chamberlain's (1967) wind tunnel measurements of

deposition to grass for his chosen parameters. We use Slinn's expression with $f = 0.01$, $A_s = 10 \mu m$, and $A_L = 500 \mu m$.

Particles are subject to impaction when they are much smaller than the collection elements but large enough that their inertia prevents them from following the fluid flow around the elements. Collection efficiency by impaction is a function of a Stokes number, which is the ratio of the particle "stop-distance" to a characteristic canopy element length. Following Slinn, we define the Stokes number

$$St = \frac{u_* \tau_g}{A_L} = \frac{u_* (v_g / g)}{A_L} \quad \text{Eq. 6-21}$$

where τ_g is the particle relaxation time. Slinn gives the impaction efficiency as

$$E_{IM} = \frac{St^2}{1 + St^2} \quad \text{Eq. 6-22}$$

The bulk canopy model used in SCICHEM involves an assumption about the velocity and turbulent diffusivity profiles because the expression (6-14) gives the local deposition rate as a function of position within the canopy. A simplified representation for the dry deposition velocity for the entire canopy is needed for implementation in SCICHEM. If we assume that E is small, the overall efficiency from Slinn's model can be written in the form

$$\bar{E} = \frac{E}{(1 - \beta)E + \beta} \quad \text{Eq. 6-23}$$

where E is defined by Equation 6-15 and β is a parameter that in general will vary for different canopies and velocity profiles. This overall collection efficiency is then used in Equation 6-17 to determine the dry deposition velocity. Slinn gives some data that indicate that the range of β is approximately 0.1 to 0.3 for a wide variety of canopy types. Fits to the data of Chamberlain (1967) using Equation 6-23 with $\beta = 0.16$, along with the full Slinn model, are shown in Sykes et al. (1993a).

For a vegetative canopy with height h_c , we specify a displacement height, $z_d = h_c/2$, and a reference height, $z_r = 2h_c$. Note that the canopy height affects only the reference heights as used in Equation 6-17. The increased deposition for a deeper canopy is represented by an increased surface roughness and friction velocity.

6.3.2.2 Rough Surface Model

In situations in which there is no canopy—for example, deposition to water, bare soil, or rock—some modifications to the collection efficiency terms are necessary. Naturally, there is no interception, so $E_{IN} = 0$. For E_B and E_{IM} , we use a generalization of Lewellen and Sheng's (1980) model for particle deposition to a smooth flat surface. Therefore, we set

$$E_B = 0.8Sc^{-0.7} \quad \text{Eq. 6-24}$$

and

$$E_{IM} = \frac{A_{IM}}{1 + A_{IM}} \quad \text{Eq. 6-25}$$

where

$$A_{IM} = 0.08St(1 - e^{-0.42St}) \quad \text{Eq. 6-26}$$

In this case, the Stokes number is given by

$$St = \frac{u_*^2 \tau_g}{\nu} \quad \text{Eq. 6-27}$$

Predictions from this model compare favorably with Sehmel's (1973) experimental data on deposition to a smooth surface.

For the rough surface, we specify a displacement height, $z_d = 0$, and a reference height, $z_r = 10$ m in Equation 6-17.

6.4 Precipitation Washout

6.5 Effects on Diffusion

Heavy particles can respond only on a finite timescale to turbulent velocity fluctuations and are also falling rapidly through the turbulent velocity field. In general, the effects of the finite timescale from particle inertia are insignificant in atmospheric dispersion because the timescale is relatively short. The response time is related to the equilibrium settling velocity as

$$\tau_g = \frac{v_g}{g} \quad \text{Eq. 6-28}$$

so that a fall velocity of 10 ms^{-1} implies a response time of about 1 s. Atmospheric eddy timescales are generally much longer than 1 second, except very close to the surface, and the dominant effect for larger particles is therefore the vertical motion through the eddies. If the settling velocity is not much larger than the atmospheric eddy component in the vertical, the response timescale will clearly be very fast—and the particles can be considered to be in equilibrium. We therefore represent only the fall velocity effect in SCICHEM.

The main effect of a particle falling through a random velocity field is a decorrelation of the eddy forcing term. The dispersion rate is determined by the velocity variance and the Lagrangian correlation timescale, so a simple representation is obtained by modifying the timescale in the turbulent correlation equations. The timescale is modeled as Λ_s/q_s in Equation 2-21; similar estimates are used in the other diffusivity correlations using the appropriate length and velocity scales. For falling particles, the timescale is modified by a factor

$$\frac{q_s^2}{q_s^2 + v_g^2}$$

so that the effective diffusivity is also reduced by this factor.

7

MULTICOMPONENT MATERIALS

7.1 Multicomponent Material Properties

SCICHEM allows the treatment of reactive chemistry (see Section 3) by specifying a gas material type as *multicomponent*. The gas-phase reaction mechanism is read by SCICHEM as input. The aqueous-phase and aerosol chemistry modules are based on the modules used in the U.S. EPA photochemical grid model, CMAQ, as described in Section 3.2. Aqueous-phase chemistry and aerosol thermodynamics may be treated optionally by a user-specified runtime flag. Reactive chemistry depletes the species masses as described in Section 3.1.

The user provides the individual chemical species properties as input. Properties include the molecular weight, deposition velocity, and wet scavenging parameter as well as the absolute tolerances for the solution of the rate equations. A multicomponent puff has all species associated with it. Individual puffs are not used to specify individual species, as is the case with the particle material size bins (Section 5). The multicomponent species include gas, aqueous, and aerosol particle phase species.

7.2 Multicomponent Dry Deposition

7.2.1 Dry Deposition and Gravitational Settling of Aerosols

The fall velocity of a multicomponent aerosol species is calculated according to the equations given in Section 6.2.1 for particle materials. The dry deposition is treated identically as for particle materials, as described in Section 6.3.

7.2.2 Dry Deposition of Gases.

The dry deposition velocity (m/s) of each gas-phase species is provided by the user as input in the IMC file. Alternatively, gaseous species dry deposition velocities are calculated internally using the Zhang et al. (2003) scheme. For this option, the user needs to specify properties of the species in the IMC file. The IMC file provided with the SCICHEM distribution includes these properties. Additional details are provided in Section 4.3.3 of the SCICHEM 3.3 User's Guide. Dry deposition velocities of particle species are calculated based on the approach used in CMAQ.

7.3 Multicomponent Precipitation Washout

7.3.1 Wet Deposition of Multicomponent Aerosols

The washout of a multicomponent aerosol species is treated identically as for particle materials, as described in Section 7.3.

7.3.2 Wet Deposition of Multicomponent Gases

The wet scavenging coefficient provided by the user as input for each gas-phase species, s (s^{-1}), is used to define the scavenging rate, sr (s^{-1}), as

$$sr = s (R/R_0)$$

where R is the precipitation rate in mm/hr and R_0 is the reference precipitation rate of 1 mm/hr. The scavenging rate is applied to the gas-phase species after the gas-phase chemistry has been advanced. If the aqueous-phase chemistry module is turned on, the wet scavenging coefficient will be ignored and the wet removal carried out inside the aqueous-phase module.

8

SOURCE SPECIFICATION

8.1 Continuous Sources

A continuous source is specified as a constant mass release rate, R_Q , for a finite duration, T_R , starting at time, t_R . The material type and the release location, $\mathbf{x}_R = (x_R, y_R, z_R)$, must also be defined. The source geometry is simply defined in terms of the spread parameter, σ_R . If a “stack” type source is defined, the source is converted internally to a continuous source type and the spread parameter is set equal to the stack radius.

At each model time step during the active period of the release, $t_R \leq t < t_R + T_R$, a new puff is initialized and added to the existing list. If the model time step is Δt , the mass of the new puff is readily determined as

$$Q = R_Q \Delta t \quad \text{Eq. 8-1}$$

The centroid location of the new puff accounts for the passive transport by the mean wind, giving

$$\bar{x}_i = x_{Ri} + \frac{1}{2} \bar{u}_i \Delta t \quad \text{Eq. 8-2}$$

which represents the center of mass of a plume segment of duration Δt originating at the source position.

The second-moment tensor also accounts for the mean transport, so that

$$\sigma_{ij} = \sigma_R^2 \delta_{ij} + \frac{1}{4} \bar{u}_i \bar{u}_j \Delta t^2 \quad \text{Eq. 8-3}$$

The addition of the mean velocity terms in Equation 8-3 produces an elongation of the puff in the downstream direction and a smooth overlap between consecutive puffs.

The turbulent flux correlation moments, $\langle x'_i \overline{u'_j c'} \rangle$, are all initialized to zero because there is no flux at the source, and the mean-square concentration integral is

$$\Delta t_{obs} \quad \text{Eq. 8-4}$$

where

$$\overline{V}^2 = \overline{u}_i \overline{u}_i + \overline{u'^2} + \overline{v'^2} \quad \text{Eq. 8-5}$$

The initial concentration fluctuation variance is therefore effectively set to zero.

The internal fluctuation length scales, Λ_c and Λ_{cV} , are set equal to σ_R , but the second horizontal scale, Λ_{cH} , reflects the continuous “plume” nature of the release. Therefore,

$$\Lambda_{cH} = \min\left(\Lambda_y, \int_{t_R}^t \bar{V} dt'\right) \quad \text{Eq. 8-6}$$

where Λ_y is the composite horizontal turbulence scale defined in Equation 2-117 and the integral represents the length of the plume.

8.2 Instantaneous Sources

Instantaneous sources involve only a single puff creation stage and are specified by a release time t_R , a release location \mathbf{x}_R , and a CLOUDTRANS puff file (Henn et al., 1995). When the SCICHEM calculation reaches the release time, the puffs in the CLOUDTRANS file are released into the dispersion domain. A collection of puffs can be released in a single source event to describe an arbitrary spatial distribution, and this input is translated directly into initial conditions for each puff. The CLOUDTRANS input must contain material identifiers that correspond to existing SCICHEM material types and must also provide mass, centroid location, and spread parameters for each puff.

The centroid location for each puff is used as a three-dimensional offset from the general release location, \mathbf{x}_R , and the puff moments, σ_{ij} , can be specified directly. The CLOUDTRANS file can also neglect the off-diagonal moments by specifying σ_x , σ_y , and σ_z or simply σ . In the latter case, a spherical puff will be released.

As for the continuous release, the turbulent flux moments are initialized to zero. The mean-square concentration integral is calculated using the interaction integrals in Section 2.2 for all the puffs in the release. This strictly gives the square of the mean, but this is equal to the mean-square under the assumption of zero fluctuation variance. The internal fluctuation scales are initialized using the puff spread moments if the scales are not directly provided on the CLOUDTRANS file. Currently, SCICHEM uses

$$\begin{aligned} \Lambda_c &= \min(\sigma_x, \sigma_y) \\ \Lambda_{cH} &= \max(\sigma_x, \sigma_y) \\ \Lambda_{cV} &= \sigma_z \end{aligned} \quad \text{Eq. 8-7}$$

8.3 Linear Decay

Linear decay can be applied to any material in SCICHEM to represent a simple reduction in concentration due to a linear chemical reaction or other linear decay effects. Each puff carries a decay coefficient, f_A , which is initialized to unity at release time. During the transport calculation, the coefficient evolves according to the relation

$$\frac{df_A}{dt} = -k_A f_A \quad \text{Eq. 8-8}$$

where k_A is the user-specified decay rate. The decay rate specification includes a diurnal variation so that effects that depend on solar radiation can be described. The actual rate is obtained from the daytime maximum, $k_A^{(\max)}$, and nocturnal minimum, $k_A^{(\min)}$, as

$$k_A = \max(k_A^{(\max)} \sin(\phi), k_A^{(\min)}) \quad \text{Eq. 8-9}$$

where ϕ is the solar elevation angle. To use a constant decay rate, the user must specify equal maximum and minimum decay rates.

All deposition and dosage integrals use the decay factor-weighted concentration, $f_A c$, so that deposition, for example, is computed as

$$\chi_D(x, y, t) = \int_0^t f_A v_D c(x, y, 0, t') dt' \quad \text{Eq. 8-10}$$

The decay calculation continues after material has been deposited on the surface so that

$$\frac{\partial \chi_D}{\partial t} = -k_A \chi_D \quad \text{Eq. 8-11}$$

This assumes that the decay process is equally effective for material on the surface and in the air. The variance of the deposition decays at twice the rate, that is,

$$\frac{\partial \overline{\chi_D'^2}}{\partial t} = -2k_A \overline{\chi_D'^2} \quad \text{Eq. 8-12}$$

9

METEOROLOGY SPECIFICATION

9.1 Background

The advection and diffusion processes modeled with SCICHEM require meteorological input of some kind. The minimum requirement is a single wind vector. Obviously, more meteorological input is usually desirable, and SCICHEM can assimilate observational data ranging from a single wind measurement to multiple profiles—which include turbulence measurements and/or boundary layer parameters such as mixing-layer height and Pasquill-Gifford-Turner stability class. In addition, with the specification of topography, SCICHEM will calculate an adjustment to the three-dimensional velocity field obtained from interpolating observations so that it has very low divergence, that is, conserves mass. Alternatively, three-dimensional gridded wind and temperature fields generated by some prognostic model or analysis may be input.

SCICHEM meteorological input is specified as one of two generic types: observational or gridded. Observational data are characterized by irregularly spaced vertical profiles with irregular horizontal locations as well as irregular reporting times. The number and locations of observations can vary from one time to the next. Observational input is specified through a file with vertical profiles and/or a file of single-level surface data. Gridded meteorological input is defined on a regularly spaced three-dimensional grid; time need not be regularly spaced. The gridded input option is intended for use with numerically generated wind fields.

9.2 Observational Input

Observational input can be of two types. A *SURFACE* observation file contains multiple records of the mean wind, temperature, and possibly boundary layer parameters. Each record represents a station location at a specified time, and the file can contain multiple stations and multiple times stored in chronological order. The surface observations are assumed to be given at the reference height, z_{ref} , unless the height is provided as part of the observation record. The reference height can be specified on the surface file or is otherwise assumed to be 10 m. If the height is given with each observation, the winds are adjusted to the mean observation height using a simple logarithmic profile assumption before any interpolation takes place. A *PROFILE* observation file is similar in character to the surface file and in fact can optionally contain surface observations such as heat flux and mixing-layer height. For a given station, there are typically multiple levels of observations, although a single observation level can be specified.

The meteorological observations are interpolated onto a rectangular grid for use in SCICHEM so that local values can be rapidly found for arbitrary puff locations. When the mass-consistent adjustment option is invoked, the vertical grid must be input. Otherwise, the vertical grid is defined from the observational input. If *PROFILE* data are given, the vertical grid is based on the heights from the station that has the most levels with valid wind measurements up to Z_{max} (the puff calculation domain height) at the nearest time before the start of the run. If required, the grid is extended to Z_{max} with a grid spacing defined by the two uppermost observation levels. If the number of levels on this profile is less than a minimum NZ_{min} ($= 3$ currently), a uniform vertical grid is constructed based on Z_{max} and NZ_{min} . Finally, the grid is checked and modified if

necessary so that it has at least one level near the ground suitable for *SURFACE* data if given. However, if only *SURFACE* data are available, only one vertical level is used.

The horizontal grid is initially assumed to be a single point but is expanded when the number of observation stations is two or more during the SCICHEM calculation. A uniform horizontal grid is then constructed based on the puff domain boundaries x_{min} , x_{max} , y_{min} , and y_{max} and horizontal resolution ΔH . It is assumed for the following discussion that the horizontal grid has more than a single point.

The assimilation of observational data into the three-dimensional gridded wind field is based on a weighted interpolation scheme. The weights given an observation are functions of the horizontal and vertical distances, temporal separation, and terrain elevation relative to the grid points. In the following, it is assumed that both *SURFACE* and *PROFILE* observations are available, but the methodology is also valid if either set is missing—the terms corresponding to the missing data type are simply ignored. Data assimilation is performed at times for which either *SURFACE* or *PROFILE* observations are available. At such a time, the interpolation scheme for any point on the grid gives

$$\phi^n = \frac{w_o \phi^{n-1} + \sum_{i=1}^{N^S} w_i^S \phi_i^S + \sum_{i=1}^{N^P} w_i^P \phi_i^P}{w_o + \sum_{i=1}^{N^S} w_i^S + \sum_{i=1}^{N^P} w_i^P} \quad \text{Eq. 9-1}$$

where ϕ^n represents any variable such as u , v , T , and so on at time t_n ; ϕ^{n-1} is the interpolated value from the previous time t_{n-1} ; ϕ_i^S is the observation at the i^{th} *SURFACE* station at time t_s ; w_i^S is its corresponding weight; ϕ_i^P is vertically interpolated from observations at the i^{th} *PROFILE* station at time t_p ; w_i^P is its corresponding weight; N^S and N^P are the number of valid surface and profile observations, respectively, at t_s and t_p ; and w_o is a weight assigned to the field at t_{n-1} . Note that either $t_n = t_s$ or $t_n = t_p$ so that $t_s, t_p \geq t_n$. Also note that the weights can vary for different field variables (but for visual clarity this dependence is not indicated in the notation). The definition of the weights, which depends somewhat on whether an observation is *SURFACE* or *PROFILE*, is discussed next.

In general, an observation weight is determined as the product of three functions dependent on the horizontal, vertical, and temporal separations between the observation and grid point:

$$w^{obs} = w_h(r)w_v(\Delta z)w_t(t_{obs} - t_n) \quad \text{Eq. 9-2}$$

where w^{obs} represents w_i^S or w_i^P , r is the horizontal distance from the observation location to the grid point, Δz is a measure of the vertical separation (accounting for terrain differences), and t_{obs} is t_s or t_p as appropriate.

The horizontal weighting function is simply based on the inverse distance squared:

$$w_h = (1 + r^2/a^2)^{-1} \quad \text{Eq. 9-3}$$

where the “core” radius a is used to avoid the singularity as r approaches zero and reduces the complete dominance of an observation near the grid point; $a^2 = 0.25(\Delta x^2 + \Delta y^2)$ where Δx and Δy are the horizontal grid spacings.

The vertical weighting function has a similar form:

$$w_v = (1 + C \Delta z^2 / a^2)^{-1} \quad \text{Eq. 9-4}$$

where C is a constant set to 1000. The purpose of setting C large is to give extra weight to observations that are vertically close in preference to observations that may be close horizontally but relatively distant vertically. Although Δz will be defined shortly, for the time being assume that it is simply the vertical separation (which is the case over flat terrain). Then, an observation with $\Delta z \neq 0$ but $r = 0$ is given the same weight as one with no vertical separation but $r \approx 32\Delta z$ (assuming $C\Delta z^2 \gg a^2$). This is motivated primarily by the vertical stability of the atmosphere, which tends to reduce velocity correlations as vertical separation increases. The following expression for Δz is an ad hoc attempt to account not only for vertical separation, but also for terrain differences:

$$\Delta z = \delta_z + \frac{\delta_h^3}{\delta_h^2 + z_h^2 + \varepsilon} \quad \text{Eq. 9-5}$$

where $\delta_h = |h - h_{obs}|$, h is the terrain height at the grid position, h_{obs} is the terrain height at the observation location, $z_h = \max(z - h, \tilde{z} - h_{obs})$, z is the grid height (above the reference or zero height level), $\tilde{z} = \max(z, z - h + h_{obs})$, $\delta_z = |\tilde{z} - z_{obs}|$, and z_{obs} is the height of the nearest observation level used to interpolate linearly to \tilde{z} . ε is a small number (set to 10^{-10}), which avoids division by zero when $\delta_h = z_h = 0$.

As indicated previously, ϕ_i^P is found from a linear interpolation of the profile data at the height \tilde{z} . However, if \tilde{z} is below the lowest observation level, ϕ_i^P is set to the value at the lowest level for temperature and humidity while horizontal velocity components are reduced using a neutral logarithmic profile (see Section 11). If \tilde{z} is above the highest observation level, ϕ_i^P is set to the value at that level—except for temperature, which is extrapolated using the temperature gradient from the U.S. Standard Atmosphere.

The vertical weight, w_v , for temperature is modified for a *SURFACE* observation: if the height of the grid point above ground is greater than 500 m, w_v is set to zero; otherwise, the expression from Equation 9-4 is multiplied by a factor $\min\{[500 - (z - h)]/300, 1\}$. Therefore, the temperature weight is unchanged for $z - h \leq 200$ m but goes linearly to zero at 500 m. This factor is used because a surface temperature measurement will usually not be representative of the atmosphere well away from the surface, particularly above a mixed layer or under stable conditions.

The temporal weight uses a simple exponential “aging” function:

$$w_t = \exp(-|t_n - t_{obs}|/\tau_{obs}) \quad \text{Eq. 9-6}$$

The time constant τ_{obs} is set to 6 hours if t_n is beyond the last or ahead of the first observation time; otherwise, it is based on the time between observations and the number of observations so that times with many observations are given relatively large weights. Therefore,

$$\tau_{obs} = f_\tau \Delta t_{obs} \tilde{N}_{n-1}^{obs} / N^{obs} \quad \text{Eq. 9-7}$$

where f_τ is an empirical constant set to 0.4323, Δt_{obs} is the time between the current and previous observations, and N^{obs} is N^S or N^P . \tilde{N}_{n-1}^{obs} is a measure of the number of observations from the previous time, which accounts for time-smoothing and is dependent of the history of the data assimilation. It is updated when $t_n = t_{obs}$ using τ_{obs} from Equation 9-7 and the current number of observations:

$$\tilde{N}_n^{obs} = N^{obs} + \tilde{N}_{n-1}^{obs} \exp(-\Delta t_{obs}/\tau_{obs}) \quad \text{Eq. 9-8}$$

where initially \tilde{N}_0^{obs} is set to zero. As an example, if N^{obs} and Δt_{obs} are fixed, \tilde{N}_n^{obs} rapidly approaches an asymptotic value of $1.16N^{obs}$.

Temporal smoothing is chiefly implemented through the weight w_o given to the fields at t_{n-1} . It is a function of the time between updates, $\Delta t_n = t_n - t_{n-1}$, and the observation weights used at t_{n-1} . For a given grid location, a time-smoothed sum of *SURFACE* observation weights is defined as

$$S_n^S = \begin{cases} S_{n-1}^S \exp(-\Delta t_n/\tau_S) & t_S > t_n \\ S_{n-1}^S + \sum_{i=1}^{N^S} w_i^S t_S = t_n & \end{cases} \quad \text{Eq. 9-9}$$

where τ_S is the time constant from Equation 9-7 appropriate to *SURFACE* observations and $S_0^S = 0$. The sum for *PROFILE* observations, S_n^P , is defined similarly. Then,

$$w_o = S_{n-1}^S + S_{n-1}^P \quad \text{Eq. 9-10}$$

This definition is an attempt to quantify the relative quality of the interpolated three-dimensional fields, for example, fields at t_{n-1} that assimilated many observations will dominate over a single observation at t_n as long as they are not too old.

9.3 Gridded Input

9.3.1 File Format Types

SCICHEM supports gridded format designated as MEDOC (Multiscale Environmental Dispersion Over Complex terrain). The MEDOC format is based on the French Electricity Board pollutant dispersion programs as developed for Defense Nuclear Agency application under

contract number DNA001-92-C-0151. Gridded data in other formats must first be converted to the MEDOC formats.

9.3.2 Terrain

The MEDOC format allows the input of terrain elevation information. If this is the case, it is assumed that the coordinate system on the file, (ξ, η, ς) , is terrain-following as defined by the transformation introduced by Clark (1977):

$$\begin{aligned}\xi &= x \\ \eta &= y \\ \varsigma &= \frac{z - h}{J}\end{aligned}\tag{Eq. 9-11}$$

where

$$J = 1 - \frac{h}{D}\tag{Eq. 9-12}$$

Here, $h(x,y)$ is the local terrain elevation, x and y are the Cartesian horizontal coordinates, z is the Cartesian vertical coordinate, and D is the depth of the model domain. It is assumed that the Cartesian velocity components are on the file. Then, only spatial gradients need be transformed in SCICHEM as follows:

$$\begin{aligned}\frac{\partial \phi}{\partial x} &= \frac{\partial \phi}{\partial \xi} + G_x \frac{\partial \phi}{\partial \varsigma} \\ \frac{\partial \phi}{\partial y} &= \frac{\partial \phi}{\partial \eta} + G_y \frac{\partial \phi}{\partial \varsigma} \\ \frac{\partial \phi}{\partial z} &= J^{-1} \frac{\partial \phi}{\partial \varsigma}\end{aligned}\tag{Eq. 9-13}$$

where ϕ represents any variable such as a velocity component or temperature and

$$\begin{aligned}G_x &= \left(1 - \frac{\varsigma}{D}\right) \frac{h}{x} \\ G_y &= \left(1 - \frac{\varsigma}{D}\right) \frac{h}{y}\end{aligned}\tag{Eq. 9-14}$$

The vertical gradient of vertical velocity, w , is treated as a special case and is set to ensure continuity:

$$\frac{\partial w}{\partial z} = \left(\frac{\partial u}{\partial x} + \frac{\partial v}{\partial y} \right)\tag{Eq. 9-15}$$

This estimate of $\partial w / \partial z$ is then used in the calculation of the horizontal Cartesian gradients of w in Equation 9-13. Simple finite differencing is employed in computing the partial derivatives in Equations 9-13 through 9-15.

9.4 Mean Field Interpolation

The mean meteorological fields are updated every large time step Δt_L using simple linear interpolation. If $\phi(t)$ represents a field at time t , the time interpolation is defined by

$$\phi(t) = \left(1 - \frac{\Delta t_L}{T_M - t + \Delta t_L}\right) \phi(t - \Delta t_L) + \frac{\Delta t_L}{T_M - t + \Delta t_L} \phi(T_M) \quad \text{Eq. 9-16}$$

where T_M is the next time when the fields are given. Note that storage for only two time levels is required.

The computation of mean wind and temperature at a puff centroid can depend on its proximity to the surface and its vertical position relative to the inversion (if one exists) in conjunction with the meteorological input type and boundary layer specifications. However, under all circumstances, horizontal interpolation is required (except for the trivial case of a single location for the meteorology). Therefore, we now describe the simple bilinear interpolation employed in SCICHEM.

The background meteorology is always defined on a rectangular, uniformly spaced horizontal grid so that $x_i = x_1 + (i-1)\Delta x$ with y_i defined similarly. The locations of the four surrounding grid locations are (x_{i_p+m}, y_{j_p+n}) , $m, n \in (0,1)$ where (\bar{x}, \bar{y}) is the puff centroid, $i_p = \text{int}((\bar{x} - x_1)/\Delta x) + 1$, and j_p is defined similarly. Then, the value of any field at the centroid location, represented by $\bar{\phi}$, is

$$\bar{\phi} = \sum_{i=0}^1 \sum_{j=0}^1 \phi_{i_p+i, j_p+j} f_i^x f_j^y \quad \text{Eq. 9-17}$$

where

$$\begin{aligned} f_i^x &= 1 - i + (\bar{x} - x_{i_p})/\Delta x \\ f_j^y &= 1 - j + (\bar{y} - y_{j_p})/\Delta y \end{aligned} \quad \text{Eq. 9-18}$$

and ϕ_{i_p+i, j_p+j} is the field variable at (x_{i_p+i}, y_{j_p+j}) . In cases in which vertical interpolation is required, a similar procedure is used, so that Equation 9-17 will have a third summation with a vertical factor f_k^z .

The interpolation scheme is used for upper air fields, that is, gridded or *PROFILE* observations interpolated using Equations 9-1 and 9-16 and *SURFACE* fields if available (again interpolated using Equations 9-1 and 9-16). If the puff centroid is located above the top of the boundary layer or if the boundary layer type is *PROFILE* or *NONE*, the above scheme using the upper air fields fully describes the interpolation procedure. Otherwise, the puff is located within the PBL. The procedure for setting the velocity and temperature is then modified as described in Section 11.

9.5 Mass Consistency

A simplified three-dimensional mass-consistency scheme is available as part of the SCICHEM meteorological input. If terrain input is specified in conjunction with observational wind input or certain kinds of gridded input, the interpolated wind field is then adjusted to ensure mass conservation; that is, its divergence is zero (or at least very small). It should be noted that this feature is invoked only if the mass-consistent module SWIFT is unavailable.

The adjustment procedure uses either an iterative FFT solver or a point relaxation scheme, depending on the magnitude of the effective terrain slopes. The FFT solver is faster but converges only for relatively small slopes. The effective slope is defined as the actual slope, s , divided by the vertical partition parameter, α . The partition parameter depends on the vertical stability and is usually small, resulting in near-horizontal flow around terrain features. The adjusted velocity fields are calculated as

$$u_i^{(mc)} = u_i^{(o)} + \frac{\partial \phi}{\partial x_i} \quad \text{Eq. 9-19}$$

where $u_i^{(o)}$ is the interpolated field based on the input winds and ϕ satisfies the Poisson equation

$$\frac{\partial^2 \phi}{\partial x^2} + \frac{\partial^2 \phi}{\partial y^2} + \frac{1}{\alpha^2} \frac{\partial^2 \phi}{\partial z^2} = -\nabla \cdot \mathbf{u}^{(o)} \quad \text{Eq. 9-20}$$

This equation is solved in a non-orthogonal terrain-following coordinate system, but the departure from a Cartesian system is small for small slopes. In this case, the direct FFT scheme is convergent. However, the slopes are too large in most cases, and a time-like iteration based on the artificial compressibility method is used. For each iteration, denoted by n , we define

$$\begin{aligned} u^{(n)} &= u^{(n-1)} - \frac{\partial \phi^{(n-1)}}{\partial x} \\ v^{(n)} &= v^{(n-1)} - \frac{\partial \phi^{(n-1)}}{\partial y} \\ w^{(n)} &= w^{(n-1)} - \frac{1}{\alpha} \frac{\partial \phi^{(n)}}{\partial z} \\ \phi^{(n)} &= \frac{\phi^{(n-1)} - \beta^2 \nabla \cdot \mathbf{u}^{(n-1)}}{1 + k_\phi} \end{aligned} \quad \text{Eq. 9-21}$$

and the “time step,” β , is chosen locally to satisfy a Courant condition. Note that the vertical velocity adjustment is made implicit by coupling it with the calculation of ϕ . This helps avoid restrictive Courant conditions in the typical case in which the vertical grid resolution is much finer than the horizontal. The damping coefficient $k_\phi = 0.15$ was found necessary to achieve numerical convergence. However, because ϕ approaches zero as the velocity field becomes divergence-free, k_ϕ should not affect the final solution.

The iterative scheme is continued until the maximum divergence in the domain falls below the convergence criterion, εD_{\max} , where the divergence scale is $0.1 \max(u_{\max}^{(o)} / \Delta x, v_{\max}^{(o)} / \Delta y)$ and ε can be selected by the user. The default value for ε is 0.01.

For small slopes, the elliptic equation is cast as the sum of the standard separable Cartesian operator plus non-orthogonal terrain terms.

$$\frac{\partial^2 \phi}{\partial x^2} + \frac{\partial^2 \phi}{\partial y^2} + \frac{1}{\alpha^2} \frac{\partial^2 \phi}{\partial z^2} = -\nabla \cdot \mathbf{u}^{(o)} + L(\phi) \quad \text{Eq. 9-22}$$

where the spatial coordinates are now the transformed variables and L represents the terrain terms. This equation is solved directly for $\phi^{(n)}$ using $\phi^{(n-1)}$ on the right-hand side. The iteration is continued until the maximum change in ϕ divided by the maximum value of ϕ is less than the specified criterion.

The vertical partition factor, α , is defined empirically as

$$\alpha = \frac{1}{1 + Fr^2} \quad \text{Eq. 9-23}$$

where the Froude number is given by $Fr^2 = \frac{N^2 (\Delta x^2 + \Delta y^2)}{(u^2 + v^2)}$ and N^2 is the Brunt-Vaisala

frequency. It should be noted that $\alpha = 1$ corresponds to potential flow (the flow tends to go over and around terrain) while $\alpha = 0$ results in flow constrained to a horizontal plane (around terrain). The user can specify maximum and minimum values for α .

9.6 Nested Meteorological Fields

As part of the modifications for SCIPUFF Version 2.0, the meteorological field description was generalized to allow multiple fields to be specified. This was specifically implemented to allow nested domains for use with urban dispersion modeling, where detailed description of a small sub-domain is required. Each meteorological field contains a complete description of the spatial grid; surface terrain and land cover; and all the associated dynamic, thermodynamic, and boundary layer field variables.

Nested meteorological fields can be specified through the gridded MEDOC input format. For nested MEDOC files, the fields are completely defined by the input files because they define the spatial grid and field variables. Any fields not defined on the MEDOC file will assume the default inputs for the project, for example, surface roughness. Note that the user is responsible for the consistency of the nested MEDOC input; SCIPUFF will simply use the meteorological information in the input files. In addition, because the fields from the multiple nested MEDOC files are treated independently, they are not required to contain the same variables or the same time breaks. However, the first file in the list is assumed to be the “outer” field, which must cover the project domain, that is, subsequent MEDOC files are assumed to be nested inside the first field.

9.7 Smoothed Meteorological Fields

As described in Section 4.2.2, puffs are permitted to grow commensurate with the variations in the velocity field. For relatively smooth fields, this implies that puffs may extend horizontally over many cells of the background meteorology grid. In this case, the interpolation procedure described in Section 9.3, in which the mean velocity and gradients are based only on the grid cell containing the puff centroid, is inappropriate. Some kind of averaging or smoothing of the velocity field over the puff volume would be ideal but computationally time-consuming. Therefore, a series of smoothed fields is constructed from the “base” gridded meteorology, with a doubling of the horizontal grid spacing for each successive field. Interpolation on the smooth fields is then as described in Section 9.3. Note, however, that these fields are constructed only if necessary; that is, a puff has grown so that $\sigma_H^2 > \Delta x^2 + \Delta y^2$ where Δx and Δy are the meteorology grid sizes. Also note that smoothing affects only horizontal resolution; vertical resolution is unchanged from the base meteorology.

A smoothed field is conceptually based on a simple 1-2-1 filtering of the base field. This filter is applied along the x - and y -coordinate directions to all fields associated with the background meteorology—velocity components (except in the case of a staggered grid; see below), terrain elevation, land use/urban parameters, boundary layer parameters, and so on. The number of grid points in the x -direction of the smoothed field is set to $n_x^s = \text{int}[(n_x + 2)/2]$ and similarly for y . When n_x is odd, this results in a doubling of the grid sizes for the smoothed field. If, however, it is even, the grid size is defined as $\Delta x^s = (x_{n_x} - x_1)/(n_x^s - 1)$ so that it is slightly less than double the base grid and the filter is based on a triangular shape with base width $4 \Delta x$.

The velocity fields generated by the mass-consistency models SWIFT and that described in Section 9.5 are on “staggered” grids; that is, the velocity components are shifted a half grid length along their respective coordinate directions. (Velocity fields with staggered grids can also be input through the MEDOC file format; see Section 9.3.) One of the fundamental features of these fields is that the divergence is nearly zero, and it is desirable that the smooth fields based on these maintain that feature. Although applying a 1-2-1 filter to all components does not guarantee that, it can be shown that applying a 1-2-2-1 filter to the horizontal velocity components in conjunction with a 1-2-1 filter on the vertical component does, at least for flat terrain. Therefore, a 1-2-2-1 filter is applied to the horizontal velocity components on staggered grids. As above, if the smoothed grid size is less than twice the base grid, the filter is defined by its shape—which here is a symmetric trapezoid with base width $5 \Delta x$.

Smooth fields can themselves be filtered to generate meteorology on coarser grids if puffs grow to the appropriate size. Clearly the process cannot continue if the base grid (which may be the result of several smoothing operations) does not have enough points to implement the filters defined above. As a practical limit, smooth fields are generated only if the base grid has at least six points in each horizontal direction.

10

PLANETARY BOUNDARY LAYER

10.1 Governing Parameters

Defining the mean wind and turbulence profiles is essential in characterizing the transport and turbulent diffusion rates in the PBL. However, because it is unlikely that detailed profiles will be available in routine use of SCIPUFF, it is necessary to consider some idealizations of the PBL structure. Extensive research on the PBL has led to a consensus on its overall structure, the applicability of similarity laws, and the governing parameters—at least for stationary flow over flat, homogeneous surfaces (see Wyngaard, 1985; Venkatram and Wyngaard, 1988; or Lewellen, 1981). It is now recognized that under ideal conditions both the mean wind and turbulence are functions principally of the following parameters:

- Surface roughness length, z_0
- Boundary layer depth, z_i
- Monin-Obukhov length, L
- Surface friction velocity, u_*

Except for the boundary layer depth and possibly the roughness length, these parameters are not measurable quantities. Therefore, they must be related to other quantities that may be directly measured or at least estimated sensibly. So, instead of friction velocity and Monin-Obukhov length, SCIPUFF uses a reference velocity, $uref = (uref, vref)$, defined at a height, $zref$, and the sensible heat flux, H . The various ways of specifying the input parameters are discussed in the following section, but first we relate them to the PBL parameters L and u_* as well as the temperature scale, θ_* , and the convective velocity scale, w_* , which is used to characterize turbulence under convective conditions. (Two other important parameters, U_g , the geostrophic wind, and f , the Coriolis parameter, are not considered here because they determine the “turning” of the wind over the boundary layer depth due to the earth’s rotation. This effect is not incorporated into SCIPUFF unless it is explicitly provided in the upper air wind fields.)

10.1.1 Monin-Obukhov Length, L

The Monin-Obukhov length is defined as

$$L = -\frac{u_*^3 T \rho_a c_p}{\kappa g H} \quad \text{Eq. 10-1}$$

where κ is von Kármán’s constant, T is the air temperature (either the actual absolute temperature if available or more typically the base temperature T_0 used for the Boussinesq approximation), ρ_a is the air density, and c_p is the specific heat at constant pressure. L represents the ratio of the shear-driven turbulence production to buoyant production and as such is a measure of the flow stability. Unstable convective conditions (positive heat flux) are associated

with a negative L while stable flows (negative heat flux) are associated with a positive L . For neutral flow, L becomes infinite.

10.1.2 Friction Velocity, u_*

The surface friction velocity, u_* , is defined by

$$\tau_s = \rho_a u_*^2 \quad \text{Eq. 10-2}$$

where τ_s is the average surface stress. Except for special output from numerical weather models, the surface stress will typically be unavailable from meteorological input data, so the surface friction velocity is determined from the well-known logarithmic velocity profile law, corrected for stability effects (see, for example, Businger, 1973):

$$u_* = \frac{\kappa U_{ref}}{\ln(z_{ref}/z_0 + 1) - \Psi_m} \quad \text{Eq. 10-3}$$

where U_{ref} is the reference speed and Ψ_m is the stability correction term. U_{ref} is determined from

$$U_{ref}^2 = u_{ref}^2 + v_{ref}^2 + \overline{u_L'^2} + \overline{v_L'^2} \quad \text{Eq. 10-4}$$

where $\overline{u_L'^2}$ and $\overline{v_L'^2}$ are the horizontal large-scale variances, all given at the reference height. The large-scale variances are included in the definition of the reference speed because they represent wind velocity fluctuations on timescales longer than the boundary layer response time and therefore contribute to the average surface friction velocity. (The reference height, z_{ref} , used in Equation 10-3 will, under certain circumstances, be the “surface layer height” defined in Section 10.3; z_{ref} is required to be less than or equal to the surface layer height in order for the surface layer relation [Equation 10-3] to apply.)

For neutral flow ($H = 0$), $\Psi_m = 0$. For the unstable case ($L < 0$), Ψ_m is given by

$$\Psi_m = 2 \ln \left[\frac{(1 + \Phi_m^{-1})}{2} \right] + \ln \left[\frac{(1 + \Phi_m^{-2})}{2} \right] - 2 \tan^{-1}(\Phi_m^{-1}) + \frac{\pi}{2} \quad \text{Eq. 10-5}$$

where the non-dimensional velocity gradient Φ_m is given by

$$\Phi_m = (1 - 15 z/L)^{-1/4} \quad \text{Eq. 10-6}$$

The most commonly used form for Ψ_m under stable conditions ($L > 0$), is (for example, Businger et al., 1971; Dyer, 1974; Högström, 1987)

$$\Psi_m = -A_m z/L \quad \text{Eq. 10-7}$$

where A_m has a value around 5. However, as Carson and Richards (1978) and others point out, this form is valid only for $z < L$. They suggest that the Wangara data presented by Hicks (1976) are suitable for describing Ψ_m for $z > L$; this is confirmed by Holtslag's (1984) analysis of data from Cabauw. Van Ulden and Holtslag (1985) give an empirical function that matches Equation 10-7 for $z < L$ and is also a good fit to the observations at larger z :

$$\Psi_m = -17 \left[1 - \exp(-0.29 z/L) \right] \quad \text{Eq. 10-8}$$

Because of uncertainties in the observations, there is some question as to the behavior of Ψ_m at large values of z/L (above 5 to 10). However, as described in Section 10.3, Equation 10-8 (and Equation 10-3 in general) is applied only within the "surface layer" and, under stable conditions, the surface layer is limited to a maximum height of $5L$.

The non-dimensional velocity gradient, as used in Equation 10-6, is defined as

$$\Phi_m = \frac{\kappa z}{u_*} \frac{\partial u}{\partial z} \quad \text{Eq. 10-9}$$

For stable conditions, using Equation 10-8 in Equation 10-3 gives

$$\Phi_m = 1 + 4.93(z/L) \exp(-0.29 z/L) \quad \text{Eq. 10-10}$$

The calculation of u_* requires an iterative procedure because u_* is a function of L , which in turn is a function of u_* . In addition, the calculation is modified under stable conditions if a *CALCULATED* boundary layer mode is specified; see Section 10.2.

As implied previously, special numerical weather model output may include u_* , and this can be used by SCIPUFF if given as a two-dimensional field on a MEDOC file (Section 9.3) and the PBL mode is *METFILE* or *OPERATIONAL*, as described in Section 10.2. In this case, the input friction velocity may be increased to account for the inclusion of horizontal large-scale variances in the definition of the reference velocity. Therefore, the enhanced friction velocity \hat{u}_* will be

$$\hat{u}_* = U_* \sqrt{1 + \min \left(\frac{u_{ref}^2 + v_{ref}^2}{U_{ref}^2}, \frac{u_*^2}{U_*^2} \right)} \quad \text{Eq. 10-11}$$

where U_* is the input friction velocity and u_* is defined in Equation 10-3. (Clearly, $\hat{u}_* = U_*$ in the absence of large-scale variance.) Then, \hat{u}_* will be used subsequently in place of u_* , including the calculation of Monin-Obukhov length (Equation 10-1).

10.1.3 Temperature Scale, θ_*

The temperature scale for stable conditions is defined as

$$\theta_* = - \frac{H}{\rho_a c_p u_*} \quad \text{Eq. 10-12}$$

and appears in the temperature profile equation given by

$$T - T_0 = \frac{\theta_*}{\kappa} \left[0.74 \ln(z/z_0 + 1) - \Psi_h \right] \quad \text{Eq. 10-13}$$

where T_0 is the temperature at z_0 . We make use of Equation 10-13 only under stable conditions, in which case, $\Psi_h = -4.7z/L$. It should be noted that L can be defined in terms of θ_* and u_* as follows:

$$L = \frac{u_*^2 T}{\kappa \theta_* g} \quad \text{Eq. 10-14}$$

10.1.4 Convective Velocity Scale, w_*

Deardorff (1970) introduced the convective velocity scale, w_* , defined as

$$w_* = \left(\frac{g H z_i}{T \rho_a c_p} \right)^{1/3} \quad \text{Eq. 10-15}$$

as the appropriate scale for convection-dominated turbulence ($L < 0$). It is related to L and u_* by

$$\frac{L}{z_i} = -\frac{u_*^3}{\kappa w_*^3} \quad \text{Eq. 10-16}$$

10.2 Specifying PBL Parameters

Specifying z_0 and u_{ref} is generally straightforward, but other input requirements depend on the PBL calculation mode chosen. There are four standard PBL modes referred to as *SIMPLE*, *METFILE*, *CALCULATED*, and *OPERATIONAL*. A fifth mode, *BLPROFILE*, is used when detailed turbulence profiles, as described in Section 11.1, are available from measurements or modeling. In the *SIMPLE* mode, boundary layer height and surface heat flux are estimated using simple functional forms with user-specified minimum and maximum values. The *METFILE* mode can be used if measurements (or estimates) of z_i and H , or L or stability class (PGT), are available on the meteorology input files. In the *CALCULATED* mode, H is estimated from a surface energy balance model and an evolution equation is solved for z_i . The *OPERATIONAL* mode is intended to use whatever relevant input is given in the meteorological files and is essentially reset to *METFILE* or *CALCULATED* mode accordingly. Therefore, the *METFILE* mode is invoked if z_i and H or L or *PGT* are given, and the *CALCULATED* mode is invoked if none of these variables is given; if either z_i or H is available, the other will be calculated as with the standard *CALCULATED* mode.

The boundary layer mode is specified with the variable *bl_type* in the meteorology scenario file (Section 9.3). *SIMPLE*, *CALCULATED*, or *OPERATIONAL* mode is invoked by setting *bl_type* = 'SBL', 'CALC', or 'OPER', respectively. The *bl_type* string associated with *METFILE* mode depends on the meteorology input type: 'OBS' when using observational input, 'MEDOC' for

MEDOC format gridded input. (See Section 9.3 for a description of various meteorology input file types.) Of course, *OPERATIONAL* mode becomes *METFILE* mode if the meteorology file contains complete boundary layer input. Although not discussed further in this section, the *BLPROFILE* mode is invoked by setting *bl_type* = 'PROF'.

The specification of z_0 and u_{ref} applies to all three modes. The *CALCULATED* mode requires additional inputs, including cloud cover and surface characteristics, as discussed next.

10.2.1 Roughness Height

Roughness length, z_0 , is a parameter related to the height of the roughness elements (that is, trees, buildings, and so on). Suggested roughness heights from Saucier (1987) are given in Table 10-1. SCIPUFF accepts only one roughness height for the entire domain and duration of the run.

Table 10-1
Suggested values for surface roughness (Saucier, 1987)

| z_0 (m) | Surface Description |
|-----------|---|
| 0.0005 | Bare ground, sand dunes, water |
| 0.001 | Nearly barren with low-growing vegetation |
| 0.01 | Grassland, cropland, wetlands |
| 0.05 | Grassland with scattered trees, brushland, scrub growth |
| 0.1 | Deciduous forest, villages, forest clearings |
| 0.5 | Mixed forest, towns, cities |
| 1.0 | Coniferous forest |

10.2.2 Reference Height and Velocity

For the purpose of defining PBL profiles, z_{ref} is taken from the lowest level of the vertical grid. The vertical grid is defined either directly through the gridded meteorology input file as described in Sections 9.3 or constructed from observational profiles as described in Section 9.2. u_{ref} is then the velocity at the lowest grid level after the interpolation procedure (Section 9.4) and mass-consistent adjustment (Section 9.5), if appropriate, are completed.

10.2.3 Surface Heat Flux

The surface heat flux may be specified in three ways, depending on the PBL mode selected:

- *METFILE*: through meteorology input files
- *SIMPLE*: as a simple diurnally varying function with prescribed daytime and nighttime values
- *CALCULATED*: using a surface energy balance model that accounts for solar radiation, cloud cover, and surface characteristics

In the *METFILE* PBL mode, surface heat flux is specified directly (typically in Wm^{-2} units) on the meteorology input file(s). Alternatively, if observation-type meteorology is given, the surface heat flux can be calculated from the Pasquill-Gifford-Turner (PGT) stability class or Monin-Obukhov length. The stability class is indicated on an observation file with a stability index. An

average Monin-Obukhov length is assumed within each stability class according to the scheme described in Sykes and Lewellen (1992). The stability index and the corresponding PGT stability class and Monin-Obukhov length are given in Table 10-2. Stability classes A, B, and C correspond to unstable conditions, D to neutral conditions, and E, F, and G to stable conditions.

The heat flux is then calculated from Equation 10-1 as

$$H = \frac{-u_*^3 T \rho_a c_p}{\kappa g L} \quad \text{Eq. 10-17}$$

Table 10-2
Relationship between stability index, PGT stability class, Monin-Obukhov length, L , and an assumed boundary layer depth, z_i , if not specified as input

| Stability Index | PGT Class | L (m) | z_i (m) |
|-----------------|-----------|---------|-----------|
| 1 | A | -5 | 1000 |
| 2 | B | -12.5 | 1000 |
| 3 | C | -50 | 1000 |
| 4 | D | -1000 | 1000 |
| 5 | E | 25 | 125 |
| 6 | F | 13 | 65 |
| 7 | G | 5 | 25 |

When the *SIMPLE* mode is specified, the surface heat flux is calculated as

$$H = \begin{cases} H_c - (H_d - H_c) \cos\left(\frac{2\pi t_d}{24}\right), & 6 \leq t_d \leq 18 \\ H_c & \text{otherwise} \end{cases} \quad \text{Eq. 10-18}$$

where H_c is the constant nighttime heat flux, H_d is the maximum daytime heat flux, and t_d is the time of day in hours. Typical values of H_c are between zero and -60 Wm^{-2} . H_d can vary widely depending on cloud cover, time of year, surface characteristics, and latitude. For example, on an overcast spring day in northern Russia, H_d might be only 10 Wm^{-2} , while it could be around 200 Wm^{-2} on a summer day in the southwest United States.

In *CALCULATED* mode, SCIPUFF computes the sensible heat flux using a surface energy balance method similar to that used in METPRO (Paine, 1987). The method differs for daytime and nighttime conditions.

10.2.3.1 Daytime Heat Flux Calculation

An analysis of the energy budget at the earth's surface balances the net incoming radiation with the total surface heat flux. This requires the partitioning of the surface heat flux into sensible and latent components. A simple parameterization for such a partition proposed by Holtslag and van Ulden (1983) is

$$H = \frac{(1 - \alpha)s + \gamma}{s + \gamma} (R_n - G) - \alpha\beta' \quad \text{Eq. 10-19}$$

$$L_v E = \frac{\alpha s}{s + \gamma} (R_n - G) + \alpha\beta' \quad \text{Eq. 10-20}$$

where $L_v E$ represents the latent heat flux due to surface evaporation, R_n is the net solar radiation at the earth's surface, G is the soil heat flux, estimated as $0.1R_n$, α is an empirical surface moisture parameter defined next and is related to the Bowen ratio $B = H/L_v E$, β' is an empirical constant set to 20 Wm^{-2} , s is the slope of the saturated vapor-pressure curve, and $\gamma = c_p/L_v$. Here, c_p is the specific heat of air at constant pressure and L_v is the latent heat of water vaporization.

The net radiation is estimated from the total incoming radiation using the method of Holtslag and van Ulden (1983)

$$R_n = \frac{(1 - r)R + c_1 T^6 - \sigma_{SB} T^4 + c_2 n_c}{1 + c_3} \quad \text{Eq. 10-21}$$

where R is the total incoming radiation, r is the surface albedo, n_c is the fractional cloud cover, $c_1 = 5.31 \times 10^{-13} \text{ Wm}^{-2} \text{ K}^{-6}$, $c_2 = 60 \text{ Wm}^{-2}$, $c_3 = 0.12$, and σ_{SB} is the Stefan-Boltzman constant, $5.67 \times 10^{-8} \text{ Wm}^{-2} \text{ K}^{-4}$.

The total incoming solar radiation is a function of solar angle (ζ) and cloud cover and is computed from a formula suggested by Kasten and Czeplak (1980):

$$R = R_0 (1 + b_1 n_c^{b_2}) \quad \text{Eq. 10-22}$$

where R_0 , the incoming radiation for clear skies, is a function of ζ and b_1 and b_2 are empirical constants set to -0.75 and 3.4 , respectively. A simple parameterization for R_0 suggested by Holtslag and van Ulden (1983) is

$$R_0 = a_1 \sin \zeta + a_2 \quad \text{Eq. 10-23}$$

where the empirical constants a_1 and a_2 are set to 990 Wm^{-2} and -30 Wm^{-2} , respectively, based on a survey of values for different northern mid-latitude sites.

The solar angle is determined from

$$\sin \zeta = \sin \lambda \sin \delta + \cos \lambda \cos \delta \cos h \quad \text{Eq. 10-24}$$

where λ is the geographical latitude, δ is the declination, and h is the hour angle (all in radians). Given the approximate nature of these calculations, we follow Holtslag and van Ulden (1983) in using simplified expression for δ and h , rather than the more accurate formulas in Paltridge and Platt (1976), for example. Therefore, δ is given by

$$\sin \delta = 0.398 \sin \sigma_s \quad \text{Eq. 10-25}$$

where σ_s , the solar longitude in radians, is evaluated from

$$\sigma_s = 4.871 + d + 0.033 \sin d \quad \text{Eq. 10-26}$$

and $d = (d_n - 1)2\pi/365.242$, d_n being the Julian day number. The hour angle is given by

$$h = (t - 12)\pi/12 + \phi + 0.043 \sin(2\sigma_s) - 0.033 \sin d \quad \text{Eq. 10-27}$$

where t is universal time in hours and ϕ is the Easterly longitude in radians.

Albedo is relatively constant for solar angles, ζ , above 30° but increases for angles below that. An empirical formula given by Paine (1987) is used to model the variation of surface albedo with solar angle (in degrees):

$$r = r_0 + (1 - r_0)e^{r_1\zeta + r_2} \quad \text{Eq. 10-28}$$

where r_0 is the albedo for the sun directly overhead, $r_1 = -0.1$, and $r_2 = -0.5(1 - r_0)^2$.

As mentioned previously, the surface moisture parameter α is related to B , the Bowen ratio. Because B is a commonly used parameter, α is expressed in terms of B using Equations 10-19 and 10-20 to give

$$\alpha = \frac{(s + \gamma)(R_n - G)}{(1 + B)[s(R_n - G) + \beta'(s + \gamma)]} \quad \text{Eq. 10-29}$$

This completes the description of the sensible heat flux computation in the *CALCULATED* mode. It requires three more input parameters than the other two modes: fractional cloud cover, n_c , surface albedo for the sun directly overhead, r_0 , and Bowen ratio, B . The specification of cloud cover is self-evident. Table 10-3 and Table 10-4 (from Paine, 1987) give suggested values for r_0 and B as functions of land use and season.

In the *CALCULATED* mode, the heat flux may be used in computing the boundary layer depth, as described in Section 10.2.4. It is also used to compute w_* in conjunction with z_i using Equations 10-15 and 10-3. It should be noted that H could be negative just after sunrise or before sunset. In that case, the calculation proceeds as for nighttime, described in the next section.

Table 10-3
Suggested values for surface albedo as a function of land use and season (Paine, 1987)

| Land Use Type | Spring | Summer | Autumn | Winter |
|-------------------|--------|--------|--------|--------|
| Water | 0.12 | 0.10 | 0.14 | 0.20 |
| Deciduous Forest | 0.12 | 0.12 | 0.12 | 0.50 |
| Coniferous Forest | 0.12 | 0.12 | 0.12 | 0.35 |
| Swamp | 0.12 | 0.14 | 0.16 | 0.30 |
| Cultivated Land | 0.14 | 0.20 | 0.18 | 0.60 |
| Grassland | 0.18 | 0.18 | 0.20 | 0.60 |
| Urban | 0.14 | 0.16 | 0.18 | 0.35 |
| Desert Shrubland | 0.30 | 0.28 | 0.28 | 0.45 |

Table 10-4
Suggested values for Bowen ratio as a function of land use and season (Paine, 1987)

| Land Use Type | Spring | Summer | Autumn | Winter |
|-------------------|--------|--------|--------|--------|
| Water | 0.1 | 0.1 | 0.1 | 1.5 |
| Deciduous Forest | 0.7 | 0.3 | 1.0 | 1.5 |
| Coniferous Forest | 0.7 | 0.3 | 0.8 | 1.5 |
| Swamp | 0.1 | 0.1 | 0.1 | 1.5 |
| Cultivated Land | 0.3 | 0.5 | 0.7 | 1.5 |
| Grassland | 0.4 | 0.8 | 1.0 | 1.5 |
| Urban | 1.0 | 2.0 | 2.0 | 1.5 |
| Desert Shrubland | 3.0 | 4.0 | 6.0 | 6.0 |

10.2.3.2 Nighttime Heat Flux Calculation

The method used under stable conditions follows Venkatram (1980), with a first estimate of θ_* based on an empirical equation due to van Ulden and Holtslag (1983):

$$\theta_{*1} = 0.09(1 - 0.5n_c^2), \quad \text{Eq. 10-30}$$

which is independent of u_* and H , although they show that Equation 10-30 is subject to the constraint $-H \leq 60 \text{ Wm}^{-2}$. Further work by Holtslag and de Bruin (1988) shows that θ_* is dependent on u_* , especially at low wind speeds, but that Equation 10-30 gives a reasonable maximum value. The semi-empirical model in Holtslag and de Bruin (1988) is rather complicated and requires more input than is typically available. Therefore, we follow Paine (1987) in defining another estimate of θ_* that depends on u_* :

$$\theta_{*2} = 0.9 \frac{\kappa U_{ref}^2}{4A_m \ln(z_{ref}/z_0)} \quad \text{Eq. 10-31}$$

where $A_m = 4.9$. Although Equation 10-31 is based only on realizability considerations when using Equation 10-7 in Equation 10-3, it does provide a simple, robust estimate for low wind speed conditions. The heat flux is then found iteratively using

$$H = -\min \left\{ \theta_{*1} u_*, \theta_{*2} u_*, [u_* \theta_*]_0, u_*^3 T / \kappa g L_{\min} \right\} \rho_a c_p \quad \text{Eq. 10-32}$$

where $\rho_a c_p$ equals $1200 \text{ Jm}^{-3} \text{ K}^{-1}$, $[u_* \theta_*]_0 = 0.05 \text{ Kms}^{-1}$, and $L_{\min} = 10 z_0$. u_* is initially estimated using Equation 10-3 assuming neutral conditions. Subsequently, L is computed using (10-1), and u_* is recomputed and substituted back into Equation 10-32. This procedure continues until the relative changes in L are less than 0.1%.

It should be noted that the heat flux itself is not of primary importance here. The friction velocity, u_* , is the key quantity because it is used to set the mean velocity profile near the surface, in scaling the turbulence profiles, and in determining the boundary layer height in the *CALCULATED* mode.

10.2.4 Boundary Layer Height

As with the surface heat flux, the planetary boundary layer height may be specified three ways depending on the PBL mode:

- *METFILE*: through meteorology input files
- *SIMPLE*: a simple diurnally varying function with a prescribed daytime maximum and nighttime minimum
- *CALCULATED*: using a model that accounts for convection and shear-stress-induced mixing as well as entrainment of an overlying stable layer

When the *METFILE* PBL mode is used, the boundary layer height can be specified directly on the meteorology input file(s). However, if the PGT class or L is given without specifying a boundary layer height (for observational input only), one will be assumed as follows:

$z_i = 1000 \text{ m}$ under neutral or unstable conditions and $z_i = 5L$ for stable conditions. The assumed boundary layer heights corresponding to the PGT stability classes are shown in Table 10-2.

In the *SIMPLE* PBL, the boundary layer height is given by

$$z_i = \begin{cases} z_i^{(\min)} + \left(z_i^{(\max)} - z_i^{(\min)} \right) \frac{(t-6)}{6} & , 6 \leq t \leq 12 \\ z_i^{(\max)} & , 12 \leq t \leq 18 \\ z_i^{(\min)} & , \text{otherwise} \end{cases} \quad \text{Eq. 10-33}$$

where $z_i^{(\min)}$ and $z_i^{(\max)}$ are the minimum and maximum daily boundary layer depths, respectively. This equation approximates typical daily boundary layer evolution by setting the depth to a minimum value during nocturnal hours, maintaining a linear growth during morning hours, and holding a constant depth during afternoon hours. Typical values for $z_i^{(\min)}$ range from 30 m to 100 m while $z_i^{(\max)}$ might range from 300 m on an overcast day to 2000 m on a sunny summer day.

In *CALCULATED* PBL mode, SCIPUFF computes boundary layer height using the H , u_* , L , and other parameters. Again, the method differs for stable and unstable conditions. However, in both cases, an evolution equation for the boundary layer is integrated in step with the dispersion calculation. This evolution equation is derived by assuming that the top of the boundary layer represents a material surface; that is, there is no fluid transport across this surface and noting that the total derivative of a material surface in a fluid is zero in the absence of source terms. An equation for a material surface in this case is given by $F = z_i - z$, so $DF/Dt = 0$ gives

$$\frac{\partial z_i}{\partial t} = -u \frac{\partial z_i}{\partial x} - v \frac{\partial z_i}{\partial y} + w$$

where the velocity vector (u, v, w) is evaluated at the boundary layer height. To account for boundary layer growth due to thermodynamic (convective) or mechanical mixing, a general source term is added to the right-hand side of the z_i tendency equation, so the final evolution equation becomes

$$\frac{\partial z_i}{\partial t} = -u \frac{\partial z_i}{\partial x} - v \frac{\partial z_i}{\partial y} + w + S_i \quad \text{Eq. 10-34}$$

where the source term S_i is described below for daytime and nighttime conditions.

The utility of Equation 10-34 lies mainly in its smoothing properties, minimizing grid point-to-point variations that might arise from using the source term alone (that is, $\partial z_i / \partial t = S_i$).

Accordingly, and for the sake of computational efficiency, the horizontal advection terms in Equation 10-34 are implemented with first-order upwind differencing using z_i from the previous time step. The equation is updated at every large time step, Δt_L .

10.2.4.1 Daytime Boundary Layer Height Calculation

The dominant mechanism driving the boundary layer growth during daytime is usually entrainment of the overlying air by convective eddies resulting from the surface heat flux. However, during early morning hours, surface shear-stress-induced (mechanical) mixing may be important. The model for S_i includes simple parameterizations of these mechanisms but ignores subsidence, latent heat effects, radiation, and advection.

The boundary layer is assumed to be capped by a thin interfacial layer separating it from the stable air above. The temperature within the boundary layer is assumed to be uniform. The heat

flux at the interfacial region due to entrainment, H_i , is assumed to be proportional to the surface heat flux, following Carson (1973) and Deardorff (1980):

$$H_i = -AH \quad \text{Eq. 10-35}$$

where $A = 0.2$. It can be shown (Carson, 1973) that the local growth rate due to convective mixing is

$$\left(\frac{dz_i}{dt} \right)_{conv} = \frac{(1 + 2A)H}{z_i \Gamma_i \rho c_p} \quad \text{Eq. 10-36}$$

where Γ_i is the potential temperature gradient at z_i .

Mechanical mixing is modeled assuming no surface heat flux and the entrainment flux is given by (Kato and Phillips, 1969)

$$H_i = -B \frac{T u_*^3}{g z_i} \rho c_p \quad \text{Eq. 10-37}$$

where $B = 2.5$. Then, analogous to Equation 10-36, we define

$$\left(\frac{dz_i}{dt} \right)_{mech} = 2B \frac{T u_*^3}{g \Gamma_i z_i^2} \quad \text{Eq. 10-38}$$

SCIPUFF assumes that the two mechanisms are independent and that the stronger one dominates. Therefore,

$$S_i = \max \left[\left(\frac{dz_i}{dt} \right)_{mech}, \left(\frac{dz_i}{dt} \right)_{conv} \right] \quad \text{Eq. 10-39}$$

10.2.4.2 Nighttime Boundary Layer Height Calculation

Under stable conditions, z_i is found from an equation due to Nieuwstadt (1981), which interpolates between Zilitinkevich's (1972) expression for very stable conditions and the neutral case solution of $0.3u_*/f$:

$$\frac{z_{eq}}{L} = \frac{0.3 u_* / f L}{1 + 1.9 z_{eq} / L} \quad \text{Eq. 10-40}$$

which is a quadratic equation for the equilibrium boundary layer height z_{eq} . To avoid unrealistic changes due to sudden changes in u_* or L (during the transition from an unstable to stable boundary layer, for example), a source term that damps toward the equilibrium height is used:

$$S_i = \frac{z_{eq} - z_i}{\tau_{eq}} \quad \text{Eq. 10-41}$$

where the relaxation timescale τ_{eq} is set to 900 s. Although somewhat arbitrary, this value for τ_{eq} is reasonable if we assume that it is equal to z_{eq}/u_* multiplied by an order 1 constant. For typical stable conditions, u_* is on the order of 0.1 to 0.2 m s⁻¹ and z_{eq} ranges from 25 m to 500 m. Lacking a theoretically rigorous way or experimental data to determine τ_{eq} , we have chosen a timescale consistent with these values of u_* and L that provides reasonable temporal smoothing of the numerical integration while ensuring that z_i is not far from the equilibrium height.

10.3 PBL Mean Profiles

The mean velocity profile in the PBL depends on height, especially with respect to the “surface layer height.” The surface layer is the region of the boundary layer next to the surface where the fluxes of momentum and temperature are essentially constant. Here Monin-Obukhov similarity is valid, which implies that the velocity and temperature profiles are functions only of the surface friction velocity u_* , the surface temperature flux H , the surface roughness z_0 , and the normalized height above the surface, z/L . Below z_s , the surface layer height, SCIPUFF uses the similarity profile to determine the mean velocity, that is, $u(z) = (u_*/\kappa)(\ln z/z_0 - \Psi_m)$. The definition of z_s is given by

$$z_s = \alpha_s z_i \tag{Eq. 10-42}$$

where

$$\alpha_s = \begin{cases} 0.1 & L \leq 0 \\ 0.1 + 0.9 \exp(-L/z_i) & L > 0 \end{cases} \tag{Eq. 10-43}$$

The factor of 0.1 for neutral and convective conditions is a rough estimate used by many investigators, for example, Schumann (1988) and Wyngaard (1988). Sykes, Henn, and Lewellen (1993b) show that the surface layer depth under free convection conditions is dependent on surface roughness and can be much less than 10% of the mixed-layer depth. However, the presence of a mean wind is assumed here, and the resulting turbulent energy production by the mean shear will increase the surface layer depth so that the 0.1 factor is a reasonable estimate.

The asymptotic limit for the very stable case is 1, which implies that the surface layer extends over the entire (but typically shallow) boundary layer. Recalling that, under stable conditions, $z \approx L$ represents the height at which shear-driven turbulence production is balanced by turbulence destruction due to the buoyancy flux, it is reasonable to assume that there is no well-mixed outer layer when L is comparable to or less than z_i . The expression in Equation 10-43 gives a surface layer of $0.43z_i$ when $L = z_i$ and $0.84z_i$ when $z_i = 5L$.

The velocity at the top of the surface layer, u_s , is set to u_{ref} if $z_s \leq z_{ref}$; otherwise, it is adjusted according to

$$u_s = u_{ref} \frac{f_{SL}(z_s; z_0, L)}{f_{SL}(z_{ref}; z_0, L)}, \quad z_{ref} < z_s \quad \text{Eq. 10-44}$$

where the surface layer profile function is defined as

$$f_{SL}(z; z_0, L) = \ln \frac{z + z_0}{z_0} - \Psi_m(z/L) \quad \text{Eq. 10-45}$$

and the functional dependence of Ψ_m on height is emphasized. Note that if $z_s \leq z_{ref}$, then z_s is used in Equation 10-3 instead of z_{ref} to calculate u_* . Therefore, z_s must be found iteratively under stable conditions because it depends, through Equation 10-42, on L , which depends on u_* , which in turn may depend on z_s through Equation 10-3.

Figure 10-1 shows a schematic illustration of the idealized wind profiles used in SCIPUFF depending on the relative position of z_{ref} and z_s . Note that if $z_s \leq z_{ref}$, the velocity profile is held constant from z_{ref} down to z_s . Below z_s , the similarity profile is used, that is,

$$u(z) = u_s \frac{f_{SL}(z; z_0, L)}{f_{SL}(z_s; z_0, L)}, \quad z < z_s \quad \text{Eq. 10-46}$$

These examples show a constant velocity over the entire boundary layer above the surface layer. This is the case only if fewer than two upper air levels are located below z_i ; otherwise, the velocity is interpolated from the upper air fields, as described in Section 10.5.

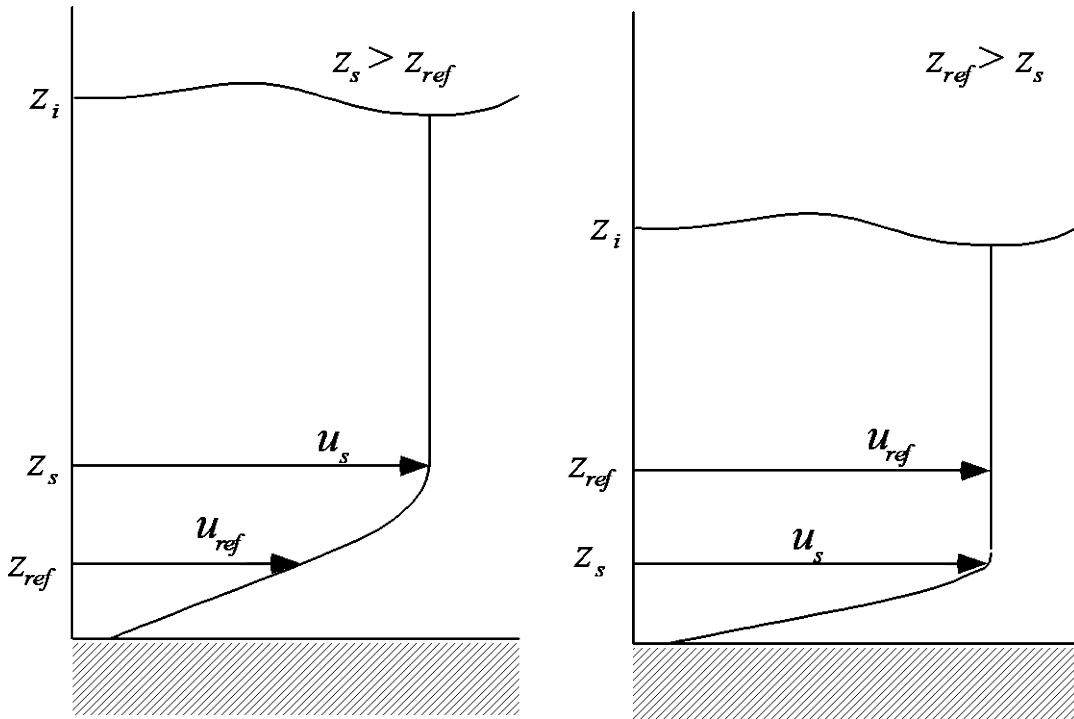


Figure 10-1
Schematic illustration of the idealized velocity profile in the planetary boundary layer

The mean temperature is determined by simple interpolation. Surface similarity is used only in defining the potential temperature gradient, $\partial\bar{\theta}/\partial z$, under stable conditions, where

$$\frac{\partial\bar{\theta}}{\partial z} = \frac{\theta_*}{\kappa} \left(\frac{0.74}{\max(z_s, z_i/2)} + \frac{4.7}{L} \right) \quad \text{Eq. 10-47}$$

The gradient is assumed to be zero for neutral and convective conditions because the temperature is well-mixed except in a thin super adiabatic layer at the surface.

10.4 Vegetative/Urban Canopy Profiles

As part of the surface land-cover description, the detailed profile within a canopy layer can be described. In this context, a canopy is considered an extended layer next to the surface containing a distribution of solid obstacles around which the air must flow. This includes vegetative canopies, such as crops or forests, as well as urban canopies, with collections of buildings forming the flow obstruction.

The canopy parameters are specified on the same surface grid as terrain elevation and include both the canopy height and the canopy flow parameter, which determine the profile shape within the canopy. The velocity profile is assumed to be exponential—this shape has been determined to give a good representation for a wide range of experimental data (Cionco, 1972). The data include both isolated obstacles, such as pegs, in addition to vegetative canopies. In addition, Macdonald et al. (1998) have shown that the exponential profile shape is a reasonably good approximation for moderate building densities in an urban canopy.

The canopy velocity profile is usually given as

$$\mathbf{u}(z) = \mathbf{u}(h_c) f_c(z), \quad \text{for } z \leq h_c \quad \text{Eq. 10-48}$$

where the canopy profile function is

$$f_c(z) = \exp \left[-\alpha_c \left(1 - \frac{z}{h_c} \right) \right] \quad \text{Eq. 10-49}$$

Here, h_c is the canopy height and α_c is the canopy flow parameter. Above the canopy, the velocity profile is as described in Section 10.3 but is shifted upward in the vertical by the displacement height, z_d , so that

$$\mathbf{u}(z) = \mathbf{u}_s \frac{f_{SL}(z - z_d; z_0, L)}{f_{SL}(z_s - z_d; z_0, L)}, \quad h_c \leq z < z_s \quad \text{Eq. 10-50}$$

To provide a smooth transition across the canopy top, the canopy profile and the surface layer profile are blended so that within the canopy we assume

$$u(z) = u(h_c) \left[F_c f_c(z) + (1 - F_c) \frac{f_{SL}(z)}{f_{SL}(h_c)} \right], \quad z \leq h_c \quad \text{Eq. 10-51}$$

where the velocity at the canopy top, $u(h_c)$, is given by Equation 10-50. The “blending” function, F_c , depends on the canopy parameter, α_c , and is given by

$$F_c(\alpha_c) = 1 - \exp\left(-\frac{\alpha_c^2}{\alpha_0^2 + \alpha_0 \alpha_c}\right) \quad \text{Eq. 10-52}$$

where $\alpha_0 = 0.5$. The function F_c varies smoothly from 0 to 1 as α_c increases from zero; it allows the canopy profile to change smoothly into the undisturbed surface layer profile as the canopy parameter tends toward zero. The displacement effect of the canopy is also a function of α_c and is simply modeled as

$$z_d = 0.7 h_c F_c(\alpha_c) \quad \text{Eq. 10-53}$$

giving a limiting displacement of 70% canopy height for a dense canopy.

The final profile shapes are illustrated in Figure 10-2, where they are compared with the experimental data of Cionco (1972).

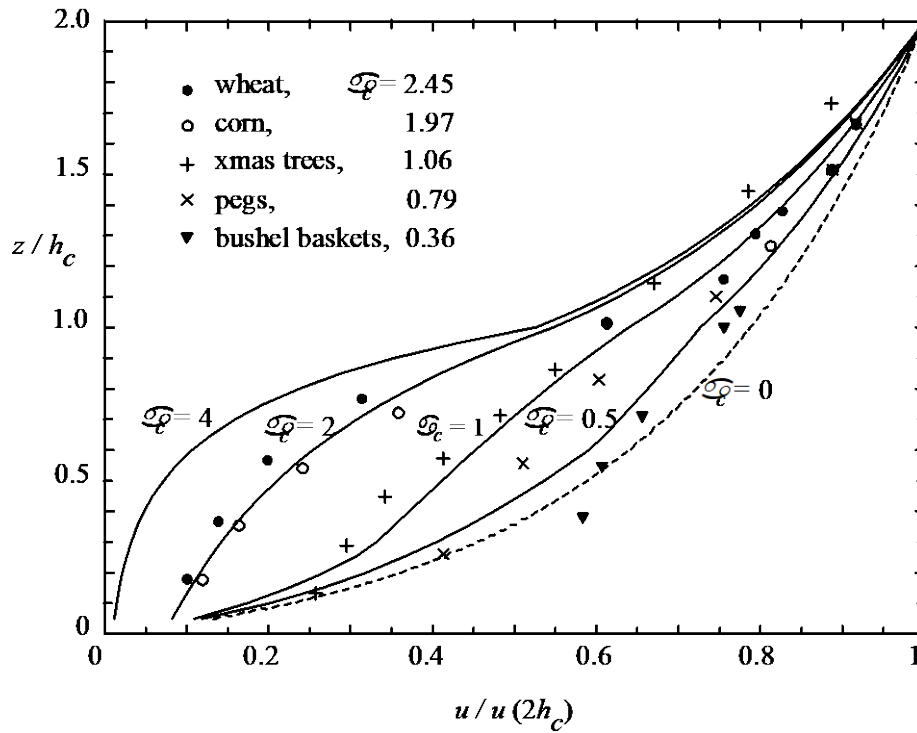


Figure 10-2
Canopy velocity profile shapes from Equations 10-50 and 10-51 compared with the experimental data of Cionco (1972)

10.5 Surface Layer Interpolation

In the course of interpolating wind profiles, both irregularly spaced observations and on regular grids, surface layer shape assumptions are used, as described in Sections 10.3 and 10.4. The procedure is straightforward when the surface characteristics are uniform or differ only slightly; this is described in Section 10.5.1. However, it is often necessary to apply these profile assumptions to locations where the surface characteristics such as canopy height or roughness are substantially different from those of the original profile location. Generally, we consider the surface characteristics to be “substantially different” if the canopy or roughness heights differ by more than 20%. In that case, modifications to the interpolated surface layer profile are necessary, as described in Section 10.5.2.

In the discussion that follows, we will refer to the interpolating profiles with superscripts “(o)”. This may be thought of as denoting “observation” for the case in which irregularly spaced observation profiles are interpolated onto a regular grid using the weights described in Section 9.2 or “outer” in the case in which profiles from an outer domain are interpolated onto a finer “inner” domain using bilinear weights. The interpolated profiles will be indicated with a superscript “(n)” (for “nest,” say).

10.5.1 Homogeneous Land Cover

The vertical interpolation factors must be modified only if either an interpolating or interpolated level is below the surface layer height, $z_s^{(o)}$. (For the case here of homogeneous land cover, we ignore any possible difference in z_s between the interpolating and interpolated points; this is not the case in the next section.) $z_s^{(o)}$ is computed from Equation 10-42, which requires $L^{(o)}$; this in turn requires estimates of heat flux and friction velocity. These quantities will be available at the grid point locations when interpolating onto a nested domain. When interpolating from observations, they are computed using the observed velocity at the lowest level as well as any observed boundary layer information such as sensible heat flux, stability class, and so on. Lacking these, estimates are derived as appropriate using the methods in Sections 10.2.3 and 10.2.4. This process may be iterative because of the relationships between $z_s^{(o)}$, $L^{(o)}$, and $u_*^{(o)}$.

In addition, this process gives an estimate of $u_s^{(o)}$, the velocity at the surface layer height.

However, this estimate may be modified to be consistent with any observations near the surface layer height.

Assume that N interpolating heights are given at $z_k^{(o)}$ where $k = 1, 2, \dots, N$ and the interpolated height is $z^{(n)}$. Note that all heights are relative to the local terrain elevation. For the general case of interpolation between two levels, denoted with subscripts K and $K+1$, we use linear vertical interpolation outside the surface layer. However, a linear profile is not appropriate inside the surface layer, so the interpolation must be modified to account for the surface layer profile shape. In general, the interpolating velocities in the surface layer will not match the idealized velocity profile, $u_k^{(o)} = u_s^{(o)} f_k / f_s$, where $f_k \equiv \mathfrak{F}(z_k^{(o)}; z_0^{(o)}, L^{(o)}, h_c^{(o)}, \alpha_c^{(o)})$ and $f_s \equiv \mathfrak{F}(z_s^{(o)}; z_0^{(o)}, L^{(o)}, h_c^{(o)}, \alpha_c^{(o)})$. Here, \mathfrak{F} is the profile shape function implicit in the surface layer descriptions, given by Equations 10-45, 10-50, and 10-51. Our interpolation procedure,

therefore, is essentially a weighted combination of surface layer profiles extrapolated from the interpolating points, with the weights taken from standard linear interpolation. This is illustrated in Figure 10-3. However, we must account for several possible situations based on the heights $z_K^{(o)}$, $z_{K+1}^{(o)}$, and $z^{(n)}$ relative to $z_s^{(o)}$ as well as $z^{(n)}$ relative to $z_K^{(o)}$. Note that because of the effects of terrain elevation on the interpolation of observations, it is not necessarily true that $z_K^{(o)} \leq z^{(n)} \leq z_{K+1}^{(o)}$. Figure 10-3 illustrates an example of surface layer interpolation.

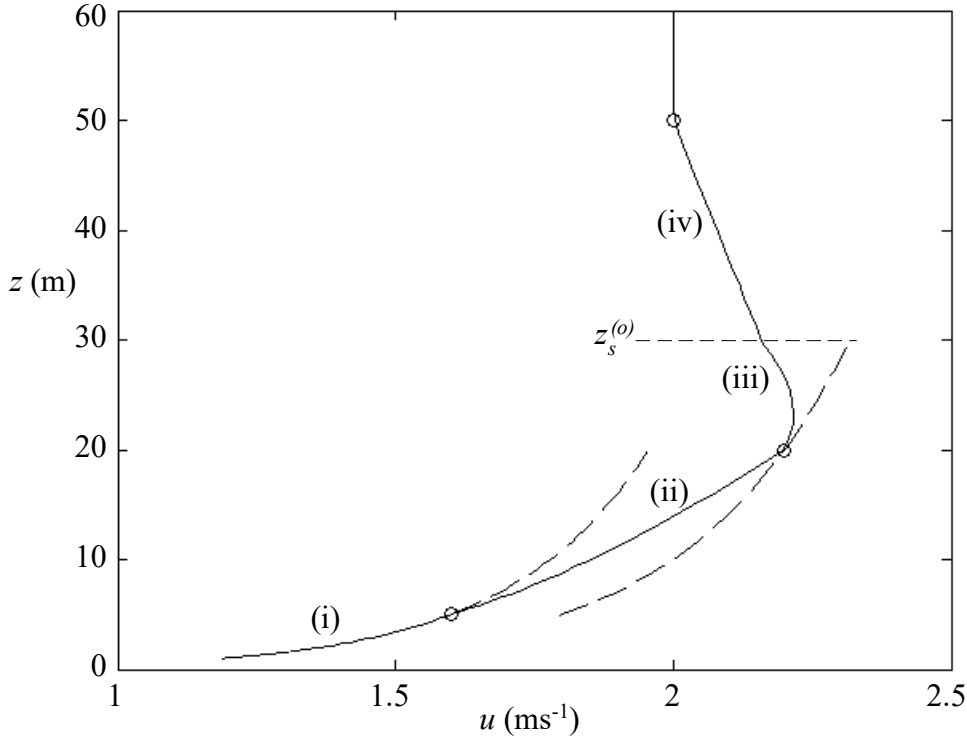


Figure 10-3

Example of surface layer interpolation. Open circles indicate observation or outer domain velocities used for interpolation. The solid line is the interpolated velocity profile. The long dash lines are surface layer profiles scaled to pass through the interpolating points below the surface layer height $z_s^{(o)}$. Sections of the interpolated profile are labeled with the corresponding cases (i)–(iv) from the text.

Several height combinations require special interpolation modifications near the surface layer. In the case of flat or no terrain, there are four distinct situations, numbered (i) through (iv) and illustrated in Figure 10-3. Note that (i) covers the typical cases requiring extrapolation, for example, the interpolation height is above or below all observation levels, including the special case of $N = 1$. Other cases arise in the presence of terrain because of the interpolation rules accounting for elevation differences, as previously noted, and are discussed below.

(i) Interpolated height is outside (above or below) the range of the interpolating heights, that is, $z^{(n)} \leq z_1^{(o)}$ or $z^{(n)} \geq z_N^{(o)}$, $z_N^{(o)} < z_s^{(o)}$. Use surface layer profile to extrapolate:

$$\begin{aligned} \mathbf{u}^{(n)} &= \mathbf{u}_1^{(o)} f_z / f_1 & z^{(n)} &\leq z_s^{(o)} \\ \mathbf{u}^{(n)} &= \mathbf{u}_s^{(o)} & z^{(n)} &> z_s^{(o)} \end{aligned}$$

Note that if $z^{(n)} > z_N^{(o)} \geq z_s^{(o)}$ then $\mathbf{u}^{(n)} = \mathbf{u}_N^{(o)}$.

(ii) Interpolated height is between interpolating levels K and $K+1$, both inside the surface layer, that is, $z_K^{(o)} \leq z^{(n)} \leq z_{K+1}^{(o)}$, $z_{K+1}^{(o)} < z_s^{(o)}$. Use weighted average of the two surface layer profiles through the interpolating points:

$$\mathbf{u}^{(n)} = f_z \left[\frac{(z_{K+1}^{(o)} - z^{(n)})}{f_K} \mathbf{u}_K^{(o)} + \frac{(z_K^{(o)} - z^{(n)})}{f_{K+1}} \mathbf{u}_{K+1}^{(o)} \right] / (z_{K+1}^{(o)} - z_K^{(o)})$$

(iii) Interpolated height is inside the surface layer and between interpolating levels K and $K+1$, but the upper interpolating level is outside the surface layer, that is, $z_K^{(o)} \leq z^{(n)} \leq z_{K+1}^{(o)}$, $z_K^{(o)} < z_s^{(o)} \leq z_{K+1}^{(o)}$, $z^{(n)} < z_s^{(o)}$. Use weighted average of surface layer profiles through lower interpolating point and the surface layer height:

$$\mathbf{u}^{(n)} = f_z \left[\frac{(z_s^{(o)} - z^{(n)})}{f_K} \mathbf{u}_K^{(o)} + \frac{(z_K^{(o)} - z^{(n)})}{f_s} \mathbf{u}_s^{(o)} \right] / (z_s^{(o)} - z_K^{(o)})$$

(iv) Interpolated height is outside the surface layer and between interpolating levels K and $K+1$, but the lower interpolating level is inside the surface layer, that is, $z_K^{(o)} \leq z^{(n)} \leq z_{K+1}^{(o)}$, $z_K^{(o)} < z_s^{(o)} \leq z_{K+1}^{(o)}$, $z^{(n)} \geq z_s^{(o)}$. Use weighted average of upper interpolating point and surface layer height:

$$\mathbf{u}^{(n)} = \left[(z_{K+1}^{(o)} - z^{(n)}) \mathbf{u}_s^{(o)} + (z^{(n)} - z_s^{(o)}) \mathbf{u}_{K+1}^{(o)} \right] / (z_{K+1}^{(o)} - z_s^{(o)})$$

The surface layer profile functions at the interpolated and interpolating levels are defined as $f_z \equiv \mathfrak{I}(z^{(n)}; z_0^{(o)}, L^{(o)}, h_c^{(o)}, \alpha_c^{(o)})$, $f_K \equiv \mathfrak{I}(z_K^{(o)}; z_0^{(o)}, L^{(o)}, h_c^{(o)}, \alpha_c^{(o)})$, and similarly for f_{K+1} .

The presence of terrain introduces further complexity because the interpolation rules account for differences in elevation between the interpolated location and the interpolating point. The choice of interpolating levels is based on the higher of the interpolated height above the local terrain or the height above the interpolating terrain. The effect is to use elevated observation levels when interpolating from a low-lying observation onto an elevated location. The surface layer profile shapes at the interpolating and interpolated locations are still used to estimate the velocity profile behavior.

10.5.2 Inhomogeneous Land Cover

The surface layer interpolation described previously must be modified if the surface characteristics at the interpolation point differ substantially from the points used for the interpolation. This is especially critical in the region most affected by the specific canopy or roughness of the points involved. We define a canopy influence height basically as twice the maximum canopy height at the interpolation point:

$$Z_{2h} = 2 \times \max(h_{eff}^{(o)}, h_c^{(n)}, 10z_0^{(n)})$$

where $h_{eff}^{(o)}$ is an effective canopy height that accounts for the influence of the canopy at neighboring points. The factor of 10 on the roughness height $z_0^{(o)}$ is based on a rule of thumb that the effective roughness height is approximately 1/10 of the canopy height.

For the case of interpolating observations, $h_{eff}^{(o)}$ is simply $\max(h_c^{(o)}, 10z_0^{(o)})$ at the observation location. Note that a canopy height is associated with an observation only if it is explicitly defined in the observation input file (see Section 15.2.1). For the (typical) case in which no such information is available, $h_c^{(o)} = 0$ is assumed even if a canopy height is nominally defined either as a user-specified uniform value (h_{cnp} in Section 15.1.4) or from terrain file input (Section 15.2.5). In these cases, $z_0^{(o)} = h_c^{(o)}/10$ will be used. ($z_0^{(o)}$ can also be specified explicitly for an observation; see Section 15.2.5.)

For interpolation onto a nested domain,

$$h_{eff}^{(o)} = \max[h_c^{(o)}(x, y), \beta h_c^{(o)}(x', y')]$$

where

$$\beta = \min\left\{1, \max\left[0, 1.5\left(1 - \sqrt{x'^2 + y'^2} / R_{eff}\right)\right]\right\}$$

and (x, y) is the horizontal location of the interpolating grid point, (x', y') is a location relative to (x, y) , and R_{eff} is the effective radius of influence at $(x + x', y + y')$. R_{eff} is set to 10 times the canopy height (at a grid point) for area densities greater than 0.25, with a linear decrease for smaller values.

Given the surface inhomogeneity, it is necessary to estimate surface layer parameters at the interpolation point: $z_s^{(n)}$, $L^{(n)}$ and $u_*^{(n)}$. This is done as for the homogeneous case, although we use $u_s^{(o)}$ (horizontally interpolated or from the observation location) as a reference velocity. We also avoid using velocities $u_k^{(o)}$ at levels within or just above the canopy (if it exists) because the large gradients in the canopy profile may result in unrealistically large velocities. Accordingly, we define the height Z_c as the lowest interpolation height $z^{(n)}$ that exceeds $1.25 h_c^{(o)}$. ($Z_c = 0$ if $h_c^{(o)} = 0$ or the lowest level of $z^{(n)}$ exceeds $1.25 h_c^{(o)}$.) The profile modifications affect levels only below Z_{2h} . The basic idea is to rescale the profile to account for the different shape due to the different land characteristics, that is, by a factor $f_z^{(n)} / f_z^{(o)}$ where the superscripts indicate which surface layer parameters are used: $f_z^{(n)} \equiv \mathfrak{F}(z^{(n)}; z_0^{(n)}, L^{(n)}, h_c^{(n)}, \alpha_c^{(n)})$ and $f_z^{(o)} \equiv \mathfrak{F}(z^{(n)}; z_0^{(o)}, L^{(o)}, h_c^{(o)}, \alpha_c^{(o)})$. However, to ensure that the results match the homogeneous results at Z_{2h} , we set

$$\mathbf{u}^{(n)} = \mathbf{u}_o^{(n)} \frac{f_z^{(n)}}{f_z^{(o)}} \frac{f_{2h}^{(o)}}{f_{2h}^{(n)}}, \quad z^{(n)} < Z_{2h}$$

If $Z_c > 0$, we use a simple local surface layer shape function below Z_c , that is,

$$\mathbf{u}^{(n)} = \mathbf{u}_c^{(n)} \frac{f_z^{(n)}}{f_c^{(n)}}, \quad z^{(n)} < Z_c$$

where $\mathbf{u}_c^{(n)} \equiv \mathbf{u}^{(n)}(Z_c)$ and $f_c^{(n)} \equiv \mathfrak{F}(Z_c; z_0^{(n)}, L^{(n)}, h_c^{(n)}, \alpha_c^{(n)})$

A schematic illustration of the interpolation from a profile at a location with no canopy to an interpolated location with a canopy is shown in Figure 10-4.

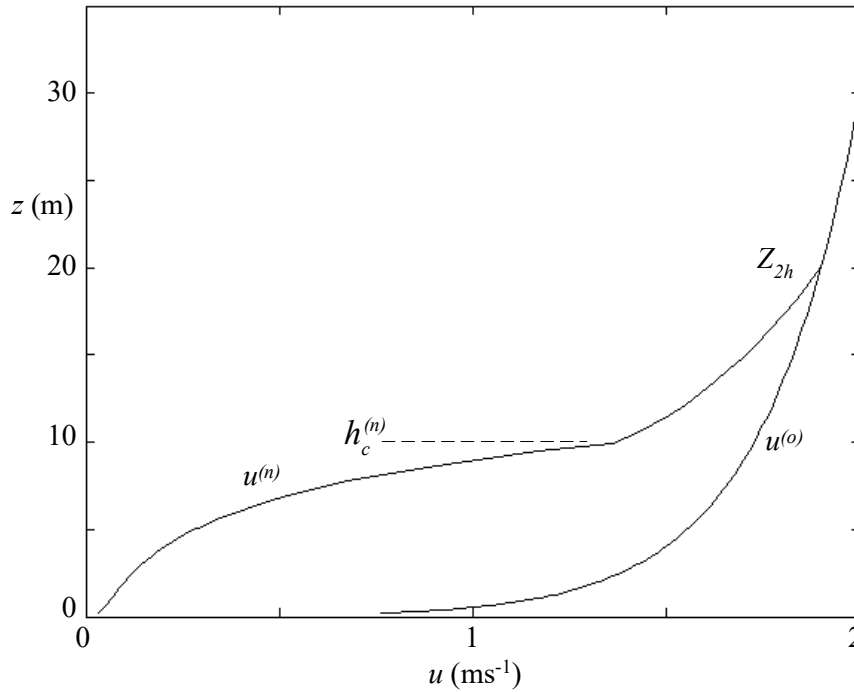


Figure 10-4

Example of surface layer interpolation for inhomogeneous land cover. This example shows how an idealized surface layer profile with no canopy is interpolated to a location where $h_c^{(n)} = 10$ m and $\alpha_c^{(n)} = 3$.

Although these adjustments to the velocity profiles apply to interpolation from observations or gridded fields, a similar adjustment may be required to the original gridded velocity fields themselves if the canopy influence height Z_{2h} from a user-specified uniform canopy is greater than the height of the lowest grid level. Note that this applies only if neither canopy height nor roughness height is specified for the gridded fields (see Section 15.2.2). In that case, a simple canopy profile (without stability effects) is used to extract velocities down from the lowest grid level greater than Z_{2h} .

11

TURBULENCE SPECIFICATION

11.1 Planetary Boundary Layer

The small-scale turbulence of the PBL is typically described analytically in terms of surface heat and momentum fluxes. However, SCIPUFF can use measured turbulence profiles through the observational meteorology input format in conjunction with the *BLPROFILE* boundary layer mode. In that case, all the profiles described in this section, $\overline{u'_2 u'_2}_S$, $\overline{u'_2 u'_2}_B$, $\overline{u'_3 u'_3}_S + \overline{u'_3 u'_3}_B$, Λ_S , Λ_B , and $\overline{w' \theta'_B}$, must be given on the observation input file.

There are two idealized situations in which turbulence profiles are well understood: neutral conditions and free convection conditions. In neutral flow, the surface heat flux is zero or is at least negligible in comparison with the mechanical shear effects. Free convection occurs under very light wind conditions with a positive surface heat flux, and the turbulence is proportional to the convective velocity scale, w_* . For the idealized situations, we can represent the vertical profiles of the turbulence velocity correlations using analytic shape functions as

$$\overline{u'_i u'_j}_S = u_*^2 F_{ij}(z/z_i) \quad \text{Eq. 11-1}$$

for the shear-driven component and

$$\overline{u'_i u'_j}_B = w_*^2 G_{ij}(z/z_i) \quad \text{Eq. 11-2}$$

for the buoyancy-driven component. Note that we use only the lateral ($i = 2, j = 2$) and vertical ($i = 3, j = 3$) components of the boundary layer velocity fluctuations in the closure model described in Section 2.1.3.

Neutral profiles are relatively close to simple linear functions. Wind tunnel studies of the aerodynamic boundary layer (Klebanoff, 1955; Townsend, 1976) and numerical calculations of the neutral Ekman layer (Spalart, 1989; Mason and Thompson, 1987) both support velocity variance profiles proportional to $(1 - z/z_i)$. Appropriate dimensionless profiles are

$$\begin{aligned} F_{22} &= 2.5(1 - z/z_i) \\ F_{33} &= 1.5(1 - z/z_i) \end{aligned} \quad \text{Eq. 11-3}$$

Free convection profiles are available from the laboratory experiments of Deardorff (1970) and large eddy simulation (LES) calculations (Mason, 1989; Schmidt and Schumann, 1989). A reasonably good representation is provided by the expressions

$$\begin{aligned} G_{22} &= 0.13(1 + 1.5e^{-z/z_i}) \\ G_{33} &= 1.1(z/z_i)^{2/3}(1.05 - z/z_i) \end{aligned} \quad \text{Eq. 11-4}$$

These representations approximate the boundary layer turbulence profiles under idealized conditions. In general, the boundary layer is characterized by a spectrum of turbulence energy over a range of eddy scales. This spectrum is modeled as made up of two distinct turbulence populations both governed by the Kolmogorov $k^{-5/3}$ law: shear-driven, near-surface turbulence with energy given by Equation 11-3, and convection-driven turbulence with energy given by Equation 11-4. The latter type of turbulence is characterized by large eddies on the scale of the mixed-layer depth, so a characteristic length scale for the horizontal components of the buoyancy-driven turbulence is

$$\Lambda_B = 0.3 z_i \quad \text{Eq. 11-5}$$

The appropriate length scale for the shear-driven turbulence is related to distance from the surface and is modeled very simply as

$$\frac{1}{\Lambda_s^2} = \frac{1}{(0.3 z_i)^2} + \frac{1}{(0.65 z)^2} \quad \text{Eq. 11-6}$$

providing a transition from the linear behavior near the surface to a constant value in the mixed layer. The vertical length scale, Λ_V , is equal to Λ_s . For stable conditions, the convective velocity scale is zero and only the neutral profile shape (Equation 11-3) with scale (Equation 11-6) should be used. However, the surface friction velocity will generally be reduced by the presence of stable stratification near the surface. In practice, the dispersion model uses the lateral component, $\overline{u_2'^2}$, for both horizontal components because we do not account for the cross-correlation for the boundary layer turbulence and the lateral dispersion is most important in actual applications.

Numerous experimental measurements and LES have shown that the heat flux profile can be represented as a linear function

$$\overline{w'\theta'_B} = H_0 (1 - z/z_i) \quad \text{Eq. 11-7}$$

These turbulence specifications are all based on boundary layer parameters and are valid only within the surface-driven boundary layer, that is, $z \leq z_i$. For situations in which the plume is released above the surface boundary layer, the turbulence conditions must be specified differently. At present, turbulence conditions in the stable atmosphere above the boundary layer are poorly understood, so we can only suggest a very crude representation. A typical value for the vertical velocity variance, $\overline{w_B'^2}$, is $0.01 \text{ m}^2\text{s}^{-2}$, and a typical vertical length scale, Λ_V , is 10 m. We suggest using these values for all locations above the boundary layer. The equilibrium vertical diffusivity implied by these values depends on the stability, but if we assume a Brunt-Vaisala frequency of 10^{-2}s^{-1} in Equation 2-32, we obtain a diffusivity of $0.39 \text{ m}^2/\text{s}$. This value is consistent with the results of Rosenberg and Dewan (1974), who analyzed the stability characteristics of detailed vertical profiles in the lower stratosphere and suggested an average effective diffusivity of $0.4 \text{ m}^2/\text{s}$ due to intermittent wave breaking in regions of shear and low Richardson number—and is also consistent with the turbulence spectrum analysis of Lilly et al. (1973). We note that these results are large-scale average results for the upper atmosphere and

that although the model diffusivity will depend on the local stability, there is significant uncertainty in the local variation of vertical velocity variance and length scale—especially near the surface.

The horizontal fluctuations are more difficult to specify because horizontal motions in a stably stratified fluid can persist long after their generation by flow over terrain or wave-breaking events. Hanna (1983) and Etling (1990) discuss some of the possible mechanisms for horizontal meandering under stable conditions and show that there is typically a root mean square (RMS) lateral velocity fluctuation between 0.5 ms^{-1} and 1 ms^{-1} , even under very light wind conditions. The timescales of these fluctuations indicate a horizontal length scale of the order of 1000 m. We therefore suggest that horizontal velocity variances, $\overline{u_B'^2}$ and $\overline{v_B'^2}$, be taken as $0.25 \text{ m}^2\text{s}^{-2}$ and the horizontal scale, Λ_B , as 1000 m outside the boundary layer.

In the standard application of the model, the stable value for the horizontal velocity variance is used as a minimum for the boundary layer values. If the surface generation mechanisms imply a smaller variance, a secondary component is added to the B -component with the stable length scale and the composite length scale is calculated as the energy-weighted average of the two scales.

11.2 Vegetative/Urban Canopy Layer

In conjunction with the velocity profile assumptions for the vegetative/urban canopy layer in Section 10.4, we also specify modified profiles for turbulence quantities. Experimental observations of turbulence profiles within either vegetative or urban canopies are limited (Raupach et al., 1986; Baldocchi and Meyers, 1988; Shaw et al., 1988; Amiro, 1990; Brunet et al., 1994), and the summary by Raupach et al. (1996) displays significant scatter. One of the simplest assumptions for the profile shape is that it is similar to the velocity profile. Therefore, we assume

$$\overline{v'^2}_s = f_c(z) u_*^2 F_{22}(0), \quad z < h_c \quad \text{Eq. 11-8}$$

where the canopy turbulence profile function, f_c , is the same as the velocity profile function, given by Equation 10-49. The use of the velocity shape factor implies that the turbulence intensity will increase as the canopy flow parameter, α_c , increases because the intensity involves the square root of the shape factor. The same reduction factor is applied to all boundary layer scale turbulence components within the canopy layer, that is,

$$\overline{v'^2}_B = f_c(z) w_*^2 G_{22}\left(\frac{z}{z_i}\right), \quad z < h_c \quad \text{Eq. 11-9}$$

$$\overline{w'^2} = f_c(z) \left(u_*^2 F_{33}(0) + w_*^2 G_{33}\left(\frac{z}{z_i}\right) \right), \quad z < h_c \quad \text{Eq. 11-10}$$

11.3 Mesoscale/Synoptic Scale

Large-scale variability is assumed to be constrained to the horizontal plane with no vertical heat flux or length scale. Therefore, the only parameters needed for large-scale characterization are the velocity fluctuation correlations $\overline{u_L'^2}$, $\overline{v_L'^2}$, and $\overline{u_L'v_L'}$ and the horizontal length scale Λ_{HL} . These parameters can be specified by model, as meteorological input, or as direct input.

The large-scale variability model used in SCIPUFF is based on research by Nastrom and Gage (1985) and a theoretical model proposed by Gifford (1988). Nastrom and Gage analyzed GASP (Global Atmospheric Sampling Program) wind data and showed a clear spectral break at a horizontal wavelength of about 400 km, with k^{-3} spectrum at longer wavelengths and $k^{-5/3}$ for shorter scales. Gifford argues that the large-scale behavior is consistent with the predictions of two-dimensional turbulence theory, while the $k^{-5/3}$ behavior indicates three-dimensional motions in that part of the spectrum.

We assume that the upper troposphere data are representative of the entire lower atmosphere, although there is probably some vertical variation. However, no data presently exist to define these fluctuation profiles, so the simplest assumption is made. Furthermore, the GASP data represent long-term averages and cannot provide any relationship between the local meteorological conditions and the local smaller scale velocity fluctuations. Use of the GASP data is therefore equivalent to a climatologically averaged spectrum. Using Gifford's suggestions and the GASP profiles, which show an increase in fluctuation variance toward the poles, the horizontal velocity variance is represented as

$$\overline{u_T'^2} = \overline{v_T'^2} = \begin{cases} \varepsilon_T / (f_0 \cos \theta), & |\theta| < 75^\circ \\ \varepsilon_T / (f_0 \cos 75^\circ), & |\theta| \geq 75^\circ \end{cases} \quad \text{Eq. 11-11}$$

where θ is the latitude, f_0 is twice the rotation rate of the earth, and ε_T is the average tropospheric energy dissipation rate. A value of $\varepsilon_T = 4 \times 10^{-4} \text{ m}^2 \text{ s}^{-3}$ is suggested by Gifford, but the inverse cosine variation is an empirical factor to provide a match with the latitudinal variation observed in the GASP data. The turbulence length scale associated with these dissipative fluctuations is taken to be

$$\Lambda_T = \left(\overline{u_T'^2} + \overline{v_T'^2} \right)^{1/2} f^{-1} \quad \text{Eq. 11-12}$$

where f is the Coriolis parameter, defined as

$$f = f_0 \times \begin{cases} \sin |\theta|, & |\theta| > 15^\circ \\ \sin 15^\circ, & |\theta| \leq 15^\circ \end{cases} \quad \text{Eq. 11-13}$$

The limit of 15° is necessary to avoid the singularity in the definition of Λ_T .

The velocity variance used in the dispersion calculation depends on the resolution of the input wind fields because the turbulence input represents only the unresolved component of the wind.

We therefore define a filter scale, Λ_G , obtained from the wind-field grid spacing ($\Delta x_G, \Delta y_G$) as $\Lambda_G = 1.4\sqrt{\Delta x_G^2 + \Delta y_G^2}$, then

$$\Lambda_{HL} = \min(\Lambda_G, \Lambda_T) \quad \text{Eq. 11-14}$$

and

$$\overline{u_L'^2} = \overline{u_T'^2} \left(\frac{\Lambda_{HL}}{\Lambda_T} \right)^{2/3} \quad \text{Eq. 11-15}$$

consistent with a $k^{-5/3}$ spectral behavior. The cross-correlation, $\overline{u'v'_L}$, is assumed to be zero in the model.

The large-scale variability parameters, $\overline{u_L'^2}$, $\overline{v_L'^2}$, $\overline{u'v'_L}$, and Λ_{HL} , can also be specified explicitly or read from the *SURFACE* and/or *PROFILE* observation files if available. Only the velocity variances can be read from the observation file; the turbulence length scale must be given explicitly. Velocity variances read from observation files are interpolated in the same fashion as the mean fields; see Section 9.4.

Near the surface, the large-scale velocity variances behave similarly to the mean wind and are therefore scaled using the velocity profile shape functions. The variances are reduced from the free atmosphere values within the surface layer, using the surface layer shape function, f_{SL} . Within a surface canopy layer, the additional reduction due to the canopy profile function is also incorporated.

11.4 Meteorological Uncertainties

Characterizing the state of the atmosphere always entails a degree of uncertainty. Even assuming that “perfect” measurements or gridded analysis fields are available, there is uncertainty in interpolating to other locations and times. Of course, numerical weather predictions grow more uncertain with forecast time, even when starting from accurate initial conditions. Characterizing the meteorological uncertainty depends on several factors—including the data quality, spatial and temporal separation from observations or calculation points, and features of a particular locale such as terrain or proximity to water bodies that may induce quasi-deterministic flows. However, a full treatment of these factors is beyond our current capabilities. Here we attempt only to make plausible quantitative estimates of the uncertainties inherent in meteorological data that can be used within the probabilistic framework of SCIPUFF. The general idea is to treat uncertainty in a fashion similar to large-scale variability. The farther away in time or space from an observation or grid location, the greater the inherent uncertainty or variance, with the asymptotic limit being the climatological variance. If suitable statistics characterizing the uncertainty of the meteorological input are available, these may be used directly through the observation file format. Some examples might be error estimates generated by numerical models as a function of space and time or long-term wind statistics given in terms of means and variances. However, this information is rarely available; therefore, we must construct appropriate models of meteorological uncertainty.

Studies on error growth in numerical weather prediction models, for example, Leith (1978), have generally found that the RMS error-doubling time is about 2 to 3 days, assuming small initial errors, with a shorter time appropriate for a null model or persistence assumption—that is, no changes from the initial state. So, in the case of forecast models, we make a crude estimation of error growth using a function that interpolates between rapid error growth on the timescale of a few days and slow asymptotic growth to the climatological variance:

$$E_u(t) = f_E(t, \tau_{fc}) E_u^\infty + (1 - f_E) E_u^0 \quad \text{Eq. 11-16}$$

where E_u is the error variance for the east-west wind component, E_u^0 is the initial error, E_u^∞ is the climatological variance, and τ_{fc} is a timescale appropriate to error growth in numerical forecast models (which we set to 3 days). Here, t is time from an initial analysis time (which is assumed to be the first time in a gridded meteorology input file or specified in the header information of a special PROFILE file). The S-shaped interpolating function f_E is given by

$$f_E(t, \tau) = 1 - \exp\left(-\frac{t^2}{\tau(\tau + t)}\right) \quad \text{Eq. 11-17}$$

Error growth under the assumption of persistence is modeled with the same functional form as Equation 11-16 but with a timescale of $\tau_{ps} = 1.5$ days. The normalized error growth curves for forecast and persistence models, that is, function f_E evaluated with τ_{fc} and τ_{ps} , are shown in Figure 11-1.

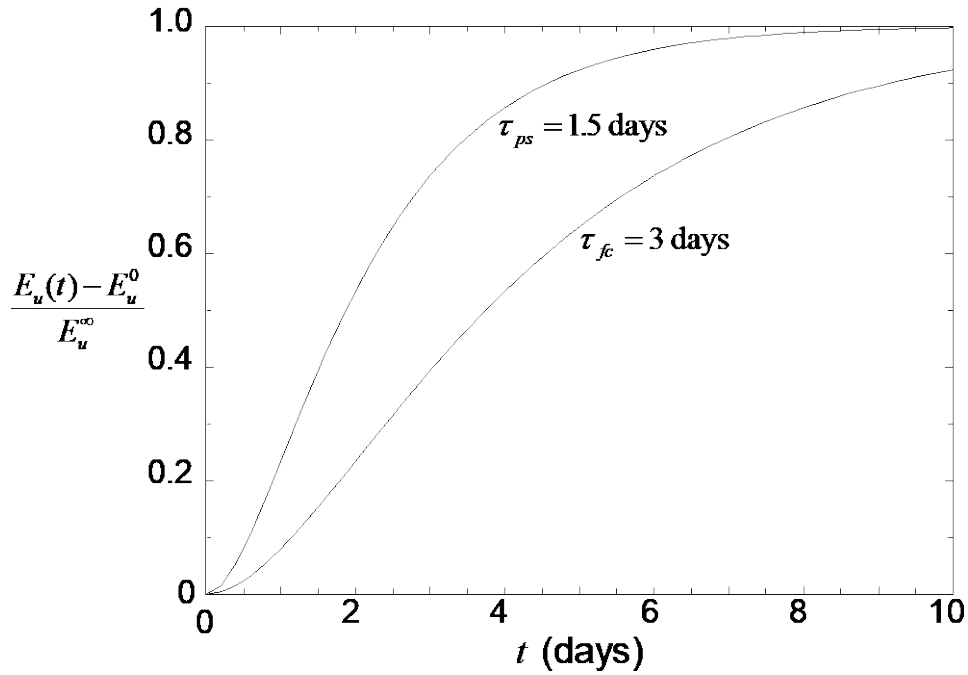


Figure 11-1
Normalized error variance growth for forecast and persistence assumptions

Separate calculations analogous to Equation 11-16 of the north-south velocity variance E_v and uv -correlation E_{uv} are made if the corresponding climatological values E_v^∞ and E_{uv}^∞ are available. SCIPUFF uses a climatology database containing E_u^∞ , E_v^∞ , and E_{uv}^∞ as functions of latitude, longitude, altitude, month, and time of day. Linear interpolation to the meteorology input grid and time is then employed. If the database is not available, we set $E_v^\infty = E_u^\infty$ and $E_{uv}^\infty = 0$ and assume a linear variation in E_u^∞ from the surface to the top of the troposphere:

$$E_u^\infty = E_{BL}^\infty + \min\left(1 - \frac{z_{trop} - z}{z_{trop}}, 0\right)(E_{Trop}^\infty - E_{BL}^\infty) \quad \text{Eq. 11-18}$$

where E_{BL}^∞ and E_{Trop}^∞ are values typical of the atmospheric boundary layer and tropopause, respectively, and $z_{Trop} = 10000$ m represents the top of the troposphere. We tentatively set $E_{BL}^\infty = 5 \text{ ms}^{-1}$ and $E_{Trop}^\infty = 12 \text{ ms}^{-1}$ based on an analysis of wind fields from the National Meteorological Center's Nested Grid Model for North America (Sykes et al., 1993c).

A length scale Λ_E is also associated with the meteorological uncertainty. Again, the functional form of Equation 11-16 is used so that Λ_E is found from an interpolation between the climatological value Λ_E^∞ and the initial length scale $\Lambda_E^0 = \min(\Lambda_G, \Lambda_E^\infty)$. The climatology length scale is determined as a function of the total variance and altitude. Based on the discussion in Section 11.3, we use a $k^{-5/3}$ assumption to extend the Gifford spectrum and set a climatological length scale representative of the troposphere as

$$\Lambda_0^\infty = \Lambda_T \left[\frac{\frac{1}{2}(E_u^\infty + E_v^\infty)}{u_T'^2} \right]^{3/2} \quad \text{Eq. 11-19}$$

However, we expect shorter length scales near the surface, especially below the mixed-layer height. Therefore, we set Λ_E^∞ by interpolating between Λ_0^∞ and a length scale Λ_{BL}^∞ representative of the atmospheric boundary layer:

$$\Lambda_E^\infty = \alpha_\Lambda \Lambda_{BL}^\infty + (1 - \alpha_\Lambda) \Lambda_0^\infty \quad \text{Eq. 11-20}$$

where

$$\alpha_\Lambda = \frac{1}{1 + \max(z - z_{BL}, 0)/\Delta z_{BL}} \quad \text{Eq. 11-21}$$

We tentatively set $\Lambda_{BL}^\infty = 100 \text{ km}$ based on a case study using observational data from a 365-day period over the Korean peninsula. We choose $z_{BL} = 1000 \text{ m}$ as a representative mixed-layer height and a “transition” depth of $\Delta z_{BL} = 200 \text{ m}$.

The initial variance is found by scaling the climatological variance down to the initial length scale.

$$E_u^0 = \left(\frac{\Lambda_E^0}{\Lambda_E^\infty} \right)^{2/3} E_u^\infty \quad \text{Eq. 11-22}$$

with E_v^0 and E_{uv}^0 determined similarly.

A slight modification to Equation 11-16 is required when t is beyond the last available forecast time because the variance grows up to that time on the timescale τ_{fc} , while it subsequently grows on the timescale τ_{ps} . In this case, we have

$$E_u(t) = f_E(t - t_{fc}, \tau_{ps}) E_u^\infty + (1 - f_E) E_u(t_{fc}) \quad \text{Eq. 11-23}$$

where t_{fc} is the last forecast time (relative to the analysis time) and $E_u(t_{fc})$ is found from Equation 11-16. Similar modifications are made for Λ and E_v as well as E_{uv} , if appropriate.

Note that Equations 11-16 or 11-23 are applied at grid locations. When interpolating to puff centroids, an additional variance should be included to account for the uncertainty due to subgrid motions, but this effect is probably small and currently ignored.

Modeling the uncertainty associated with observational meteorology is conceptually similar, but we also include spatial separation from the “nearest” observation location. Here, we work on a three-dimensional grid that is generally of finer resolution than the one described in Section 9.1 for the mean field interpolation. The observation nearest to any location on this grid is taken to be the one that produces the greatest weight as defined in Section 9.2. The weight is then converted into a horizontal distance based on Section 9.3 so that

$$r_{\min}^2 = a^2 (w_{\max}^{-1} - 1) \quad \text{Eq. 11-24}$$

where the core radius a is defined as in Section 9.2 using the finer grid spacing. w_{\max} is the maximum weight from the *SURFACE* or *PROFILE* observations (but is never greater than unity) and is a function of horizontal separation, vertical separation, and possibly temporal separation as given by Equation 9-6. We then use r_{\min} and Λ_E^∞ in f_E to estimate the uncertainty variance on the grid as

$$E_u^0 = f_E(r_{\min}, \Lambda_E^\infty) E_u^\infty \quad \text{Eq. 11-25}$$

and similarly for \tilde{E}_v^0 and \tilde{E}_{uv}^0 . \tilde{E}_u^0 can be evaluated at each observation time t_{obs} , but because we generally are interpolating wind fields between observation times, we must also account for added uncertainty due to temporal separation. The total variance associated with a given observation time is therefore

$$\tilde{E}_u(t) = f_E(|t - t_{obs}|, \tau_{ps}) E_u^\infty + (1 - f_E) \tilde{E}_u^0 \quad \text{Eq. 11-26}$$

where the persistence timescale is used. The total variance at time t , $E_u(t)$, is then found by linear interpolation between the values of $\tilde{E}_u(t)$ evaluated at the two bracketing observation times. Obviously, no interpolation is required if t is before the first observation time or after the last one.

The length scale associated with observational uncertainty is found from the Gifford spectrum as

$$\Lambda_E = \Lambda_T \left[\frac{\frac{1}{2}(E_u + E_v)}{u_T'^2} \right]^{3/2} \quad \text{Eq. 11-27}$$

Because the calculations for observational meteorology are performed on a three-dimensional grid, the variance and length scale at a puff centroid are found from linear interpolation. This means that if no grid point corresponds exactly with the observation location, there will be a non-zero uncertainty associated with a puff even if it coincides exactly in time and space with an observation. This dependence on the grid is certainly not ideal, but the methodology allows an initial examination into the effects of uncertainty. For calculations involving extrapolations of more than a few hours from observation times, this effect is probably negligible.

The observational input can be characterized as standard “OBSERVATION” type (just described), “ANALYSIS” type, or “FORECAST” type. The latter two are intended for use with profiles extracted from numerical models. “ANALYSIS” profiles are assumed to represent the numerical model after suitable assimilation and analysis of observations, that is, appropriate for initializing a numerical prediction model. In this case, the meteorological uncertainty is treated as described for standard observational input, with the “observation locations” corresponding to the selected model grid points. Therefore, the meteorology at grid locations is assumed to be “perfect.” The initial uncertainty for “FORECAST” input is also set as for standard observational input. This is assumed to correspond to an “analysis time” given in the PROFILE file or the first time on the profile file if no analysis time is explicitly given. The subsequent time evolution is then described by Equation 12-2.

12

MODEL OUTPUT

12.1 Local Concentration Values

12.1.1 Tracer Concentration

The description of the concentration field is based on summing contributions from each puff using the generalized Gaussian shape given in Equation 2-1. The only complicating factor in this process is the treatment of reflections at the surface and possibly at the boundary layer capping inversion. The notation is simplified by using $D = \text{Det}(\sigma)$ and using the tensor α defined as

$$\alpha_{ij} = \frac{\sigma_{ij}^{-1}}{2} \quad \text{Eq. 12-1}$$

Using these variables, the mean concentration field of an individual puff is

$$\bar{c}(\mathbf{x}) = \frac{Q}{(2\pi)^{3/2} D^{1/2}} \exp\left[-\alpha_{ij}(x_i - \bar{x}_i)(x_j - \bar{x}_j)\right] \quad \text{Eq. 12-2}$$

The usual reflection condition corresponds to a zero normal gradient boundary condition on c , which is consistent with zero flux through the surface. In general, there is a deposition flux at the ground, but we assume that the flux is small so that a zero gradient is justified. When the Gaussian is skewed in the vertical, however, there is no simple reflection condition that maintains a zero normal gradient. The skewness effects are most pronounced under stable conditions with vertical wind shear and are generally small under the diffusive conditions of the turbulent surface layer. The skewness can be important under stable conditions with terrain, where horizontal impact on a hillside can occur. We therefore require a simple self-consistent reflection condition for skewed puffs.

For a surface reflection, the location of the maximum surface concentration in the unreflected Gaussian (Equation 12-2) is obtained by examining the exponential argument at $z = h$. Here, h is the local terrain elevation; if the terrain slopes are non-zero, the puff moments are all rotated into the local coordinate frame one axis normal to the surface prior to the reflection calculation. The surface location, (x_s, y_s) , is given by

$$x_s - \bar{x} = (\alpha_{13}\alpha_{22} - \alpha_{23}\alpha_{12}) \frac{\bar{z}}{D_H} \quad \text{Eq. 12-3}$$

$$y_s - \bar{y} = (\alpha_{23}\alpha_{11} - \alpha_{13}\alpha_{12}) \frac{\bar{z}}{D_H} \quad \text{Eq. 12-4}$$

where

$$D_H = \alpha_{11}\alpha_{22} - \alpha_{12}^2 \quad \text{Eq. 12-5}$$

The reflected puff is then positioned on the projection from the original puff centroid through the surface maximum location, that is,

$$\bar{x}_r = 2x_s - \bar{x} \quad \text{Eq. 12-6}$$

where $x_s = (x_s, y_s, 0)$. The reflected puff moments are the same as the original puff so that the skewness is the same. For a non-skewed puff, the reflection is the normal vertical reflection, but a skewed puff will reflect from the surface maximum point back toward the original centroid. For the special case in which $\bar{z} = 0$, the reflection will simply double the concentrations in $z > 0$. This reflection does not give a zero slope at $z = 0$ for a skewed puff but is the simplest mass-conserving scheme that maintains a smooth transition as a puff approaches the surface.

The total concentration in $z > 0$ can be written as the sum of the original and reflected puffs, giving

$$\bar{c}_T(x) = \bar{c}(x) + \frac{Q}{(2\pi)^{3/2} D^{1/2}} \exp\left[-\alpha_{ij}(x_i - \bar{x}_{ri})(x_j - \bar{x}_{rj})\right] \quad \text{Eq. 12-7}$$

where \bar{c} is defined by Equation 2-6. Using the definition of the reflected centroid in Equation 2-11, Equation 2-13 can be rewritten as

$$\bar{c}_T(x) = (1 + \exp(-Rz))\bar{c}(x) \quad \text{Eq. 12-8}$$

where the reflection coefficient, R , is given by

$$R = \frac{\bar{z}}{2DD_H} \quad \text{Eq. 12-9}$$

For puffs located within the PBL, that is, $\bar{z} < z_i$, the puff mass is assumed to be entirely contained within the turbulent layer. This is consistent with the assumption that vertical diffusion across the capping inversion is small. Reflection at the inversion, $z = z_i$, is treated similarly to the surface reflection and gives an additional reflection factor of

$$\hat{f}_r = 1 + \exp\left[-\hat{R}(z_i - z)\right] \quad \text{Eq. 12-10}$$

for points within the boundary layer, where

$$\hat{R} = \frac{z_i - \bar{z}}{2DD_H} \quad \text{Eq. 12-11}$$

If the puff centroid is within the boundary layer, then $c = 0$ for $z \geq z_i$.

12.1.2 Multicomponent Species Concentration

Equation 12-2, as well as the reflection methods that follow, are also applied to determine the multicomponent species concentrations, \bar{c}_k , using the individual species masses, Q_k , in place of the tracer mass, Q , to define a perturbation concentration. The species perturbation concentrations are then added to the background concentrations to define the total species concentrations. Figures 12-1 and 12-2 illustrate the two possible scenarios for the species

concentrations. If the species mass is positive, the total concentration will be above the background. This is the situation for species that are emitted or formed through chemical reaction. If the species mass is negative, the total species concentration will be below the background, as is the case for species that are depleted through chemical reaction.

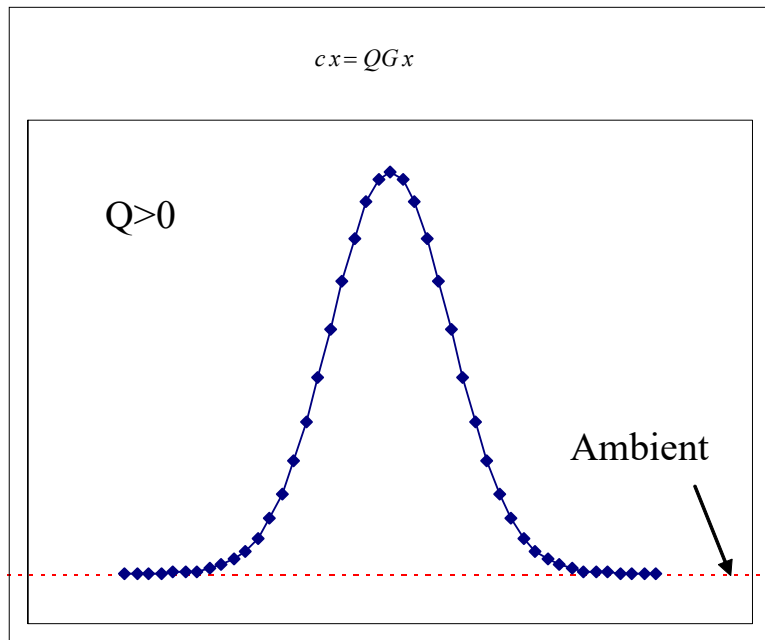


Figure 12-1
Schematic illustration of a positive species perturbation concentration

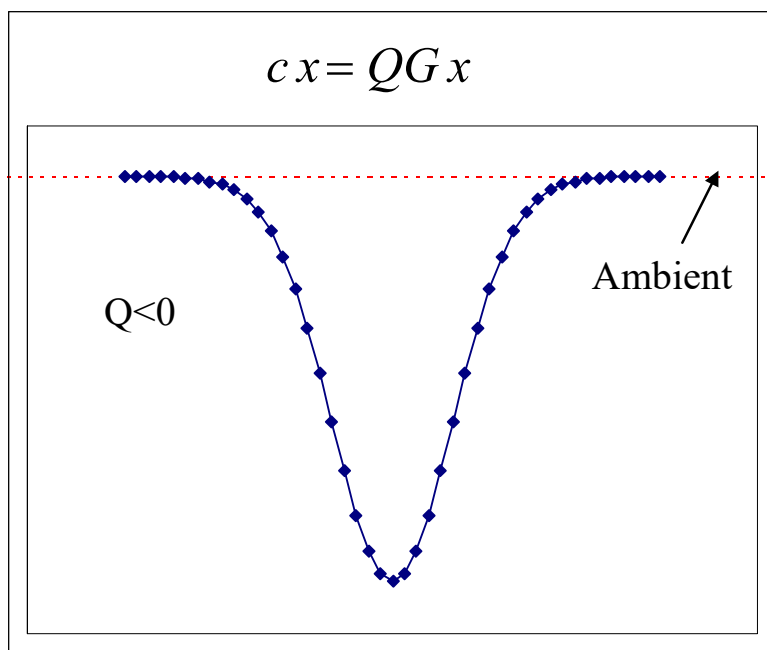


Figure 12-2
Schematic illustration of a negative species perturbation concentration

Because the chemistry simulation maintains the average puff concentration at minus the ambient concentration, it is possible for the minimum local concentration to fall below this limit. Therefore, the total concentration is adjusted using both a modified Gaussian function with a spread that is increased by a factor of $\sqrt{2}$ and the original Gaussian shape function. This is done to ensure that the final total concentration will be equal to or greater than zero. The required amount of enhanced spread is determined by the ratio of the puff-average total concentration to the ambient. For example, the ratio for species-A is as follows:

$$r_A = \frac{\hat{S}_A + S_A}{S_A} \quad \text{Eq. 12-12}$$

Where \hat{S}_A is the average puff perturbation concentration and S_A is the ambient concentration. The factor used to determine the local perturbation concentration is then

$$G(\mathbf{x})^{Mod} = r_A G(\mathbf{x}) + (1 - r_A) G(\mathbf{x})^{Incr} \quad \text{Eq. 12-13}$$

$G(\mathbf{x})$ for puff- α is (as shown in Equation 12-13)

$$G^{(\alpha)}(\mathbf{x}) = \frac{\exp(-A^{(\alpha)}(\mathbf{x}))}{(2\pi)^{3/2} D_\alpha^{1/2}} \quad \text{Eq. 12-14}$$

where

$$A^{(\alpha)}(\mathbf{x}) = \alpha_{ij} (x_i - \bar{x}_i^{(\alpha)}) (x_j - \bar{x}_j^{(\alpha)}) \quad \text{Eq. 12-15}$$

and

$$\alpha_{ij} = \frac{(\sigma_{ij}^{(\alpha)})^{-1}}{2} \quad \text{Eq. 12-16}$$

$G(\mathbf{x})^{Incr}$ for puff- α is then

$$G^{(\alpha)}(\mathbf{x})^{Incr} = \frac{\exp(-0.5 A^{(\alpha)}(\mathbf{x}))}{(4\pi)^{3/2} D_\alpha^{1/2}} \quad \text{Eq. 12-17}$$

As an example, consider a species whose background concentration is 12 ppb. If the average perturbation concentration is -10 ppb, the total average concentration is 2 ppb. However, if the average perturbation concentration is -10 ppb, the minimum perturbation concentration can be approximately -16 ppb, giving a non-physical total concentration of -4 ppb at the minimum. Using an enhanced spread adjusts the perturbation concentrations so that the total concentrations will not fall below zero at any point along the Gaussian shape. Figure 12-3 illustrates the example, showing the local total concentration with and without the enhanced spread.

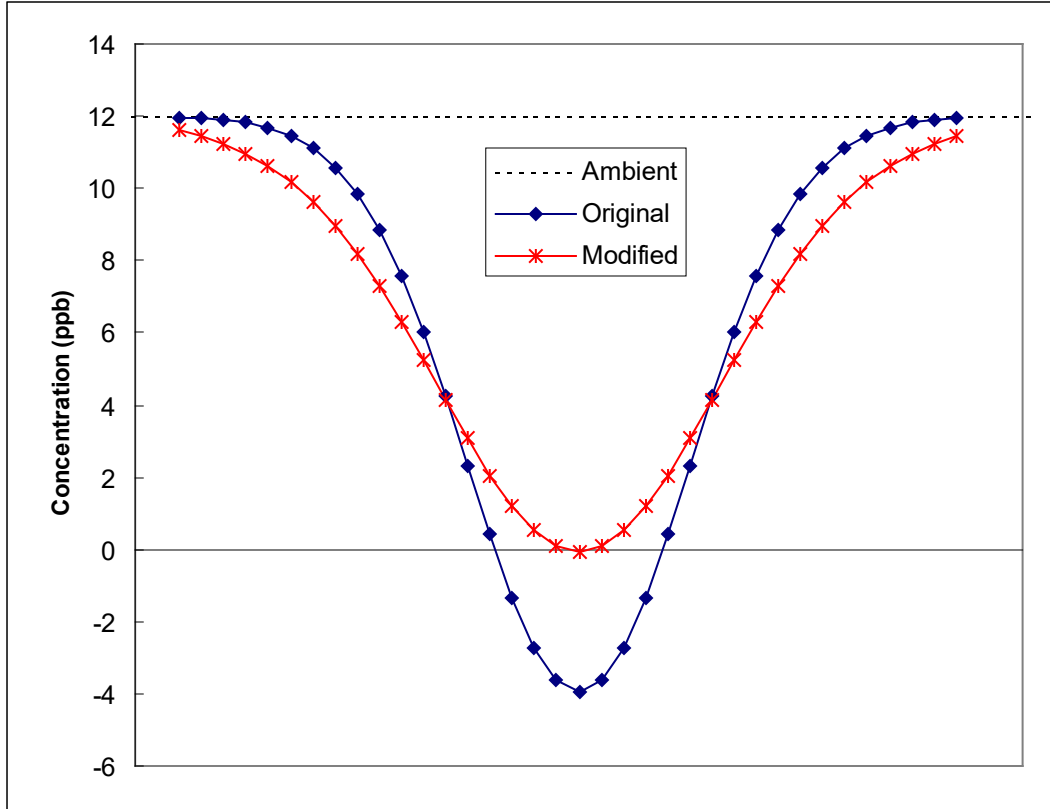


Figure 12-3
Local total concentration with and without enhanced spread

12.2 Probabilistic Calculation

12.2.1 Probability Density Function

The SCICHEM prediction does not provide a complete description of the probability distribution for the concentration value, but the two moments (mean and variance) can be used to generate an empirical distribution function with a specified shape. Analysis of atmospheric observations (Lewellen and Sykes, 1986; Yee, 1990) has shown that the truncated Gaussian or clipped normal distribution provides the best description of short-term concentration fluctuations if only the mean and variance are available. The clipped normal distribution is obtained by replacing all the non-physical negative values in a general Gaussian distribution with zero values. Therefore, a Gaussian distribution

$$p_G(c) = \frac{1}{\sigma_G \sqrt{2\pi}} \exp\left(-\frac{(c - \mu_G)^2}{2\sigma_G^2}\right) \quad \text{Eq. 12-18}$$

with mean μ_G and standard deviation σ_G becomes

$$p_C(c) = \gamma\delta(c) + \frac{1}{\sigma_G \sqrt{2\pi}} \exp\left(-\frac{(c - \mu_G)^2}{2\sigma_G^2}\right), \quad c \geq 0 \quad \text{Eq. 12-19}$$

where the intermittency, γ , is given by

$$\gamma = \frac{1}{2} \left[1 - \operatorname{erf} \left(\frac{\mu_G}{\sigma_G \sqrt{2}} \right) \right] \quad \text{Eq. 12-20}$$

The mean and variance of the clipped distribution, p_C , can be related to the Gaussian parameters.

$$\mu = \frac{\sigma_G}{\sqrt{2\pi}} \exp \left[- \left(\frac{\mu_G^2}{2\sigma_G^2} \right) \right] + \frac{\mu_G}{2} \left[1 + \operatorname{erf} \left(\frac{\mu_G}{\sigma_G \sqrt{2}} \right) \right] \quad \text{Eq. 12-21}$$

and

$$\sigma^2 = -\mu^2 + \sigma_G^2 \left[1 + \operatorname{erf} \left(\frac{\mu_G}{\sigma_G \sqrt{2}} \right) \right] + \mu_G \mu \quad \text{Eq. 12-22}$$

SCICHEMgui displays contours of the probability that the concentration will exceed a user-prescribed value. SCICHEMgui can also plot contours of the areas in which the probability of exceeding concentrations is greater than the user-specified probability.

13

MODEL EVALUATION STUDIES

13.1 Short-Range Diffusion

13.1.1 Pasquill-Gifford-Turner Stability Categories

The commonly used Pasquill-Gifford-Turner (PGT) stability curves for plume dispersion are valid for short-range dispersion from surface releases and are based on an averaging time of about 10 minutes. The PGT dispersion estimates are empirical fits to atmospheric observations and are therefore representative of real data. The PGT classification system requires a self-similar solution to the diffusion equation so that the plume spread is a function of downstream distance and stability class only. This is possible if the turbulent velocity scales are proportional to the transport speed and the turbulent length scales are dependent only on the vertical height. The standard surface layer representation fulfills most of these conditions because the turbulence and mean wind speed are generally specified in terms of u_* and dimensionless height z/L , where L is the Monin-Obukhov length.

We note that the buoyancy component requires knowledge of the mixed-layer depth, and we assume a fixed value of 1000 m for these comparisons. The Monin-Obukhov length corresponding to each stability category is given in Table 10-2. The contributions from the shear and buoyancy components are scaled as described in Section 11.1. With this specification for the atmospheric turbulence, we can compute an almost self-similar solution for the vertical dispersion using the closure model, but the horizontal dispersion is more complicated. We use a release at $z_{rel} = 5$ m with a surface roughness length of 3 cm and a wind speed of 5 ms^{-1} at $z = 10$ m, although it should be noted that the results depend on all these choices. The SCIPUFF predictions for horizontal and vertical plume spread are shown in Figure 13-1; stable conditions are omitted because the horizontal turbulence generation mechanisms in a stable stratification are poorly understood. The closure model is in reasonable agreement with the generally accepted dispersion curves for surface layer dispersion, although we note the dependence on wind speed and other input choices.

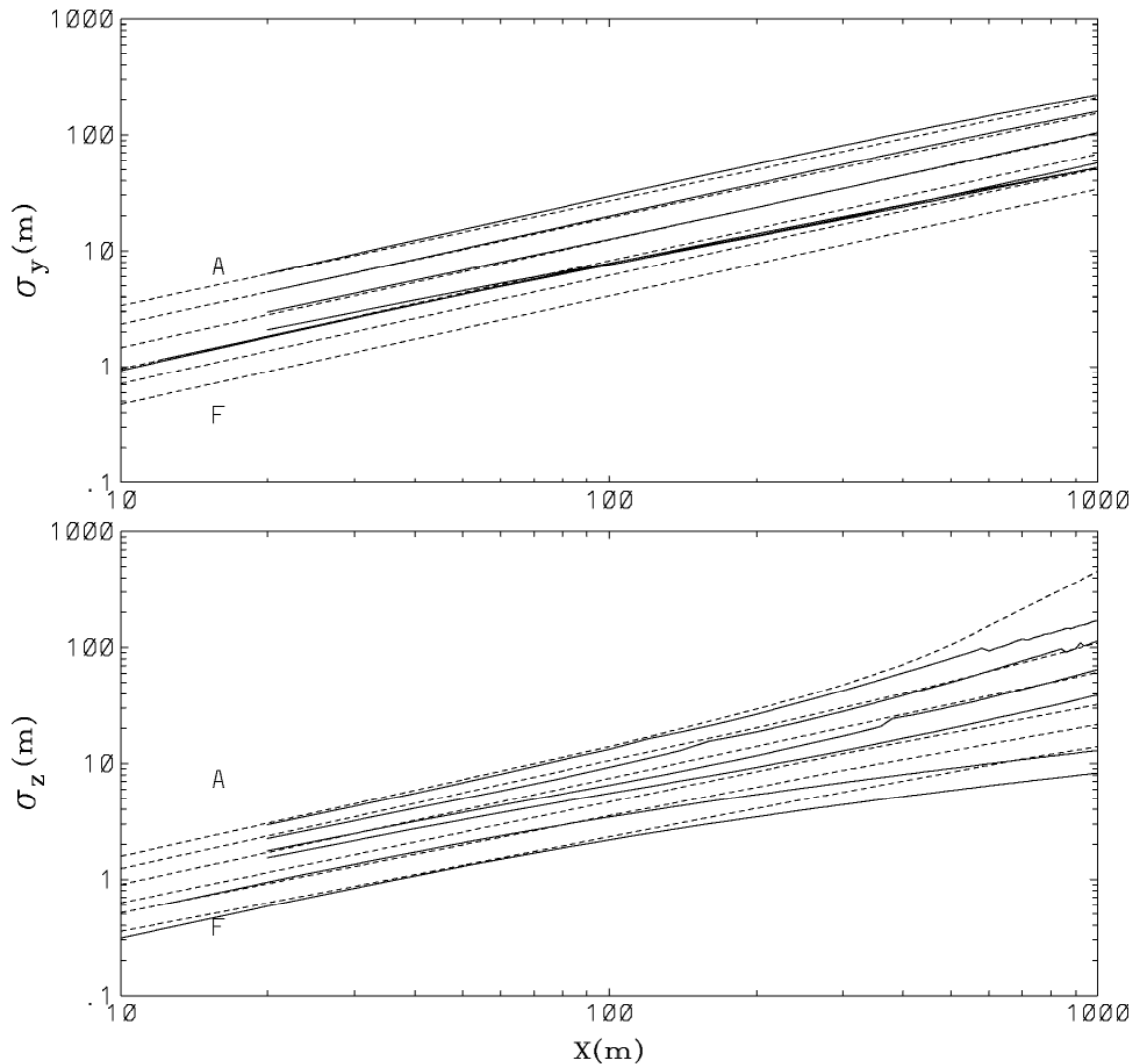


Figure 13-1
Comparison between SCIPUFF predictions (solid lines) and the PGT dispersion curves for Categories A through F

13.1.2 Model Data Archive

The Model Data Archive (MDA), compiled by Sigma Research Corporation, is an extensive collection of field experiment data for both dense and passive tracer gas releases. The data set contains both continuous and instantaneous sources with different sampling times and has been used to evaluate several existing atmospheric dispersion models (Hanna et al., 1991).

Using the model coefficients defined from the preliminary test calculations, SCIPUFF has been compared with the test cases in the MDA. The experimental data are divided into a passive release set and a dense gas release set, but we deal only with the passive cases here; the dense gas comparisons are described in Section 13.4.

The passive releases are relatively straightforward because the only source parameters are the mass flow rate and the source size. The initial standard deviation of the puffs is set equal to the source radius for these releases, which include the Prairie Grass and Hanford data. The

meteorology for the dispersion calculation was specified as a single wind speed at the appropriate observation height, together with a surface heat flux and a boundary layer depth, z_i . The Prairie Grass data set includes an estimate of the Monin-Obukhov length, L , and the surface friction velocity, which directly provide a heat flux. The Hanford data includes a vertical temperature difference, which was used in conjunction with the wind speed to determine the surface heat flux. Measurements of the boundary layer depth were not available, so z_i was set to 1000 m for neutral and unstable cases and to $5L$ for the stable cases.

The data specify an averaging time for the concentration data, and both short- and long-duration measurements are included. The observed values represent the maximum recorded over all sampling locations at a given distance and over the sampling period. For the long-duration measurements, which usually correspond to the release duration, the model is run using the conditional dispersion mode, described in Section 2.2.5. The concentration sampling period, T_{avg} , is the appropriate averaging time for filtering the turbulence, and the centerline maximum prediction at the sampler downstream distance is then used for comparison.

For the short-duration data, we use the statistical SCIPUFF prediction to estimate the expected value. When a short-duration peak, say a 1-second average, is reported from several samplers over a sampling period, T_{sample} , it must be recognized that this is a random variable. For an idealized continuous release of infinite duration, we expect the maximum observed value to increase as the sampling period increases because there is a higher probability of measuring an extreme value. To model the expected peak value, we use the predicted probability distribution for the centerline concentration, c_0 , using a turbulence filter of T_{avg} . If only one measurement (in time) of the maximum concentration over several sampler locations across the plume is made, the expected value would be \bar{c}_0 . However, if we sample for a longer time, the expected value must increase because the chances of encountering a higher value are increased.

Suppose that the probability density function for c_0 is such that

$$\text{Prob}(c_0 < X) = P_0(X)$$

Then, if the maximum from N independent observations of c_0 is denoted as c_N , then

$$\begin{aligned}\text{Prob}(c_N < X) &= P_N(X) \\ &= [P_0(X)]^N\end{aligned}$$

because all N observations must be less than X . If we can estimate N , therefore, we can determine the expected value of c_N as the predicted value for the observed maximum concentration. N is estimated from the reduction in the concentration fluctuation variance with averaging time (Sykes, 1984). If we identify this reduction with the factor $1/N$ for the variance reduction from averaging N independent samples of a discrete variable, we obtain

$$N^{-1} = \frac{2}{\beta^2}(\beta - 1 + e^{-\beta}) \quad \text{Eq. 13-1}$$

where $\beta = T_{sample}/T_c$ and T_c is the integral timescale of the fluctuations.

The calculation procedure, therefore, is:

1. Reduce $\overline{c'^2}$ to account for the averaging time, T_{avg} .
2. Determine the clipped normal distribution $P_0(X)$ for the reduced variance.
3. Determine the exponent N from Equation 13-1.
4. Calculate the expected maximum value from the distribution P_N .

This procedure is applied to the sampler time series to obtain the predicted maximum value.

Results for the overall comparison are shown in Figure 13-2 for the passive data sets. The overall agreement with the range of data is relatively good. Most of the predictions are within a factor of 2 of the observations, and there is reasonable skill in predicting the effect of time averaging on the maximum concentration. The values for two of the statistical measures proposed by Hanna et al. (1991)—the geometric mean and geometric variance—are 0.952 and 1.263, respectively, indicating very small bias (<5%) and small variance.

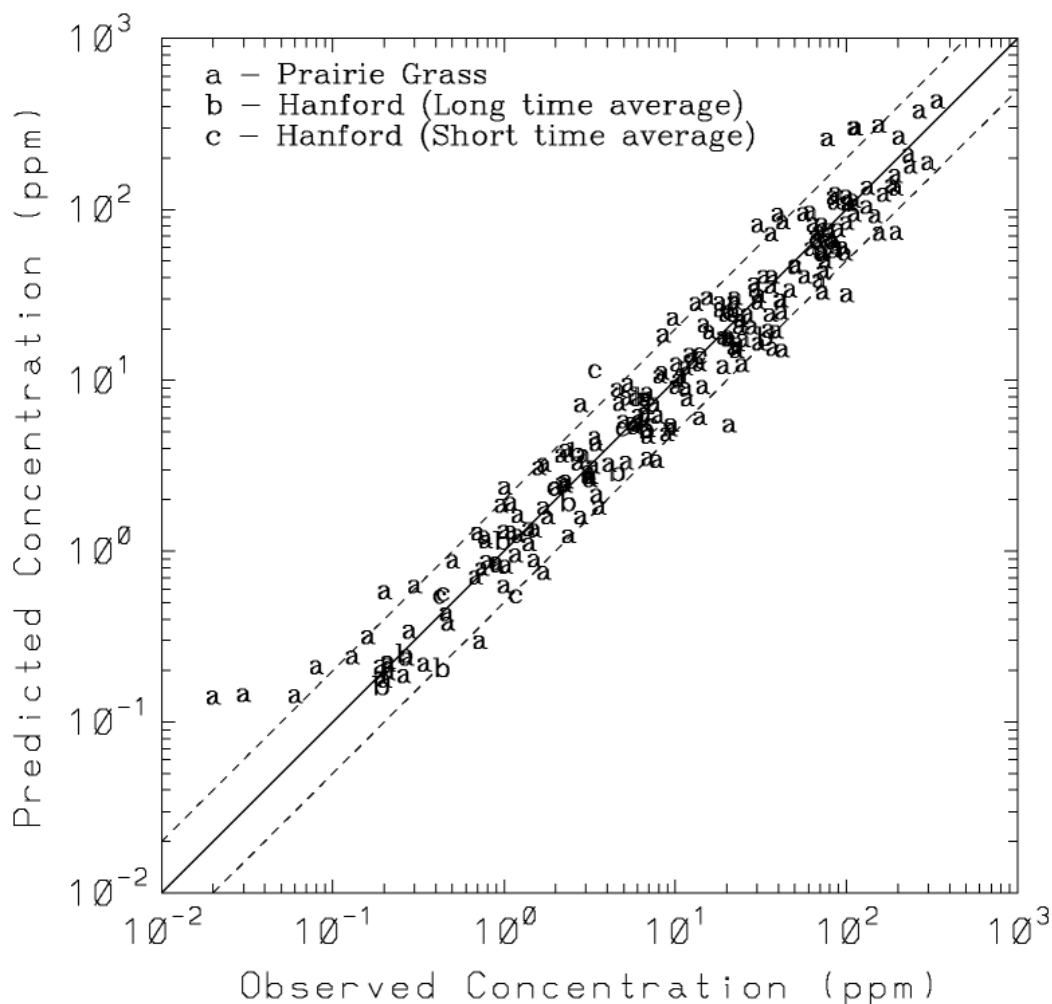


Figure 13-2

Comparison between the observed maximum concentrations and SCIPUFF predictions for the passive releases in the Model Data Archive. Various experiments are indicated by the letter codes.

13.1.3 Instantaneous Dispersion

Several short-range instantaneous dispersion experiments have been compared with SCIPUFF predictions. These comparisons are presented in the paper by Sykes and Gabruk (1997) and are briefly described here.

The first data comparison uses the ice crystal experiment results of Weil et al. (1993). A cluster of ice crystals was formed within a natural cloud by seeding with dry ice pellets from an aircraft; the evolution of the ice crystal cloud was then measured from the aircraft along with relevant turbulence statistics. Weil et al. present averaged results for the dimensionless cloud spread from an ensemble of about 25 releases, and the data are compared with the closure model prediction in Figure 13-3. We use an initial source size of 53 m, which corresponds to the larger of the source sizes considered by Weil et al., and the data have been made dimensional using the observed average values, $\overline{v'^2} = 3.6 \text{ m}^2\text{s}^{-2}$ and $\varepsilon = 0.013 \text{ m}^2\text{s}^{-3}$. We assume isotropic conditions to determine the other velocity variances, and the turbulence length scales are obtained from the dissipation rate (see Lewellen, 1977) as

$$\Lambda_s = \Lambda_v = \frac{bq^3}{\varepsilon} \quad \text{Eq. 13-2}$$

which implies $\Lambda_s = 341 \text{ m}$ for the Weil et al. data.

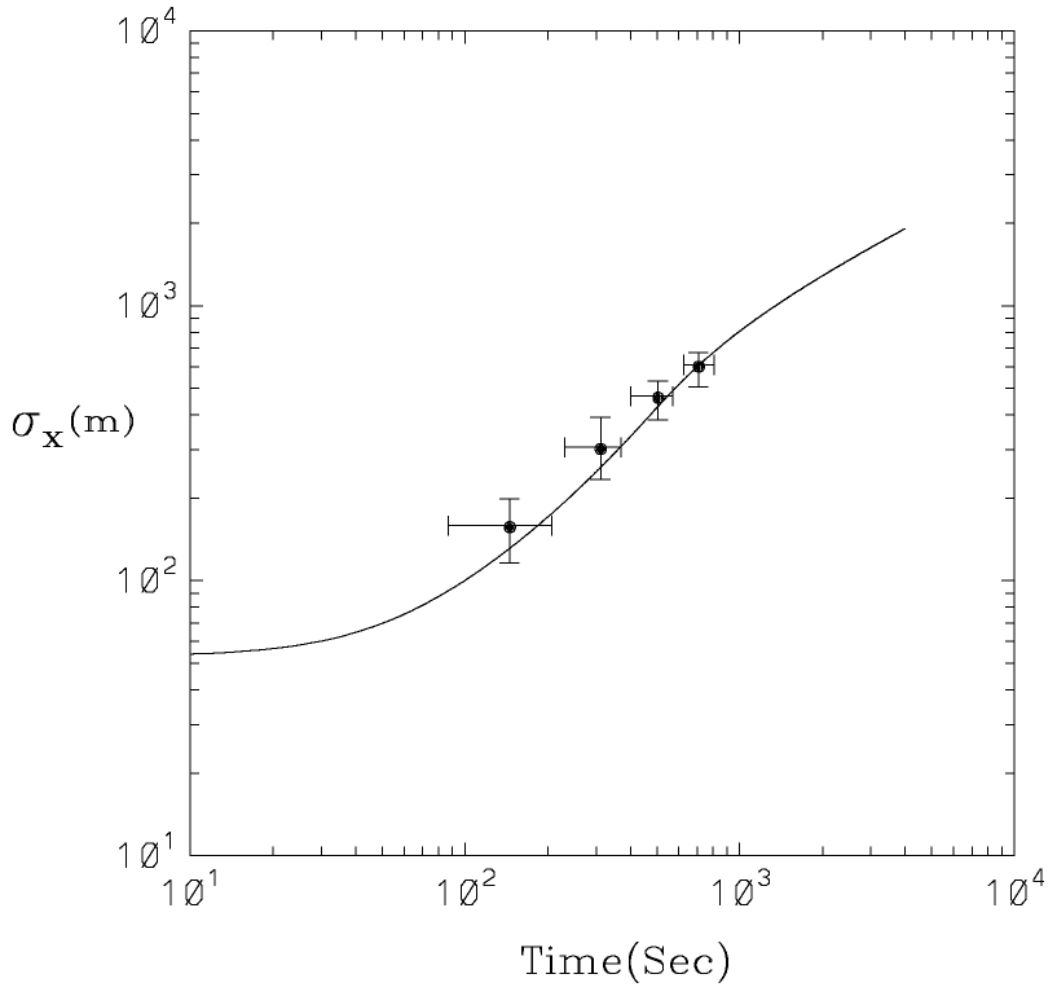


Figure 13-3
Comparison between SCIPUFF predictions and the observational data of Weil et al. (1993)

Figure 13-4 shows the SCIPUFF comparison with the data of Mikkelsen et al. (1987) for smoke dispersion in the atmospheric surface layer. The lateral turbulent velocity variance, $\overline{v'^2}$, was measured as $0.98 \text{ m}^2\text{s}^{-2}$, and the Lagrangian integral timescale was estimated to be 100 s from the measured Eulerian spectrum. The mean velocity at the plume height was 4.72 ms^{-1} . We again assume isotropic conditions for simplicity because the other turbulence components were not reported, although we note that this assumption is not strictly valid in the atmospheric surface layer. The length scale is derived from the Lagrangian timescale, which corresponds to Λ/Aq in the closure model, and the vertical and horizontal scales are assumed to be equal. The initial source size is taken to be 0.5 m, corresponding to the larger value tested by Mikkelsen et al. The results are not sensitive to the assumption of isotropy, because we use the observed value of the Lagrangian timescale to determine the length scale. A test calculation using $\Lambda_s = 6.5 \text{ m}$, as appropriate for a plume at $z = 10 \text{ m}$, and reducing the vertical velocity variance in accord with the $-5/3$ law, gave almost identical results to the isotropic calculation.

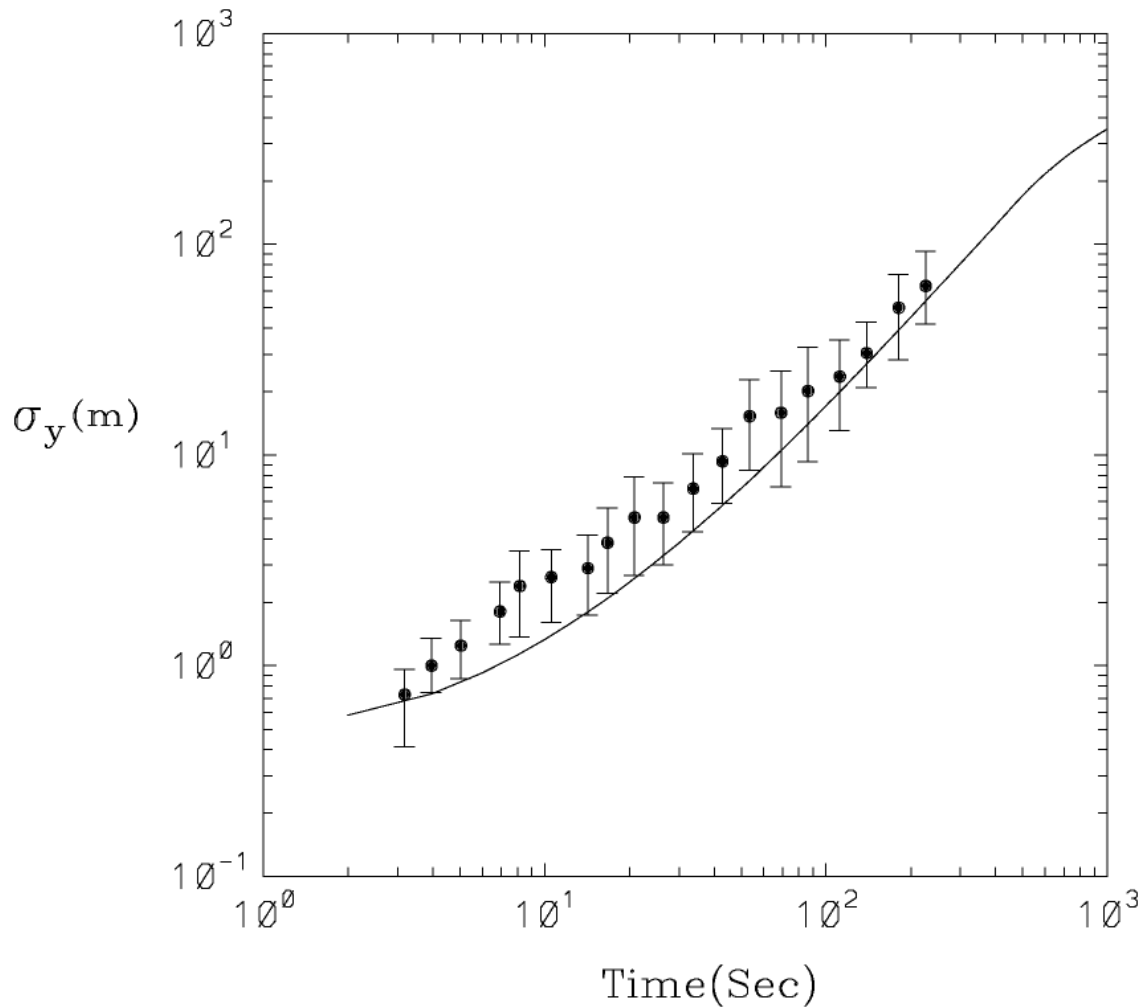


Figure 13-4
Comparison between SCIPUFF predictions and the observational data of Mikkelsen et al. (1987)

Figure 13-5 compares the closure model prediction with the neutral relative dispersion data of Högström (1964), as described by Sawford (1982). The release was made at 50 m, and there is considerable uncertainty about the turbulence conditions. We follow Sawford in determining the effective length scale from the late-time dispersion measurements. We use a turbulence intensity of 0.1, as suggested by Sawford, and again assume isotropic conditions. Therefore,

$\overline{u'^2} = \overline{v'^2} = \overline{w'^2} = 0.01 U^2$, and the length scales, Λ_S and Λ_V , were taken to be 16 m. A source size of 1 m was used in the calculation because this is the midrange value considered by Sawford. The turbulence specifications enforce agreement with the data at late time, but the model does predict the proper early time growth of the plume.

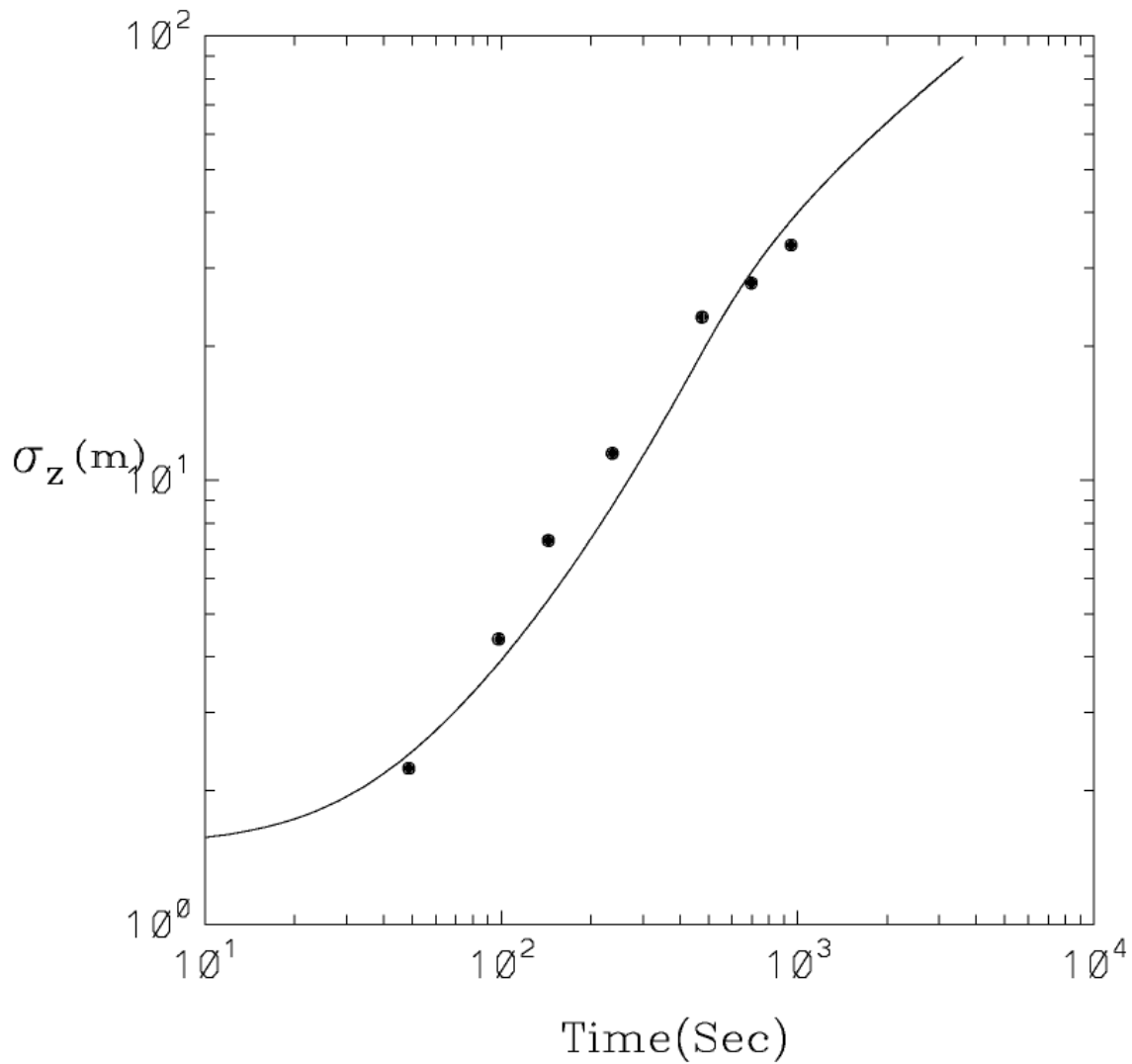


Figure 13-5
Comparison between SCIPUFF predictions and the observational data of Högström (1964)

13.1.4 CONFLUX

SCIPUFF simulations were compared with data from the Concentration Fluctuation Experiments (CONFLUX) project of 1994 (Biltoft, 1995). Figures 13-6 and 13-7 show the vertical profiles of mean concentration and standard deviation to mean concentration ratio of the CONFLUX data and SCIPUFF simulations.

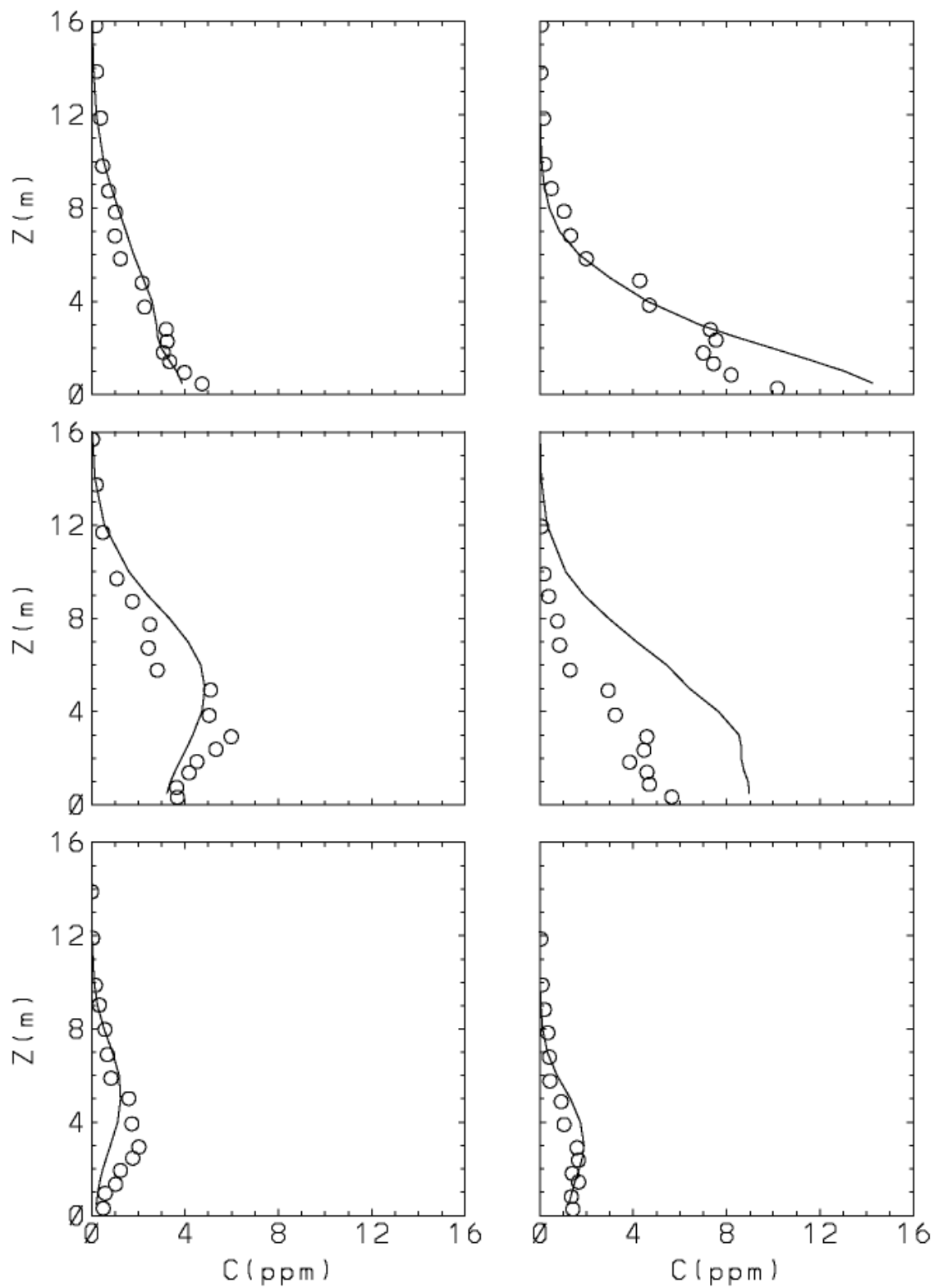


Figure 13-6
Comparison between SCIPUFF predictions of mean concentration and the observational data from CONFLUX 1994

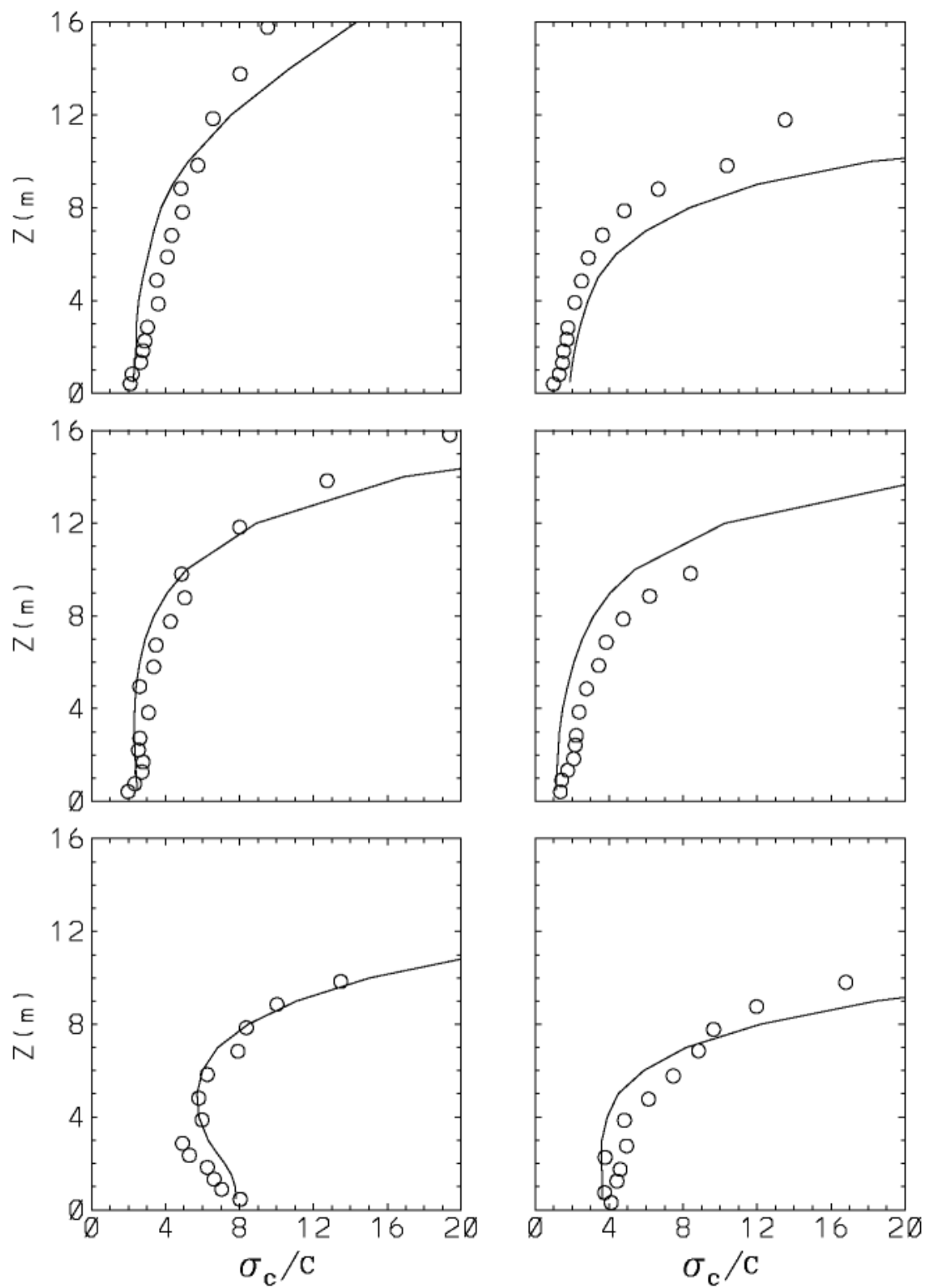


Figure 13-7
Comparison between SCIPUFF predictions of standard deviation to mean concentration ratio and the observational data of CONFLUX 1994

In this field study, concentration time series were constructed from measurements of neutrally buoyant plumes in slightly convective to moderately stable meteorological conditions. All concentration data were obtained with a vertical array of 16 photoionization detectors at downwind locations between 12.5 m and 100 m. Contemporaneous measurements of wind velocity and temperature supplied the meteorological input needed to perform SCIPUFF simulations. We assumed isotropic conditions and partitioned the horizontal velocity variance into shear and buoyant components as described in Section 11.1, with length scales, Λ_B and Λ_S , of 250 m and $0.65 z$, respectively. The shear component was determined from the observed shear stress, using Equation 11-3, and the remainder of the horizontal energy was assigned to the buoyancy-driven component. A source size of 0.05 m with a release height of 3 m was used in the calculation. The sampling period of the concentration measurements was approximately 35 minutes, which was sufficiently long to sample most of the turbulent energy spectrum. Profiles of mean concentration and concentration variance were calculated by time-averaging the data. SCIPUFF simulations were conducted in the conditional dispersion mode using a concentration averaging time, T_{avg} , equal to the measurement sampling period.

The comparisons indicate reasonably good agreement on the vertical dispersion rate and concentration levels. Note that the scales are linear so that most of the predictions are closer than a factor of 2. The concentration fluctuation intensity is also in good agreement with the observations, and high values are observed. This is due to the small source size, which produces a narrow plume that is meandered by the large atmospheric eddies. Both the magnitude and shape of the distribution are predicted accurately.

13.2 Long-Range Diffusion

SCIPUFF has been tested against two major long-range atmospheric dispersion experiments. First, the Across North America Tracer Experiment (ANATEX) comparisons were described by Sykes et al. (1993c). The published results were obtained using an earlier version of SCIPUFF, but the dispersion algorithms are effectively the same. A more sophisticated treatment of the different turbulence populations from the boundary layer and mesoscale has been implemented, as described in Section 2.1.3, but the longer range predictions are dominated by the mesoscale component and are not sensitive to the combination methodology.

The second experiment is the more recent European Tracer Experiment (ETEX) (Mosca et al., 1997). Figure 13-8 shows a comparison between a SCIPUFF simulation and ETEX data at several times after the start of the release. In this study, an inert tracer was released for 12 hours at an average rate of 7.95 gs^{-1} . The evolution of the tracer cloud was measured for a period of 72 hours (from the beginning of the release) with a sampling network of 168 sites. The meteorological input to SCIPUFF was the uninitialized, gridded analysis supplied by the European Centre of Medium Range Weather Forecasts (ECMWF). In addition, turbulence input for the second-order closure model was specified as two separate populations, representing the PBL eddies and the larger scale contribution. Boundary layer turbulence profiles were determined using the diurnal boundary layer calculation described in Section 10.2 with no cloud cover. We used a Bowen ratio of 0.6 and a surface albedo of 0.16; these values are typical of mid-latitude rural terrain but clearly cannot represent the detailed variations over the dispersion domain. The large-scale turbulence represents the mesoscale fluctuations and is based on the work of Gifford (1988).

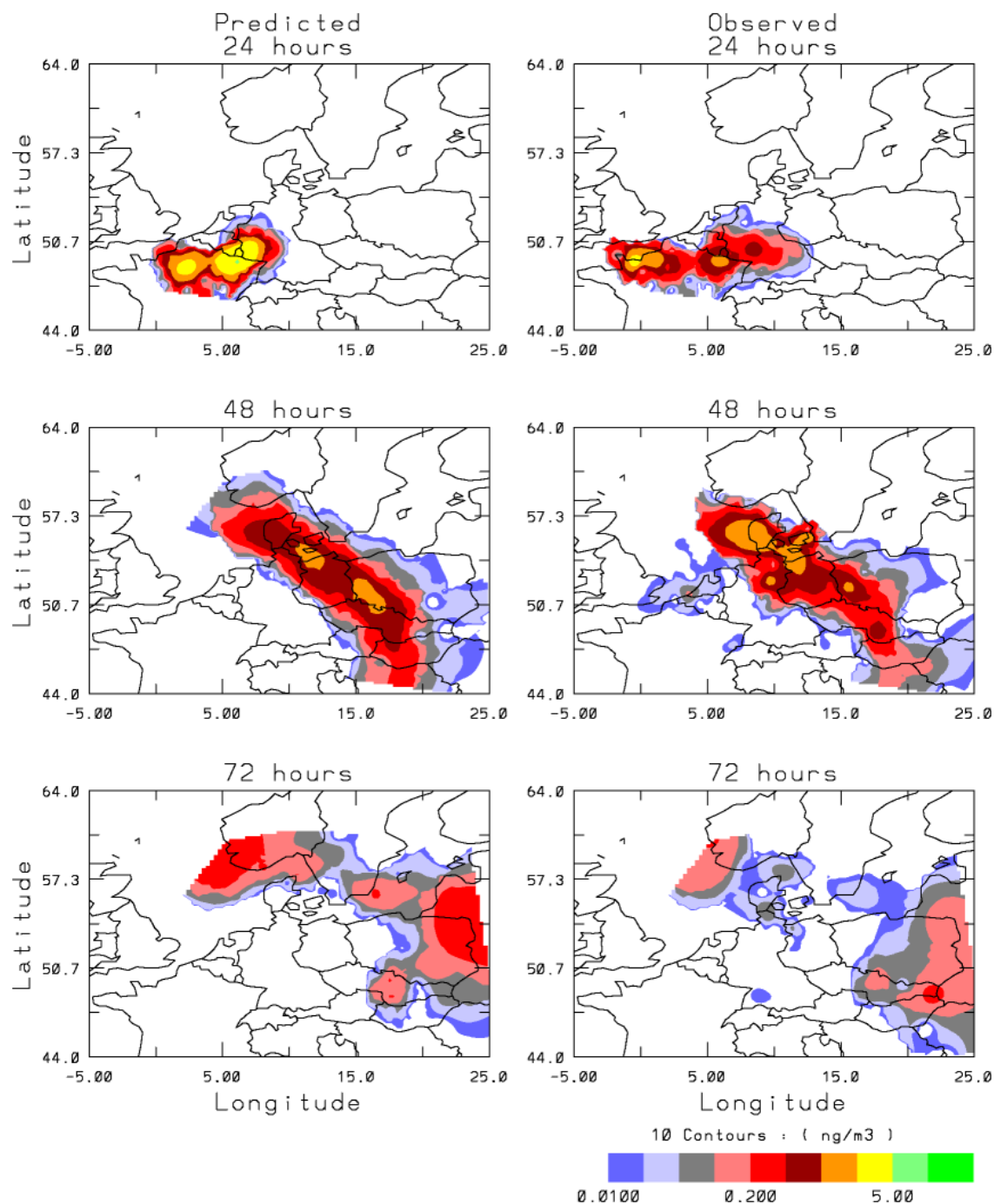


Figure 13-8
Comparison of mean concentration between SCIPUFF predictions and ETEX data
 (Mosca et al., 1997). Contours are 0.01, 0.02, 0.05, 0.1, 0.2, 0.5, 1, 2, 5, 10, 20, and 50 ngm⁻³.

The comparison with the observations shows that the location and shape of the cloud are reasonably well predicted as it travels across the continent—and the magnitude of the predicted surface concentration is also in reasonable agreement with the observed values. Figure 13-9 shows the measured concentration at several sampler locations and also the SCIPUFF prediction. The concentrations are averaged over 3-hour periods, and the time is shown relative to the start

of the release. The agreement in arrival time and peak concentration magnitude is reasonably good.

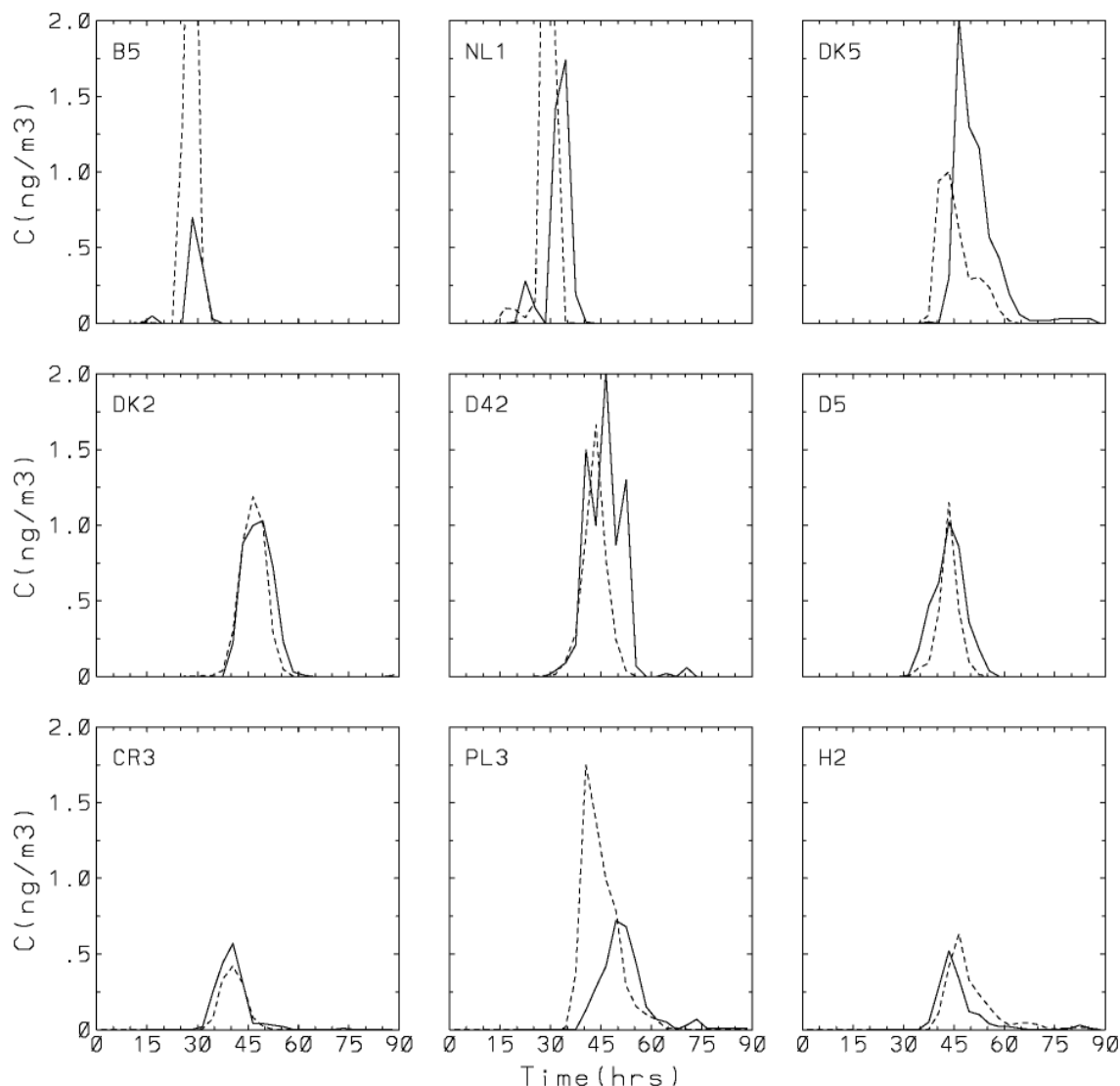


Figure 13-9
Comparison between 3-hr average concentrations from SCIPUFF predictions (dashed) and ETEX data (solid line) at 9 selected locations (Mosca et al., 1997). Concentration is in ngm^{-3} .

The 9 stations were chosen from the two sampler arcs analyzed by Mosca et al., showing passage of the plume at roughly 24 hours and 48 hours. Only 2 samplers from the middle of the first arc are shown; there are 2 other samplers on this arc, but they generally showed the poorest model performance. The reason for this is apparently that the actual plume moved farther to the north than predicted by the given wind field. Most of the models under-predict the northern station and over-predict the southern station, and we note that the SCIPUFF results are consistent with this trend although they are not shown here.

The results shown in Figure 13-9 are not identical to the SCIPUFF predictions reported by Mosca et al. (1997) because an older version of the model was used there. However, the ETEX

predictions have not been changed significantly by the model enhancements, so some comment on the relatively low ranking of SCIPUFF by Mosca et al. is in order. The official model evaluation exercise reported by Mosca et al. uses several statistical measures to compare observations and predictions. The two measures that influenced the ranking of SCIPUFF most adversely were the bias and normalized mean-square error (NMSE). These measures are defined as

$$Bias = \frac{1}{N} \sum_i (P_i - M_i)$$

$$NMSE = \frac{1}{N} \sum_i \frac{(P_i - M_i)^2}{\bar{M} \bar{P}}$$

where

$$\bar{M} = \frac{1}{N} \sum_i M_i \quad \text{and} \quad \bar{P} = \frac{1}{N} \sum_i P_i$$

are the mean measured and predicted values, respectively. N is the number of observations, and the subscript i denotes individual samplers.

The difficulty with these measures is the lack of normalization of the concentrations so that errors in the large values can dominate the statistics. In the SCIPUFF predictions, the sampler location closest to the release completely determines these two statistics because it contains the highest observations and SCIPUFF overpredicts the values. The sampler at Rennes, which is about 20 km east of the source, is located close to the centerline of the predicted plume and therefore receives a high concentration. The meteorological data provided for the calculation also lacked a boundary layer description, so the early plume development is strongly influenced by the model choice for the boundary layer. Because SCIPUFF does not routinely accept the ECMWF data as input and no special effort was made to develop an interface, the boundary layer description was relatively uncertain.

Table 13-1 shows the two statistics computed for all the samplers and with the Rennes sampler omitted. The numbers are not identical to those reported by Mosca et al. but illustrate the effect of this one location on a similar SCIPUFF prediction. The total number of samplers was 168, so the influence of Rennes is clearly disproportionate. The bias and NMSE without Rennes data lie well within the range of the other models used in the ETEX study, although it is noted that the reported statistics all contain the Rennes data—so we cannot directly compare these values with the report. The conclusion of Mosca et al. that SCIPUFF overpredicts the concentration is obviously restricted to the Rennes location; there is very little bias for the remainder of the data.

Table 13-1
Statistical measures for the SCIPUFF prediction of ETEX data

| | \bar{M} (ngm ⁻³) | <i>Bias</i> (ngm ⁻³) | <i>NMSE</i> |
|----------------|--------------------------------|----------------------------------|-------------|
| All ETEX data | 0.212 | 1.59 | 2160 |
| Rennes omitted | 0.193 | 0.06 | 14.8 |

13.3 Dynamic Rise Effects

The vertical rise dynamics in SCIPUFF have been validated principally against idealized laboratory experiments or in comparison with well-accepted empirical relations based on laboratory and field experiments. These include momentum jets in a crossflow, buoyant plumes in neutral or stable temperature gradients with a crossflow, and buoyant spherical bubbles released into a neutrally stable quiescent background.

13.3.1 Momentum Jet

The first experiments considered are momentum jets (no buoyancy) in a crossflow. Gordier (1959) (from Hirst, 1971) presents near-source data for a variety of exit velocity ratios,

$R = W_0 / U_a$, where U_a is the crossflow velocity and W_0 is the jet exit velocity. The jet source in SCIPUFF is characterized by a momentum flux F_m and Gaussian spread σ_0 so that W_0 is estimated by assuming an initially uniform velocity distribution such that $W_0^2 = F_m / r_0^2$ where r_0 is the source radius. [F_m is related to the SCIPUFF momentum flux Q_m by $F_m = Q_m / \pi$]. We

assume that $\sigma_0 = r_0$. A comparison with the mean jet centerline data of Gordier is shown in Figure 13-10. SCIPUFF tends to under-predict the jet heights; this is particularly the case near the source, but the discrepancies tend to decrease with downstream distance. The high R data show much less downstream displacement of the jet close to the source; this is probably due to distortion of the background flow—a phenomenon not included in the SCIPUFF model.

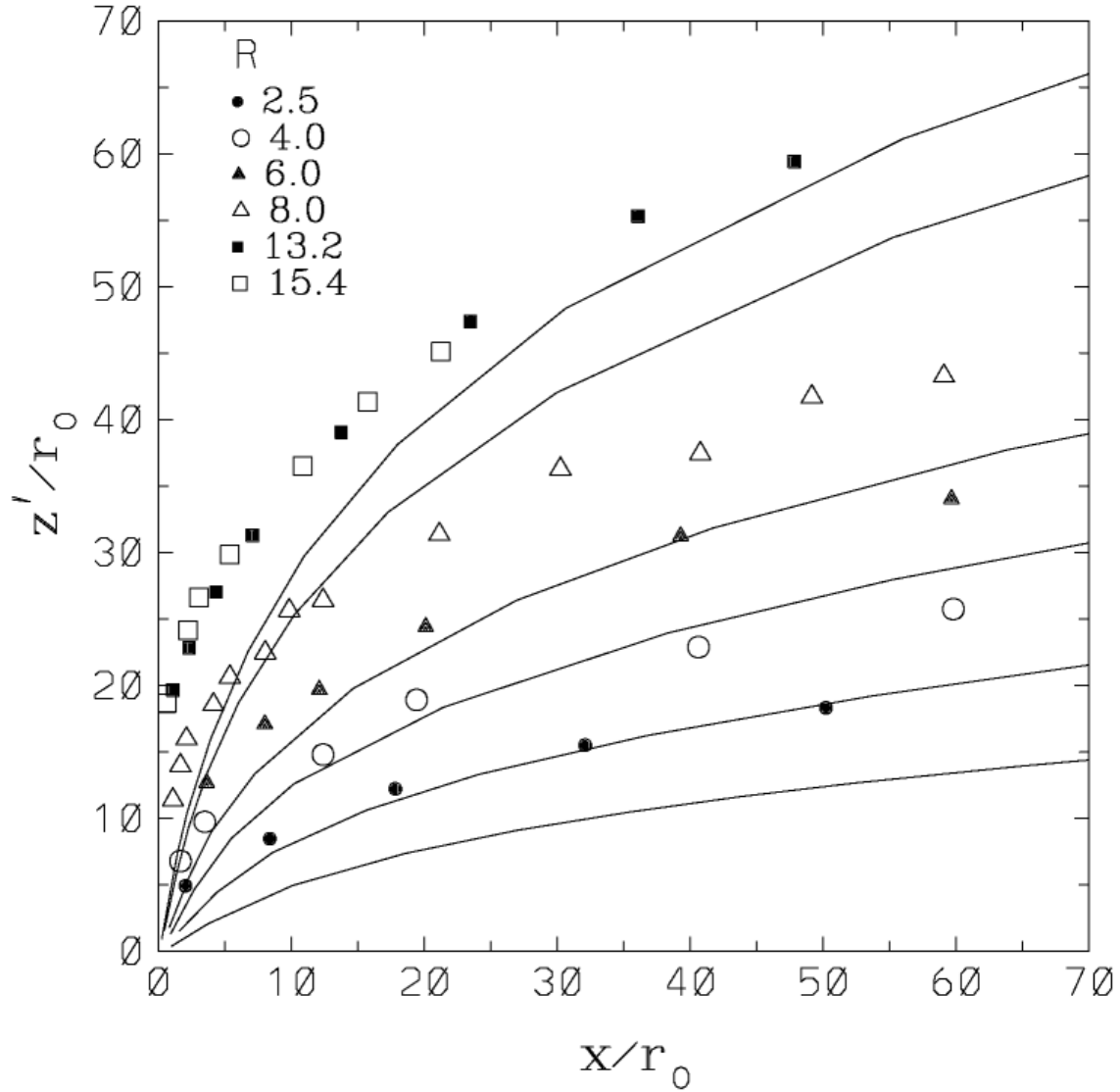


Figure 13-10

Momentum (non-buoyant) jet centerline height, z'/r_0 , as a function of downstream distance for a range of R . Symbols are the data of Gordier (1959), from Hirst (1971); solid lines are the SCIPUFF predictions.

The asymptotic behavior of the momentum jet far downstream is also of interest, and here we compare SCIPUFF with the well-known expression (see Weil, 1988 or Briggs, 1975):

$$\frac{z'}{\ell_m} = \left(\frac{3}{\beta^2} \right)^{1/3} \left(\frac{x}{\ell_m} \right)^{1/3} \quad \text{Eq. 13-3}$$

where x is downstream distance, z' is the jet centerline height above the source, β is an empirical entrainment constant typically set to 0.6, and the momentum length scale $\ell_m = Rr_0$. Figure 13-11 shows the SCIPUFF calculations for three exit velocity ratios compared with Equation 13-3. It can be seen that, although there is naturally some initial dependence on R , the three cases show

the same asymptotic behavior. The model predictions are consistent with the “one-third” power law but indicate a value for β around 0.5.

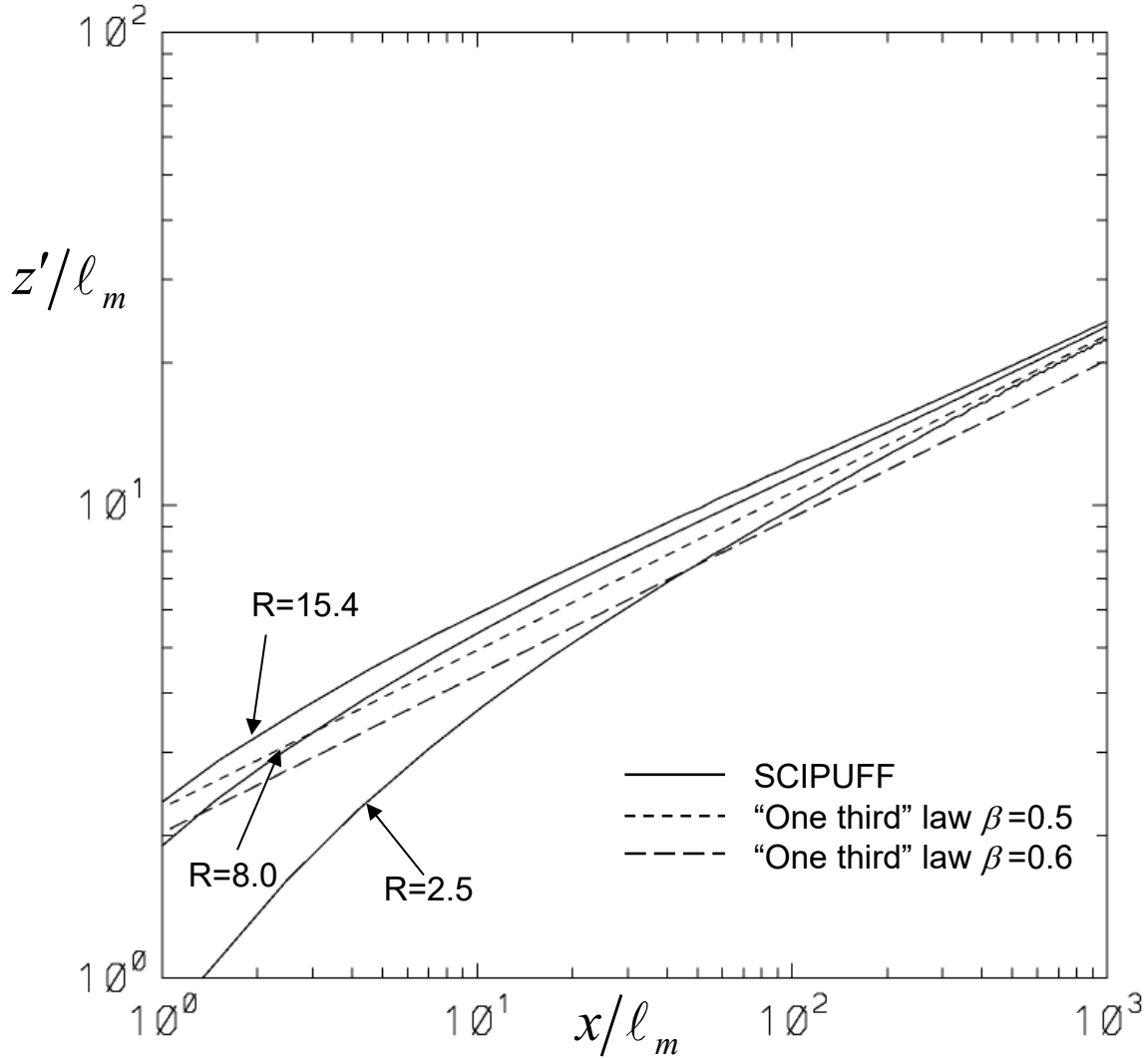


Figure 13-11
Comparison between SCIPUFF predictions of momentum jet centerline heights for a range of R (solid lines) and the “one-third” law (Equation 13-3), with two values of β (short dashes, $\beta = 0.6$; long dashes, $\beta = 0.5$)

13.3.2 Buoyant Plume

For a buoyancy-dominated plume in a neutral background, the plume height is given by the “two-thirds” power law (Briggs, 1975):

$$\frac{z'}{\ell_b} = \left(\frac{3}{2\beta^2} \right)^{1/3} \left(\frac{x}{\ell_b} \right)^{2/3} \quad \text{Eq. 13-4}$$

where the buoyancy length scale is given by $\ell_b = F_b / U_a^3$. The buoyancy flux, F_b , is defined as $F_b = W_0 r_0^2 g \Delta T_0 / T_a$ where ΔT_0 is the source temperature perturbation relative to the ambient temperature T_a . [F_b is related to the SCIPUFF buoyancy flux Q_T by $F_b = Q_T g / T_a \pi$]. The “two-thirds” law has been shown to compare well with numerous field and laboratory data (Briggs, 1975). The “one-third” and “two-thirds” laws are essentially limiting cases of a more general expression. Therefore, for plumes with significant buoyancy and momentum fluxes, the trajectory is given by

$$\frac{z'}{\ell_b} = \left[\frac{3}{\beta^2} \left(\frac{\ell_m}{\ell_b} \right)^2 \frac{x}{\ell_b} + \frac{3}{2\beta^2} \left(\frac{x}{\ell_b} \right)^2 \right]^{1/3} \quad \text{Eq. 13-5}$$

which reduces to Equation 13-4 for $x \gg \ell_m^2 / \ell_b$ and to Equation 13-3 with $x \ll \ell_m^2 / \ell_b$. A comparison of Equation 13-5 with the SCIPUFF predictions for a range of buoyancy fluxes and source sizes is shown in Figure 13-12. As expected, there are some discrepancies near the source, but the agreement with the two-thirds law is excellent further downstream.

Plume rise in a uniformly stratified environment ($N^2 = \text{a positive constant}$) has been investigated by Briggs (1975) who gives the following expression, which accounts for the “added mass” due to the displacement of ambient fluid by the plume:

$$\frac{z'}{(F_b / U_a N'^2)^{1/3}} = \left(\frac{3}{\beta'^2} \right)^{1/3} \left(N' \frac{F_m}{F_b} \sin \frac{N' x}{U_a} + 1 - \cos \frac{N' x}{U_a} \right)^{1/3} \quad \text{Eq. 13-6}$$

for $N' x / U_a \leq \pi$ where $N' = N / (1 + k_v)^{1/2}$, $\beta' = \beta / (1 + k_v)^{1/2}$ and k_v is the added mass coefficient (set to 1, the value for a circular cylinder). Based on an extensive survey of field and laboratory data, Briggs (1975) also determined an empirical expression for the “final” plume rise in stable air as

$$z'_{\text{final}} = 2.6 (F_b / U_a N^2)^{1/3} \quad \text{Eq. 13-7}$$

SCIPUFF predictions for a range of buoyancy fluxes and N compare quite favorably with Equations 13-6 and 13-7, as shown in Figure 13-13.

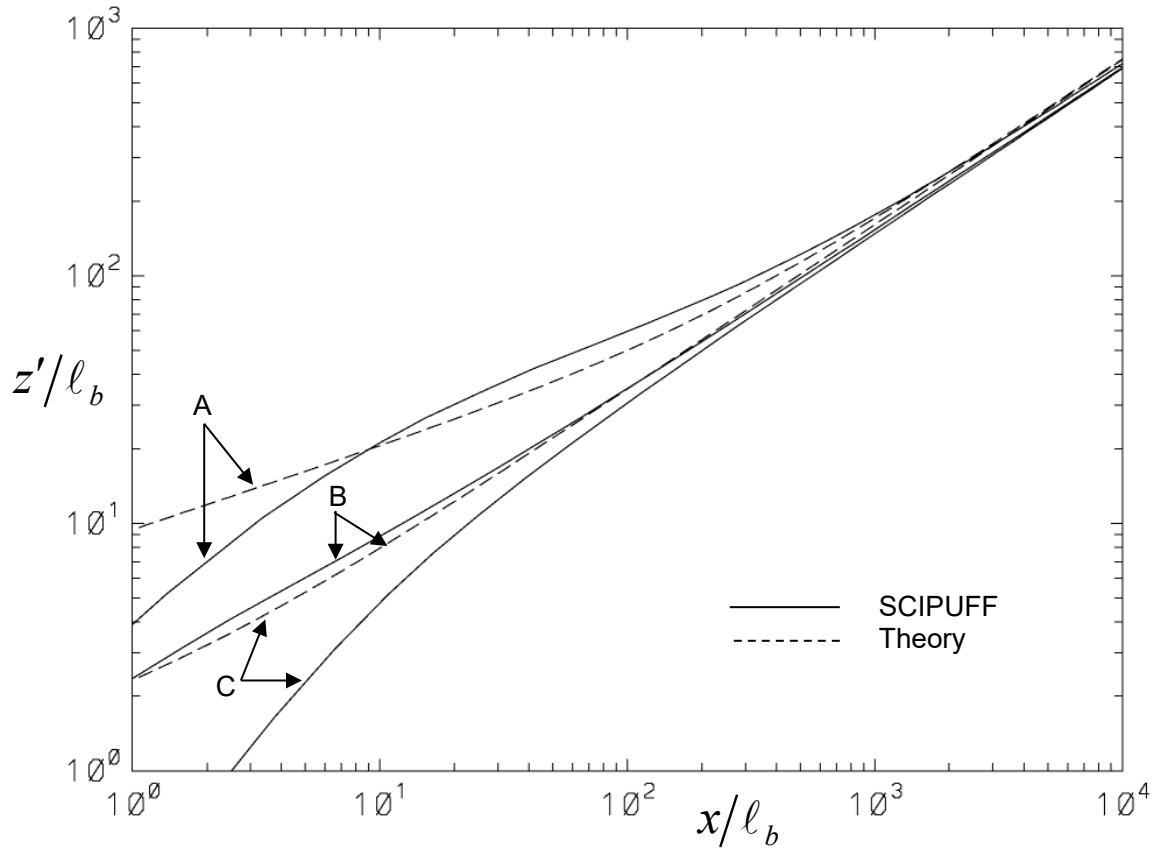


Figure 13-12
Comparison between SCIPUFF predictions for buoyancy-dominated jet centerline heights
(solid lines) and theory given by Equation 13-5 (dashed lines). Case A: $R = 10$, $F_b^2/U_a^4 F_m = 0.01$;
Case B: $R = 10$, $F_b^2/U_a^4 F_m = 1$; Case C: $R = 1$, $F_b^2/U_a^4 F_m = 1$.

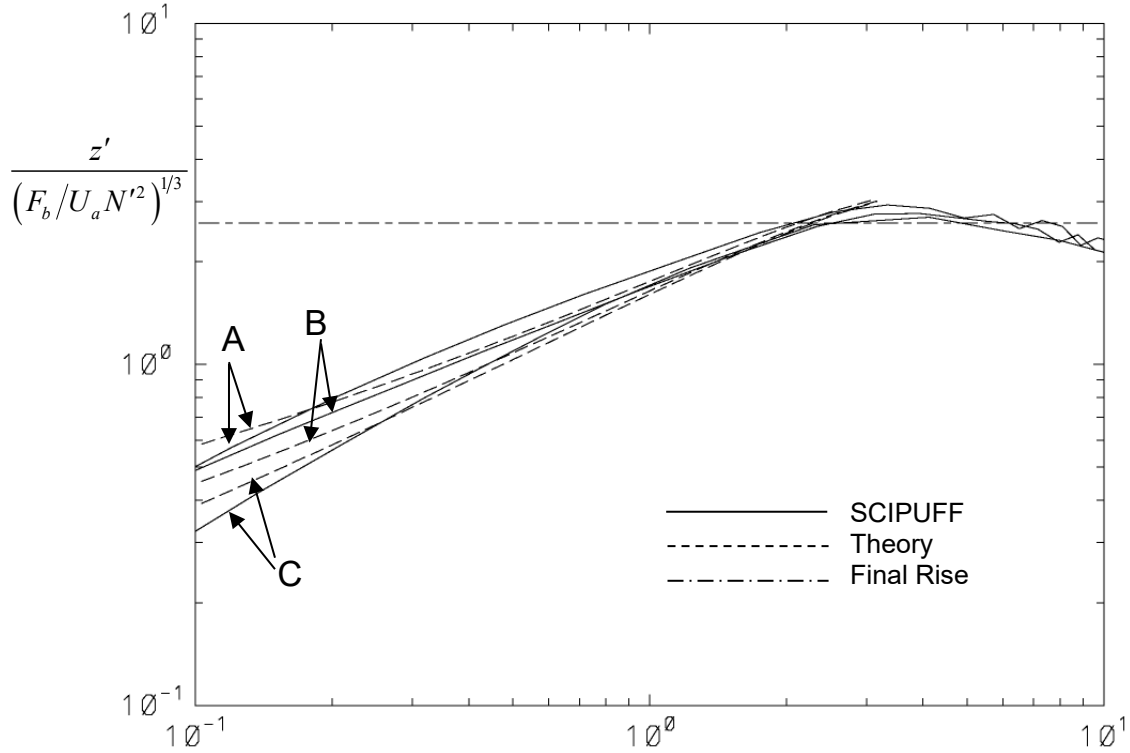


Figure 13-13

Comparison of SCIPUFF buoyancy-dominated jet centerline heights in a uniformly stratified background (solid lines) with Equation 13-6 (dashed lines). For all cases, $R = 10$. Case A:

$F_b^2 / U_a^4 F_m = 0.01$, $F_b N / U_a^4 = 0.00572$; **Case B:** $F_b^2 / U_a^4 F_m = 1$, $F_b N / U_a^4 = 0.00572$;

Case C: $F_b^2 / U_a^4 F_m = 1$, $F_b N / U_a^4 = 0.181$.

13.3.3 Buoyant Puff

The plume rise relations just presented are based on extensive laboratory and field experiments and are universally accepted, at least under the idealized conditions assumed. In contrast, the paucity of data for short-duration or nearly instantaneous buoyant releases precludes any generally accepted simple formulas. The only data we currently can compare SCIPUFF with come from experiments on the rise of light density spherical bubbles conducted in the early 1970s under DNA sponsorship (Mantrom and Haigh, 1973). These tests involved the release of helium bubbles in air or N_2 bubbles in SF_6 for a range of Reynolds numbers. The backgrounds were neutrally stratified and quiescent. For large enough Reynolds numbers, the bubble rise data generally collapse to a single curve of z'/D_0 vs. $t\sqrt{g/D_0}$ where, z' is the bubble centroid height above its release point, D_0 is the initial mean bubble diameter, and t is time after release. The SCIPUFF predictions are compared with the data in Figure 13-14. Two releases are considered for the model calculations—the first uses a single spherical puff with an initial Gaussian spread equal to the bubble radius; the second uses 136 puffs in an attempt to model explicitly an initial spherical bubble with a uniform mass distribution. It can be seen that the agreement with the data is generally quite good for both releases, although the multi-puff calculation tends to under-predict the bubble rise slightly. The late-time behavior in both the data and model calculations seems consistent with a power law exponent slightly less than two-thirds.

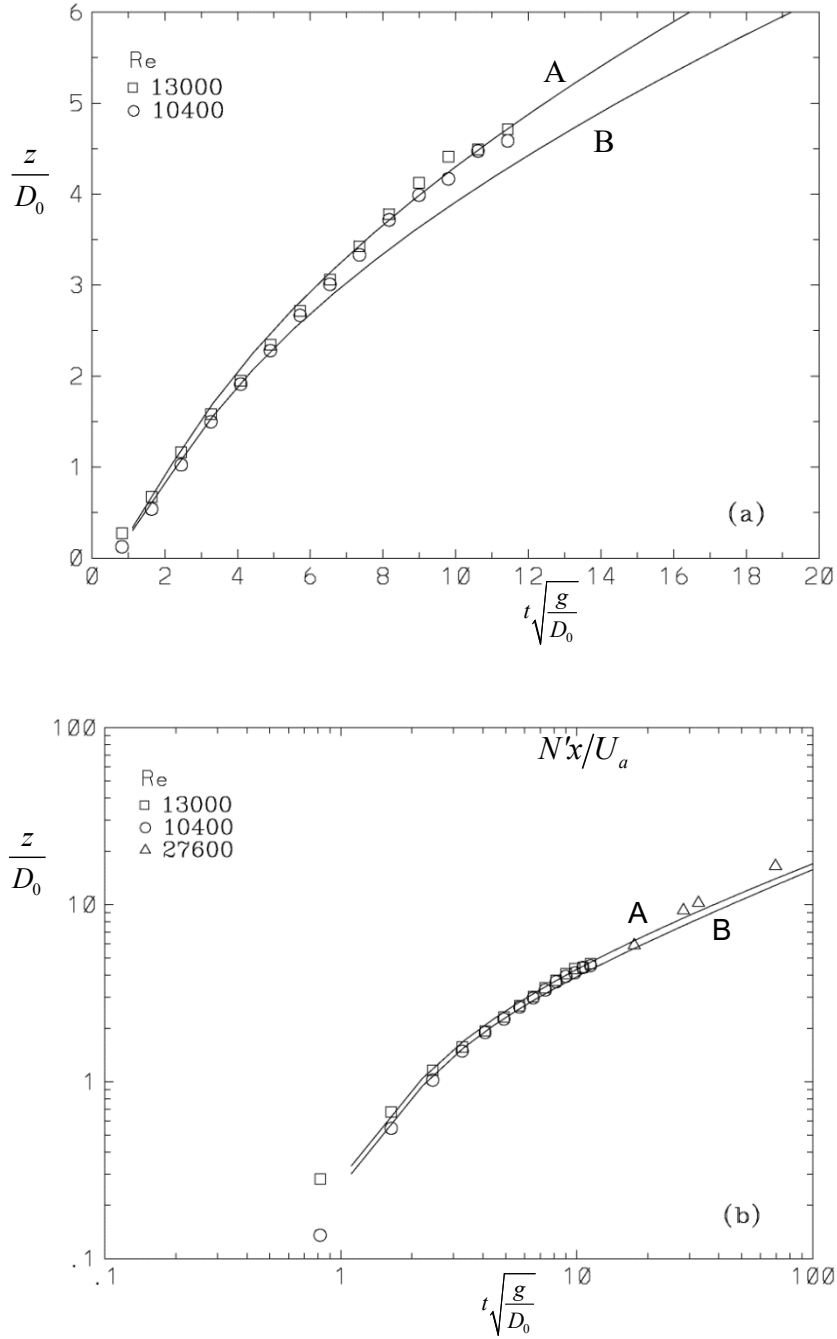


Figure 13-14

Centroid height of a light bubble released into a neutral quiescent background. Symbols are the data of Mantrom and Haigh (1973); solid lines are the SCIPUFF predictions. The Reynolds number for the experiments is based on the initial bubble diameter and the terminal velocity of a corresponding non-entraining sphere. Case A is for a single puff release with a Gaussian spread of $D_0/2$; Case B is for a release composed of 136 puffs representing a uniform distribution of mass within a spherical bubble of diameter D_0 . (a) early time behavior; (b) expanded scale showing late-time behavior.

13.4 Dense Gas Effects

The MDA, discussed in Section 13.1.2, also contains a dense gas release set composed of several experiments. The dense releases include evaporating pools (Burro, Coyote, and Maplin Sands experiments), continuous plumes and instantaneous clouds of heavy gas (Thorney Island), and two-phase aerosol jets (Desert Tortoise and Goldfish).

The Thorney Island tests used Freon gas and involved no evaporative effects, so the mass and mass fluxes were used directly for the continuous and instantaneous releases, respectively. The standard deviations were set to 75% of the specified source diameter.

For evaporating pools, we use a lateral standard deviation equal to 75% of the specified pool radius and a vertical standard deviation of 0.5 m for all cases. The vertical size is chosen arbitrarily to represent a typical vertical growth during transport across the pool, and results are not sensitive to the precise value. The initial buoyancy flux was determined from the given mass flux and the difference between the gas boiling temperature and the ambient value. We assume that the vaporizing material is released at the boiling point so that the buoyancy flux is

$$F_B = \frac{Q(T_b - T_a)c_p^{(gas)}}{\rho_{air} c_p^{(air)}} \quad \text{Eq. 13-8}$$

where c_p is the specific heat, T_b is the boiling point, T_a is the air temperature, and Q is the mass flow rate.

The Desert Tortoise and Goldfish releases involve a two-phase aerosol jet and exothermic reaction with the environment. Because SCIPUFF does not contain a model for aerosol evaporation—and the thermodynamics of the reactions were not prescribed—any model result will depend significantly on the choice for initial buoyancy conditions. We use a simplified representation, modeling the source jet as an expanding 7° cone until sufficient air has been entrained to evaporate the liquid aerosol. The SCIPUFF source is then initialized at this downstream location at the boiling temperature. The initial size is chosen to match the area implied by the expanding cone but with a horizontal spread that is twice the vertical. This procedure is similar to that used by Hanna et al. (1991) for other models that do not address the phase change effects.

The meteorology was specified in the same way as for the passive releases, except that no surface heat flux information was available for the Thorney Island continuous releases. For these cases, the estimate of the Monin-Obukhov length provided by Hanna et al. (1991) as input for the SLAB model was used.

The effects of time averaging were accounted for as described in Section 13.1.2, and the predicted centerline maxima are compared with the MDA observations in Figure 13-15. Agreement with the observations is slightly better than the passive releases shown in Figure 13-2; the geometric mean is 1.098 and the geometric variance is 1.355.

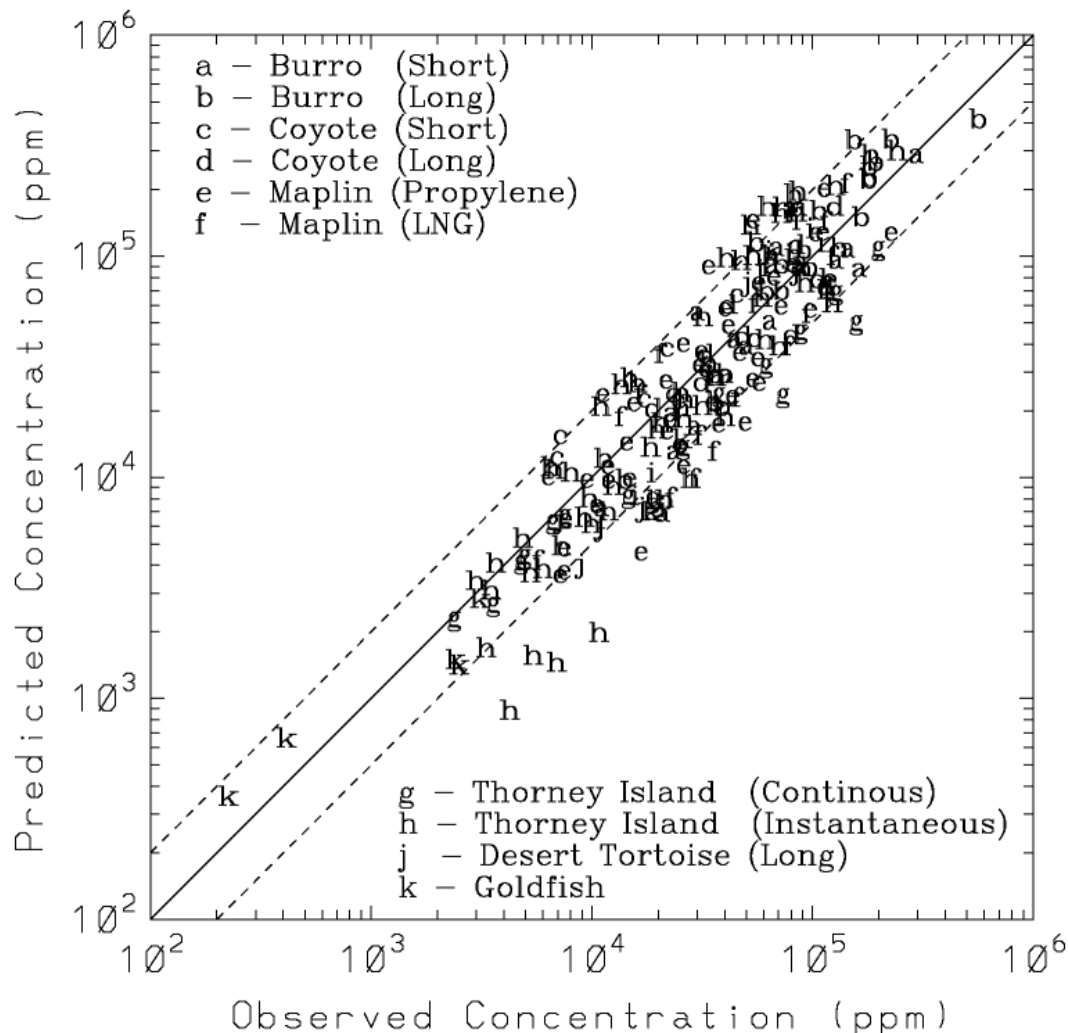


Figure 13-15

Comparison between the observed maximum concentrations and SCIPUFF predictions for the dense gas releases in the Model Data Archive. Various experiments are indicated by the letter codes.

13.5 Chemical Transformations

In 1998 and 1999, the Tennessee Valley Authority (TVA), the Department of Energy National Energy Technology Laboratory (DOE-NETL), and EPRI conducted an extensive study of secondary pollutant formation downwind of the Cumberland Power plant (Tanner et al., 2002). The TVA helicopter made multiple traverses to collect samples of the Cumberland plume at various downwind distances.

The SCICHEM model is used to simulate the Cumberland plume events and compare the results with helicopter measurements on the August 25 and 26, 1998, and July 6 and 15, 1999. The simulations were run for a period of 17–24 hours starting at midnight for a 300 km x 300 km x 2 km domain. The profiler meteorological data from Cumberland were used for the 1998 simulation (Figures 13-16 through 13-19) and the metrological data from Dickson (30 miles SE) were used for the 1999 simulation (Figures 13-20 through 13-23).

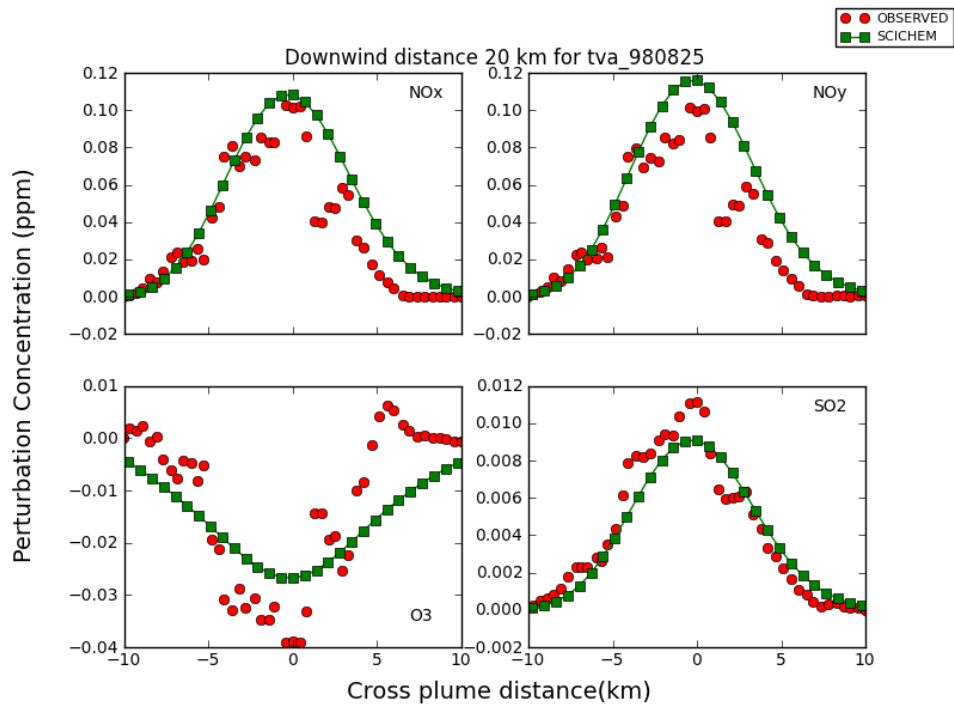


Figure 13-16
Results for Plume 5 at 20 km on August 25, 1998

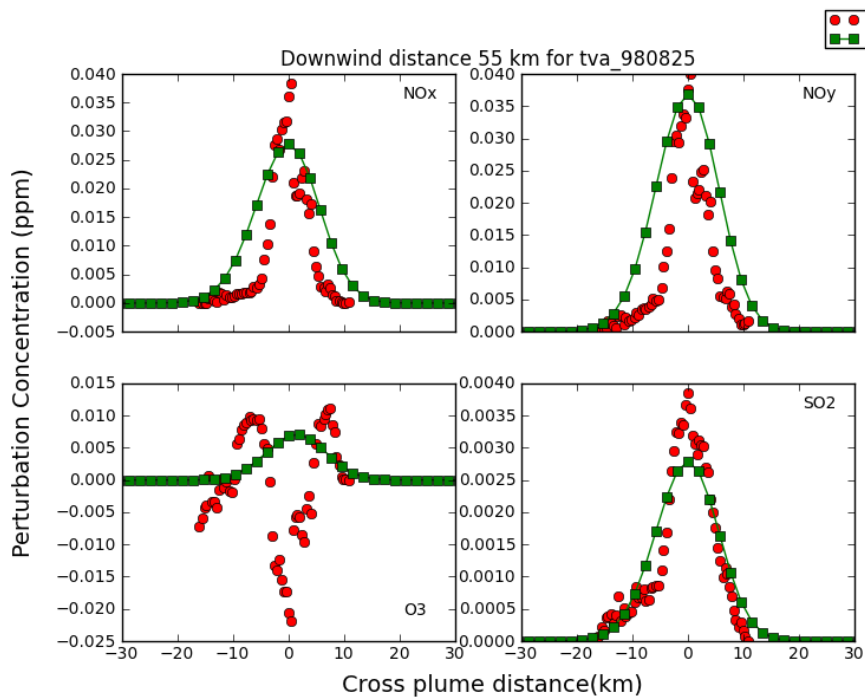


Figure 13-17
Results for Plume 7 at 55 km on August 25, 1998

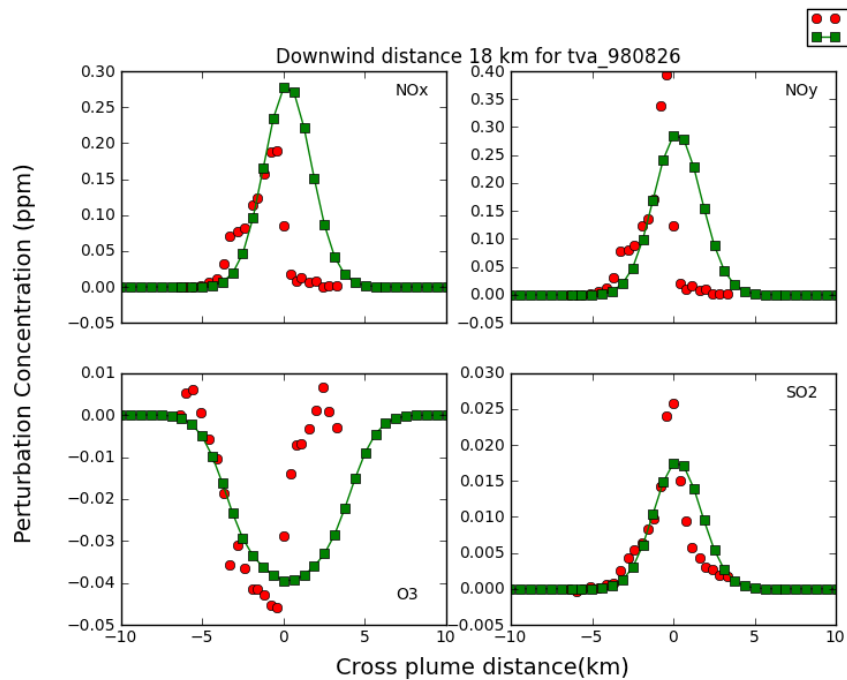


Figure 13-18
Results for Plume 2 at 18 km on August 26, 1998

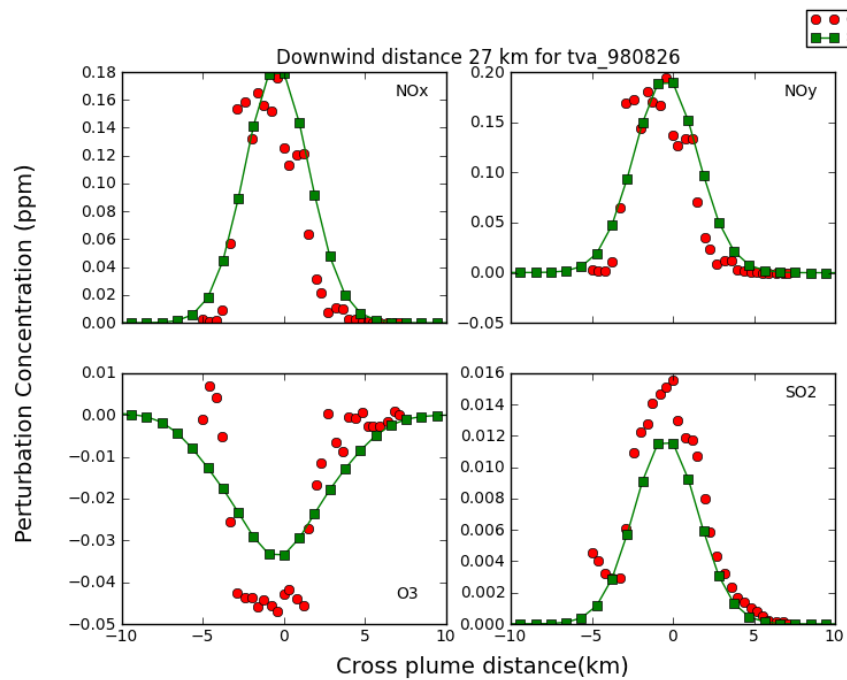


Figure 13-19
Results for Plume 4 at 27 km on August 26, 1998

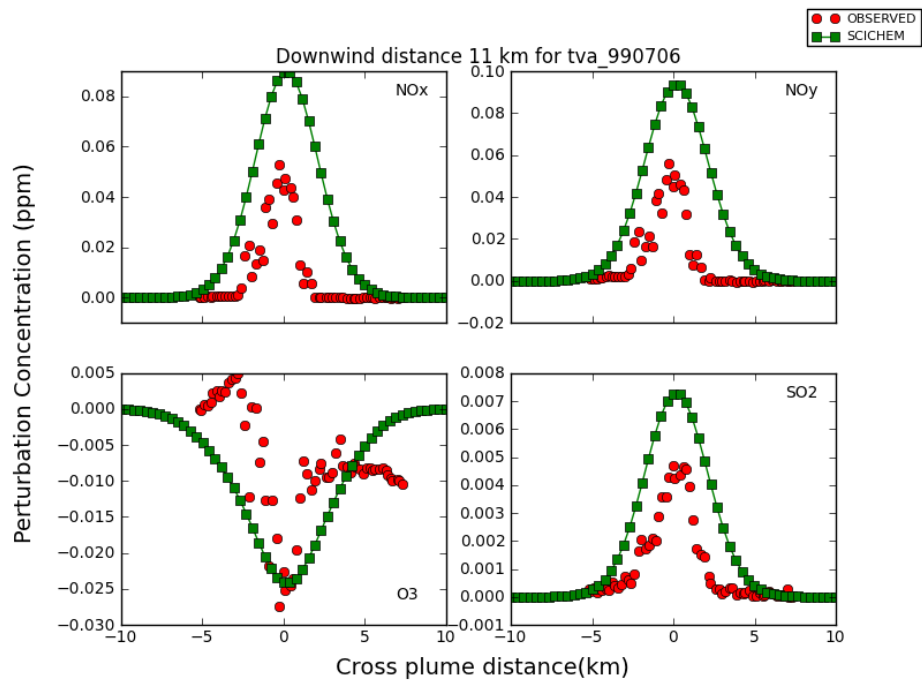


Figure 13-20
Results for Plume 2 at 11 km on July 6, 1999

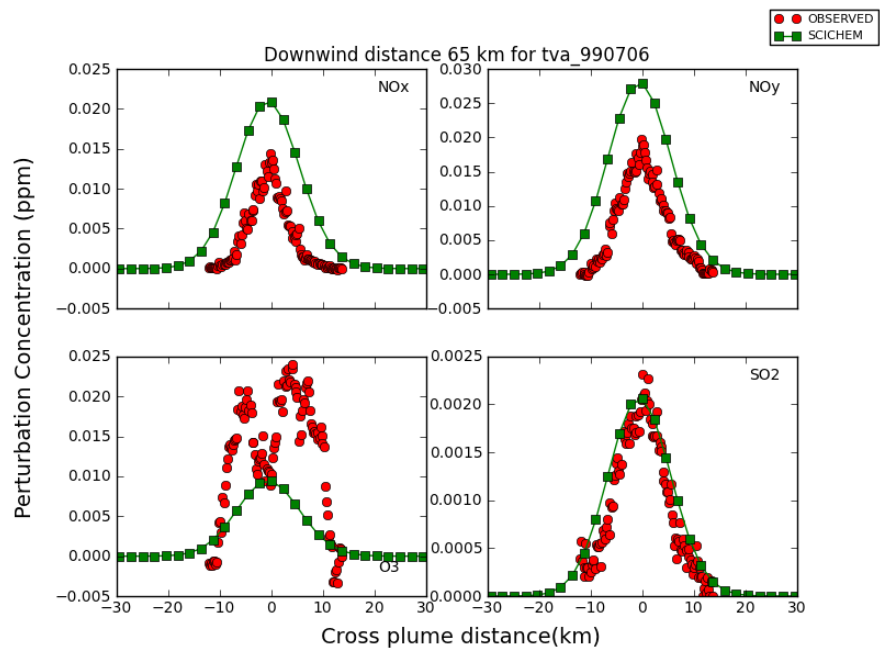


Figure 13-21
Results for Plume 9 at 65 km on July 6, 1999

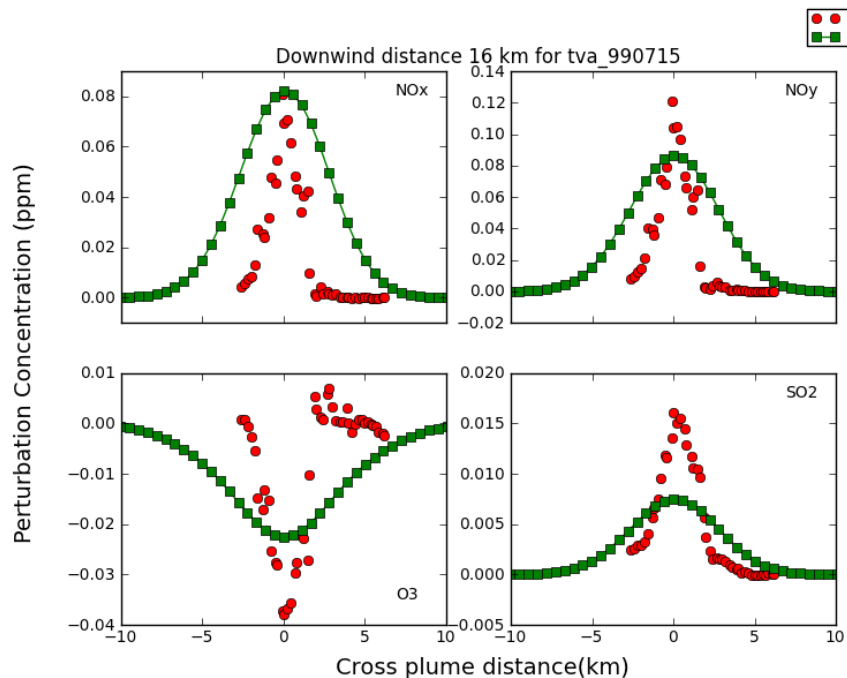


Figure 13-22
Results for Plume 2 at 16 km on July 15, 1999

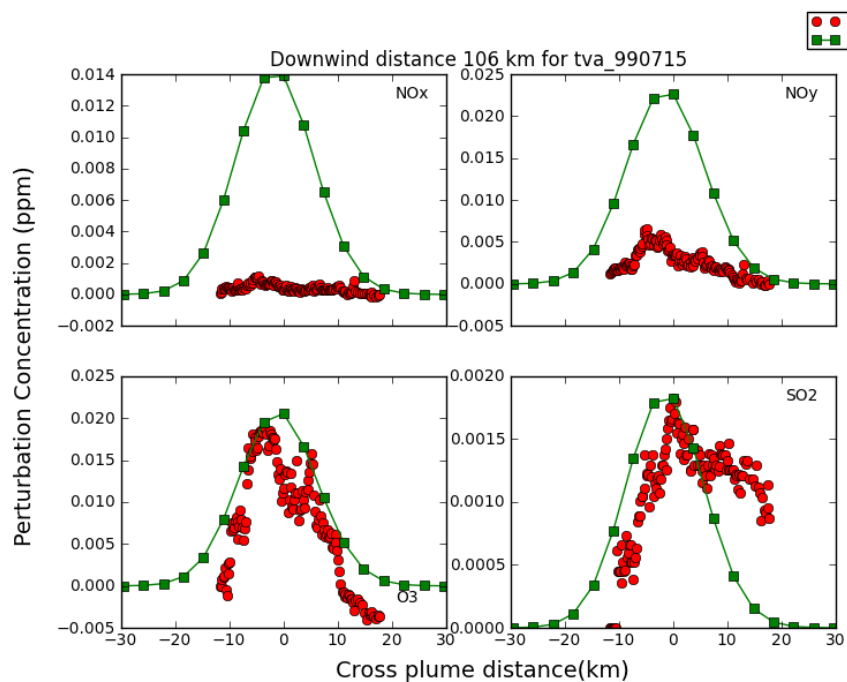


Figure 13-23
Results for Plume 11 at 106 km on July 15, 1999

Average hourly emissions were obtained from continuous emission monitoring system (CEMS) data and the values presented in Table 13-2. The species used in the comparison study were SO₂, NO_x (NO and NO₂), NO_y (NO, NO₂, NO₃, N₂O₅, HNO₃, HONO, and PAN), and O₃. The

preliminary SCICHEM results are compared at the mean time and height, with the average observed concentrations at various downwind distances. There was some deviation in the observed and modeled plume centerlines due to the difference between the actual and modeled wind fields. So, for ease of comparison, the plume centerlines are aligned with one another. To remove any differences due to the species background, the cross plume concentration perturbations are compared, where the perturbation is the difference between the actual plume concentration and the background or ambient concentration.

Table 13-2
Average Hourly Emissions Data

| Date | SO ₂ (Tonnes/hr) | NO _x (Tonnes/hr) |
|------------|-----------------------------|-----------------------------|
| 08/25/1998 | 2.5 | 15.2 |
| 08/26/1998 | 2.0 | 15.8 |
| 07/06/1999 | 1.1 | 6.7 |
| 07/15/1999 | 2.1 | 11.5 |

The evolution of the plume chemistry for a power plant plume has been studied extensively (Sillman et al., 2000; Ryerson et al., 2001), and the factors influencing the ozone production efficiency are well documented. Some of the important factors affecting the formation of ozone are the meteorological conditions such as boundary layer height, emission rates, and the NO_x to volatile organic compound (VOC) ratios.

Near the source, the background O₃ is scavenged by the excess NO_x in the plume, resulting in plume concentrations that are lower than the background. This plume behavior is captured by the model simulation as seen from the concentration perturbation plots of the different species near the source in Figures 13-16, 13-18, 13-20, and 13-22.

At this distance, there are large uncertainties in the measured values for the different traverses—especially for the nitrate species—due to the difficulty in measuring the concentrations for these species (Luria et al., 2000). The model predicted values at these distances differ from the mean observed concentration, but the values are within 1 standard deviation. Further downwind, at distances greater than 30 km, the NO_x to VOC ratios are more favorable for O₃ production but the levels of O₃ still stay below the ambient levels. From Figure 13-19, we can see that the SCICHEM model predicts depletion of O₃ concentration in the plume center and that the minimum predicted values matched the observed minimums. However, at these distances, the observed O₃ concentrations show wing-like structures that are formed due to the difference in NO_x concentrations at the edge of the plume and the plume center. In SCICHEM, the puff splitting is based on the meteorology and the puff resolution is adapted to the appropriate length scale for computational efficiency. Using the default resolution, the plume cross-section is represented by a fewer number of Gaussian puffs; therefore, the model is unable to capture the non-Gaussian shape of the wings at the plume edges. As the plume moves further downwind, VOC entrainment leads to the production of excess O₃ as shown by the predicted and observed values in Figures 13-21 and 13-23.

The downwind distance at which the ozone production starts is sensitive to the VOC concentration, such as isoprene emitted from biogenic sources (Ryerson et al., 2001). Similarly,

the background concentration values of radical species such as OH and HO₂ also play a vital role in determining the ozone production efficiency. The range of concentrations in the background for VOC and radical species is very broad and depend on various conditions such as temperature and cloud cover. For isoprene, the background concentration values can range from 1.5 ppb to 10 ppb near the surface to lower values at higher altitude (Luria et al., 2000). Similarly, the background OH and HO₂ concentration as reported by Martinez et al. (2003) varied day to day during the 1999 Southern Oxidant Study at Nashville. Therefore, some of the difference in the predicted and observed values can be attributed to incorrect or varying VOC and OH background concentrations as well as measurement errors in recording the observations. Another factor that influences the width of the predicted plume is the large-scale variances in the troposphere. The large-scale variance is a function of $\bar{\epsilon}$, the tropospheric energy dissipation rate, which varies over a wide range of values as reported by H. Siebert et al. (2006). In this study, we found that the lower values of $\bar{\epsilon}$ provided a better estimate of the plume width.

14

REFERENCES

- Bass, A. (1980), "Modelling long range transport and diffusion," *Second Joint Conf. on Appl. of Air Poll. Met.*, AMS & APCA, New Orleans, LA, pp. 193–215.
- Biltoft, C. A. (1995), "Surface effects on concentration fluctuation profiles," Joint Contact Point Directorate, Dugway Proving Ground, DPG/JCP-95019.
- Boris, J. (1986), "A vectorized 'near neighbors' algorithm of order N using a monotonic logical grid," *J. Comp. Phys.*, **66**, 1–20.
- Briggs, G. A. (1975), "Plume rise predictions," *Lectures on Air Pollution and Environmental Impact Analysis*, 59–111, ed. D. A. Haugen, Am. Met. Soc., Boston MA.
- Businger, J. A. (1973), "Turbulent transfer in the atmospheric surface layer," *Workshop on Micrometeorology*, ed. D. A. Haugen, American Meteorological Society, Boston, MA.
- Businger, J. A. (1986), "Evaluation of the accuracy with which dry deposition can be measured with current micrometeorological techniques," *J. Clim. & Appl. Met.*, **25**, 1100–1124.
- Byun D. and K.L. Schere (2006), "Review of the governing equations, computational algorithms, and other components of the Models-3 Community Multiscale Air Quality (CMAQ) modeling system," *Appl. Mech. Rev.*, **59**(2), 51-77, doi:10.1115/1.2128636.
- Carlton, A.G., B.J. Turpin, K.E. Altieri, S.P. Seitzinger, R. Mathur, S.J. Roselle, and R.J. Weber (2008), "CMAQ model performance enhanced when in-cloud secondary organic aerosol is included: Comparisons of organic carbon predictions with measurements," *Environ. Sci. Technol.*, **42**, 8798-8802.
- Carlton, A.G., P.V. Bhave, S.L. Napelenok, E.O. Edney, G. Sarwar, R.W. Pinder, G.A. Pouliot, and M. Houyoux (2010), "Model representation of secondary organic aerosol in CMAQv4.7," *Environ. Sci. Technol.*, **44**, 8553-8560.
- Carson, D. J. (1973), "The development of a dry inversion-capped convectively unstable boundary layer," *Quart. J. Roy. Met. Soc.*, **99**, 450–467.
- Carson, D. J. and P. J. R. Richards (1978), "Modelling surface turbulent fluxes in stable conditions," *Boundary-Layer Met.*, **14**, 67–81.
- Chamberlain, A. C. (1967), "Transport of *Lycopodium* spores and other small particles to rough surfaces," *Proc. Roy. Soc.*, **296A**, 45–70.
- Clark, T. L. (1977), "A small-scale dynamic model using a terrain-following coordinate transformation," *J. Comp. Phys.*, **24**, 186–215.
- Davidson, C. I., J. M. Miller, and M. A. Pleskow (1982), "The influence of surface structure on predicted particle dry deposition to natural grass canopies," *Water Air Soil Pollut.*, **18**, 25–43.

- Deardorff, J. W. (1970), "Convective velocity and temperature scales for the unstable planetary boundary layer and for Rayleigh convection," *J. Atmos. Sci.*, **27**, 1211–1213.
- Deardorff, J. W. (1980), "Progress in understanding entrainment at the top of a mixed layer," Workshop on the Planetary Boundary Layer, Amer. Meteor. Soc., 36–66.
- Donaldson, C. du P. (1973), "Atmospheric turbulence and the dispersal of atmospheric pollutants," *AMS Workshop on Micrometeorology*, ed. D. A. Haugen, Science Press, Boston, pp. 313–390.
- Egan, B. A. and J. R. Mahoney (1972), "Numerical modeling of advection and diffusion of urban area source pollutants," *J. Appl. Met.*, **11**, 312–322.
- Etling, D. (1990), "On plume meandering under stable stratification," *Atmos. Env.*, **24A**, 1979–1985.
- Fackrell, J. E. and A. G. Robins (1982), "Concentration fluctuations and fluxes in plumes from a point source in a turbulent boundary layer," *J. Fluid Mech.*, **117**, 1–26.
- Friedlander, S. K. (1977), *Smoke, Dust and Haze*. Wiley, New York, 317 pp.
- Foley, K.M., S.J. Roselle, K.W. Appel, P.V. Bhave, J.E. Pleim, T.L. Otte, R. Mathur, G. Sarwar, J.O. Young, R.C. Gilliam, C.G. Nolte, J.T. Kelly, A.B. Gilliland, and J.O. Bash (2010), "Incremental testing of the Community Multiscale Air Quality (CMAQ) modeling system version 4.7," *Geosci. Model Dev.*, **3**, 205–226.
- Fountoukis, C. and A. Nenes (2007), "ISORROPIA II: a computationally efficient thermodynamic equilibrium model for K^+ – Ca^{2+} – Mg^{2+} – NH_4^+ – Na^+ – SO_4^{2-} – NO_3^- – Cl^- – H_2O aerosols," *Atmos. Chem. Phys.*, **7**, 4639–4659.
- Fuchs, N. A. (1964), *The Mechanics of Aerosols*. Pergamon, New York.
- Gifford, F. A. (1959), "Statistical properties of a fluctuating plume dispersal model," *Adv. Geophys.*, **6**, 117–137.
- Gifford, F. A. (1988), "A similarity theory of the tropospheric turbulence energy spectrum," *J. Atmos. Sci.*, **45**, 1370–1379.
- Gordier, R. L. (1959), "Studies on fluid jets discharging normally into moving liquid," St. Anthony Falls Hyd. Lab., University of Minnesota, 28, Series B.
- Hanna, S. R. (1983), "Lateral turbulence intensity and plume meandering during stable conditions," *J. Clim. Appl. Met.*, **22**, 1424–1431.
- Hanna, S. R., D. G. Strimaitis, and J. C. Chang (1991), "Hazard response modeling uncertainty (a quantitative method). Volume II. Evaluation of commonly used hazardous gas dispersion models," Air Force Engineering and Service Center.
- Henn, D. S., R. S. Gabruk, S. F. Parker, and R. I. Sykes (1995), "CLOUDTRANS: A TASS and DIAL-A-CLOUD Output Translator Code," Defense Nuclear Agency, DNA-TR-94-85.

- Hindmarsh, A. C. (1983), "ODEPACK: a systematized collection of ODE solvers," in *Numerical Methods for Scientific Computing* (edited by Stepleman, R.S., et al.), p. 55–64, North Holland, New York.
- Hirst, E. A. (1971), "Analysis of round, turbulent, buoyant jets discharged to flowing stratified ambients," Oak Ridge National Laboratory, ORNL-4685.
- Högström, U. (1964), "An experimental study on atmospheric diffusion," *Tellus*, **16**, 205–251.
- Holtslag, A. A. (1984), "Estimates of diabatic wind speed profiles from near-surface weather observations," *Boundary-Layer Met.*, **29**, 225–250.
- Holtslag, A. A. M. and A. P. van Ulden (1983), "A simple scheme for daytime estimates of the surface fluxes from routine weather data," *J. Clim. & Appl. Met.*, **22**, 517–529.
- Kasten, F. and G. Czeplak (1989), "Solar and terrestrial radiation dependent on the amount and type of cloud," *Solar Energy*, **24**, 177–189.
- Kato, H. and O. M. Phillips (1969), "On the penetration of a turbulent layer into a stratified fluid," *J. Fluid Mech.*, **37**, 643–655.
- Klebanoff, P. S. (1955), "Characteristics of turbulence in a boundary layer with zero pressure gradient," Nat. Adv. Ctee. Aero., Wash., Report no. 1247.
- Launder, B. E., G. J. Reece, and W. Rodi (1975), "Progress in the development of a Reynolds-stress turbulence closure," *J. Fluid Mech.*, **68**, 537–566.
- Lewellen, W. S. (1977), "Use of invariant modeling," *Handbook of Turbulence*, ed. W. Frost and T. H. Moulden, Plenum Press, pp. 237–280.
- Lewellen, W. S. (1981), "Modeling the lowest 1km of the atmosphere," AGARD, AGARD-AG-267.
- Lewellen, W. S. (1985), "Modeling turbulent exchange in forest canopies," *The Forest-Atmosphere Interaction*, ed. B. A. Hutchison and B. B. Hicks, D. Reidel, Dordrecht, pp. 481–499.
- Lewellen, W. S. and Y. P. Sheng (1980), "Modeling of dry deposition of SO₂ and sulfate aerosols," EPRI, EA-1452, Project 1306-1, 67 .pp.
- Lewellen, W. S. and R. I. Sykes (1986), "Analysis of concentration fluctuations from lidar observations of atmospheric plumes," *J. Clim. & Appl. Met.*, **25**, 1145–1154.
- Mantrom, D. D. and W. W. Haigh (1973), "Fireball Entrainment Study," Defense Nuclear Agency, DNA 3248F.
- Mason, P. J. (1989), "Large-eddy simulation of the convective atmospheric boundary layer," *J. Atmos. Sci.*, **46**, 1492–1516.
- Mason, P. J. and D. J. Thompson (1987), "Large-eddy simulations of the neutral-static-stability planetary boundary layer," *Quart. J. Roy. Met. Soc.*, **113**, 413–444.

Mellor, G. L. and H. J. Herring (1973), "A survey of mean turbulent field closure models," *AIAA J.*, **11**, 590–599.

Mikkelsen, T., S. E. Larsen, and H. L. Pécseli (1987), "Diffusion of Gaussian puffs," *Quart. J. Roy. Met. Soc.*, **113**, 81–105.

Mosca, S., G. Graziani, W. Klug, R. Bellasio, and R. Bianconi (1997), "ATMES-II - Evaluation of long-range dispersion models using 1st ETEX release data: Volume 1," JRC-Environment Institute.

Nastrom, G. D. and K. S. Gage (1985), "A climatology of atmospheric wavenumber spectra of wind and temperature observed by commercial aircraft," *J. Atmos. Sci.*, **42**, 950–960.

Nieuwstadt, F. T. M. (1981), "The steady-state height and resistance laws of the nocturnal boundary layer: Theory compared with the Cabauw observations," *Boundary-Layer Met.*, **20**, 3–17.

Paine, R. J. (1987), "User's guide to the CTDM meteorological preprocessor (METPRO) program," Atmos. Sci. Res. Lab., USEPA, Contract No. 68-02-3421.

Paltridge, G. W. and C. M. R. Platt (1976), *Radiative Processes in Meteorology and Climatology*. Elsevier, 318 pp.

Saucier, R. (1987), "NUSSE3 model description," Chemical Research and Development & Engineering Center, CRDEC-TR-87046.

Sawford, B. L. (1982), "Comparison of some different approximations in the statistical theory of relative dispersion," *Quart. J. Roy. Met. Soc.*, **108**, 191–206.

Schmidt, H. and U. Schumann (1989), "Coherent structure of the convective boundary layer derived from large-eddy simulations," *J. Fluid Mech.*, **200**, 511–562.

Schumann, U. (1988), "Minimum friction velocity and heat transfer in the rough surface layer of a convective boundary layer," *Boundary-Layer Met.*, **44**, 311–326.

Sehmel, G. A. (1973), "Particle eddy diffusivities and deposition velocities for isothermal flow and smooth surfaces," *Aerosol Sci.*, **4**, 125–138.

Slinn, W. G. N. (1982), "Predictions for particle deposition to vegetative canopies," *Atmos. Env.*, **16**, 1785–1794.

Spalart, P. R. (1989), "Theoretical and numerical study of a three-dimensional turbulent boundary layer," *J. Fluid Mech.*, **205**, 319–340.

Sykes, R. I. (1984), "The variance in time-averaged samples from an intermittent plume," *Atmos. Env.*, **18**, 121–123.

Sykes, R. I., W. S. Lewellen, and S. F. Parker (1984), "A turbulent-transport model for concentration fluctuations and fluxes," *J. Fluid Mech.*, **139**, 193–218.

Sykes, R. I., W. S. Lewellen, and S. F. Parker (1986), "A Gaussian plume model of atmospheric dispersion based on second-order closure," *J. Clim. & Appl. Met.*, **25**, 322–331.

- Sykes, R. I., W. S. Lewellen, S. F. Parker, and D. S. Henn (1988), "A hierarchy of dynamic plume models incorporating uncertainty, Volume 4: Second-order Closure Integrated Puff," EPRI, EPRI EA-6095 Volume 4, Project 1616–28.
- Sykes, R. I. and D. S. Henn (1992), "An improved moment conservation method for the advection-diffusion equation," *J. Appl. Met.*, **31**, 112–118.
- Sykes, R. I. and W. S. Lewellen (1992), "Review of potential models for UF₆ dispersion," Martin Marietta energy Systems, Inc., K/GDP/SAR-19.
- Sykes, R. I., Henn, D. S., and S. F. Parker (1992), "Large-eddy simulation of a turbulent reacting plume," *Atmos. Environ.*, **26A**, 2565–2574.
- Sykes, R. I., D. S. Henn, and C. P. Cerasoli (1993a), "Near surface dust: Late time atmospheric effects," Defense Nuclear Agency, DNA-TR-93-175.
- Sykes, R. I., D. S. Henn, and W. S. Lewellen (1993b), "Surface-layer description under free-convection conditions," *Quart. J. Roy. Met. Soc.*, **119**, 409–421.
- Sykes, R. I., S. F. Parker, D. S. Henn, and W. S. Lewellen (1993c), "Numerical simulation of ANATEX tracer data using a turbulence closure model for long-range dispersion," *J. Appl. Met.*, **32**, 929–947.
- Sykes, R. I., Parker, S. F., and D. S. Henn (1994), "Turbulent mixing with chemical reaction in the planetary boundary layer," *J. Appl. Met.*, **33**, p. 825–834.
- Sykes, R. I. and R. S. Gabruk (1997), "A second-order closure model for the effect of averaging time on turbulent plume dispersion," *J. Appl. Met.*, **36**, 165–184.
- Sykes, R. I., L. P. Santos, and D. S. Henn (1998), "Large Eddy Simulation of a turbulent reacting plume in a convective boundary layer," *Proc. 10th Conference on Appl. of Air Pollut. Meteor.*, Jan. 1116, 78th Annual AMS Meeting, Phoenix, AZ, 539–543.
- Taylor, G. I. (1921), "Diffusion by continuous movements," *Proc. Lond. Math. Soc. (Ser. 2)*, **20**, 196–211.
- Thomson, D. J. (1987), "Criteria for the selection of stochastic models of particle trajectories in turbulent flows," *J. Fluid Mech.*, **180**, 529–556.
- Townsend, A. A. (1976), *The structure of turbulent shear flow*. Cambridge University Press, Cambridge, 429 pp.
- Van Ulden, A. P. and A. A. M. Holtslag (1983), "The stability of the atmosphere surface layer during nighttime," *Sixth Symp. on Turbulence and Diffusion*, American Meteorological Society, Boston, MA, 257–260.
- Venkatram, A. K. (1980), "Estimating the Monin-Obukhov length in the stable boundary layer for dispersion calculations," *Boundary-Layer Met.*, **19**, 481–485.
- Venkatram, A. and J. C. Wyngaard (1988), "Lectures on air pollution modeling," American Meteorological Society, Boston, MA.

Weil, J. C. (1988), “Dispersion in the convective boundary layer,” *Lectures on Air Pollution Modeling*, 167–227, ed. A. Venkatram and J. C. Wyngaard, Amer. Met. Soc., Boston.

Weil, J. C., R. P. Lawson, and A. R. Rodi (1993), “Relative dispersion of ice crystals in seeded cumuli,” *J. Appl. Met.*, **32**, 1055–1073.

Wyngaard, J. C. (1985), “Structure of the Planetary Boundary Layer and Implications for its Modeling,” *J. Climate Appl. Meteor.*, **24**, 1131–1142.

Yarwood, G., J. Jung, G.Z. Whitten, G. Heo, J. Mellberg, and M. Estes (2010), *Ninth Annual CMAS Conference*, Chapel Hill, NC, October 11-13, 2010.

Yee, E. (1990), “The shape of the probability density function of short-term concentration fluctuations of plumes in the atmospheric boundary layer,” *Boundary-Layer Met.*, **51**, 269–298.

Zilitinkevich, S. S. (1972), “On the determination of the height of the Ekman boundary layer,” *Boundary-Layer Met.*, **3**, 141–145.

Zhang, L., J. R. Brook, and R. Vet (2003), “A revised parameterization for gaseous dry deposition in air quality models,” *Atmos. Chem. Phys.*, **3**, 2067–2082.

The Electric Power Research Institute, Inc. (EPRI, www.epri.com) conducts research and development relating to the generation, delivery and use of electricity for the benefit of the public. An independent, nonprofit organization, EPRI brings together its scientists and engineers as well as experts from academia and industry to help address challenges in electricity, including reliability, efficiency, affordability, health, safety and the environment. EPRI also provides technology, policy and economic analyses to drive long-range research and development planning, and supports research in emerging technologies. EPRI members represent 90% of the electricity generated and delivered in the United States with international participation extending to nearly 40 countries. EPRI's principal offices and laboratories are located in Palo Alto, Calif.; Charlotte, N.C.; Knoxville, Tenn.; Dallas, Texas; Lenox, Mass.; and Washington, D.C.

Together...Shaping the Future of Energy™